DEGRADATION
OF CIGS SOLAR CELLS

Mirjam Theelen

DEGRADATION
OF CIGS SOLAR CELLS

Proefschrift

ter verkrijging van de graad van doctor
aan de Technische Universiteit Delft
op gezag van de Rector Magnificus prof. ir. K. C. A. M. Luyben,
voorzitter van het College voor Promoties
in het openbaar te verdedigen op
vrijdag 2 oktober 2015 om 15:00 uur

door
MARIA JOHANNA THEELEN
Master of Science, Radboud Universiteit Nijmegen
geboren te Eindhoven

Dit proefschrift is goedgekeurd door de promotor:
Prof. dr. M. Zeman

Copromotoren:
Dr. Z.A.E.P. Vroon
Dr. N. Barreau

Samenstelling promotiecommissie:

Rector Magnificus	voorzitter
Prof. dr. M. Zeman	Technische Universiteit Delft, promotor
Dr. Z.A.E.P. Vroon	TNO, Hogeschool Zuyd, copromotor
Dr. N. Barreau	Université de Nantes, Frankrijk, copromotor

Onafhankelijke leden:

Prof. dr. J. Schmitz	Universiteit Twente
Prof. dr. W.A. Groen	Technische Universiteit Delft, Holst Centre
Dr. D.F.C. Lincot	IRDEP, Frankrijk
Prof. dr. A.W. Weeber	Technische Universiteit Delft

This study was carried out under project number M71.9.10401 in the framework of the Research Program of the Materials innovation institute M2i (www.m2i.nl). Further financial support came from TNOs' Enabling Technology Program Materials Technology.

Book design: Ilse Schrauwers - www.isontwerp.nl
Illustrations titlepages: Cécile Verleg - www.cecileverleg.nl

Cover photograph: Mirjam Theelen
Molybdenum under a light microscope (unmodified picture)

Printing: Ipskamp Drukkers - www.proefschriften.net

ISBN: 978-94-6259-348-0

TABLE of Contents

1. Introduction 7

2. Stability of Cu(In,Ga)Se_2 Solar Cells - A literature review 25

3. In-situ monitoring of the degradation of CIGS solar cells 91

4. Temperature dependency of the electrical parameters of CIGS solar cells 105

5. Degradation mechanisms of the molybdenum back contact 125

6. Degradation mechanisms of the aluminium doped zinc oxide front contact 175

7. The impact of alkali elements on the degradation of CIGS solar cells 213

8. The impact of atmospheric species on the degradation of CIGS solar cells 239

9. Overview and outlook 259

10. Summaries 267
  Summary in English 268
  Samenvatting in het Nederlands 272
  Résumé en Français 276

APPENDICES 281
  Appendix A: Analysis techniques 282
  Appendix B: Abbreviations 283
  List of Publications 285
  Dankwoord / Acknowledgements 288
  Curriculum Vitae inside cover


WE
RUle

CHAPTER 1

Introduction

1.1 Photovoltaics

Switching from finite and polluting energy sources to renewable and clean sources is one of the great challenges of our age. As such, many kinds of renewable energy technologies are major areas of current research. One of these technologies is based on the photovoltaic (PV) effect, which allows the direct conversion of solar radiation into electricity by 'solar cells'. This technology is showing rapid growth and also has great future potential [1], as is shown in Figure 1.1: the potential of the solar radiation on a small part of the globe is large enough to provide electricity for the whole world.

The potential of electricity generated by photovoltaics based technologies as well as other renewable energy sources is more and more recognised. This is for example visible in Figure 1.2, which shows the installation and decommissioning of power sources in the European Union in 2013. While facilities for energy production based on fossil fuels have a larger decommissioning than installation rate, capacity for renewable sources grows rapidly. For solar energy, this is not surprising, since electricity generated with solar modules, which are panels with connected solar cells has reached 'grid parity' in large parts of world. This indicates that the sales price of electricity obtained with solar modules is now the same or lower than for electricity obtained with fossil fuels. In The Netherlands,

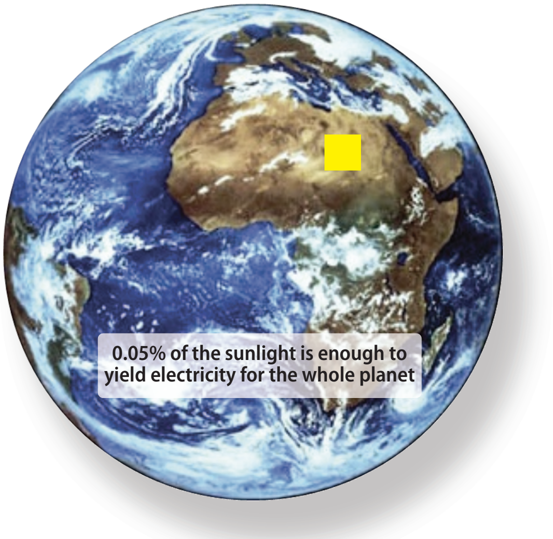

Figure 1.1:

Estimated required surface of the earth (yellow) required to fill with solar modules in order to provide the whole world with energy (Based on a global solar irradiation of 5.000.000 ExaJoule/year, an energy use of 500 ExaJoule/year and 20% efficient solar modules).

the investment for photovoltaic systems, including all wiring and electrical components, on residential rooftops, will nowadays be earned back by consumers in less than eight years, while the modules are designed for a lifetime of at least 20-25 years.

In order to drive the cost of electricity from solar system down even further, extensive studies on the improvement of these modules are executed: A wide variety of technologies exist in various stages of development, from the standard crystalline silicon modules that currently dominate the market, all the way to early stage research efforts, such as quantum dot solar cells.

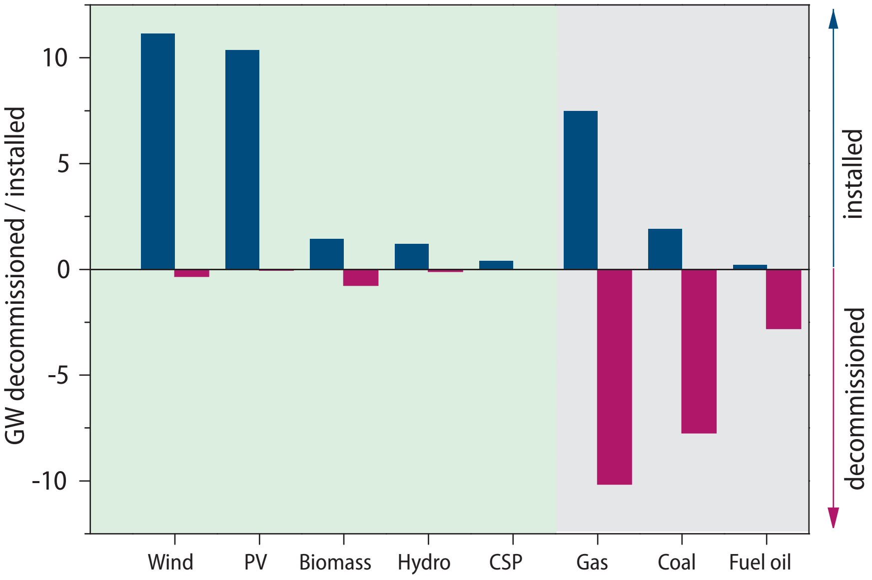

Figure 1.2:

Power generation capacities installed and decommissioned in the EU in 2013. The green techniques are the 'renewables', while the grey techniques are based on the burning of fossil fuel. Modified based on [2].

In between these extremes are the 'thin film' photovoltaics, which are various types of solar cells with thicknesses of only a few micrometres. This is significantly thinner than the crystalline silicon solar cells, which have thicknesses of around 100-200 µm. The 'thin film' solar cells include cadmium telluride (CdTe), thin film silicon (amorphous, nano- and microcrystalline), perovskites and copper indium gallium selenide (Cu(In,-Ga)Se_2 or CIGS). Since only a small quantity of solar cell material is required, these cells can be very cost-effective. Furthermore, this thickness allows the formation of flexible, bendable solar modules, which opens the way to many new applications.

Polycrystalline SIGS based solar cells have already reached efficiencies as high as 21.7% [3], which is the highest among the thin film PV technologies and even higher than multicrystalline silicon solar cells. Therefore, it is expected that CIGS solar cells will play a large role in the power generation in the near future. Additionally, the use of CIGS solar cells allows many new design possibilities, due to the freedom in shape and colour, as can be seen in Figure 1.3.

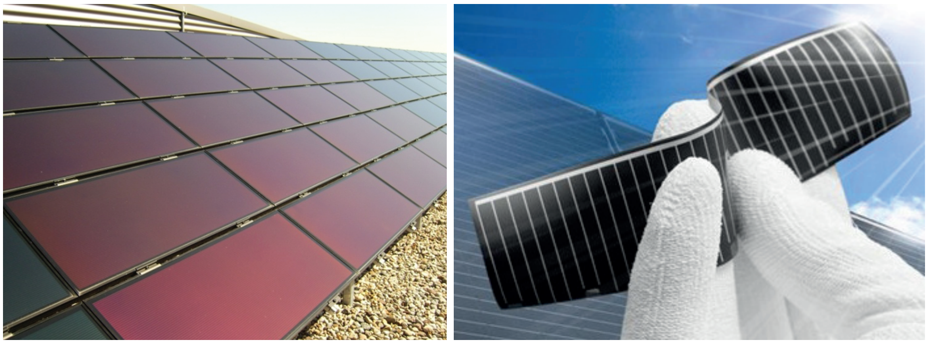

Figure 1.3:

Examples of the freedom of colour and shape of CIGS modules: (a) Red CIGS modules from Bosch (b) Flexible cell and module from Solarion

1.2 Market position of the CIGS PV technology

Due to the large potential of electricity obtained with CIGS solar cells, their production capacity has been ramped up rapidly in the last years by companies like Solar Frontier (Japan) and Hanergy (China, Germany, USA), so the shipment of CIGS modules is rapidly increasing (Figure 1.4). Alongside with them, a large number of smaller companies is also producing CIGS solar modules applying a great number of production procedures [4]. Therefore, improvements in module production methods, power output and module design as well as new possibilities for integration in e.g. buildings or textile, are reaching the market every year.

Nevertheless, current industrial production of CIGS modules only represents a few percent of the solar module manufacturing industry, which is currently dominated by silicon-based technologies (see Figure 1.5).

However, it is expected that the market share of CIGS modules in the Netherlands will quickly grow due to an agreement between the furniture company IKEA and the CIGS producer Hanergy, who have decided to join forces for large scale sales of CIGS

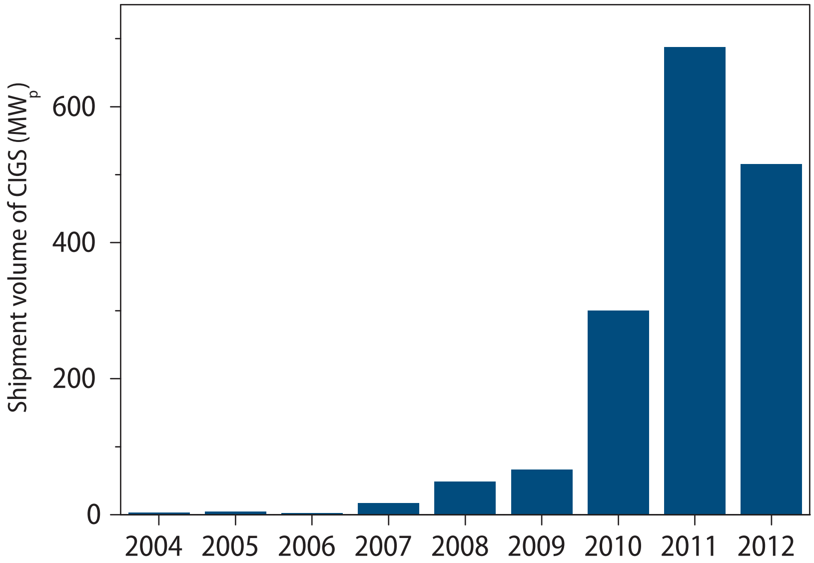

Figure 1.4:

Annual shipment of CIGS modules until 2012. Numbers are based on [5].

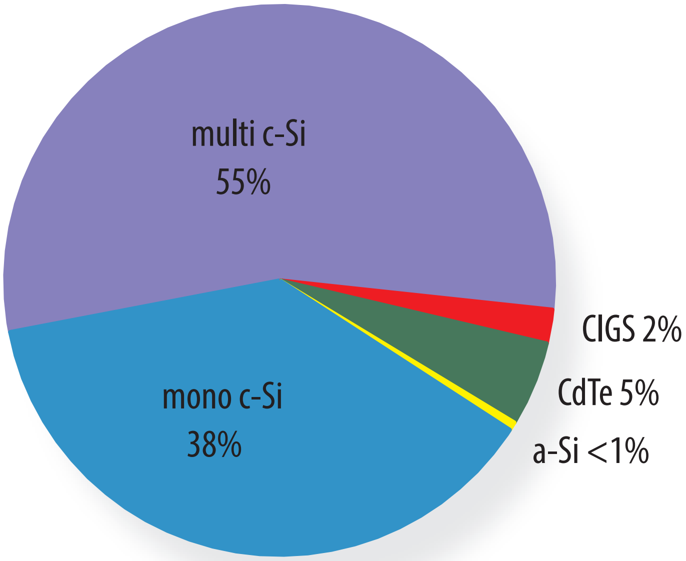

Figure 1.5:

Division of the module shipments in 2014 (40 GW$_p$) over the various commercially available solar module technologies [6].

modules. After introduction of CIGS modules at IKEA shops in the UK, they decided in October 2014 to also start sales in the Netherlands [7] In the near future, the sales of flexible modules can also add to their market potential due to their limited weight and flexible nature. This for example allows integration in clothing and tents, or their installation on large building that cannot support heavy loads..

Nevertheless, challenges for the optimisation of CIGS modules still exist before they can become a competitive technology for the large scale electricity production. These challenges include the minimisation of their manufacturing costs, the maximisation of their power output and the improvement of their lifetime.

1.3 CIGS solar cells structure

The CIGS solar cells with a thickness of a only 3-5 micrometres consist of at least five individual layers:, but a large number of variations of stack sequences exist between research institutes and companies. Figure 1.6 shows the cross-section of a typical un-encapsulated CIGS solar cells as well as the typical thicknesses of the layers. This 'standard' stack sequence is used in this thesis.

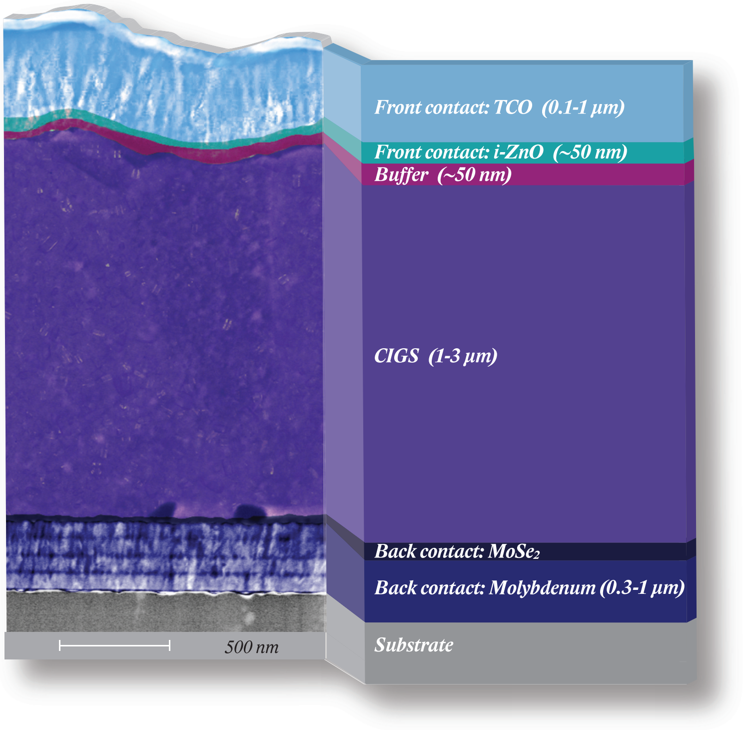

Figure 1.6:

Typical build-up of a CIGS solar cell

The functional layers used in this thesis are summarised:

Substrate: Soda lime glass (SLG): A substrate is used to offer support to the thin solar cells. SLG is mostly used as substrate since it is relative cheap and contains sodium as well as potassium. Flexible substrates, such as polyimide or metal foils, can also be used. In these cases, sodium and in some cases potassium are mostly added from an alternative source. In this thesis, SLG has been used as a substrate, unless mentioned otherwise.

Barrier (SiN_x, Al_2O_3, SiO_x): optional layer to prevent migration of species from the substrate. This is required for e.g. stainless steel substrates to prevent diffusion of iron, but it is also used to prevent sodium and potassium migration from soda lime glass, so these elements can be added at another point of the production process, in desired quantities. SiN_x deposited by Plasma Enhanced Chemical Vapour Deposition (PECVD) has been used as barrier within this thesis, this layer is not depicted in Figure 1.6.

Back contact: Molybdenum: The metal molybdenum is used as conductive layer beneath the absorber, in order to transport the generated holes. Molybdenum layers show good conductivity, acceptable adhesion, are reasonably smooth and allow beneficial sodium diffusion, which is necessary for the formation of good CIGS absorbers [8,9]. Furthermore, they can withstand the temperatures required for CIGS production processes and do not react with the metals in the CIGS absorber (copper, indium and gallium). The main drawback of molybdenum is the relatively low reflectance compared to other metals. Molybdenum films are deposited by direct current (DC) sputtering. The sputtering conditions, including sputter pressure and power, which have been varied in this thesis, have a large impact on the CIGS absorber composition.

Back contact: Molybdenum diselenide ($MoSe_2$): Molybdenum reacts with selenium during the CIGS deposition process, which results in the formation of beneficial molybdenum diselenide ($MoSe_2$) layers [9], which function as an ohmic contact between molybdenum and CIGS.

Absorber: $Cu(In,Ga)Se_2$: In this layer, light is absorbed and electron-hole pairs are generated. This layer consists of copper indium gallium diselenide (or $CuIn_{1-x}Ga_xSe_2$, $Cu(In,Ga)Se_2$ or CIGS) and is a p-type polycrystalline semiconductor with a direct bandgap and a high optical absorption coefficient. These features allow the use of relatively thin (2 µm) absorber layers [10].

$Cu(In,Ga)Se_2$ is a solid solution of $CuInSe_2$ and $CuGaSe_2$ and can have all compositions for Ga/(In+Ga) from 0 to 1. With the variation of the gallium and indium ratio, the lattice parameters as well as the bandgap of the material can be changed: Pure $CuInSe_2$ has a bandgap of 1.04 eV, while pure $CuGaSe_2$ has a bandgap of 1.67 eV. It has been empirically shown that a Ga/(In+Ga) ratio of 20–35%, resulting in a bandgap of approximately 1.15–1.25 eV gives the best solar cell efficiencies. Higher gallium contents will lead to a higher bandgap, but do generally not lead to large increases in Voc [10]. Cu(In,Ga)Se2 absorbers have the chalcopyrite crystal structure and are tetrahedrally bound as is shown in Figure 1.7. The word chalcopyrite is also often used to refer to CIGS type solar cells. Cu(In,Ga)Se_2 solar cells are deposited slightly copper poor (Cu/(In+Ga) ≈ 0.9) in order to prevent the formation of copper selenides [10,11]. This copper poor nature can be explained by the fact that chalcopyrite compounds with large deviations from stoichiometry are heavily compensated, with simultaneous formation of acceptors and donors, for example by the coexistence of copper vacancies and indium atom at copper places [10].

A further degree of freedom for the composition and the bandgap can be achieved by the partial substitution of selenium for sulphur (Cu(In,Ga)$(S,Se)_2$), while the addition of sodium and potassium are required to obtain high efficiency solar cells. More information about these elements follows in chapter 7.

Buffer: CdS: n-type semiconductor, which forms a heterojunction together with the CIGS absorber. This material is generally applied with Chemical Bath Deposition

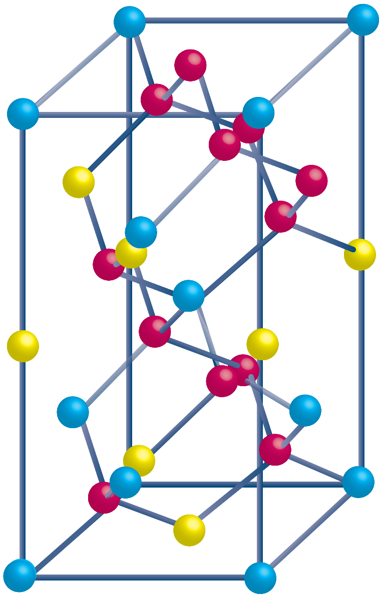

Figure 1.7:

CIGS chalcopyrite unit cell – the blue spheres represent copper, the yellow spheres can represent both indium and gallium, while the pink spheres indicate the positions for selenium or in some cases sulfur.

(CBD). Some CIGS solar cell designs avoid this material due to environmental concerns regarding the use of cadmium, or its wetchemical deposition method using substances such as Zn(O,OH,S) or In_2S_3 instead. Within this thesis, only CBD CdS has been used.

Front contact: Intrinsic ZnO (i-ZnO): This highly resistive material is used to prevent the formation of shunt paths within CIGS solar cells. This layer is normally applied by RF sputtering.

Front contact: Aluminium-doped ZnO (ZnO:Al): This n-type semiconductor is both transparent and conductive. These characteristics are critical, since this layer should be transparent to enable light to penetrate through to the CIGS absorber layer and conductive to transport the electrons. Other conductive and transparent oxides, such as the more expensive indium tin oxide (ITO) can also be used. In this work, RF sputtered ZnO:Al has been used as front contact.

1.4 Reliability of the CIGS PV technology

For large scale market introduction of CIGS modules, reliability of product performance is, alongside with initial costs and efficiency, an important prerequisite. Reliability is defined as the probability of failure-free performance over a given lifetime, under specified operating conditions. In order to optimise this reliability of solar modules, two factors of the product performance should be assessed:

- **Performance stability** 'How long does the module generate electricity in an economically attractive way?' This time is called the economic 'lifetime' and is often defined as the period that the module produces 80% or more of the original power.
- **Predictability** 'How well can we predict their lifetime?' and 'How reproducible is the lifetime of modules?'

These factors greatly impact the cost of electricity obtained with solar modules (Figure 1.8). First of all, lower electricity costs can be obtained for stable long lifetime solar modules. Additionally the predictability of the performance is also important: financiers, home-owners, utilities, planners and especially module producers need to be able to predict when a module will no longer function in order to evaluate their financial risks. Therefore, reliability aspects are very important in order to obtain the lowest and best predictable electricity costs. In order to comply with market demands, most suppliers provide a guarantee that the modules will still provide at least 90% of their initial efficiency after 10 years or 80% after 25 years [12].

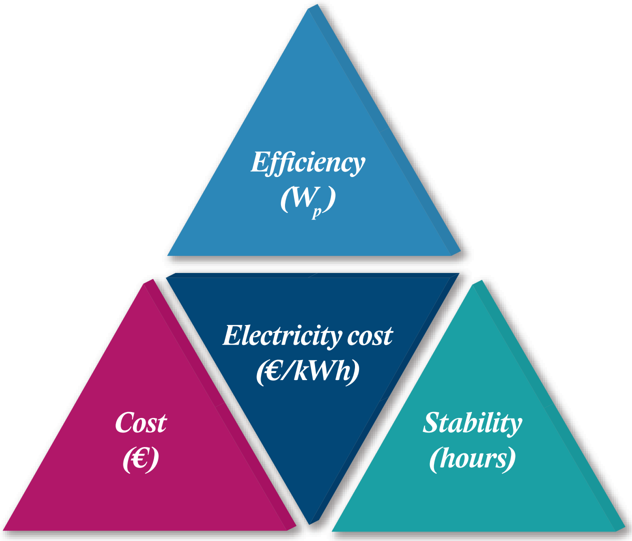

Figure 1.8:

The three main parameters determining the cost competiveness of electricity from a PV system.

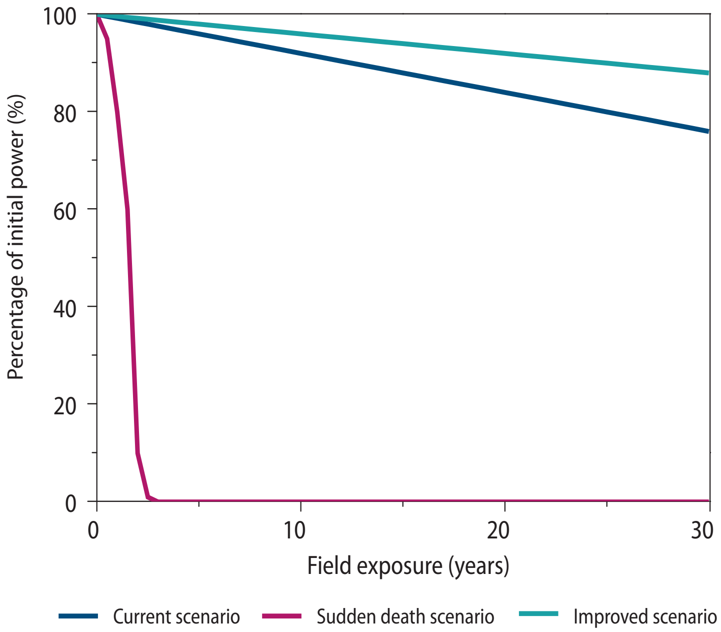

Figure 1.9:

Various scenarios depicting the output efficiency of solar modules.

This is also shown in the scenarios in Figure 1.9. The blue scenario is the one that is currently desired, with a slow but steady degradation rate, which leads to an end of the economic lifetime after 25 years. However, in many cases, the solar modules lose their efficiency earlier, as is for example depicted in the red line. These 'sudden death' scenarios, caused by infant mortalities, reduce the predictability of photovoltaic products, as well as the electricity output and the trust of investors, installers and potential owners. By optimising both the stability (lower degradation rate) and the predictability (no sudden death scenarios), e.g. by reduction of infant mortalities, the green scenario could be reached. It should be noted that the total electricity yields of these scenario can be determined by the integration of these curves.

However, for the thin film PV industry, the long term field performance of their modules is especially hard to assess, because predicting their lifetime is a complicated process.
In order to give an assessment of the lifetime of solar modules and how fast they lose their efficiency (their 'degradation behaviour'), a set of Accelerated Lifetime Tests (ALT), based on the IEC standards [13], are used. These test procedures should ideally tell whether the requirements related to performance stability and predictability are met. However, literature [14-16] reveals that a positive outcome of these tests not always means that the solar module can stand outdoor conditions for twenty years, while it is likely that the opposite can also be true.
This weak correlation between tests and reality is especially true for thin film PV technologies [16], for which a set of tests named the 'IEC 61646 standard' [13] is used. While crystalline silicon modules has been tested in the laboratory and used in the field since the 1970s, for thin film modules, field experience has not yet been extensively compared with laboratory tests. For crystalline silicon, many tests have been altered in the last 25 years, but this learning curve has not yet been followed for thin film modules. Furthermore, the IEC standard does not focus on fundamental understanding of the degradation process within a module. However, knowledge of the failure mechanisms, which are the processes happening inside the module leading to failure and the possibility to link these with the observed field failure of modules is very important. This can help to link the loss of the power output of a module with its production process, in order to obtain modules with a better stability and predictability. Due to the limited knowledge about the field failure in thin film PV, many issues about the stability and the predictability, like the influence of the interfaces between the components and the role of the barrier materials, are still open.
As one of the thin film PV technologies, also for thin film CIGS, more research was required into the failure mechanisms occurring in CIGS solar cells and modules in order to enhance their stability and predictability. Literature revealed that humidity was often a

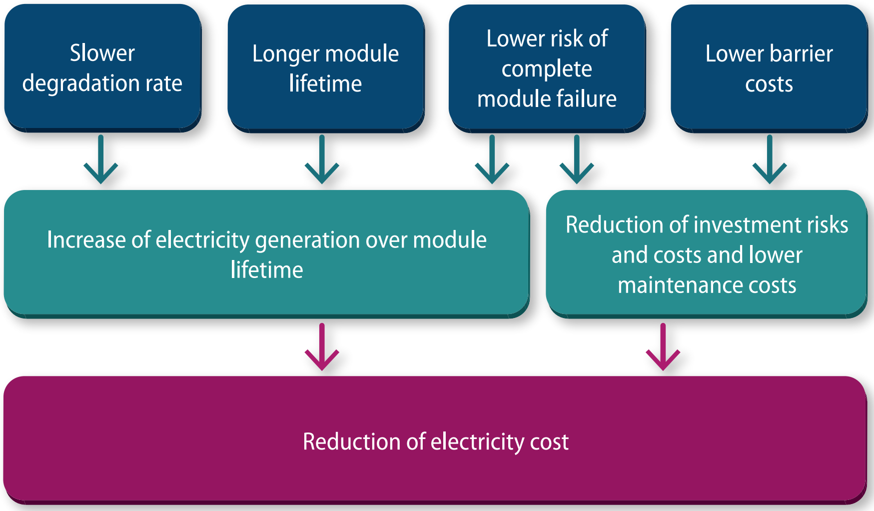

Figure 1.10:

Mechanisms through which more stable and predictable CIGS solar cells lead to reduced electricity costs.

key factor for the stability and predictability of CIGS solar cells and modules.

This was shown in Accelerated Lifetime Tests including liquid or gaseous water, like 'damp heat' tests (exposure to 85°C/85% relative humidity (RH)), in which CIGS solar cells and modules often failed as is shown in chapter 2. It was therefore concluded that CIGS solar cells and modules are very sensitive to humidity ingress. Furthermore, sensitivity to among others temperature (shocks), electrical bias and illumination has been observed, but the impact of these loads is not necessary detrimental. Generally, the exact nature of the degradation mechanisms of CIGS solar cells and modules is still unknown, while their bottleneck materials and interfaces are also not yet identified.

Since the knowledge about both the stability and predictability of CIGS PV is still limited, CIGS solar cells and modules are currently exposed to very thorough accelerated lifetime tests. In order to optimise their stability and predictability during accelerated lifetime tests as well as field exposure, CIGS modules are protected against water ingression, by the use of barrier materials. For rigid modules, glass is an excellent barrier material, while for flexible modules, often expensive inorganic/organic multistack materials are selected. Although this enhances the lifetime of the CIGS modules, it also leads to higher costs and hinders the large scale market introduction of flexible modules. Therefore, it would be attractive to have CIGS modules which consist of CIGS solar cells that are already stable under humidity, as well as under electrical biases, temperature and illumination, without barrier materials. Producing these ‘intrinsically’ stable CIGS cells would contribute to lower production costs due to reduced barrier costs as well as accelerate the introduction of flexible CIGS modules to the market. Knowledge about intrinsically more stable CIGS solar cells might thus also help CIGS module producers that are currently producing stable, but relatively expensive modules. An overview of the reduction of electricity cost due the improvement of the stability and predictability of CIGS solar cells is shown in Figure 1.10.

1.5 Aim and scope of this thesis

Within this thesis, we aimed to obtain better understanding about the long term stability of CIGS solar cells and modules. This knowledge was then used to optimise CIGS solar cells and modules concerning their stability. For this, several research questions have been addressed in this thesis:

1. What is the influence of humidity, temperature, illumination and various atmospheric species on the stability of CIGS solar cells?
2. Which layers or interfaces in CIGS solar cells are the most critical materials during exposure to these conditions?
3. Which electrical parameters of CIGS solar cells are most influences by exposure to these conditions?
4. Which chemical reactions are associated with the changes in electrical parameters?
5. How can we modify the deposition conditions or composition of the CIGS solar cells to prevent these chemical reactions?

In order to answer these questions, the following scope has been determined for this thesis:

1. The exposure of CIGS solar cells to various accelerated lifetime tests, in which temperature, humidity, illumination and atmospheric species are used as a load. In order to obtain better understanding, the changes in electrical parameters and the associated occurring chemical reactions, have been determined.
2. Since the complete CIGS solar cell is a very complicated system, various individual layers, including molybdenum and ZnO:Al films have also been exposed to various loads. For these layers, the changes in electrical parameters and chemical reactions were also identified. The knowledge obtained in these experiments has helped the identification of the changes occurred in complete CIGS solar cells.
3. Since the required test methods for points 1) and 2) did not all exist, new testing methods for solar cells and its individual layers have been developed: a hybrid degradation set-up was designed and built in order to in-situ monitor the de

degradation properties of the CIGS solar cells under humidity, illumination and temperature. Additionally, an 'atmospheric species' test was developed, in order to learn more about the impact of atmospheric species.

1.6 Outline of the thesis

In this chapter, a short introduction about photovoltaics in general and more in-depth on CIGS solar cells and modules and their individual layer is given. Additionally, the reason for reliability research on these materials is introduced. Finally, the scope, research objectives and structure are presented.

In **chapter 2**, a detailed literature overview on the degradation behaviour of CIGS solar cells and their individual layers is given. In this chapter, results from this thesis have also been included to yield a complete overview. The hybrid degradation set-up allowing in-situ monitoring of the degradation properties is described in **chapter 3**. Additionally, the theory behind current-voltage measurements and the data interpretation as is used in this thesis are introduced. The special design for CIGS solar cells as used in this thesis is also described.

The temperature dependency of the electrical parameters of CIGS solar cells on polyimide and soda lime glass is shown in **chapter 4**. In this chapter, it is shown that the output of CIGS solar cells strongly depends on their temperature, while this impact differs for different types of CIGS solar cells. This knowledge is relevant for CIGS modules in the field, but is also very important for the interpretation of lifetime results as described in this thesis, since many experiments have been executed at elevated temperatures (like 85°C or 107°C). In this chapter, it is shown that the studied CIGS solar cells have temperature dependencies of their efficiency varying from -0.36 to -0.70 relative %/°C. It is also described that the temperature dependency of the short circuit current can be either positive and negative and likely depends largely on the recombination in the solar cells. It is also shown that solar cells with a higher open circuit voltage actually have a lower temperature dependency.

Chapters 5, 6, 7 and 8 present the actual behaviour of CIGS solar cells and individual layers under the various degradation conditions. These chapters also include recommendations which deposition conditions lead to the most stable solar cells, preferably without the loss of initial properties.

In **chapter 5,** the behaviour of molybdenum films exposed to damp heat conditions is extensively described. In order to learn more about their damp heat stability and its relationship with the deposition conditions, molybdenum films were deposited at different pressures, which led to changes in their morphology: Films deposited at lower deposition pressures resulted in more dense films. Furthermore, some films were degraded ‘as-deposited’ (without any post-processing), while other films were selenised before degradation in order to form a thin layer of $MoSe_2$.

In **chapter 6**, the impact of various degrading conditions on aluminium doped zinc oxide films (ZnO:Al) is presented. Both variations in deposition conditions (room temperature versus 200°C) and in degradation conditions (damp heat versus water purged with either N_2, O_2 or CO_2) are described. Here it is shown that damp heat exposure leads to increased resistivity of these transparent conductors.

Chapter 7 and chapter 8 discuss the degradation of complete CIGS solar cells. **Chapter 7** demonstrates the degradation of CIGS solar cells with different quantities of sodium and potassium (alkali-elements) when degraded in the hybrid degradation setup. The impact of damp heat and illumination exposure on these solar cells on both the electrical and the compositional properties is presented.

Chapter 8 describes the impact of atmospheric species on complete CIGS solar cells. Analogue to chapter 6, it demonstrates that exposure of these solar cells to water and large quantities of CO_2 led to rapid loss of efficiency. This was caused by partial dissolution of the ZnO:Al, likely in the regions near the grain boundaries, which resulted in a large decrease in the short circuit current and an increase in the series resistance.

The last two chapters present the overview, outlook and summaries. **Chapter 9** discusses an overview of the degradation mechanisms and their impact on the electrical parameters of CIGS solar cells. This information is both obtained from the studies in this thesis and from the literature. Additionally, recommendations for further studies on CIGS solar cell and module reliability are given. **Chapter 10** provides summaries for this thesis in English, Dutch and French.

Appendices A and **B** show an overview of the used analysis techniques and the used abbreviations, respectively. The thesis ends with the 'dankwoord / acknowledgements', an overview of publications, presentations and awards and the curriculum vitae of Mirjam Theelen.

1.7 Contribution to the research field

The reliability of relatively mature photovoltaic techniques, like crystalline silicon as well as CdTe and CIGS modules, is often considered as a development theme for the industry, while the academic world focuses more on the research on new materials. However, industry is often driven by rapid market introduction of solar modules instead of answering fundamental questions regarding their reliability. This study has aimed to increase the fundamental apprehension of the stability and predictability of CIGS solar cells and modules.

Within this thesis, CIGS solar cells and their individual layers have been studied and the deposition conditions leading to the most stable and predictable devices or layers have been selected. This knowledge can directly be applied in order to obtain more stable solar cells and modules and allow the use of less and more cost-effective barrier materials. Additionally, the identification of chemical species leading to the degradation of the devices and layers can also help a more effective selection of the barrier material.

Finally, the two accelerated degradation tests developed within this thesis will likely be introduced in other places: an improved version of the more complicated 'in-situ hybrid' degradation test can be purchased from three Dutch SME's, which have chosen to commercialise the setup. The 'atmospheric species' test described in articles and this thesis and can be replicated easily by interested parties.

1.8 Acknowledgements

I would like to acknowledge A. Kuypers (TNO) for the image courtesy of Figure 1.1 and N. Barreau (IMN-UMR), M. Verheijen (Philips Innovation Services) and I. Schrauwers (IS design) for the image courtesy of Figure 1.6, while I. Schrauwers is also acknowledged for Figure 1.7 and Figure 1.8. P. Mints (SPV Market Research) is acknowledged for providing the data in Figure 1.4 and Figure 1.5. F. Ruske (HZB) is acknowledged for Figure 1.10.

1.9 References

[1] N. Dhere, Solar Energy Materials and Solar Cells, 91 (2007) 1376-1382

[2] European Photovoltaic Industry Association, Global Market Outlook For Photovoltaics 2014-2018 (2014)

[3] Best Research Cell Efficiency Chart. The National Renewable Energy Laboratory, Golden, CO. http://www.nrel.gov/ncpv/images/efficiency-chart.jpg. accessed 8 December 2014

[4] P. Reinhard, S. Bücheler, A. Tiwari, Solar Energy Materials & Solar Cells 119 (2013) 287–290

[5] P. Mints, SPV Market Research, Global Markets for Sun Energy Technologies - A Supply/Demand Perspective to 2017, SUNday 20 Novem-

ber 2013

[6] P. Mints, SPV Market Research, Madico Quarterly Call, 12 December 2014

[7] IKEA and Hanergy launch Dutch solar offering, 28 October 2014, http://www.solar-international.net/article/95499-IKEA-and-Hanergy-launch-Dutch-solar-offering.php,– accessed 22 December 2014

[8] P. Salomé, J. Malaquias, P. Fernandes, A. da Cunha, Journal of Physics D: Applied Physics 43 (2010) 345501

[9] D. Fisher, I. Repins, J. Schaefer, M. Beck, W. Batchelor, M. Young, S. Asher, Proc. 31st IEEE SPIE (2005) 371-374

[10] T. Unold, C. Kaufmann, Chalcopyrite Thin-Film Materials and Solar Cells, from Comprehensive Renewable Energy, chapter 1.18 (2012) 399-422

[11] J. Wennerberg, Design and Stability of Cu(In,Ga)Se_2-Based Solar Cell Modules.
Dissertations from the Faculty of Science and Technology 683 (2002) 91 pp. Uppsala.

[12] D. Coyle, Progress in Photovoltaics: Research and Applications, 21 (2) (2013) 156-172

[13] International Electrotechnical Commission IEC 61646 ed. 2, International Standard, Geneva, Switzerland, 2008

[14] C. Osterwald, T. McMahon, Progress in Photovoltaics: Research and Applications, 17 (2009) 11–33

[15] D. Jordan, S. Kurtz, Progress in Photovoltaics: Research and Applications 21 (2013) 12–29

[16] T. Carlsson, A. Brinkman, Progress in Photovoltaics: Research and Applications 14 (2006) 213 – 224

CHAPTER 2

Stability of $Cu(In,Ga)Se_2$ Solar Cells

A literature review

This chapter has been submitted as the following publication:

M. Theelen and F. Daume

Stability of $Cu(In,Ga)Se_2$ Solar Cells: A literature review,

submitted to Progress in Photovoltaics (2015)

Abstract

As $Cu(In,Ga)Se_2$ (CIGS) photovoltaic technology matures to production on an industrial scale, its long-term stability becomes increasingly important: the electric yield and thus the revenue of a PV system depend on both the initial conversion efficiency as well as its development over time. Increasing the long term stability of CIGS modules by understanding and lowering the degradation of this PV technology is therefore a key strategy for market success of this technology. Furthermore, increasing the long-term stability of solar cell materials allows to lower the demands and thus the cost of barriers within CIGS modules.

In this review chapter, the result of an extensive literature on the stability of CIGS solar cells and modules is presented. This review focuses on the behaviour of unencapsulated CIGS solar cells and (mini)modules when exposed to different accelerated lifetime tests, like elevated temperature and humidity. The changes in electrical and physical performance due to these tests, as well as the chemical reactions that are causing these changes, are described.

Additionally, the influence of these accelerated lifetime tests on the individual layers of the CIGS solar cell has been summarised. In the following chapters, the stability of both the transparent conducting ZnO:Al front contact and the molybdenum back contact, as well as on the CIGS and buffer layers is discussed. Stability issues related to the design of CIGS modules, like the application of grid structures and monolithic interconnection, are presented as well.

2.1 Introduction

In chapter 1, it is presented that a long and predictable lifetime is crucial for the large scale introduction of CIGS modules. However, field data show that CIGS modules can fail during outdoor exposure (Table 2.1). In order to limit power loss of these modules and to compensate for lack of knowledge about the intrinsic stability of CIGS solar cells, the protective measures within modules, like water barriers and edge seals, are overdesigned. In order to better understand the degradation behaviour of CIGS solar cells and modules, this chapter contains a literature review about the existing knowledge in 2015 including data that can be found in this thesis.

In order to estimate the lifetime of CIGS modules in the field, an overview of degradation rates of their efficiencies is shown in Table 2.1.

Table 2.1 Literature overview of degradation rates (relative percent/year) of CIGS modules obtained from field tests at different locations.

	Panel type / producer	Period	Location	Degradation rate (rel %/year)
Makrides [1]	Würth WS11007/75	2006-2011	Nicosia, Cyprus	1.9 to 2.4
Dhere [2]		2005-2007	Florida, USA	4.5 to 5.1
Musikowski [3]	Würth WS11007/75	2003-2010	Magdeburg, Germany	0
Del Cueto [4]		1990 (2002)-2008	Colorado, USA	0.2 to 2.3
Del Cueto [4]		2005-2008	Colorado, USA	2.5 to 4.7 (with bias)
Jordan [5]	Shell Solar PowerMax Eclipse® 80-C	2006-2011	Colorado, USA	0
Jordan [5]			Colorado, USA	0 to 3.7
Meyer [6]		2001 (10 months)	South-Africa	48
Meyer [6]		2001-2003	South-Africa	8.1
Niki [7]	ZSW	2003-2007	Widderstall, Germany	0.2
Ermer [8]	Siemens Solar	Until 1990 (17.5 months)	Colorado USA	4.1
Tarrant [9]	Siemens Solar	1988-2006	Colorado USA	-0.2 to 1.7
Kushiya [10]	Showa Shell Sekiyu	2003-2006	Japan	0
Radue [11]		2007-2009 (13 months)	Port Elizabeth – South-Africa	-1.8 to 4.1

These degradation rates are determined assuming a linear decrease of output. This linear determination of the degradation rate is the simplest approximation and in many cases it does not represent the real progression of the degradation accurately. However, without any further assumptions the linear approximation allows to compare the degradation data from different sources which are represented differently in each publication.

Table 2.1 shows that the tested modules vary from very stable (no degradation after seven years) to very vulnerable to outdoor exposure. It should be noted that degradation rates do not need to be linear as a function of time, since large differences between years have been observed. These mixed stability results show that a general statement about the lifetime of CIGS modules cannot be made at this moment. The main reason for this limited knowledge about CIGS module lifetime can be found in:

1. Limited field experience with CIGS modules, which generally have not been in the field for a long time.
2. Results from field experiments can vary greatly. Degradation depends on many parameters such as module production techniques, module type, production year, orientation of the panel and climate of the installation location, as well as installation parameters like system voltage. So far, not enough field testing data is available to apply reliable statistics.
3. Lessons learned for crystalline silicon modules (for both field and accelerated testing) cannot always be applied to CIGS modules due to deviations in module design and cell composition and build-up.

More information on the field performance of many types of PV modules, including CIGS can be found in an excellent review paper [12]. In general, Table 2.1 and references [12,13] show that some CIGS modules show excellent outdoor stability, while other modules degrade very quickly. When the change of the individual PV electrical parameters of the degraded modules was studied, it was observed that the efficiency decrease was mostly caused by deterioration of the fill factor (FF), while a small change in open circuit voltage (V_{oc}) and minimal change in short circuit current (I_{sc}) were also observed [4,12]. Unfortunately, most references only report the changes in electrical parameters of their modules and not in their material properties.

In order to better predict the lifetime and reliability of CIGS modules, they are exposed to Accelerated Lifetime Testing (ALT) according to International Electrotechnical Commission (IEC) module testing procedure 61646. These tests should ideally show whether the requirements related to performance stability are met. However, literature [12,14] reveals that a positive outcome of the IEC tests does not necessarily indicate that the

PV module can withstand the predicted outdoor conditions. This weak correlation between tests and reality is currently a challenge, specifically for thin film PV technologies including CIGS [15]. These modules show different failure mechanisms from crystalline silicon modules, on which the ALT procedure are based. As described in reference [14], the ALT procedures have been optimised multiple times based on field experience, while this optimisation process for thin film modules only started recently.

The degradation of (CIGS) modules can be caused by causes which only occur for CIGS 'CIGS specific', as well as 'CIGS non-specific' reasons, which can also be found in other types of PV modules, such as connection wires or junction box corrosion. Table 2.2 shows an overview of failure modes leading to CIGS module degradation, and a global categorisation whether they are specific for CIGS or also observed for other (thin film) modules.

When the circumstances leading to degradation specific for CIGS solar cells or modules were studied, humidity was often a key factor. ALT tests including liquid or gaseous water, like damp heat tests (exposure to 85°C/85% relative humidity (RH)) very often led to the failure of CIGS solar cells or modules. It was therefore concluded that CIGS solar cells and modules are very sensitive to humidity ingress. Furthermore, sensitivity to e.g. temperature (shocks), electrical bias and illumination has been found, but the impacts of these loads are not necessary detrimental.

In order to protect the CIGS cells against water ingression, barrier materials are applied in modules. For rigid modules, glass is an excellent barrier material, while for flexible modules often expensive inorganic/organic multi-stack materials are applied. These materials have a low water vapour transmission rate (WVTR), which is a measure of the passage of water vapour through a material. Although this low WVTR generally enhances the lifetime of CIGS modules, it also leads to higher costs and hinders the large scale market introduction of flexible modules. Therefore, intrinsically stable CIGS cells and modules would be very attractive. They would contribute to lower production costs due to reduced encapsulation costs and accelerate the introduction of flexible CIGS modules to the market. Knowledge about intrinsically more stable CIGS material might thus also help CIGS producers that are currently producing stable, but relatively expensive modules.

The objective of this chapter is the presentation of an overview of the research on long term stability of CIGS solar cells and the discussion of the results obtained from field and accelerated lifetime testing. Additionally, the failure mechanisms occurring

Table 2.2: Summary of failure modes as observed for CIGS (modified but based on reference [15]).

Failure modes	CIGS specific	Impacted physical parameters	Possible failure mechanisms
Cell degradation			
Main junction: increase of recombination	Yes	Loss in fill factor, J_{sc} and V_{oc}	Diffusion of dopant, impurities etc + electromigration
Shunting	Yes	R_{shunt} decreases	Diffusion of metals, impurities etc.
Series resistance increase by TCO and Mo degradation	Yes	R_s increases	Corrosion, diffusion
Delamination of back metal contact	Yes	J_{sc} decrease	Lamination stresses
Module degradation			
Interconnect resistance (ZnO:Al/Mo or Mo)	Yes	R_s increases	Corrosion, electromigration
Interconnect degradation – shunting: across isolation scribe	Yes	R_{sh} decreases	Corrosion, electromigration
Busbar failure	No	R_s increase or open circuit	Corrosion, electromigration
Solder joint	No	R_s increase or open circuit	Fatigue, coarsening (alloy segregation)
Encapsulation delamination	No	Loss in fill factor, J_{sc} and possible open circuit	Surface contamination, UV degradation, hydrolysis of silane/glass bond, warped glass, 'dinged' glass edges, thermal expansion mismatch
Encapsulation: loss or hermetic seal	No		
Encapsulation: glass breakage	No		
Encapsulation: Loss of high-potential isolation	No		

within CIGS solar cells and modules as well as individual layers, are discussed. Short time effects, like buffer diffusion due to heat or illumination are not included, and information about barriers, encapsulants, edge sealing and other 'module constituents' are omitted, unless an influence between the module constituents or the cell materials has been observed.

This chapter will first discuss the long term stability tests on the individual layers in CIGS cells, including the molybdenum (Mo) back contact (chapter 2.3.1), the CIGS and buffer layers (chapters 2.3.2 and 2.3.3) and the transparent conductive oxide (TCO) front contact (chapter 2.3.4). Then, the degradation behaviour of complete CIGS solar cells and the physical degradation mechanisms are presented (chapter 2.4). In the final chapter, the impact of module formation techniques on the stability of CIGS modules is described (chapter 2.5).

In this chapter, the terms 'CIGS solar cells' and 'CIGS modules' are used to generally refer to solar cells and modules based on Cu(In,Ga)Se$_2$, but also to related materials like CuInSe$_2$ and Cu(In,Ga)(Se,S)$_2$. However, when the word 'CIGS' is used to describe only the absorber material, this refers to Cu(In,Ga)Se$_2$, while it is separately mentioned when solar cells based on other materials, like CuInSe$_2$, are described.

2.2 Degradation test conditions

In the chapters below, the results of various types of accelerated lifetime tests are described. The most important tests are introduced here:

1. 'Standard' **damp heat** exposure at 85°C/85% RH - according to IEC standard 61646, 1000 hours exposure to these conditions should mimic 25 years field exposure in Miami. However, the similarities between field and accelerated testing are still under debate [12,13]. In this thesis – as in most publications – the term 'damp heat' refers to these conditions unless other conditions are explicitly stated.
2. **Mild damp heat**, e.g. 60°C/90% RH or 60°C/60% RH [e.g. 16-19]. It should be noted that the relative water concentration is higher for 60°C/90% RH than for 85°C/85% RH, but the absolute water concentration is lower, due to lower saturation concentrations at lower temperatures (e.g. 90% RH at 60°C is 109 g/m^3, while 85% RH at 85°C is 241 g/m^3 [20]).
3. **Dry heat** is mostly 85°C or 90°C combined with low relative humidity grade (e.g. 10% RH) [21]. Articles about pure heat treatments at temperatures above 100°C are only included in this review chapter if these results can be assumed relevant for long term stability.
4. **Combined damp heat and illumination** testing [10,22], which allows the in-situ monitoring of the degradation behaviour [23]. Furthermore, damp heat can be combined with UV illumination as well [24]. It should be noted that the temperature and humidity conditions as reported in combined damp heat illumination experiments are generally the chamber conditions. The sample conditions can be different due to additional heating caused by the

> illumination, which also leads to a reduction in the relative humidity of the sample. Therefore, when comparing between damp heat and damp heat illumination experiments, these deviations should be taken into account.

The temperatures used during accelerated lifetime testing (typically 85°C) are much higher than typical environmental temperatures. However, it should be noted that module temperatures are often higher than the environmental temperature: McMahon et al. [15] measured the temperatures at the back of modules in New Mexico as high as 71°C.

It is important to note that the accelerated lifetime tests sometimes include the removal of samples from the climate chamber for analysis purposes. The samples are then returned to the chamber several hours or days later. These actions could lead to additional degradation phenomena like the introduction of drying stains (evapouration of surface water due to the lower humidity of ambient air) and stress related effects due to large and fast temperature ('thermo-shock') and humidity changes. On the other hand, this ‘drying effect’ can also be positive, for example due to intermediate drying of the samples, as described by Pern et al. [25].

2.3 Degradation of the individual layers

In this chapter, the changes in properties due to exposure to various test conditions as well as the derived degradation mechanisms of the individual layers in the CIGS cell are presented. Chapters 2.3.1 describes the vulnerability of the back contact molybdenum, chapters 2.3.2 and 2.3.3 describe the CIGS and buffer layer respectively, while chapter 2.3.4 discusses the stability of the TCO front contact, with the emphasise on the widely used material ZnO:Al. The cross-section of a typical CIGS solar cell is shown in Figure 1.6.

2.3.1 Molybdenum degradation

Sputtered molybdenum (Mo) is used by almost all research groups and CIGS manufacturers as a back contact material. The properties of these as-deposited layers are attractive for use in CIGS solar cells, since they can among others withstand high temperatures and a selenium atmosphere, which is required for the further CIGS deposition [26]. Additionally, molybdenum films have relatively good conductivity and reflectivity, which are the main requirements for good performance in CIGS solar cells. However, the material properties of molybdenum can change as a function of time, leading to changes in conductivity and reflectivity. More information about the function and position of molybdenum in a solar cell can be found in chapter 5. In order to show the impact of molybdenum degradation, these layers can be divided into two groups:

1. Stability of bare metallic molybdenum: molybdenum which is not immediately used for further solar cell processing can be stored, but exposure of bare molybdenum to the atmosphere can lead to a change in the electrical properties of the later processed CIGS solar cells.
2. Long term stability of the molybdenum layer back contact in the CIGS cells.

This distinction was made since the impact of the atmosphere must be considered for the first group (on bare metallic molybdenum). For the second group, the chemical environment of molybdenum film in a solar cell must also be taken into account, including the presence of a thin layer of $MoSe_2$ and the impact of the scribing procedure. More information about the impact of the scribing process can be found in chapter 2.5.1.

For both types of molybdenum, it was noticed that molybdenum degradation started mainly at places in the CIGS solar cell that were damaged. This includes accidental damages [27] as well as scratches from zinc oxide particles due to scribing and scratches from sand blasting during edge preparation [28]. Since conductivity is the most important requirement for a molybdenum back contact, an overview of the degradation

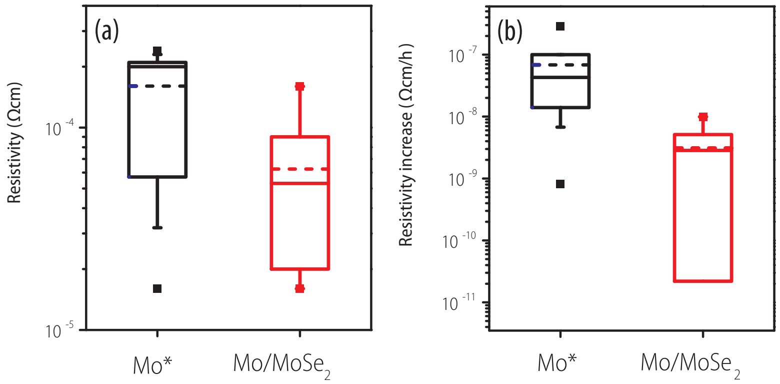

Figure 2.1

The box plots show (a) the initial resistivity and (b) the degradation rate under 85°C/85% RH of molybdenum (including molybdenum alloyed with aluminium or with a chromium bilayer) and molybdenum with a $MoSe_2$ top layer. The degradation rates are determined by assuming a linear decrease of the resistivity ρ: $\frac{\Delta\rho}{\Delta t}$ *. The top and bottom of the box show the 25% and 75% intervals, while the whiskers depict the 10% and 90% borders. The squares are the minimum and maximum values and the dashed line is the average value. The resistivity changes for $MoSe_2$ was negative in one case (-1×10^{-9} Ω cm/h) which is not depicted in the graph.*

rate of the electrical properties as caused by humidity and temperature exposure of the different groups of molybdenum is shown in Figure 2.1. Additional information on all the reviewed layers can be found in the supplementary material. The degradation rates are determined by assuming a linear decrease of the electrical parameter D: $\frac{\Delta D}{\Delta t}$, where D is $R_{\square}$ (sheet resistance) or ρ (resistivity). This is the simplest approximation and in many cases it does not represent the real progression of the degradation accurately. However, without any further assumptions the linear approximation allows to compare the degradation data from different authors which are represented differently in each publication.

2.3.1.1 Stability of bare metallic molybdenum

Several studies have reported the impact of moisture, oxygen and temperature on molybdenum films. It has been concluded that molybdenum degrades through the formation of a molybdenum oxide (MoO_x) [18,24,26-27] or $Mo(OH)_3$ [24] layer on top of metallic molybdenum. This formation can be accompanied by large volume expansion due to the incorporation of oxygen and to the lower density of molybdenum oxides. The formation of the MoO_x layer is highly inhomogeneous and often starts at positions that were already damaged. Figure 2.2 shows the typical blue and brown degradation structures that are often observed on degraded molybdenum, which naturally led to increased resistance and decreased reflectivity. Reflectivity could decrease from ~40% down to ~10% [26], when the coloured and grey/black spots completely covered the molybdenum surface. Typical degradation rates for the resistivity are shown in Figure 2.1, but do not show the complete picture: the conductivity, as measured on top of the molybdenum film, can first decrease very slowly, but suddenly becomes unmeasurable. This is probably caused by the formation of the non-conductive molybdenum oxide layer, which then becomes too thick to be pierced through with the measurement probes.

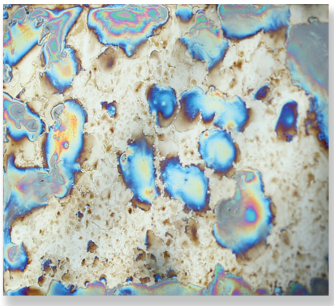

Figure 2.2

Photograph of a molybdenum sample (30x25 mm^2) after 17 hours exposure to damp heat (obtained from [26]).

Theelen et al. [18,26] studied the chemical structure of the molybdenum oxide. The molybdenum oxide formed after 105 hours of damp heat exposure contained Mo^{5+} and Mo^{6+} and had an average composition of $MoO_{2.88}$. Raman spectroscopy indicated the presence of MoO_3 and MoO_2 bindings, suggesting the presence of suboxides, which are oxides with a molybdenum oxide ratio in between MoO_2 and MoO_3 [26]. They also observed that the oxide layers can crack, caused either by the volume expansion due to the oxide formation or by the thermal and/or humidity shocks that occur when the samples are removed from the climate chamber. Since this leads to the exposure of a new surface of metallic molybdenum to degrading species, a second underlying layer of molybdenum oxide can be formed. Reference [26] also reported the occurrence of needles on the oxide surface, which may consist of Na_2CO_3. More information about these experiments can be found in chapter 5.

Pern et al. [24] reported the formation of yellow-blue materials when molybdenum was exposed to damp heat. This might be MoO_3 or a molybdenum hydroxide. The occurrence of large structural and morphological changes like the formation of microcracks, as well as the loss of reflectivity, were also observed in this case.

Wennerberg et al. [27] also observed the oxidation of molybdenum under damp heat conditions, leading to the formation of a non-conductive milky MoO_3 material. The corrosion started at point defects randomly scattered across the surface, from where the corrosion grew laterally with time, leading to the formation of clusters of larger corroded areas. This led to an exponential increase in sheet resistance which had already reached a 6.5 fold increase from the initial value after 180 hours of damp heat.

It was also shown that the sputter pressure influenced the stability of molybdenum exposed to humidity and temperature. Reference [26] showed that denser molybdenum, deposited at lower sputter pressure, was more resistant to damp heat. These molybdenum layers had a thinner oxide layer and thus retained higher conductivity and reflectivity: The reflectivity (measured from 340 to 1120 nm) of the porous sample decreased from 34% to 17% after only four hours of damp heat exposure, while the dense sample showed a decline from 45% to 40%.

In order to discover which degradation conditions lead to the molybdenum degradation, molybdenum films were exposed to temperature and humidity conditions, which became higher in time [19]. The films showed a stable resistance up to 70°C/70% RH conditions, but became highly resistant after exposure to 85°C/70% RH. Under these conditions, the colour also changed to dark brown with small white dots. Feist et al. [29] exposed molybdenum films for 48 hours to several degradation conditions, like dry heat (85°C), damp heat (85°C/100% RH) and room temperature (RT) water. The sample in the damp heat test increased in thickness from 700 to 900 nm, while the samples in water and dry heat did not change in thickness. The sample in the RT water bath showed a slight increase in resistivity, while the resistivity of the other samples remained largely unchanged.

Reference [18] showed that molybdenum also degraded under 60°C/60% RH conditions, but that the change in the properties of the molybdenum was much slower than under 85°C/85% RH. A rough estimation indicated that the degradation occurs approximately 20 times faster under the more severe conditions.

Pern and Noufi [30] showed that encapsulation also influenced the stability of molybdenum. When molybdenum was covered with a moisture permeable back sheet, no colour change or significant resistance change was observed even after 1250 hours damp heat exposure, although a number of small 'dots' appeared on the surface after 500 hours. This was surprising, since bare molybdenum on soda glass already degraded after 50 to 100 hours. The authors concluded that the presence of a back sheet either changed the reaction mechanism or that the reaction rate was largely reduced in the encapsulated test structure, in which the moisture vapour had to diffuse through the back sheet.

The relationship between long-time air exposure and short-term accelerated lifetime testing conditions is hard to identify. In order to make this comparison, Schmid et al. [31] compared the impact of several days of ambient air exposure and one hour 200°C heat treatment on molybdenum layers. The ambient air exposure combined with surface cleaning (several minutes at 400°C in vacuum) led to the formation of MoO_2 as well as some higher oxides, like MoO_3. The 200°C heat treatment, however, resulted in the exclusive formation of MoO_3, while sodium, which might have migrated from the substrate, was also found in these layers. Therefore, it is suggested that the oxidation state of the molybdenum might influence the sodium migration through the molybdenum layer.

In a later stage, $CuInSe_2$ was deposited on the molybdenum film exposed to ambient air, which led to a decrease in the oxygen content due to selenium incorporation. This was due to the reduction of MoO_3 to MoO_2 and the formation of either $MoSe_2$ or Mo-O-Se. However, the oxygen was not completely replaced by selenium, even after longer selenisation times.

By further studying of the $CuInSe_2$ sample, it was observed that the MoO_2 presence led to the formation of a Schottky-type barrier of about 0.3 eV at the CIS-MoO_2/Mo interface (Figure 2.3). It was suggested that this number is deviating from the 0.6 eV which was found for an ideal single crystal CIS/Mo system, due to differences in the interface chemistry, like the presence of oxygen.

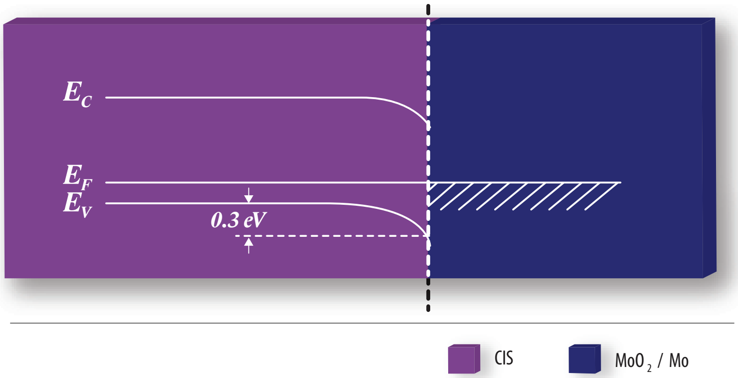

Figure 2.3:

Band bending of the energy band diagram of a $CuInSe_2$ solar cell at the interface towards the Mo/MoO_2 back contact. Modified based on reference [31].

A proposal for a general degradation route of non-selenised metallic molybdenum on soda lime glass via the formation of molybdenum oxide is shown in Figure 2.4. The change from metallic molybdenum to oxidised molybdenum has a negative effect on the reflectivity and later also on the conductivity, as is described in reference [18].

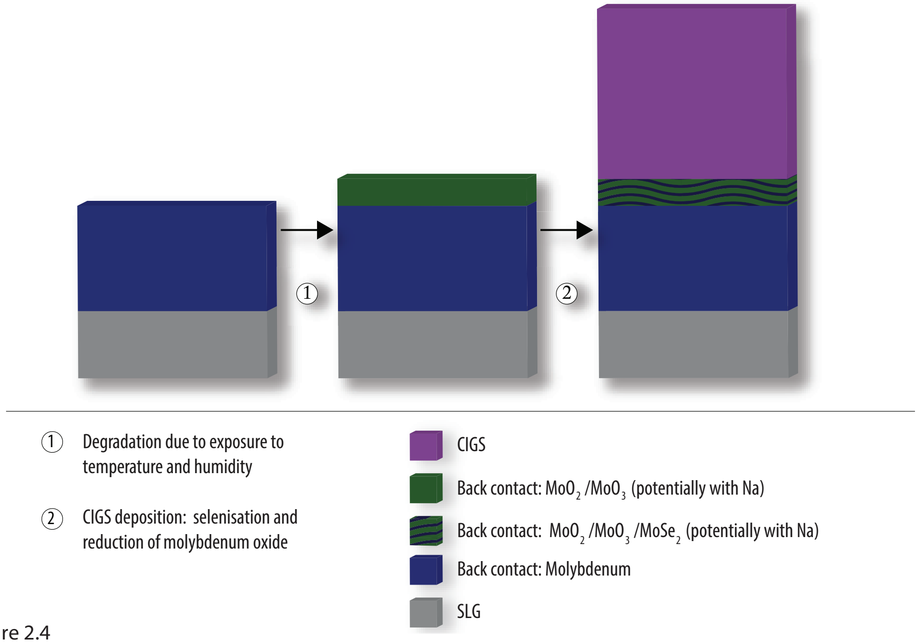

Figure 2.4

General reaction mechanism for the degradation of metallic molybdenum and the impact on the subsequent CIGS deposition.

2.3.1.1.1 Impact of aluminium incorporation

Wang et al. [32] looked at the addition of aluminium to molybdenum in order to improve the stability. $Mo_{1-x}Al_x$ (x=14-39 at%) was deposited by co-sputtering and exposed to a damp heat test for 168 hours. It was shown that these films retained their electrical and optical properties better than the pure molybdenum films. It was proposed that the formation of amorphous Mo-Al alloy regions reduced the surface area where oxygen and water molecules can diffuse. Furthermore, the formation of a passive Al_2O_3 film instead of MoO_3 on the surface was reported to enhance the stability of the film. However, the presence of aluminium led to the formation of a thinner $MoSe_2$ layer and its impact on the cell efficiency was not included.

2.3.1.1.2 CIGS cells from degraded molybdenum

The impact of molybdenum oxidation on the efficiency of the subsequent CIGS solar cells is not necessarily detrimental as was shown by Salomé et al. [33]. Both as-deposited molybdenum and molybdenum stored in a dry N_2 cabinet without H_2O but with low concentrations of O_2 were used to prepare CIGS cells. Electrical and compositional characterisation of the cells showed that devices prepared with degraded molybdenum actually had a higher efficiency (+0.8 %-points) than devices prepared with as-deposited molybdenum. This was caused by an increase of the V_{oc}, while the J_{sc} had decreased. Elemental profiling via SIMS showed that the sodium concentration in the molybdenum near the CIGS interface might be higher for the degraded samples, but no further conclusions could be drawn.

As-deposited molybdenum was also placed in an oxygen atmosphere (60 minutes at 200°C) in order to simulate the degradation process. This resulted in a very small increase of the V_{oc}, but it is not clear whether the same mechanism is involved as it is for the high N_2/low O_2 degraded samples.

Hempel et al. [34] also deposited CIGS solar cells on degraded molybdenum. The molybdenum was exposed to damp heat or elevated temperatures (up to 300°C). Both treatments were reported to result in the formation of MoO_3, which was reduced to MoO_2 after CIGS deposition. The exposure to a damp heat test and 200°C and 300°C dry heat tests were reported to lead to decreased cell performances. This could be linked to the observed gallium in-diffusion in the molybdenum, as well as the prevention of the formation of $MoSe_2$ when molybdenum oxide is present.

2.3.1.2 Long term stability of the molybdenum in the CIGS cells

While the previous chapters have shown that molybdenum can oxidise very easily, molybdenum degradation does not seem to be the key-parameter when the loss of efficiency of CIGS solar cells is considered. However, molybdenum degradation seems to impact CIGS modules at the scribes that separate the individual solar cells within a monolithically integrated module. In these regions, the molybdenum is less protected against humidity ingression [27] and more vulnerable due to scribing damage [28]. The chemical composition of the molybdenum surface might also be different due to the scribing process. More information about the specific impact of scribe degradation can be found in chapter 2.5.1.

In order to learn more about the long term stability of molybdenum within CIGS solar cells, the information on the stability of bare molybdenum films, described in chapter 2.3.1.1, must be considered. The chemical environment of molybdenum in a CIGS solar cell is different than the environment of metallic molybdenum without further treatment. One difference can be found in the migration of sodium into the molybdenum layer due to high temperatures used during CIGS absorber deposition [35].

Reference [26] showed that the presence of $MoSe_2$ can greatly influence the degradation of this molybdenum. This work showed that the decrease of conductivity due to degradation was not large and more or less similar for selenised and non-selenised molybdenum. However, dense selenised molybdenum retained most of its reflectance after 105 hours at 85°C/85% RH, while non-selenised molybdenum became non-reflecting. It is proposed therefore that the presence of $MoSe_2$ prevents the formation of molybdenum oxide.

Theelen et al. [35] also reported on the degradation of selenised bilayer molybdenum on soda lime glass. Bilayers consisting of a porous bottom layer with good adhesion and a dense top layer with good conductivity are mostly used in CIGS solar cells. Exposure to damp heat led to the formation of MoO_x on top of the samples, but also within the more porous bottom layer. Furthermore, XPS studies showed the presence of a potentially conductive material, which was proposed to be a ‘molybdenum bronze’. This material was likely formed by the so-called ‘intercalation’ of Na^+ into a matrix of MoO_3, which according to the following redox reaction:

$$Na_xMoO_3 \leftrightarrows xNa^+ + MoO_3 + xe^- \qquad (2.1)$$

It was thus proposed that the formed molybdenum oxide layer contained Na_xMoO_3 with different Na^+ contents and different grades of conductivity. This intercalation process can also explain the high mobility of Na^+ via the grain boundaries in molybdenum. More information about this intercalation can be found in chapter 5.

It should be noted that the deposition method of CIGS on the molybdenum film can also impact the stability of molybdenum in the presence of moisture: Feist et al. [21]

studied the degradation of molybdenum in CIGSSe cells by lifting off the CIGSSe layer in order to obtain a soda lime glass/Mo sample. Doing so for a non-degraded sample, Cu-Ga-O particles which were broken from the CIGSSe layer, as well as a Mo-Se film were observed, while indium was not present on the molybdenum surface. When a device was exposed to O_2 purged water at 85°C, the Cu-Ga-O particles were also present, but in this area a higher Ga-O concentration was found. The occurrence of these particles was reported to likely be specific for the deposition process (e.g. incomplete selenisation) and to likely facilitate moisture and/or oxygen transfer to the Mo/CIGSSe interface.

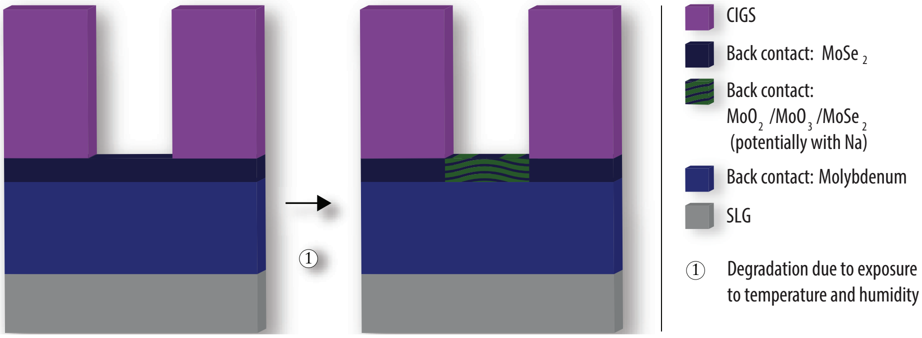

Figure 2.5

General reaction mechanism for the degradation of molybdenum in CIGS cells at an isolation scribe, showing the formation of molybdenum oxides from $MoSe_2$ *and metallic molybdenum.*

A proposal for a general route for degradation of molybdenum as present in CIGS solar cells is shown in Figure 2.5. This shows that the top $MoSe_2$ layer and the associated metallic molybdenum can also form into an molybdenum oxide layer, although this reaction is likely slower for selenised molybdenum than for metallic molybdenum.

2.3.1.3 Summary on molybdenum degradation

When molybdenum and selenised molybdenum films are exposed to water and oxygen, especially under elevated temperatures, black and blue stains can occur on the metallic molybdenum surface. These stains contain molybdenum oxide (MoO_2/MoO_3), which is generally badly conducting and reflecting. This likely has a negative impact on the solar cell. Furthermore, the molybdenum oxide layers can crack and needles can be formed. The formation of a thick layer of non-conductive molybdenum oxide presumably leads to a very fast decrease of the conductivity when measured from the top. The degradation effects are the most severe for molybdenum deposited at high pressures during sputter deposition, thereby forming more porous molybdenum layers, which are more susceptible for ingression of among others water and oxygen. Selenised molybdenum also degraded in damp heat tests via the formation of molybdenum oxide, but this process occurred slower, probably since it is easier to oxidise metallic molybdenum than $MoSe_2$.

Although the oxide formation seems very detrimental for later deposited solar cells, mild oxidation could actually result in slightly improved efficiency. When CIGS is deposited onto oxidised molybdenum the molybdenum oxide is likely reduced ($MoO_3 \rightarrow MoO_2$) as well as transformed into $MoSe_2$.

Various references reported on the presence of sodium, which likely plays a role in molybdenum degradation. Sodium can e.g. occur in the form of needles on the molybdenum surface, however it is also possible that it intercalates via a reduction reaction into MoO_3, thereby forming Na_xMoO_3.

2.3.2 CIGS absorber degradation

The CIGS absorber layer is the core of a CIGS solar cell and also the layer with the biggest variety of deposition techniques and material parameters. Variations include the deposition temperature (depending on the substrate choice), one/two/multi-step processing, gallium-grading (flat or sophisticated), sulphur/selenium ratio and alkali supply (quantity and source type). The variety lead to a diversity of startups and companies that are offering CIGS based products, each with individual intellectual property about their specific CIGS absorber [36].

There are two fundamental techniques to deposit the CIGS absorber:

1. Thermal co-evapouration of all the constituent elements, i.e. the deposition of copper, indium, gallium and selenium onto a substrate with suitable growth temperature (typically between 400 and 600°C)
2. Two stage processing: Deposition of copper, indium and gallium precursors onto the cold substrate followed by annealing under a selenium atmosphere at high temperatures (this can sometimes also be called rapid thermal processing (RTP)).

Since the chalcopyrite absorber always crystallises under selenium-supply, it should be denoted that co-evapourated absorbers grow 'bottom-up', i.e. from the back contact towards the (later) absorber surface, while two stage absorbers crystallise 'top-down', i.e. the precursor (and thus later absorber) surface selenises first.

As noted in the introduction, the stability of non-encapsulated CIGS solar cells is mainly threatened by humidity [37]. Many research groups report a reduction of the open circuit voltages and the fill factors of their CIGS solar cells after damp heat exposure [38-41]. More information about factors majorly influencing the fill factor is given in other chapters (the molybdenum contact (chapter 2.3.1), the TCO (chapter 2.3.4), the isolation scribes (see chapter 2.5.1) and the grid (chapter 2.5.2)).

The changes in open circuit voltage are often related to the CIGS absorber. Lower

open circuit voltages after damp heat may be caused by changes inherent to the polycrystalline CIGS absorber such as point defects, doping, elemental diffusion, oxidation or grain boundaries. Or, they may be related to the properties of the pn-junction, e.g. band bending, Fermi-level-pinning or interface defect states. Either way, these effects are typically studied by electrical measurement techniques, e.g. admittance spectroscopy, which rely on the existence of a pn-junction.
This chapter is limited to the stability issues measurable in the CIGS absorber (this chapter), while complete solar cells and modules are described in chapter 2.4. In this chapter, we will first discuss the limitations considering the study of the stability of the CIGS absorber. Then, the intrinsic stability, which is the stability without environmental exposure, is presented. Finally, the stability of the CIGS absorber with respect to chemical changes and to sodium content under exposure to humidity and/or temperature will be discussed.

2.3.2.1 Experimental aspects regarding the long-term stability of CIGS absorber layer

When investigating the properties of a CIGS absorber in a solar cell under ALT conditions, one faces the challenge of revealing properties of one specific layer within a stack of interacting layers. This is particularly the case since creating model samples, i.e. an 'isolated' CIGS layer, of similar quality as in the actual device is nearly impossible. For example, if one removes the TCO/buffer/CIGS stack from the back contact, then the buffer and TCO, which are more conductive than the CIGS, are still underneath the CIGS. Thus, electrical measurements on the CIGS absorber alone are difficult. If, on the other hand, one stops the solar cell manufacturing process after absorber deposition or chemically etches away layers from the top, creating a substrate/molybdenum/CIGS sample, the more conductive molybdenum back contact causes the same problems. In the case of etching, an additional challenge is to stop the etching process right at the absorber surface.

Another option to allow testing of the CIGS absorber would be the growth of the absorber directly onto an alternative, non-conducting substrate. In that case, however, the crystal growth would be different, the sodium and potassium contents would be different, no $MoSe_2$ could form and the layer properties would not be comparable to a real solar cell anymore. Apart from the fact that the absorber properties are most likely different from the CIGS layer in the solar cell, the aforementioned techniques are destructive. This is also the case for many valuable analysis techniques for structure and composition, like SIMS and XPS. Thus, the comparison of the electrical properties of the as-prepared and aged solar cells as well as the individual layer properties at the same time is impossible.

Therefore, electrical measurements are typically performed on complete devices. This is also necessary to obtain the very basic information about the conversion efficiency. The main challenge is to separate the influences of all individual layers (from substrate to TCO) in the interpretation of these electrical measurements. A common approach is to investigate a series of solar cells that are manufactured the in same way, except for some intentional variations in the absorber layer (e.g. alkali doping, Ga grading, thickness). By comparing the degradation results from different samples, conclusions of the influence of the absorber and its composition on the stability of the solar cells are possible.

2.3.2.2 Intrinsic CIGS stability

Intrinsic instabilities of Cu(In,Ga)Se_2, like the mobility of constituent elements or interface reactions between the layers of the final device, are potentially detrimental for the long-term stability of a CIGS solar cell. However, Guillemoles et al. [37,42,43] argue that these fundamental instabilities are actually beneficial to the device: possible interface reactions (back contact/absorber, absorber/buffer, buffer/window) are thermodynamically or kinetically limited. In contrast to a-Si:H solar cells, defects are self-annealed at room-temperature and are actually beneficial to the cell performance, since they effectively increase the doping level in the CIGS absorber.

Regarding the defects in CIGS absorbers, the two most important features considering the stability are the presence of a large defect pool and the possibility of ionic migration, mostly of copper. Their synergetic action makes CIGS absorbers radiation hard and impurity tolerant materials. In that sense, the stability of CIGS absorbers is not static but dynamic or, as Guillemoles et al. [42] put it, ´CIGS absorbers are strong because they are flexible´. In that sense, they are called a ´smart material´, which is by their definition ´capable of sensing changes in its environment and responding to them´.

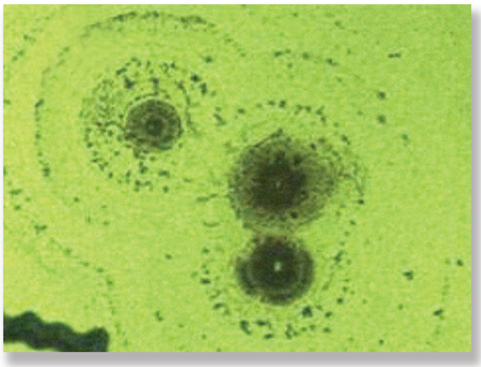

Figure 2.6

Optical image of spot formation on ambient-degraded CIGS film at a magnification of 16x obtained from reference [44] with artificial colours.

2.3.2.3 Chemical changes in the absorber

In this chapter, we present data about chemical changes in CIGS absorbers that are not embedded in a solar cell. In chapter 2.4, more extensive information about changes in full solar cells is given.

Pern et al. [44] exposed CIGS absorbers to damp heat tests (15 minutes to 5 hours) and for 8-12 months to the laboratory atmosphere. Both the 5 hours damp heat and the air exposure led to the formation of spots (Figure 2.6), which were also reported by references [21] and [45]. The spotty areas showed low gallium, copper and selenium concentrations, while the concentration of sodium was relatively high.

It was expected that hydrolysis or oxidation led to these degradation processes. These spots did not have an impact on the optical properties between 250 and 900 nm. Scanning Kelvin Probe (SKP) and Atomic Force Microscopy (AFM) measurements were used to observe the correlation grain topography and the work function distribution. Before degradation, the work function depended closely on the grains' surface facets and its values on the grain boundaries might have depended on specific grain boundary structures. After one and five hours of damp heat exposure, SKP AFM measurements showed that small spots occurred on the surface. It was also observed that the work function had lost its correlation with the grain geometric feature due to damp heat exposure. After five hours, the initially well-defined work-function images became blurred, which could be a results of the electronic property breakdown of the CIGS grains.

Solar cells were made from the absorbers exposed to ambient conditions and to 15 and 30 minutes damp heat. The cells exposed to ambient conditions showed a severe decrease of all solar cell parameters, while the damp heat degradation showed a much smaller decrease of only V_{oc} and FF.

The degradation of bare CIGS absorbers under damp heat or under ambient conditions agreed with the large decrease in carrier lifetime observed by Metzger et al. [46], who studied air exposed CIGS absorbers by Time Resolved Photo Luminescence (TRPL). This degradation process can be prevented by CdS deposition, which leads to absorbers that are stable in the air for months.

Suggestions about the possible degradation products on the absorbers were given by Würz et al. [47] and Heske et al. [48]. Würz et al [47] reported the formation of $Cu(OH)_2$ on $CuGaSe_2$ solar cells that were stored under ambient conditions for months. Heske et al. [48] reported the formation of sulphate, which resulted from the damp heat induced oxidation of sulphur in $Cu(In,Ga)(Se,S)_2$ solar cells.

2.3.2.4 Role of the sodium on the absorber stability

Large variations in composition and structure of the CIGS absorber can be observed, which are often related to the sodium content. In this chapter, the impact of the alkali supply - typically sodium - on the stability of the CIGS absorber was studied. Sodium can be added during growth or in a post-treatment and is a key to achieve high-efficiency CIGS solar cells. Additionally, it is known that sodium is an important factor in the long-term stability of CIGS solar cells [49-52]. In this chapter, only studies on the individual absorber are included, while more information about full cells can be found in chapters 2.4.

According to Braunger et al. [49], the oxidation of CIS or CIGS is accelerated in the presence of sodium. The oxidation of the absorber at elevated temperatures barely influences the efficiency, but oxidation of the absorbers in humid air at room temperature results in a drastic decrease in electrical performance. They [49] describe that reactions of sodium with selenium species are possible at very low temperatures. For temperatures under 500°C, sodium polyselenides (Na_2Se_x) form, while above 500°C, sodium monoselenides (Na_2Se) are formed. CIGS absorbers grown on soda lime glass, therefore in the presence of sodium, showed less indium or gallium oxides at the surface, but more elemental selenium and selenium oxides, compared to CIGS grown on sodium-free substrates. As humidity was found to promote the degradation, water catalysed reactions for the incomplete oxidation of Na_2Se_X, which is present as precipitate / intergranular segregation in the polycrystalline CIGS film, in air were suggested:

- $Na_2Se_X + 1/2\ O_2 \rightarrow Na_2O + x\ Se$ (2.2)
- $Na_2Se_X + 3/2\ O_2 \rightarrow Na_2SeO_3 + (x\text{-}1)\ Se$ (2.3)
- $Na_2Se_X + 1/2\ O_2 + CO_2 \rightarrow Na_2CO_3 + x\ Se$ (2.4)

Accordingly, a water and sodium catalysed reaction pathway of the absorber was suggested:

- $2\ Cu(In_{1\text{-}X}Ga_X)Se_2 + 3/2\ O_2 \rightarrow 2\ \text{´}Cu(I)\text{´} + (1\text{-}x)\ In_2O_3 + x\ Ga_2O_3 + 4\ Se$ (2.5)

Since Braunger et al. detected a partial oxidation of selenium in their degraded samples, they assumed another reaction pathway: $Se + O_2 \rightarrow SeO_2$ [49]. According to the authors, the presence of water leads to the hydrolysis of the oxides, i.e. the formation of $In(OH)_3$, $Ga(OH)_3$, H_2SeO_3 and NaOH. In conclusion, Braunger et al. found sodium to promote an enhanced removal of selenium from the absorber layer via the formation of Na_2Se_x compounds. During degradation, the oxidation of the absorbers leads to the oxidation of both CIGS and Na_2Se_x. If that oxidation is incomplete, an increased production of elemental selenium from CIGS and Na_2Se_x following the above described reactions occurs, which severely affects the device performance, mainly due to the decrease of the shunt resistance.

The impact of sodium content on absorber stability was also reported by Sakurai et al. [51], who varied the molybdenum sputter pressure. Since this impacted the sodium migration, the resulting CIGS absorbers had different sodium contents. The stability of these layers was studied: at high sputter pressures, large holes in the molybdenum layer perpendicular to the substrate were observed. CIGS layers deposited on these layers showed low efficiencies and poor reproducibility. Dark spots occurred on the absorbers under air exposure and increased in size and number with time. These spots were physical distortions of the CIGS layers and contained high concentrations of sodium and oxygen. These elements were found up to 1 µm depth in the CIGS layer. It is proposed that this resulted from NaOH damage, formed by a reaction from a sodium product with water vapour. When the sputter pressure was decreased and the molybdenum became denser, the spots were not formed.

2.3.2.5 Summary on CIGS absorber degradation

The CIGS absorber has a variety of defects with complex interactions that determine their benign electronic behaviour. Due to the synergetic interaction of a large defect pool and the possibility of ionic migration (mainly copper), CIGS is a radiation hard and impurity tolerant material. CIGS grains themselves are thus intrinsically stable, irrespective of their complicated structure. Changes of the CIGS absorber due to extrinsic influences such as damp heat are therefore generally with respect to grain boundaries within the polycrystalline absorber film and the interfaces to other layers (back contact and buffer layer).

Due to experimental limitations, CIGS absorbers are mostly studied within the thin film layer stack of CIGS thin film solar cells, so generally limited experimental information is available about the stability of the absorbers themselves.

However, it is known that the exposure of bare CIGS layers to ambient conditions leads rapidly to a significant reduction of the carrier lifetime. This degradation process can be prevented by CdS deposition on top of the CIGS which yields stability for several months.

Under the exposure to damp heat, spots were formed on the surface of bare CIGS layers. These spots exhibited low gallium, copper and selenium concentrations, but high sodium contents. It was assumed that hydrolysis or oxidation led to these degradation processes. The formation of $Cu(OH)_2$ on $CuGaSe_2$ solar cells that were stored under ambient conditions was also reported. Furthermore, the formation of sulphate was reported as a result the damp heat induced oxidation of sulphur in $Cu(In,Ga)(Se,S)_2$ solar cells.

Sodium was found to have a very large impact on CIGS absorber stability: in the presence of sodium and water, oxidation of CIGS absorbers occurred. Experiments showed that this oxidation catalysed by water promotes an enhanced removal of selenium from the absorber layer containing Na_2Se_X compounds leading to severe efficiency loss, mainly following reduced shunt resistance. Additionally, the presence of a large sodium content due to porous molybdenum also led to the formation of physical distortions in the CIGS absorber layer.

2.3.3 Buffer degradation

In CIGS solar cells, a n-type buffer is used to form the pn-junction together with the p-type CIGS absorber. The most used buffer is CdS, which is deposited via Chemical Bath Deposition (CBD). However, for both environmental and practical issues and the relative low bandgap of CdS (2.4-2.5 eV), many alternatives for CdS, like $Zn(O_xOH_yS_z)$ and In_xS_y have been studied and implemented [52]. In this chapter, the stability of CdS as well as alternative buffers are described. It should be noted that the same experimental restrictions as described for CIGS absorber layers also exists for buffer studies, so no studies about individual buffer layers are included.

2.3.3.1 CdS buffer degradation

Wennerberg et al. [38] studied the degradation of the window layer with model structures, which consisted of a substrate (glass or silicon)/CdS (no/one/two CBD-dips)/ZnO/ZnO:Al. ZnO:Al grown on a substrate without CdS buffer were more stable regarding the sheet resistance under damp heat conditions. Furthermore, the TCO sheet resistance degradation was enhanced by an increasing CdS buffer thickness. Therefore, the CdS seems to have a negative influence on the ZnO:Al stability.

CIGS solar cells on glass with CBD CdS buffer layers were studied with respect to their degradation behaviour under damp heat exposure (100 hours, 1000 hours) by Schmidt et al. [40]. IV measurements revealed that, besides V_{oc}, most significantly the fill factordegrades. The degradation of the ZnO/CdS window layer was considered as likely explanation. Decreasing ZnO conductivity with increasing duration of damp heat was argued to lead to the observed losses in fill factor. The authors stated that different ZnO deposition techniques and various CdS thicknesses lead to more or less degradation of the ZnO/CdS window layer.

Heske et al. [48] analysed ZnO/CIGSSe and ZnO/CdS/CIGSSe interfaces by XES (soft

X-ray emission spectroscopy). The authors observed the formation of a sulphate species at or near the ZnO/CdS and the ZnO/CIGSSe interfaces after damp heat treatment. In both cases, sulphur atoms diffused into the ZnO layer and formed a sulphate species there (such as $ZnSO_4$). In contrast, a series of similar samples that were tested under dry heat conditions showed no evidence for sulphur oxidation or sulphate formation. Thus Heske et al. concluded that the source of oxygen for the sulphate formation is predominately the ambient humidity rather than the ZnO layer. The authors propose that the losses in fill factor observed by [40] and the commonly observed increase in ZnO resistivity are enhanced by a change in the electronic and chemical structure at and near the ZnO/(CdS)/CISSe interface, as well as by the altered electronic properties of the ZnO film containing a detectable fraction of $ZnSO_4$ 'contamination' in the vicinity of the interface [48].

Ramanathan et al. [53] described the impact of exposure to high temperature air and argon on borosilicate glass/i-ZnO/ZnO:Al and borosilicate glass/CdS/i-ZnO/Al:ZnO stacks. The stack containing CdS showed an increase in sheet resistance from 18 Ω/□ to 60 Ω/□ due to 2 minutes annealing at 200°C, while the stack without CdS has a constant series resistance. Optical measurements showed a decrease in absorption in the wavelengths where CdS absorbs (380 up to 540 nm) due to the heat treatments. It is proposed that a reaction between i-ZnO and CdS occurred, resulting in the formation of an intermediate material with a higher band gap. Suggested candidates are $Cd_{1-x}Zn_xS$ and $ZnO_{1-x}S_x$.

This effect was also seen for full CIGSe cells, which showed an increase in blue response of up to 20% in EQE due to heat treatment (2 minutes at 250°C). The treatment also led to shift of the absorption edge to lower wavelengths, suggesting that the absorber itself has an increased band gap as well, maybe due to sulphur diffusion from CdS to CIGSe.

2.3.3.2 Degradation of alternative buffers

A growing number of alternatives for CBD CdS buffers have been introduced [52]. In this chapter, the stability of these alternative buffers is described.

Allsop et al. [54] studied the damp heat stability of CIGS solar cell with spray-ILGAR (ion layer gas reaction) deposited indium sulphide buffers. Encapsulated mini-modules without edge sealing, like PVB laminates, were exposed to approximately 1000 hours to a damp heat test. Mini-modules that had lower initial efficiencies due to poor buffer layer homogeneity from an non-optimised process showed an approximately 30% higher degradation compared to those with initially higher efficiencies due to an optimised homogeneous buffer.

Spiering et al. [55] compared CIGS mini-modules (15 x 30 cm^2) with ALD indium sulphide buffers to those with CBD CdS buffers. The mini-modules were exposed to a damp heat test for 1000 hours. Mini-modules with both buffer technologies still showed more than 95% of the initial power after 1000 hours damp heat, while no differences in the degradation behaviour was found.

As will be described in chapter 2.4.2, Kushiya et al. [10] exposed CIGS modules with a CBD $Zn(O,S,OH)_x$ buffer to a combined test with damp heat and illumination. The changes in fill factor as observed within this experiment might be related to this buffer. The hydration of ZnO by free water molecules in the buffer might have led to $Zn(OH)_2$ formation, leading to deterioration of the properties of the pn-interface and the fill factor. The reverse reaction, which is the dehydration of the $Zn(OH)_2$ to ZnO, might have explained increases in fill factor.

2.3.3.3 Summary on buffer degradation

Under damp heat exposure, the thin CdS buffer seems to diffuse into the CIGS and ZnO layers. Possible reaction products are $ZnSO_4$ or a similar sulphate and $Cd_{1-x}Zn_xS$ and $ZnO_{1-x}S_x$. The interaction between CdS and the doped ZnO can possibly lead to an increase in the sheet resistance of the latter layer. Interaction between these layers was also found when $Zn(O,S,OH)_x$ was used as buffer, which likely resulted in the hydration and dehydration of ZnO into $Zn(OH)_2$ and vice versa. When In_2S_3 was used as alternative buffer, no large differences in stability with CdS based solar cells could be found.

2.3.4 TCO degradation

The transparent conductive oxide (TCO) functions as a front contact of CIGS solar cells or modules. It should be transparent to allow the influx of photons to the CIGS layer, while its conductivity is required for the transport of the produced electrons. Therefore, the main requirements for a TCO in a solar cell or module are the conductivity as well as the transparency.

Studies on the effects of field and accelerated testing of CIGS modules have indicated that the primary observed reason for module failure is the decrease of fill factor as a result of an increased series resistance of the TCO [4,56]. The TCO is therefore often stated as the key element in CIGS module degradation. This can be explained by the vulnerability of some TCOs for water, but also by the fact that cell sizes are mostly optimised based on initial TCO conductivity. Therefore, small decreases in the conductivity can already greatly influence the series resistance and thus the efficiency of a CIGS solar cell or module.

The main type of TCO used in CIGS modules is sputtered aluminium doped zinc oxide (ZnO:Al), but other types, including indium tin oxide (ITO), indium zinc oxide (IZO) and chemical vapour deposited (CVD) boron doped zinc oxide (ZnO:B) are also used.

In order to compare the different types of TCOs with each other, the degradation rate

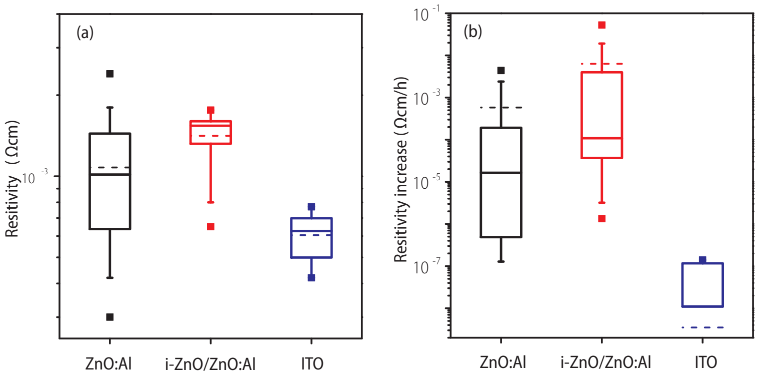

Figure 2.7

Box plots of the (a) initial resistivity and (b) linear resistivity increase per hours for ITO, i-ZnO/ZnO:Al stacks and ZnO:Al layers exposed to damp heat (85°C/85% RH). The top and bottom of the box show the 25% and 75% intervals, while the whiskers depict the 10% and 90% borders. The squares are the minimum and maximum value and the dashed line is the average value. The resistivity chances for especially ITO and in one case ZnO:Al can be zero or negative. These values are not depicted in these graphs.

of a large numbers of TCOs under various conditions has been determined by assuming a linear decrease of electrical parameters D:$\frac{\Delta D}{\Delta t}$. This linear decrease is the simplest approximation and in many cases not representing the rate of the degradation accurately. Therefore, these numbers should only be considered as a guide to the eye for the stability of various types of TCOs. However, without any further assumptions, the linear approximation allows to compare the degradation data from different authors which are represented differently in each publication. For the data generation, it is assumed that the underlying CIGS and buffer layers can withstand temperatures up to 200°C that may occur during TCO deposition. This temperature is selected since it is often quoted by experts on CIGS solar cells or modules. It should be noted that Sharma et al. [57] already observed gradual loss of efficiency for TCOs deposited at 150°C, while Kijima et al. [58] showed CIGS solar cells which were stable up to 350°C. This indicates that a sharp border cannot be drawn, but nevertheless references with TCO deposition temperatures above 200°C are only included in this work if they present interesting new routes to more stable TCOs. However, they can be described in the further chapter, for the description of the observed degradation mechanisms.

Figure 2.7 shows the initial resistivity as well as the change in resistivity of the three most relevant TCOs in CIGS PV. These plots show that large differences exist within the initial resistivity of ZnO:Al, while the resistivity changes of i-ZnO/ZnO:Al and ZnO:Al show an even larger spread. ITO on the other hand has a lower initial resistivity and is also more stable during damp heat exposure. It should be noticed that the included data are taken from the literature studied in this work, but might not give a complete picture, since many reports about a certain material (e.g. i-ZnO/ZnO:Al) come from one dominant source, while other sources might show different degradation rates for the resistivity. It can therefore also not be concluded that a significant difference in degradation behaviour between ZnO:Al and the combined i-ZnO/ZnO:Al stack exists. However, it is clear that ITO is more stable and far more predictable than the zinc oxide based stacks. These stacks show degradation rate of the resistivity varying over more than five orders of magnitudes.

Additionally, in the supplementary information, a table shows a literature overview of the degradation rates of the resistivity (ρ), Hall mobility (μ_{Hall}) and carrier concentration (n_{Hall}) under different degradation conditions. A wide range of TCOs (type, layer thickness and deposition technique) for CIGS cells are included.

Based on this information and on the information of Pern et al. [59], that is based on the electrical, optical, structural and morphological analysis of various types of TCOs, the order of degradation rates for TCO materials is

$$\text{ZnO} \gg \text{IZO} > \text{ITO} > \text{FTO}$$

This indicates zinc oxide has the highest and fluorine-doped tin oxide the lowest degradation rate.

It should be noted that tin oxide as well as indium zinc oxide are not further described in this chapter, since only few studies using these TCOs in high efficiency CIGS solar cells exist. Nevertheless, the impact of the stability of SnO$_2$ in a CIGS solar cell is described in chapter 2.3.4.3 [60,61].

2.3.4.1 Zinc oxide degradation

2.3.4.1.1 General degradation mechanisms

Zinc oxide based materials are in general non-toxic, inexpensive and abundant and therefore often chosen as a TCO in CIGS samples. In general, the samples are deposited by sputtering without additional heating or at least below 200°C to prevent damage to the underlying layers.

Studies by Greiner [62,63], Ando [64-66], Minami [67,68], Zhan [69], Tohsophon [70], Theelen [71], Hüpkes [72], Pern [19,24,25,30,44,59,73], Sundaramoorthy [74], Feist [29] Lin [75], Owen [76], Hamasha [77], Kim [78], Steinhauser [79], Illiberi [80] and their coworkers have focused on 'damp heat' degradation of doped ZnO. Additionally, an interesting overview about degradation of zinc oxide for CIGS was written by Klenk [81]. In all these publications, the focus often lies on sputtered aluminium doped zinc oxide (ZnO:Al), which is used by most companies and research centres as TCO on CIGS, while other zinc oxide compounds, like CVD ZnO:B are also included. The latter is for example used in industrial production by Solar Frontier. Relations between the electrical and optical properties and deposition temperatures [68,71], crystallinity [68,71], sample thickness [25,67,68,75] and doping content [64,79] were found.

Literature [29,77] reported that ZnO:Al is generally stable in *dry* heat tests while *damp* heat exposure led to a decrease in conductivity. This is mostly caused by a decrease in electron mobility, while changes in carrier concentration were observed in some cases but can be minor to negligible for other ZnO:Al films. Changes in the optical properties were also observed, but in general, these minor changes will have a relatively small impact on module performance, when compared to the impact of the changes in electrical properties. Pern et al. [25,59] for example observed the disappearance of fringes in the transmission spectra, which did not necessary lead to a lower transmission. Greiner et al. [62] and Theelen et al. [71] have also shown the minor impact of damp heat treatment on optical properties, like transmission and the Drude frequency.

Various references [71,76,79] suggested that ZnO:Al degradation is mostly driven by an enhanced potential barrier at the grain boundaries, while in-grain degradation probably has a smaller impact. The difference between these processes is shown in Figure 2.8.

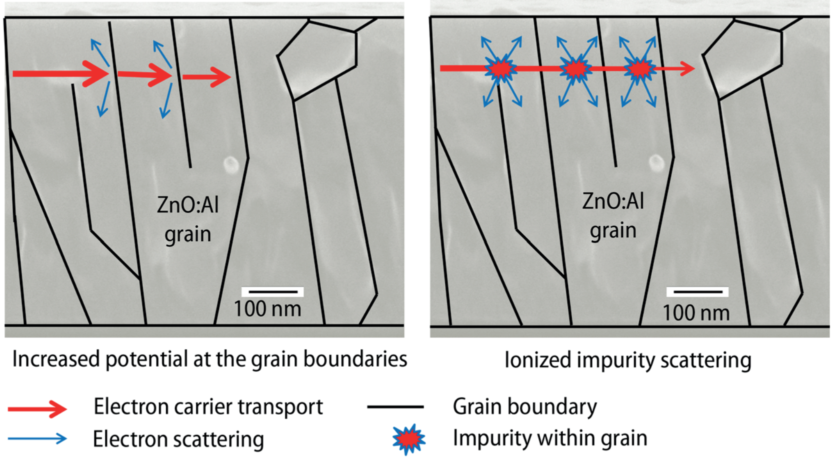

Increased potential at the grain boundaries

Ionized impurity scattering

Figure 2.8:

Possible electron scattering mechanisms in zinc oxide samples based on references [71,82].

Several fitting models were reported to distinguish between degradation based on grain boundary and grain degradation. These are based on the comparison of the decrease of electrical properties obtained by optical ('intra grain') and electrical Hall measurements ('inter grain').

Steinhauser et al. [79] concluded the dominance of grain boundary degradation in Low Pressure Chemical Vapour Deposition (LPCVD) ZnO:B based on measurements. Calculations based on these experiments also allowed the estimation of the barrier width and height. The change of the current path due to degradation of grain boundaries in ZnO:B in shown in Figure 2.9. They described that for non-degraded ZnO:B samples, both tunneling and thermionic emission can be considered as the path of the current through the grain boundary potential barrier. When samples were exposed to a damp heat test, this leads to an increase of the trap state density N_t at the grain boundary and thus to a higher and wider potential barrier. The latter are depicted by a larger barrier width W and barrier height V_b. Therefore, the current path through the barrier by tunneling is decreased, so thermionic emission becomes the dominant way of transport. When the sample is exposed to a damp heat test, a shift toward a more thermionic-emission governed conductivity is therefore made. It can be expected that a similar trend occurs for sputtered ZnO:Al.

Greiner et al. [62,63] showed very strong degradation of ZnO:Al conductivity when ZnO:Al films are grown on rough substrates, due to the formation of 'extended grain

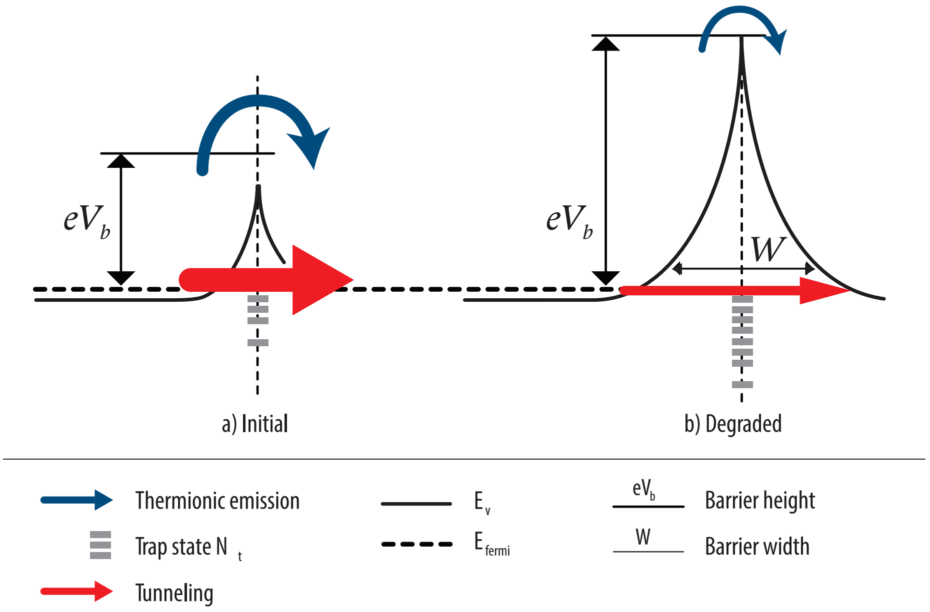

Figure 2.9

Schematic drawing of the current path through the barrier at a grain boundary based on [79] of a (a) as grown and (b) damp heat degraded LPCVD ZnO:B sample. In the degraded state the barrier width W and height V_b are larger, while more traps states are present.

boundaries'. These are localised layers of small grains within the ZnO:Al layer that have non-perpendicular crystallographic axes and a higher percentage area of grain boundaries as compared to the rest of the ZnO:Al layer, which consists of compact grains with grain boundaries in parallel. These extended grain boundaries are even more unstable than standard grain boundaries. These are local perturbations of the ZnO:Al morphology, which also allow fast diffusion of environmental species into the material. Owen et al. [76] has also shown that etched, structured ZnO:Al degraded quicker than the same ZnO:Al in an unetched state.
This important role for the grain boundaries in the electrical properties of zinc oxide is also confirmed by Beyer et al. [83]. It was reported that neon cannot effuse out of the bulk material of sputtered zinc oxides for temperatures as high as 1000°C. However, transport through the grain boundaries was possible. Therefore, the transport of molecules like oxygen, carbon dioxide and water is also only possible through the grain boundaries.

Arzel et al. [84] also compared the changes induced by damp heat in optical (intragrain) and Hall (intergrain) resistivity of four types of sputtered ZnO:Al. They concluded that a large change in resistivity for less stable ZnO:Al was caused by grain boundary degradation, while the stable ZnO:Al samples degraded only slightly and mostly within the grains.

Based on these references, it can be concluded that in general, *extended* grain boundaries are the most sensitive to damp heat exposure. If these structures are either stable or not present, than the degradation of normal grain boundaries will become dominant. If this does not happen, ingrain degradation will have the most important influence on the degradation of the sample.

2.3.4.1.2 Degrading species in ZnO:Al

Many references (e.g. [71,72,76]) describe that the deterioration of the electrical properties and the change of the composition of the ZnO:Al film and its grain boundaries was accompanied by migration of atmospheric species, like water, within the ZnO:Al samples. Due to the square root shape of the evolution of the resistivity as a function of degradation time, it was concluded in reference [71] that the degradation of ZnO:Al is a diffusion process. Many studies included in Figure 2.8 for zinc oxide degradation also show a shape that could be fitted with a square root function. However, a large number of data points is required in order to find this relationship, which are not available in all studies.

The changes in electrical properties are probably caused by changes in the grain boundaries, where a small change in composition can have a large impact on the conductivity. Furthermore, in some cases, the composition of the grains also had changed. At present, the chemical mechanisms leading to these composition changes are not completely clarified. In this chapter, we discuss which species can be involved in the degradation. Suggestions about the molecules that are formed during ZnO:Al degradation include $Al(OH)_3$ [25,64], $Zn(OH)_2$ [25,64,71,76], ZnOH-complexes and hydrates [20], $ZnCO_3$ [76] and $Zn_5(CO_3)_2(OH)_6$ and related species [71] which are mostly non-conductive materials. The presence of a hydroxide was also shown in reference [29]. These materials can function as an electrical potential barrier in the grain boundaries as shown in Figure 2.10. They might also be present in the grains, thereby simply decreasing the conductivity of the films.

It is clear that these chemical reactions occur due to reactions between the zinc oxide and molecules from the atmosphere. It was suggested in reference [75] that the penetration of oxygen and water molecules into the bottom part of the film can strengthen the effect of grain boundary scattering, while other references [72,72,76] suggested a role for water and CO_2.

Theelen et al. [85] studied the role of various atmospheric species, by exposing ZnO:Al layers at room temperature to the atmospheric gases carbon dioxide (CO_2), oxygen (O_2), ogen/argon (N_2/Ar) and air as well as liquid water purged with these gases, in order to investigate their influence on the stability behaviour of these layers. It was shown that O_2 and CO_2 gases in the absence of water did not cause any degradation at all during the tested period, while water purged with O_2 or N_2 only led to a small increase in resistivity, likely due to the formation of a limited amount of $Zn(OH)_2$. However, when CO_2 was also present alongside with water, the concentration of OH^- increased greatly in the bulk and even more at the air/ZnO:Al and the ZnO:Al/glass interfaces. It could thus be concluded that ZnO:Al was stable in water as well as CO_2 individually, but degraded quickly in these species combined. Furthermore, O_2 exposure does not lead to degradation of ZnO:Al. More information about these experiments can be found in chapter 6.

It was proposed that migration of species during degradation of ZnO:Al on borosilicate glass occurs in two directions [71]. Water, CO_2 and other atmospheric species can migrate from the environment into the ZnO:Al, thereby increasing the resistivity. On the other hand, elements from the glass, including calcium, silicon and aluminium migrated to the ZnO:Al surface, where they react with carbon and oxygen to form spots and stains of carbonates and oxides. These spots and stains likely formed after removal from the climate chamber, due to the drying of the condensed water. Spots were also observed by Hamasha et al. [77] where they occurred on samples exposed to 100% humidity. They were described as drying stains.

2.3.4.1.3 Material changes during ZnO:Al degradation

The nature of the structural and compositional changes in ZnO:Al exposed to temperature and moisture is hard to detect, because changes mainly happen at the grain boundaries, thereby only influencing a small volume fraction of the thin film material. However, two possible processes can explain the degradation at the grain boundaries due to diffusion of atmospheric species, like water and CO_2 [71]:

- Molecular adsorption (physical reaction)
- Chemical reaction of the species with the ZnO:Al

Hüpkes et al. [72] used deuterium as an isotopic marker to identify the amount of deuteriated water (D_2O) taken up by the films during damp heat exposure. They concluded that the water uptake does not saturate even after 1000 hours and that the diffusion of the atmospheric species is the rate limiting step for the degradation rate. This was confirmed by SIMS measurements in reference [71], which showed a gradient in OH^- content even after 2876 hours of damp heat exposure.

Theelen et al. [71] proposed that the ingression of water leads to the formation of $Zn(OH)_2$, which does not greatly influence the properties of the ZnO film. However, in the presence of CO_2, materials like hydrozincite ($Zn_5(CO_3)_2(OH)_6$) can be formed, while related chloride and sulphate containing species can also form. These molecules are probably present in the grain boundaries and can then function as electrical potential barriers (Figure 2.9). More information about this proposition can be found in chapter 6.

Kim et al. [78] described the composition of the grain boundaries before and after degradation. It was observed that before degradation, grain boundaries had a higher local conductance and a higher zinc to oxygen ratio than the material in the middle of the grains. After 24 hours at 80°C/100% RH, the conductance and the zinc to oxygen ratio had decreased at both positions. This suggests that the oxidation of zinc was responsible for the loss of local conductance. In this reference, it is proposed that the excess of zinc, which is present in conductive ZnO forms in the presence of water into undoped, stoichiometric ZnO with a high resistance and hydrogen gas:

$$\mathrm{Zn(excess)} + H_2O \rightarrow Zn^{2+} + 2e^- + 2H^+ + O^{2-} \rightarrow \tag{2.6}$$
$$\mathrm{ZnO\ (stoichiometric,\ high\ resistance)} + H_2\uparrow \text{ [78]}$$

The formation of the undoped ZnO is here linked to the dissociative chemisorption of water, which leads to the removal of free electrons from donor sites, which are more populated at the grain boundaries. It should be noted that the measured decrease of zinc to oxygen ratio can also be caused by the formation of other species like $Zn(OH)_2$.

Owen et al. [76] also proposed the formation of stoichiometric ZnO in the grain boundaries due to the adsorption of water. This would lead to the loss of the effect of aluminium doping and thus to a decrease of the local carrier concentration. This can then lead to an increase of depletion regions and potential barriers at the grain boundaries. This effect is not visible in the global carrier concentration, since this reduction only happens locally.

2.3.4.1.4 Influence of substrate temperature and crystallinity

Pern et al. [25] observed that ZnO:Al and (Zn,Mg)O:Al samples sputtered at a higher substrate temperature degrade slower than those deposited at ambient temperature. Theelen et al. [71] confirmed this observation: a higher sputtering temperature (200°C compared to RT) of ZnO:Al led to the formation of larger grains, which were also more stable under damp heat treatments.

This relationship was not found for all deposition techniques: for Pulsed Laser Deposition (PLD) samples, it was observed that a varying substrate temperature between 68°C and 200°C did not influence the degradation greatly [68]. However, it was also found that films with a better crystallinity had a higher mobility, due to bigger crystallite size and more crystals with the same orientation, reducing the effect of grain boundary scattering.

2.3.4.1.5 Influence of sample thickness

It was observed that thick samples degrade slower than thin samples [25,67,68,75]. This behaviour can be expected if diffusion is the degradation rate determining step in the degradation process. Pern et al. [25] described that thicker ZnO:Al or (Zn,Mg)O:Al samples degrade slower than thinner ones. This was explained by either a degradation process that started from the surface and gradually deepened into the bulk [25] or a difference in grain sizes or structures for different thicknesses [75]. Since the penetration of the atmospheric species is a slow process, the thick samples can have a non-degraded bottom layer even after long exposure to a damp heat test, while thin samples are then completely degraded.

In several studies, an increase in TCO layer thickness due to water exposure was observed. Very strong effects were observed by Feist et al. [29], who degraded conductive, low-transparent ZnO:Al samples to 85°C dry heat, 85°C/100% RH and liquid water at room temperature. They saw a thickness increases for these conditions from an initial 110 nm to thicknesses as large as ~130 nm, 350 nm and 1000 nm respectively. At the same time, the ZnO:Al resistivity increased by three to four orders of magnitude following exposure to the water bath and 85°C/100% RH environments.

Additionally, as described in chapter 3.3.4.1.1, the roughness of the layer beneath the TCO film also greatly influences the stability.

2.3.4.1.6 Influence of doping concentration

Minami et al. [68] observed that a high concentration of the aluminium (up to 8%) in ZnO:Al films led to a higher initial resistivity, but also to a more stable TCO when exposed to mild damp heat conditions (60°C/90% RH) for 1.000 hours. The influence of aluminium was also observed in reference [64], where aluminium contents of 1 to 10% were compared and a reduction in the internal stress of the ZnO:Al film for higher aluminium concentration (above 3%) was observed. The best moisture resistance was obtained for aluminium concentrations between 3 and 5 %. However, a concentration of 2% is standard for CIGS.

Steinhauser et al. [79] observed a large difference in stability of ZnO:B for different boron concentrations. He explained this relationship between doping concentration and damp heat stability by the higher carrier concentrations for the boron-rich samples. This relation can be explained by the increase of charge states at grain boundaries during damp heat treatment. Heavily doped ZnO grains allow extra tunneling through the potential barriers and thus more stable films. It has been shown that a-Si:H solar cells made with ZnO:B with high boron contents are stable under damp heat, in contrast to the cells with low boron concentrations.

Pern et al. [25] added magnesium to the ZnO:Al, leading to $(Zn_{0.9}Mg_{0.1})O{:}Al$ and $(Zn_{0.99}Mg_{0.01})O{:}Al$. The film with 10% magnesium was non-conductive, while the 1% magnesium film showed the same degradation behaviour as standard ZnO:Al, so no influence was observed. Kang et al. [16] added 1 wt-% Ga_2O_3 to the ZnO:Al. The electrical changes of these films due to 60°C/90% RH were relatively small, but due to the use of these mild conditions, comparison with ZnO:Al without gallium cannot be made.

In summary, a small increase of the aluminium concentration from values normally used in CIGS solar cells likely has a positive influence on the damp heat stability of the doped zinc oxide layers, while high boron doping concentrations are also desirable.

2.3.4.1.7 Reversibility

As described in chapter 2.3.4.1.3, it is likely that moisture and temperature exposure lead to changes in the grain boundaries. These changes can either be physical adsorption and/or chemical reactions. The adsorption of species like water is a reversible process under elevated temperatures, since the water incorporated during damp heat treatment is only weakly bound and can therefore be easily removed [76].

Chemical reactions, on the other hand, can also be reversible. It is likely that the formation of $Zn(OH)_2$ is reversible at temperatures above 114°C, which is its decomposition temperature. At this temperature, this material can decompose into ZnO and water. The same effect can likely occur for hydrozincite (chapter 2.3.4.1.3), which is known to decompose at temperatures around 220-250°C [86]. It should also be noted that complete CIGS cells are likely not stable at temperatures above 200°C, so heat treatment at high temperature cannot easily be used to reverse the ZnO:Al degradation on CIGS solar cell.

This reversibility effect was shown by various researchers for ZnO:Al on glass or silicon substrates. Tohsophon et al. [70] showed that the resistivity increase could be reversed by annealing in vacuum at temperatures of at least 150^0C. At this temperature, the effusion of water was reported. As a result of the annealing, the resistivity decreased and the carrier concentration increased to its initial values. At a higher temperature (500°C), effusion of CO_2 and H_2 was also involved, indicating tat least two different reversibility phenomena, like molecular adsorption and chemical reactions occurred during ZnO:Al degradation.

Minami et al. [67,68] reported that resistivity increase of 50 – 300 nm ZnO:Al films induced by damp heat exposure could be completely restored to the initial resistivity by annealing in a reducing atmosphere (Ar with H_2) at approximately 300^0 C.

These results showing reversible behaviour could not be imitated in an N_2 atmosphere by Ntinas et al. [87]. ZnO:Al films were deposited on both soda lime glass and borosilicate glass and degraded for 1032 hours in a damp heat test. This led to an increase in resistivity. Afterwards, they were exposed for two to eight hours to temperatures between 100 and 250°C under a N_2 atmosphere. This did not lead to a decrease of the resistivity. It must be noted that heating to 250°C led to a small improvement of the sheet resistance of the film deposited on sodium rich substrate, but it was unclear whether this was significant. It might be possible that a low pressure or reducing environment is required for annealing, allowing easy out-diffusion of environmental species.

2.3.4.1.8 ZnO:Al annealing

Instead of annealing after degradation, which can reverse the effects of damp heat exposure, annealing can also be applied as a part of the deposition process:

Hüpkes et al. [72] applied a special annealing step at 650°C in order to prepare highly stable ZnO:Al films. These films, which retain their charge carrier mobility of 70 cm^2/Vs after 1000 hours of damp heat treatment, probably have 'reconstructed grain boundaries'. This indicates that grains grow together due to the treatment, so the grain boundaries are 'closed'.

ZnO:Al films prepared via a low temperature deposition and annealing process which can be used for application in CIGS solar cells showed an increase in initial mobility from 13 cm^2/Vs to 35 cm^2/Vs due to the annealing treatment. They also showed a stable carrier concentration and mobility after 1000 hours damp heat exposure. However, it should be noted that in the reference sample without the annealing step also retained it mobility, but it showed a decrease in the carrier concentration.

2.3.4.2 Indium tin oxide degradation

An alternative to ZnO:Al is tin doped indium oxide (ITO). This material is especially attractive for small area cells and is less used for modules because of its relatively high cost. As shown in Figure 2.8, ITO is generally reported to be more stable than ZnO:Al.

Kim et al. [78] reported that the conductivity of a 1 µm thick ITO layer did not change after 24 hours of exposure to 80°C/100% RH. Guillen et al. [88] described that the structural and optical properties of sputtered ITO samples did not change due to 1000 hours exposure to a damp heat test. Small changes in sheet resistance were observed: it was found that samples with a higher partial pressure of O_2 during the sputtering process have a lower stability to a damp heat test. This is explained by the prominent presence of (222) oriented grains, which can accommodate a large amount of interstitial oxygen atoms. Due to their higher lattice distortion than for the (400) oriented grains, they are more vulnerable for humidity and oxygen ingress, since these species can now more easily migrate through the material via the defect paths.

Xu et al. [17] reported that a difference in degradation behaviour was observed for different sputtering temperatures. The structure of the ITO films changes from amorphous to polycrystalline for an increasing deposition temperature. The films deposited at higher temperature, had both a lower initial resistivity and a better stability when exposed to a damp heat test. Since the samples deposited at low temperatures are less crystalline, it was proposed that water and alkaline species (NaOH) can easily penetrate through amorphous ITO films. On these samples, white spots were found –

it was proposed they were formed due to a reaction with alkaline species.
Spots were also observed by Mei-Zhen et al. [89], who studied the degradation of amorphous ITO deposited at RT and 75°C and observed the formation of two types of spots. These circular patterns are likely formed by a reaction of the amorphous indium with water, which leads to decomposition and the formation of crystalline In_2O_3, while tin granules are formed at the same time. These effects can be caused by the heterogeneous distribution of tin and indium in the samples, which allows galvanic corrosion. This is an electrochemical process in which one metal corrodes preferentially to another when both metals are in electrical contact, in the presence of an electrolyte such as water.

2.3.4.3 Degradation of TCOs in CIGS solar cells

The impact of the TCO on the stability of a complete CIGS solar cell or module can be found in four ways:

1. The impact of increasing resistivity and transmission due to the diffusion of species. The effect of the resistivity increase can mainly be seen in a series resistance increase and thus a fill factor decrease of a solar cell or module, while transmission changes may impact the current of the solar cell or module.
2. Changes in TCO properties due to chemical reactions between TCO and, e.g., the encapsulation. The effects on a solar cell can be similar to the first point.
3. The changes in carrier concentration in both the TCO and CIGS layer, can lead to changes in the Fermi level, which will induce a change in V_{oc}.
4. The possibility for atmospheric species to diffuse through the TCO, thereby allowing the underlying CIGS/buffer layers to react with these atmospheric species, leading to a change in the absorber or buffer properties. This can e.g. result in changes of V_{oc}.

In this chapter, we will mainly focus on the impact of increasing resistivity (point 1), while the other points are mostly discussed in chapter 2.4.

Lee et al. [56] investigated the impact of damp heat exposure on CIGS modules and concluded that fill factor and efficiency losses of the modules were linked to the appearance of discoloured areas. The failure analysis of the ZnO:Al film indicated that a change in resistivity and surface morphology occurred in these areas. This was attributed to the formation of $Zn(OH)_2$ due to water penetration. Non-encapsulated solar cells were also exposed to a damp heat test: zinc hydroxide was found in small amounts on their ZnO:Al surface, while encapsulated modules contained the hydroxide inside the ZnO:Al as well as on the its surface. Furthermore, carboxylic acid was also present in the encapsulated modules. Dry heat treatment, on the other hand, did not lead to discolouration and had only minor impact on sheet resistance and module efficiency. The observed fill factor loss and discolouration were therefore concluded to be caused by a reaction between H_2O, Ethylene-Vinyl Acetate (EVA) and ZnO:Al.

A German consortium [81,90] studied the impact of damp heat on different types of ZnO:Al layers on nominally identical CIGS/CdS stacks. The ZnO:Al sheet resistance was measured before, during and after exposure to a damp heat test and increased for all samples. A clear correlation between this increase in series resistance and the decrease of the fill factor of the module test structures was observed. It was also observed that conditions which favour the growth of dense films with a good step coverage, i.e. the use of RF sputtering at a low pressure and high temperature as well as the use of a moving substrate, led to better stability.

Klaer et al. [91] used a sample design which allowed to determine the sheet resistance of zinc oxide on top of different types of CIGS. They noticed that the degradation of ZnO:Al when exposed to damp heat conditions can be very different depending on the underlying layers: while the zinc oxide sheet resistance was more or less stable on co-evapourated $Cu(In,Ga)Se_2$ absorbers, (increase $R_\square$ =10 mΩ/□/h) during 540 hours of damp heat, the sheet resistance increased very fast on sequentially deposited $CuInS_2$ (increase $R_\square$ =148 mΩ/□/h). This difference is probably caused by the very high roughness of the $CuInS_2$, compared to the smooth $Cu(In,Ga)Se_2$. This effect was described in reference [62] and in chapter 2.3.4.1.1.
Furthermore, the impact of the ZnO:Al series resistance was shown by the comparison of the series resistances in similar $CuInS_2$ cells with a different cell length (3 mm vs 8 mm). This difference in series resistance increase has a large influence on the efficiency of the solar cells: a difference of 2% absolute between the cells of 0.15 cm^2 and 0.40 cm^2 was observed.
The TCO itself can also function as a water barrier. Thompson et al. [22] discovered that a layer of i-ZnO on top of the CIGS and its surroundings can prevent water ingression. Experiments showed that 50 nm nanocrystalline i-ZnO and 150 nm amorphous ITO layers had a water vapour transmission rate (WVTR) of 1.3×10^{-3} and 0.7×10^{-3} $g/day/m^2$ respectively. Therefore, a thin large area i-ZnO layer can function as a water barrier, if it is not disrupted by scribes. This knowledge is especially relevant for thin film PV manufacturers using traditional modules based on ‘tabbed cells, who can greatly save on the costs of the additional water barriers necessary in a CIGS module in this way.
A similar effect was obtained by Selin-Tosun et al. [60], who deposited SnO_2 on top of unencapsulated CIGS cells with a ZnO/ITO TCO structure. This greatly decreased the water

ingression and therefore the efficiency loss of the solar cells due to exposure to damp heat. This layer was not described as a water barrier, but its presence can make the cells more intrinsically stable, so the costs of the barrier layers can be reduced.

SnO_2 has also been used as TCO for CIGS solar cells. Selin-Tosun et al. [61] described the difference in degradation behaviour between cells with a top layer of SnO_2/ITO and with i-ZnO/ZnO:Al. The unencapsulated solar cells had comparable initial efficiencies, but it was observed that SnO_2/ITO solar cells showed an efficiency decrease of only 5% after 120 hours of exposure to damp heat, while the efficiency of the standard i-ZnO/ZnO:Al samples decreased by more than 70%. The parameters mainly responsible for this difference are the V_{oc} and the R_{sh}. Since the V_{oc} and R_{sh} decreases were associated with water permeation into the pn-junction, it was concluded that the SnO_2 window layer hinders this migration. The least degradation was observed for a cell with a SnO_2 layer with a semi-crystalline nature: it consisted of nano-crystals embedded in an amorphous matrix. Therefore, no grain boundaries were present, so the migration of atmospheric species through the SnO_2 to the p-n junction was hindered.

As described above, ITO and other alternative TCOs are more expensive than the standard ZnO:Al, but they are also more stable. Therefore, the financial choice between low costs ZnO:Al compared to the expensive ITO is not as straightforward as expected, since the barrier materials required for the ZnO:Al based CIGS modules are more expensive. Since the barrier materials add greatly to the cost of the modules, ITO based CIGS modules can end up to be more cost-effective than ZnO:Al based modules.

2.3.4.4 Summary on TCO degradation

Several types of TCOs are candidate as front electrode for CIGS solar cells, of which sputtered ZnO:Al is most often used, while sputtered ITO can be implemented as well. Increased resistivity of ZnO:Al is often found to be the main cause for the loss of efficiency of solar cells. This increased resistivity is primarily driven by mobility decrease and is typically caused by the diffusion of 'foreign' species from the atmosphere into the grain boundaries. The migration of among others water and CO_2 can lead to the formation of molecules like $Zn(OH)_2$ and $Zn_5(CO_3)_2(OH)_6$, which can form a potential barrier at the grain boundaries. Adsorption of atmospheric species in the grain boundaries is also possible.

More stable ZnO:Al layers can be obtained by thicker layers, higher deposition temperatures or doping concentrations or post-deposition treatments at elevated temperature. Furthermore, the increase in resistivity can largely be reversed by annealing at vacuum or a reducing atmosphere at elevated temperatures. Furthermore, it was found that ZnO:Al on rough substrates show a faster increase in resistivity than on smooth substrates in the presence of humidity and elevated temperatures. Therefore, rough underlying absorber and buffer layers in the CIGS cell can also negatively impact the damp heat stability of the ZnO:Al film.

The more expensive ITO is generally more stable than ZnO:Al in the presence of humidity and elevated temperatures. Conditions that favour the deposition of damp heat resistant films are higher substrate temperatures and lower partial pressures of oxygen. Degradation of ITO can be caused by the migration of water and alkaline species into the layer. It was also observed that decomposition of the layer into tin and indium containing materials occurred due to the heterogeneous division of these elements. Furthermore, the degradation of both ZnO:Al and ITO was often accompanied by the formation of spots.

Interaction between the TCO and barrier material also plays a large role for CIGS module stability: a barrier with a high WVTR can prevent the ingression of water into the TCO. It was reported that alongside to the materials specifically designed to function as water barrier, i-ZnO, ITO and SnO_2 also showed barrier properties. Alternatively, the barrier properties of various materials for CO_2 could be considered.

2.4 Degradation of the device

While chapter 2.3 was focused on the degradation of the individual layers in a CIGS solar cell, this chapter describes the degradation of the complete solar cell stacks. The focus will lay on the changes actually occurring in the CIGS solar cell itself, but since many articles include information on complete modules as well as encapsulated cells and (mini-) modules, these devices can also be described in this chapter. In this chapter, the literature about the degradation of complete devices is reviewed. First, an overview of the changes in electrical properties of the considered solar cells and modules is depicted in graphs. Chapter 2.4.2 gives information on the degradation of CIGS cells and mini-modules without encapsulation under damp heat testing, while chapter 2.4.3 describes the impact of exposure to damp heat combined with illumination or a bias. Chapter 2.4.4 gives an example that multiple degradation reactions can occur within one degradation process. Finally chapter 2.4.5 focuses on articles in which the influence of barrier and encapsulant materials on the stability of CIGS solar cells and modules is taken into account.

2.4.1 Overview of device degradation data

The change in electrical parameters of both encapsulated and non-encapsulated CIGS solar cells and minimodules in depicted in the additional information in the electronic version. In this chapter, various graphs are shown, depicting aspects of the degradation of the samples.

First of all, Figure 2.10 shows the degradation rate of the efficiency in relative percent per hour for CIGS solar cells and modules exposed to damp heat and dry heat conditions. For the damp heat conditions, an average rate of 0.18 relative percent per hour of exposure was found, but this rate can be as high as 0.62% per hour. For the dry heat exposure, this values are lower. Since many samples actually became more stable under dry heat conditions, the median degradation rate is close to 0% per hour. This confirms that water plays an important role in the degradation of CIGS solar cells and modules. An overview of the normalised efficiency of CIGS solar cells with and without packages after exposure time to damp heat conditions is shown in Figure 2.11. This graph shows that a wide range of efficiency changes can occur for these samples. It also shows that most packages contribute to the damp heat stability.

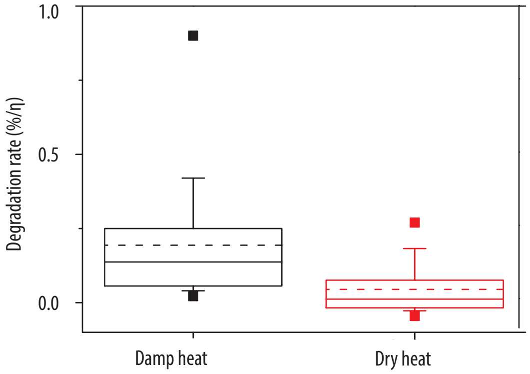

Figure 2.10:

Box plots of the degradation rate (%/η) of the efficiency of CIGS solar cells and modules exposed to damp heat (black) and dry heat (red). The top and bottom of the box show the 25% and 75% intervals, while the whiskers depict the 10% and 90% borders. The squares are the minimum and maximum value and the dashed line is the average value.

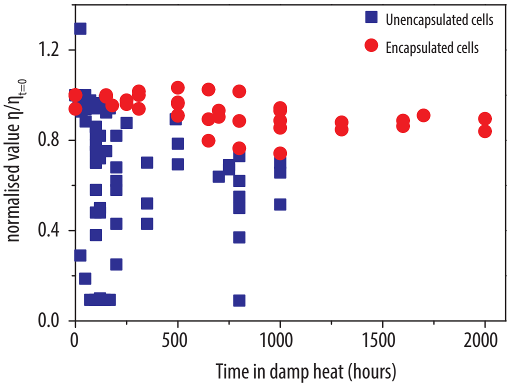

Figure 2.11

The normalised efficiency of unencapsulated CIGS solar cells (blue squares) and CIGS solar cells with a package (red circles) as a function of exposure time to damp heat conditions.

Additionally, the normalised changes of the electrical parameter of CIGS solar cells due to damp heat exposure are shown in Figure 2.12. All values are assumed 1 before exposure, while the values after various periods are shown in Figure 2.11. The number of data points varied per electrical parameter, since many references have reported on e.g. the efficiency change, while the change in other parameters is not often recorded. The resistances are not depicted due to the limited number of data points for these parameters.

Figure 14 shows that the main parameters changing due to damp heat exposure are the open circuit voltage and the fill factor. The short circuit current, on the other hand, is relatively stable. These results are in agreements with trends observed for CIGS modules in the field (chapter 2.1).

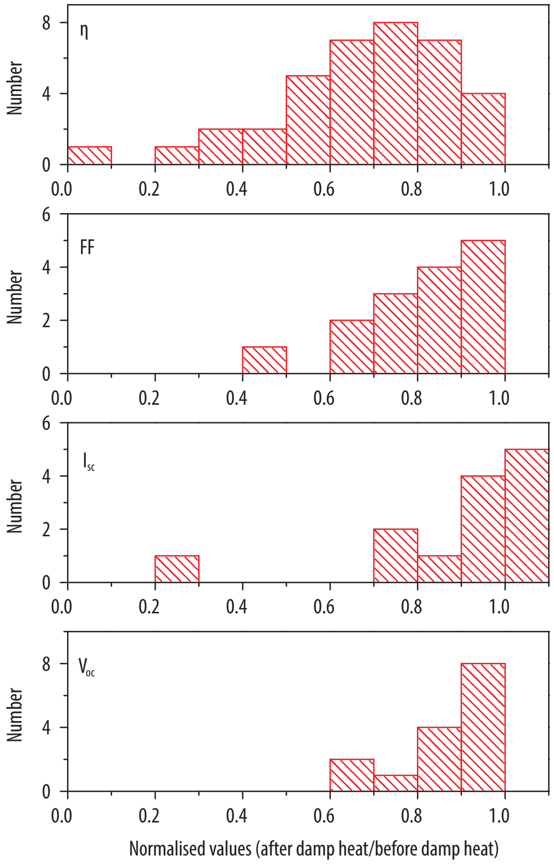

Figure 2.12:

Distributions of the normalised value of electrical parameters of CIGS solar cells and modules after exposure to damp heat conditions for different periods.

In the literature, the conditions leading to changes in these electrical parameters as well as their influence on the composition of the solar cells and modules are described.

2.4.2 Degradation of CIGS cells and mini-modules

In order to learn more about the impact of several degradation conditions on mini-modules, Feist et al. [21] exposed encapsulated mini-modules to dry heat and damp heat tests (here 85°C and 100% RH) and placed them in various water baths (non-purged/purged with O_2/purged with argon and at room temperature/85°C). After maximal 1008 hours, the following global trend in the loss of efficiency due to the treatments was observed:

Water bath/O_2/85°C > 85°C/100% RH > water bath/Ar/85°C > control sample (not exposed) > water bath/RT and 85°C/dry > Water bath/RT/Ar and Water bath/RT/O_2

A similar trend was reported in Feist et al. [29], although the control sample was the most stable in this case. This trend indicates that moist conditions at elevated temperatures are the most detrimental for CIGS mini-modules, which is not surprising based on the information in the previous chapters. As stated above, the effects of the damp heat (85°C/100% RH) tests were severe. For this mini-module, the IV curve quickly changed from an exponential diode-characteristic to a linear ohmic behaviour characteristic. O_2 purged water at 85°C had a similar effect and this mini-module already lost all efficiency after 336 hours. The treatments with water at 85°C, water purged with O_2 and damp heat tests led to the formation of voids in the ZnO:Al layer. The voids were concentrated on the ZnO:Al/CdS and CdS/CIGSSe interfaces and were also present in the CdS and ZnO:Al layer.

For samples exposed to dry heat conditions, it was observed that the efficiency was not changing, although a roll-over in the current voltage curve measured under forward bias was observed. This might indicate the formation of an additional blocking barrier, perhaps due to formation of a resistive contact.

In order to learn more about the degradation mechanisms, an as-deposited mini-module and a mini-module exposed to O_2 purged water at 85°C were cleaved at the Mo/CIGSSe interface and studied by TOF-SIMS and SEM-EDX. In as-received devices, unreacted Cu-Ga particulates were found at the molybdenum back contact. Corresponding with these particles were CIS-rich defects in the absorber layer. After exposure to O_2 purged water bath at 85°C, these CIS-regions were enriched with sodium and surrounded by an area enhanced in oxidation. This may be detrimental to device performance.

It The observation of sodium indicated that sodium may play a role in device degradation. It was suggested that sodium, in combination with sites of unreacted Cu-Ga and/or CIS areas, can facilitate oxygen transport, leading to the formation of metallic oxides.

The formation of particles surrounded by a circular pattern was also observed by Britt et al. [45]. They exposed Mo/CIGS/CdS thin films deposited on stainless steel substrates without TCO to a damp heat test. Already after fifty hours, particles at the surface of the sample surrounded by discoloured rings were observed. They could grow up to 15 mm in diameter and the core of the defect contained high levels of carbon, sodium and oxygen, while high levels of sodium were found through the whole sample. This kind of defects might lead to the formation of pin-holes and shunting.

Malmström et al. [92] demonstrated that the composition of the CIGS absorber also influenced the stability in damp heat testing. They investigated the influence of different gallium contents in the absorber of their $Cu(In_{1-x}Ga_x)Se$ solar cells. When these solar cells were exposed to a damp heat test for 800 hours,the lowest efficiency drop (efficiency -27%) was for an absorber with x = 0.4. Solar cells based on $CuInSe_2$ (x=0) and $CuGaSe_2$ (x=1) showed relative efficiency decreases of 92% and 64% relatively.

Daume et al. reported an influence of the sodium content of absorbers on the damp heat stability of CIGS solar cells on flexible polyimide substrates. They reported that solar cells with initially higher sodium contents degraded faster than those with lower sodium contents [50]. It was found that the sodium dependent decrease in efficiency was mostly driven by a decreasing fill factor which was mainly caused by an increasing series resistance.

The authors showed that the degradation of CIGS solar cells is not a homogeneous process in the lateral direction [50]. CIGS solar cells on polyimide foil without encapsulation were exposed several times to damp heat tests and their electroluminescence (EL) images were taken after each step. Darker areas evolved in some parts of the cell after 15 hours of damp heat testing, which indicated a more severe degradation than in other parts of the cell. The spatial inhomogeneity in the EL intensity was explained by a laterally inhomogeneous corrosion of the back contact (interface) that limits the current injection to the pn-junction in certain areas of the cell. While these areas appear as dark spots in EL testing, according to the reciprocity theorem [93], the exact same areas will contribute less to the power output of the solar cell under normal operating conditions. A new interpretation of the capacitance-voltage-measurements, essentially assuming a reduced `effective contact area´, supported this argument [50]. Before damp heat exposure, SIMS measurements showed the aggregation of sodium at two positions: in the region of the pn-junction and at the CIGS/Mo interface [94] (chapter 2.4.3). The latter aggregation nearly disappeared after damp heat treatment. In the context of the sodium dependent degradation it was concluded that a main corrosion mechanism is present at the CIGS/Mo interface [50]. This spatial inhomogeneous corrosion leads to an increase in the contact resistance between absorber and back contact, thus increasing the overall series resistance of the solar cell as well as the inhomogeneous appearance in electroluminescence imaging.

Radue et al. [11] looked at the changes caused by outdoor exposure of CIGS modules. It was observed that the modules with large cell mismatch showed most severe efficiency decrease, influencing the I_{sc} and fill factor. Generally, the degradation mostly resulted in the increase in series resistance and the large decrease of shunt resistance. An observed change in the V_{oc} was probably caused by the latter effect.

The effect of simple indoor storage of CIGS modules was described by Yanagisawa et al. [95]. After six months in darkness, the efficiency of the sixteen modules had increased by 7% on average (from 2.5% to 12%), largely due to an increase in short circuit current. However, large differences between the modules were observed, especially due to changes in short circuit current and fill factors. The latter showed both increase and decrease. Furthermore, it was also observed that modules with a low initial series resistance were stable during indoor storage, while sample with a high initial series resistance showed a rapid decrease in efficiency.

2.4.3 Degradation under illumination or electrical bias

Since PV modules in the field are exposed to light, various degradation tests have used illumination for the testing of CIGS cells or modules. In various cases, the illumination was also combined with elevated temperatures and humidity, to simulate outdoor exposure [10,22]. An additional advantage of the presence of illumination is the possibility to do in-situ measurements of the degradation, which was done by e.g. Theelen et al. [23,96]. Since combined damp heat-illumination testing requires a specially designed setup, another reference [97] used an electrical bias to simulate the current flow in an operating solar cell. This also allows the possibility to speed up or slow down certain degradation processes by the change of the direction and magnitude of the electrical bias. In this chapter, we describe the impact of both illumination and electrical bias on CIGS cells and modules.

Kushiya et al. [10] reported already in 2006 on the impact of illumination. This reference reported that modules exposed to 1000 hours of dark damp heat conditions (-25% reduction of the efficiency) recovered when exposed to illumination (+20% increase of efficiency). Therefore, the impact of light exposure during degradation was studied by the placement of CIGS modules in a damp heat chamber with 150 W/m^2 illumination in open-circuit and short-circuit conditions.

It was observed that modules in open circuit degraded less than modules in short-circuit conditions, which can mostly be observed if the fill factor is studied. The modules under open-circuit conditions also recovered after two hours light soaking at 1000 W/m^2 and 25^{o}C. The degradation in short-circuit condition was similar to standard damp heat exposure. It was proposed that the fill factor degradation was caused by the formation of $Zn(OH)_2$ in the $Zn(O,S,OH)_x$ buffer, which can dehydrate into ZnO under light soaking. It was additionally proposed that electrons could compensate the increased number of shallow defects, which occurs in the module when it is in open-circuit conditions. In general, it was concluded that the degradation of PV modules was remarkably reduced if the module is tested in open-circuit conditions under weak illumination [10]. Thompson et al. [22] also exposed CIGS cells to combined damp heat and illumination. The results of this study are described in chapter 2.3.4.3.

Theelen et al. [23] studied the impact of sodium and potassium on CIGS solar cell stability by in-situ measurements in a hybrid damp heat-illumination setup. CIGS solar cells with low, medium and high sodium and potassium (alkali) concentrations showed large differences in initial V_{oc} and efficiency values, but also in degradation rates. The initial values were the highest for the samples with the highest alkali contents. The solar cells with the high alkali content degraded very quickly, especially in R_{sh}, V_{oc} and fill factor and demonstrated the appearance of many small spots. The medium alkali sample also demonstrated rapidly loss of efficiency and the occurrence of spots. The low alkali samples were more or less stable and barely any spots could be found. Therefore, it was proposed that the rapid loss of efficiency was dominantly driven by the presence of a high alkali content. The effects of sodium and potassium could not yet be distinguished.

A possible explanation for this phenomenon was introduced by Theelen et al. [96]. It was proposed that in the presence of the illumination and water, especially sodium migrates from the CIGS/Mo interface and the CIGS bulk to the pn-junction. In this region, the positive sodium ions cluster together, forming sodium rich spots. On these positions, the local electric field is reduced, leading to the formation of shunting paths. This leads to the decrease of the V_{oc} and the fill factor, and the appearance of sodium in the ZnO:Al layers.

Fjällström et al. [97] studied the impact of sodium oxide (Na_2O) and potassium oxide (K_2O) in the glass on the presence of Potential Induced Degradation (PID) in CIGS solar cells. Experiments were conducted on CIGS solar cells deposited on glass substrates with different sodium and potassium contents. All samples, regardless of the substrate composition, contained CIGS absorbers with additionally evapourated NaF, except for one soda lime glass sample. These solar cells were exposed to the following conditions for up to 50 hours:

- Heat (85°C) and voltage (50V) (´PID sample´),
- Heat (85°C) (´heat sample´)
- Air at room temperature (´reference´)

If Na_2O was present in the glass, additional sodium migrated in the PID samples due to the voltage from the glass to the solar cell. Already after 25 hours exposure to heat and voltage, all samples with a high Na_2O content in the glass had degraded severely. On the other hand, solar cells on glass without or with small quantities of Na_2O did retain most of their efficiency. It should be noted that the sample with a relatively high amount of K_2O and a low amount of Na_2O did have a constant efficiency, but it did show a roll-over in the IV curve. It was observed that the degraded samples contained a large amount of sodium in the CdS layer and maybe also in the top region of the CIGS layer. It was proposed that this sodium actually migrated from the glass and that the sodium flux is the product of the concentration of sodium in the glass and the mobility of the sodium ions. High ion mobilities occur within glass with low electrical resistivity, which is more susceptible to sodium ion drift and subsequent out-diffusion.
Based on the results of Fjallström et al., it can be expected that the diffusion of alkali elements, and likely mainly sodium, plays a dominant role in the degradation of CIGS solar cells and modules under combined damp heat and electrical bias exposure. The presence of an electrical bias can be obtained by both illumination and an externally applied electrical bias. Due to the limited studies on this topic, the differences and similarities between the influences of electrical bias and illumination exposures was not yet distinguished.

Several studies based on dry heat tests combined with the application of electrical biases have been executed by Mack and Ott [98-100].
Mack et al. [98] compared the impact of 200 hours simultaneous exposure to various biases (electrical biases of +100, +200, +400 or -100 mV or illumination) and 165°C. They observed that illumination and positive electrical biases had a positive impact on the net doping content and the non-radiative recombination and thus on the V_{oc}, while the negative electrical bias led to faster performance decrease. A positive electrical bias also led to stabilisation of the fill factor, which otherwise changed due to the accumulation of negative charges at the hetero-interface. Since the changes can be induced by light soaking or by a voltage, it was concluded that they are caused by the bias across the junction and not the photogeneration itself. It was proposed that the change in net doping concentration, which impacted the V_{oc}, influenced the position of the Fermi level at the hetero-interface. This leads to the formation of a p^+ layer, which influences the fill factor as well, as is described extensively by Ott et al. [99]:
Mack et al. exposed CIGS solar cells to elevated temperatures in the dark (24 hours at 165°C). When the current voltage curves of these solar cells were measured under spectral edge filters, it was observed that the fill factor decreased when measured by light with a wavelength over 550 nm, while shorter wavelength measurements still

show the original fill factors. This effect is related to the above mentioned accumulation of negative charges at the hetero-interface and is also called the ´blue metastability´. This can be reversed by a 3 hours light soak.

Ott et al. [99] used photoluminescence (PL) and electroluminescence (EL) as well as SCAPPS simulations, capacitance-voltage (CV) and IV measurements to study the influence of light and dark exposure at elevated temperatures. It was found that the PL and EL intensities were governed by the net doping density and interface charges respectively. They concluded that exposure to illumination and positive electrical biases lead to more stable solar cells. They also demonstrated that PL and EL are well suited for the detection of the degradation mechanisms and can distinguish between bulk and interface properties by the appropriate operation conditions during luminescence measurements, for example by the selection of the applied electrical bias.

More information on the impact of electrical biases, was provided by Ott et al. [100], who exposed CIGS solar cells to lower positive and negative biases (+400 mV and -100 mV) under dry heat. The negative electrical bias had a negative impact on the cell behaviour, while the positive electrical bias initially had a positive impact on the V_{oc} and fill factor, while later, these factors decreased. It was suggested that the degradation was driven by the occurrence of a barrier at the back contact of the device. However, this degradation phenomenon was very slow, so combined exposure to dry heat conditions and electrical biases do probably not lead to the most critical degradation mechanisms.

2.4.4 Superposition of degradation mechanisms in CIGS solar cells

In many references, one important mechanism regarding the degradation has been emphasised. An overview of the separated degradation mechanisms is shown in chapters 2.4.2 and 2.4.3. However, in most cases, multiple mechanisms seem to be involved, which can be dominant at different times. In this chapter, an example of the superposition of multiple mechanisms is shown.

Daume et al. studied the evolution of the degradation process of flexible CIGS solar cells on polyimide substrates with various sodium contents [94] under damp heat exposure as well as combined damp heat and illumination exposure. It was observed that the efficiencies of two sets of CIGS solar cells with different sodium contents in the absorber showed different trends during damp heat exposure. The solar cells with low sodium contents showed an increase in fill factor and efficiency after 5 to 15 hours of exposure to damp heat conditions followed by a decrease. This indicated a superposition of an improving and a degrading mechanism involved in the degradation process of the CIGS solar cell. On the other hand, the solar cells with high sodium contents demonstrated an immediate decrease in efficiency without initial improvement.

Similar solar cells were also exposed to damp heat conditions combined with illumination in the setup described in reference [23]. By the in-situ studying of the evolution of the V_{oc} and efficiency a two stage aging process was found consistently for the samples with low sodium. The IV parameters of both types of solar cells increased during the first 50 hours, after which they showed a rapid decrease. Similar to damp heat exposure, the improvement phase was not visible for the samples with very high sodium contents. It was therefore concluded that the improving mechanism was negligible compared to the degradation mechanism when the sodium content is very high [50,94].

The nature of the improving mechanism could not be revealed exactly. However, Daume et al. speculated that the diffusion of copper ions within the CIGS may be relevant [101]. Under the influence of the internal electric field, a slow tendency towards a copper depletion of the CIGS surface was proposed. Since this is essentially a widening of the ordered vacancy compound (OVC) phase, this can lead to an increase of the band gap near the CIGS/CdS interface. It was confirmed by SCAPS simulations that this would lead to an increase in open circuit voltage which was actually observed experimentally. Considering the degradation mechanism, Daume et al. argued that it was mainly driven by the corrosion of the back contact. Since the decrease in efficiency was mainly caused by a decrease of the fill factor, which was caused by an increase in series resistance, while V_{oc} and J_{sc} remained fairly constant, the pn-junction was assumed to be stable compared to the planar contacts [50]. SIMS measurements of the sodium depth distribution before and after damp heat revealed a decrease of the sodium contents at the Mo/CIGS interface [94]. At the same time, samples with higher sodium content exhibited a stronger degradation. While other degradation processes (such as TCO degradation and the degradation at various interfaces) could not be ruled out, it was thus concluded that corrosion at back contact (interface) was the main contribution to the overall cell degradation of these solar cells on polyimide substrates.

2.4.5 Degradation of CIGS modules with encapsulation and barriers

Since the ingression of water and other atmospheric species is often a reason for CIGS solar cell degradation, barriers are applied. The most prominent example is glass, which is often used as front and back sheet and serves as a perfect water barrier when combined with a good edge seal. However, for flexible modules, other flexible front- and back sheets are required, which need to have competitive pricing combined with a good barrier function. Additionally to the front- and back sheets, also encapsulants like EVA and PVB play a role in the degradation of CIGS modules. In this chapter, we describe the impact of all these package materials, like the front- and back sheets and barrier and encapsulation materials on the stability of CIGS solar cells and modules. Extensive information about the stability of encapsulants and its impact on CIGS solar cells was reported by Coyle et al. [13,102,103]. The authors described the development of a model for the diffusion of moisture into the module package and the subsequent degradation of the CIGS solar cells [13]. This model is based on both experimental work and calculations. The degradation rate was proportional to the degree of saturation of the encapsulant. It was observed that moisture ingress and thus degradation rate scale with both the climate and the characteristic package diffusion half-time. The latter determines the rate at which the module approaches its environment's average humidity. Diffusion half-times of the package should be approximately equal to the target years of the module, which translates into moisture barriers with a WVTR of 10^{-4} g/m^2/day at 25°C for a module with EVA encapsulant.

It was also concluded that the ´acceleration factor´ between accelerated 'damp heat' testing (85°C/85% RH) and real exposure in 'Miami' is actually non-linear and ranges from 10 to 700 times, depending on the package and the kinetics of the cell degradation. It should be noted that the standard comparison between 1000 hours exposure to 85°C/85% RH and 20 years of exposure the climate in Miami translated into an acceleration factor of 175 times.

Coyle et al. noted that the degradation rate and the water permeability of the package both depend exponentially on temperature, while the degradation rate is strongly increasing, in a non-linear way, with humidity. This can explain why both moisture ingress and degradation occur mostly at higher temperatures and humidity.

Coyle et al. [102] describe that the degradation rate is proportional to the relative saturation of the encapsulant and not to the absolute water concentration. Furthermore, for encapsulants with a small WVTR, the water solubility is important: thick encapsulants with a high water solubility will extend cell life, whereas thin encapsulants with low water solubility shorten the lifetime.

Various references [104-109] have described experimental data of studies of encapsulation and barrier materials on CIGS solar cells and (mini)modules.

Westin et al. [104] showed that modules without encapsulation were stable under dry heat testing, but degraded mostly in fill factor and V_{oc} when exposed to a damp heat test. It was observed that the severity of the V_{oc} loss was similar for 85°C/85% RH and 85°C/65% RH exposure, while the fill factor loss was slightly worse for the 85°C/85% RH conditions. When EVA/glass encapsulation was applied, it was observed that only the fill factor and the series resistance deteriorated, while the V_{oc} remained constant. Westin et al. described that encapsulation can impact the degradation in three ways:

1. Difference in relative humidity.
2. Difference is O_2/H_2O ratio.
3. Encapsulant material interactions, like the formation of acetic acid from EVA. It is expected that this is not the problem in this case, since PVB and EVA encapsulated samples degraded similarly.

Sundaramoorthy et al. [105] tested and compared cells with a grid with different back sheets (TPT (WVTR = 5.5 g/m^2 day), TEFZEL® (WVTR = 4 g/m^2 day), TPAT (WVTR = 1x10^{-3} g/m^2 day) and glass (reported WVTR = 1x10^{-5} g/m^2 day) plus an edge sealant (WVTR < 1x10^{-2} g/m^2 day). The impact of 50 hours damp heat exposure was studied by electrical measurements via specially designed connection paths. It was observed that the solar cells with TPT and TEFZEL® back sheets lost most of their initial efficiency due to damp heat exposure, which was mostly caused by decreasing short circuit current and fill factor, while the V_{oc} was reasonably stable. The samples encapsulated in TPAT were initially stable, but several solar cells became shunted after 20 hours of exposure to damp heat. The samples with glass back sheets retain about 90% of their efficiency after 50 hours of damp heat exposure. These results show that barriers with a lower WVTR limits the degradation of the CIGS solar cells.

The impact of barrier materials was also demonstrated by Olsen et al. [106]. The authors described that unencapsulated cells with a smooth CIGS absorber, an ITO top contact and a NiAl grid, retain most of their efficiency during 600 to 1000 hours of damp heat exposure. Once they were encapsulated with a multistack of Al_2O_3 and polymers, significant degradation only occurred after 2500 to 3000 hours of damp heat exposure. They also showed that this coating protected CIGSSe mini-modules made from rough CIGSSe, with a ZnO:Al TCO and monolithical interconnection. The unencapsulated mini-modules degraded very fast (<100 hours) under damp heat exposure, while the encapsulated samples survived longer. The main electrical parameter that decreased due to the exposure of the unencapsulated mini-modules was the fill factor, which occurred within ten hours. It was concluded that water ingression first influenced the zinc oxide, after which subsequently the junction was affected, leading to changes in current transport mechanisms.

Yanagisawa et al. [107] encapsulated CIGS solar cells in EVA and EVA/glass and exposed them as well as an unencapsulated solar cell simultaneously to a damp heat test and illumination. It was assumed that the degradation of the EVA/glass solar cell was only caused by temperature and light, while the unencapsulated reference cell was also affected by humidity. It was shown that the unencapsulated cell degraded quickly in the beginning, while the sample with EVA started to degrade later.

The degradation of V_{oc} was proposed to result from an increase in carrier recombination caused by the impurity level at the grain boundaries, the surface and the bulk of the CIGS, and the shift of the Fermi level in the CIGS/CdS layer interface. The fill factor loss was attributed to both increased resistance of the ZnO:Al and the increase of the electronic barrier caused by a shift of the diffusion potential in the junction.

The impact of the encapsulants EVA and silicone were studied by Kempe et al. [108]. They studied damp and dry heat exposure of Shell Solar mini-modules with EVA or the silicone GE RTV615, while glass or TEFZEL® was used as front sheet. After 457 hours (TEFZEL®) and 935 hours (glass) of damp heat, the mini-modules demonstrated a large increase in series resistance and a small decrease in V_{oc}, which indicates that this degradation was driven by moisture ingress. As explained in chapter 2.3.4, this is mainly caused by changes in zinc oxide conductivity. The samples were also exposed to 85°C and 0% RH conditions (´dry heat´) for a long period (up to 8770 hours). After this time, it was observed that exposure to damp heat conditions led to a faster increase in series resistance and decrease in fill factor for EVA than for silicone as encapsulant .
Hegedus et al. [109] reported that the use of only a single 55 nm ALD layer of Al_2O_3 deposited directly on a gridded $Cu(In,Ga)Se_2$ device provides excellent protection during the standard 1000 hours damp heat exposure, while a sample only protected by a PET foil lost 50% of its initial efficiency.

2.4.6 Summary on device degradation

Exposure of complete CIGS solar cells and mini-modules to liquid water as well as humidity at elevated temperatures generally leads to a decrease in efficiency. This was mostly caused by a decrease of the fill factor and the open circuit voltage, while the short circuit current degraded less. Dry heat exposure did lead to only a small or no reduction of the efficiency, but could influence the electrical behaviour of the samples, e.g. visible by the occurrence of roll-overs in the IV curves. Degradation was often accompanied by the appearance of circular structures, like spots or particles, which can be rich in sodium and oxygen. On the other hand, long term exposure to the atmosphere, like during storage in the dark, could have a positive impact on the efficiency.
When humidity and elevated temperatures were combined with a bias, either by an electrical bias or illumination, additional degradation phenomena occurred. Under these conditions, migration of sodium (either from the glass or the CIGS layer) to the CdS region was observed which led to a severe efficiency decrease.
Experiments with CIGS cells with varying gallium content in the absorber showed that for a medium content of gallium, the degradation of the was the lowest, while the cell degraded more intensely for pure CIS or CGS absorbers.

The encapsulation materials and humidity barriers impacted the stability of solar cells significantly. Samples with water barriers with a higher WVTR retain their efficiency longer than samples with low WVTR. EVA was often the encapsulation material with the least positive impact, potentially due to the formation of acetic acid, which can lead to the dissolution of ZnO:Al.

2.5 Degradation from the module perspective

According to the focus of this review chapter, the previous sectins have described the material degradation happening within the individual layers within CIGS solar cells and modules. However, some issues specific for CIGS modules do also influence the degradation. These issues have to be discussed as well since module producers use various CIGS specific techniques in order to make modules from large area CIGS solar cell stacks. These techniques can be separated into two categories:

1. Monolithic integration by scribing – this leads to cells of typically 5 to 10 mm width (Figure 2.13 en chapter 2.5.1).
2. Large area deposition of metallic grids, normally followed by cutting into smaller cells that are interconnected (width and length of one cell typically 10 to 200 mm (chapter 2.5.2).)

In this chapter, the available but limited knowledge about the impact of these techniques on CIGS module reliability is presented.

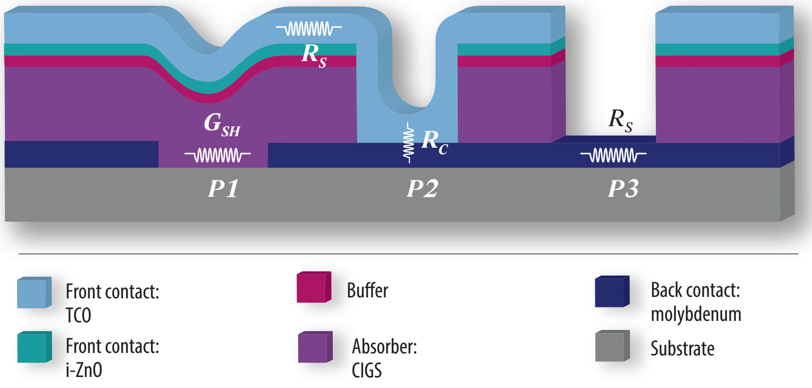

Figure 2.13:

A monolithic interconnect structure for CIGS modules. Functional parts that may degrade and thereby lead to a reduction in conversion efficiency are indicated. This figure is based on reference [27].

2.5.1 Degradation of interconnection scribes

Figure 2.13 shows a schematic drawing of the cross-chapter of a typical monolithic interconnection in a CIGS module. In this structure [27], multiple regions were reported to be vulnerable to degradation:

1. P1: The formation of a shunt path through the CIGS absorber in the back contact scribe (G_{sh})
2. P2: The increase in resistance at the ZnO:Al/Mo contact in the contact scribe (R_c)
3. P3: The corrosion of the exposed molybdenum back contact in the isolation scribe (R_s)
4. Series resistance in the front TCO, as described in chapter 2.3.4

These effects can either influence the material in the scribe itself, or due to the occurrence of debris and heat during scribing, the process can also influence the surrounding materials. In order to distinguish between the degradation effects of the three scribes, the impact for each type of scribe is described individually in the following three chapters.

2.5.1.1 Shunting in P1

If the CIGS material in the P1 scribe becomes more conductive, an alternative current pathway in the CIGS module can be created. This can be observed by a decreased shunt resistance and, if the effect is severe, also by a decrease in open circuit voltage. Shunting in P1 was not observed in most references: Wennerberg et al. [27] showed that the open circuit voltage decrease is larger for four interconnected cells (a decrease of 75 mV or 13% per cell) than for individual cells (a decrease of 35 mV or 6% per cell), which might be attributed to additional shunting in P1. However, calculations also indicated this would greatly influence the fill factor (drop to fill factor < 30%), which did not happen. Therefore, shunting in the P1 could not explain the V_{oc} drop in this case.

However, Allsop et al. [110] reported a large decrease in shunt resistance of solar cells that were exposed to damp heat conditions, which were defined in size by scribing. After degradation, their efficiency was measured and the cell was remade by scribing a smaller cell into the original area, thereby excluding the impact of the degraded scribe lines. This led to the recovery of the original shunt values. Therefore, the shunting in these cells was likely caused by the formation of short circuit paths across the damaged portion of the cell adjacent to the scribe line, which implies that damp heat degradation can lead to shunting of P1.

2.5.1.2 Degradation in P2

The Mo/TCO contact in the P2 scribe is necessary for the current transport between the individual cells within the CIGS module. Loss of conductivity in this scribe could thus have a large impact on the power output of the modules. However, the impact of conductivity loss of ZnO:Al and Mo and the degradation in P2 are hard to distinguish, since the measured series resistance includes the impact of all three elements. Several references [27,91,104,111] have tried to distinguish between these effects, mostly by the use of testing structures.

Wennerberg et al. [27] found that the degradation of P2 was the principle cause of fill factor degradation due to damp heat exposure of unencapsulated interconnected solar cells. It was observed that the contact resistance in the P2 scribe increased by a factor of ten within ten hours of exposure. After one hundred hours, the resistance had increased by a factor 50 Theelen et al. [108] observed that the series resistance of two interconnected cells increased with 12±3 mΩ/h, while single cells increased in series resistance with 4.7±0.3 mΩ/h. When corrected for the changed cell size, the interconnected cells degraded faster than expected.. Therefore, it was suggested that part of the increase was caused by increased resistivity in P2.

Similar observations were made by Westin et al. [104]. An unencapsulated test structure, that was exposed to damp heat allowed the separate determination of the increase of the series resistance of zinc oxide/CdS layer (average 8 mΩ/□/h) and of the total resistance (average 73 mΩ/□/h). Since it is expected that molybdenum degradation leads to a very sudden change in resistance, the difference (average 65 mΩ/□/h) is considered to be an estimation of the impact of the degradation in P2. It is therefore concluded that resistance of the P2 contact quickly became dominant under damp heat exposure, while the increased resistance of the ZnO:Al front contact played a minor role.

A similar approach was chosen by Klaer et al. [91], who used a test structure that allowed the separation of sheet resistance of the zinc oxide and the sum of the contact resistance of the Mo/ZnO plus the resistance of the Mo. They showed that the contact resistance of a P2 scribe containing i-ZnO increased more rapidly (27 mΩ/h) than that of a scribe that did not contain i-ZnO (2.8 mΩ/h).

Wennerberg et al. [27] proposed that the formation of an oxide layer between the ZnO:Al and the molybdenum, or the depletion of free carriers at the ZnO:Al interface could be the cause for the degradation in P2.

2.5.1.3 Corrosion in P3

As shown in chapter 2.3.1.2, the corrosion of molybdenum is a very rapid process, leading to the formation of a non-conductive molybdenum oxide layer on top of a metallic matrix. This is especially the case if the protective $MoSe_2$ layer is removed in the scribing process, leading to decreased protection and thus damaging of the molybdenum surface. This oxidation can be detrimental for the module, but this is not necessarily the case, since conductivity in the P3 area is only relevant in the lateral direction. Therefore, a back contact with a non-conductive top layer and a highly conductive molybdenum bottom layer can still function as back contact as long as the conductive bottom layer is still thick enough for a sufficent conductivity. Furthermore, the length of the exposed molydenum in the scribe is only tens of micrometres.

Wennerberg et al. [27] calculated that the sheet resistance of the molybdenum that is present in P3 has to increase by three orders of magnitude (from approx. 0.3 Ω/□ to 500 Ω/□) to cause a fill factor loss of 10 %. Therefore, no effect of molybdenum degradation will be seen in P3 until the contact is completely oxidised and thus interrupted.

Westin et al. [104] used a special test structure to study the influence of damp heat exposure on P3 conductivity. The authors reported the very large impact of P3 corrosion. The back contact remained conductive for 100 to 200 hours, even when strong evidence of a corrosive attack on the Mo surface was visible. After this time, the initially 450 nm thick molybdenum film was completely corroded, leading to a very large resistance increase. Something similar was seen for test structures prepared to analyse the loss of conductivity in CIGS modules: After 400 hours exposure to a damp heat test, conductivity could no longer be measured. This coincided with the point in time when the P3 isolation scribes became completely transparant. For several modules, loss of connection in the P3 scribe area was detected. It was noticed that the surface corrosion was the strongest along the centre of the scribe line, where the mechanical tip had damaged the Mo.

Furthermore, it should be noticed that the popularity of laser scribing is increasing, compared to the conventionally applied mechanical scribing. Laser scribing might introduce new starting points for degradation.

2.5.1.4 Impact of module design

The design of the mini-module also impacts its degradation behaviour: Kempe et al. looked at damp heat treated encapsulated mini-modules and observed that the main changes occurred on the side of the cell adjacent to the P1 scribe [108]. These changes were not attributed to ohmic losses, but to the module design (Figure 2.14): as the current crosses the cell in the zinc oxide front contact, its voltage drops, while the voltage in the Mo back contact remains more constant because of the unchanged conductivity. This results in the reduction in voltage drop across the cell when moving away from the P1 scribe. Because of the strong voltage-current relationship of a diode, this small voltage drop change creates a much large change in current crowding adjacent to the scribe where current enters the ZnO layer (Figure 2.14). This can be observed by faster heating of this side. This effect was also observed after 8770 hours of dry heat exposure.

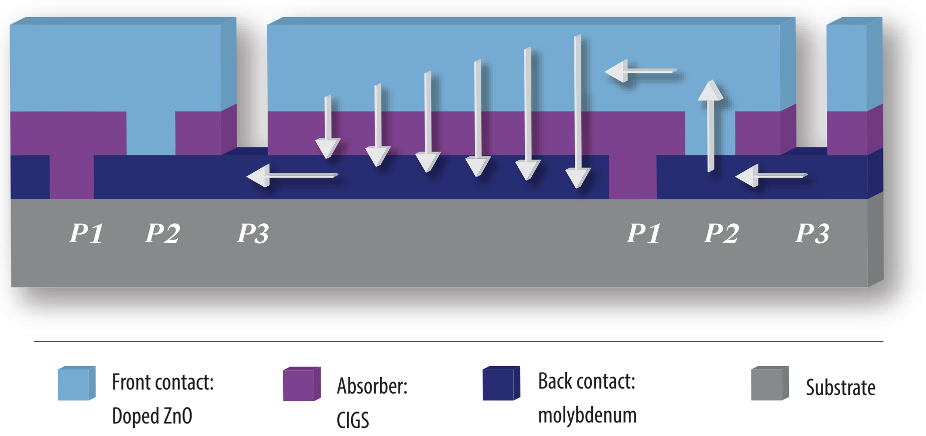

Figure 2.14

Schematic picture of the current flow through a CIGS module containing a TCO with increased resistance. This figure is based on reference [108].

2.5.1.5 Summary on scribe degradation

The monolithic interconnection scheme of a CIGS module plays a large role in module degradation. The most vulnerable scribe is P2, where a Mo/ZnO:Al contact is responsible for the current transport between solar cells. Increased resistance of this scribe due to dam heat exposure was often observed with the help of model systems. Possible reasons are the introduction of an oxide layer at the Mo/ZnO:Al interface or decreased resistivity of ZnO:Al films.

Furthermore, degradation of P3 was also observed, due to the transformation of molybdenum in molybdenum oxide, for example on positions that have been damaged by the scribing process. Since the metal molybdenum has a high conductivity, its degradation only impacts the module efficiency when the molybdenum layer is almost completely oxidised, which will likely only happen after very long exposure to humidity and oxygen. Finally, shunting around the P1 scribe could also influence the module stability, but this could not be observed in a module.

Furthermore, the increased resistivity of the TCO also has an additional impact on modules, in case the molybdenum resistivity remains largely constant. This leads to the creation of a difference in voltage drops at different positions, resulting in local heating of the module.

2.5.2 Degradation of conductive grids

Generally, metal grids are used to overcome the limitations in the conductivity of TCOs. By providing an additional low-resistance path for current collection, they reduce the overall series resistance of the cell and thus ohmic power losses. As any other part of the solar cell, grids are subject to degradation but, at the same time, a strategy to deal with a degrading solar cell.

In a solar cell or module with a grid, the ohmic losses in the TCO can be controlled by varying the spacing between the grid fingers. When decreasing the grid finger distance, the shading increases and thus some of the initial power of the solar cell is lost due to a reduction of the current density [112]. However, the module efficiency can be kept at a higher level after damp heat exposure because additional grid fingers compensate for the increasing sheet resistance of the TCO. From that point of view, the gridded module design is preferable from a long-term performance point of view [39]. Wennerberg et al. pointed out further advantages of a gridded module such as:

- Less inactive area (the cell stripes in a monolithically interconnected module can be wider)
- Higher tolerance for variations
- A cheaper TCO process, since a thinner TCO can be used
- Increased degrees of freedom in the module geometry [113].

Nevertheless, the authors noted that the benefits of a gridded module have to overweight the cost of an additional grid deposition in order to pay off in production.

A typical grid for solar cells in many research labs consists of a thin nickel layer (e.g. of 50 nm thickness), followed by a thick aluminium layer (e.g. 2-3 μm thickness) that are typically applied by an evapouration method. Wennerberg et al. reported that this structure corroded considerably and led to uncertainty in the interpretation of changes in the IV characteristics [38]. A modified grid structure, however, with an additional nickel capping (50 nm), which resulted in a Ni/Al/Ni stack, improved the stability. No visual degradation was observed after 1000 hours of damp heat exposure and the statistics showed better reproducibility.

Pern et al. reported that a standard metallic grid of a 3 μm aluminium layer on top of a 50 nm nickel layer was instable under damp heat [30]. The stack was subject to hydrolytic corrosion within 50 to 100 hours of damp heat exposure thus becoming highly resistive. Since nickel is known to be more stable against oxidation and hydrolysis than aluminium, Pern et al. prepared solar cells with only nickel grids. At a grid thickness of 0.2 to 0.3 μm, the solar cells with nickel-only grids showed a lower initial efficiency (compared to those with standard Ni/Al grid) due to the higher resistance of the nickel grid. At nickel grid thicknesses of 1.6 to 1.8 μm, the devices demonstrated comparable efficiencies. Due to high mechanical stress, some of the nickel-only grids exhibited cracking and peeled off, resulting in damaged or failed devices. However, four-point resistance measurements on simple test structures consisting of a 0.1 µm thin nickel layer demonstrated no change in resistance after 50 to 100 hours of damp heat exposure, thus motivating further optimisation of a potential grid purely out of nickel.

A different grid application technology is screen-printing. Typically, polymer matrices with silver particles are printed and subsequently annealed. Britt et al. reported that silver containing grid fingers exhibited visual signs of corrosion after 50 hours of damp heat exposure [45]. Widespread pinhole-like defects were found on the surface of damp heat treated stainless steel/Mo/CIGS/CdS samples. These defects consisted of sodium, oxygen and carbon in their core. It was suggested that shunting paths would be produced if a silver grid was printed on top of these pinholes. It remained unclear and subject to further investigation whether such a pinhole defect could form and would be harmful to the solar cell performance if a TCO and a gridwere applied before damp heat exposure.

Similar to TCOs, grids can also degrade due to the interaction with barrier or encapsulation materials. DeGroot et al. [114] and Elowe et al. [115] exposed SLG/Mo/CIGS/CdS/ITO/NiAg grid cells with various moisture barriers to a damp heat test. It was observed that Si_3N_4 moisture barriers had poor adhesion to the silver grid, while Si_3N_4 kept its adherence to the ITO during damp heat exposure. A test structure consisting of SLG/Al/ITO/NiAg and moisture barriers was used to study the degradation mechanisms. It was found that the Si_3N_4 film could oxidise into an oxynitride or oxide. It was also measured that sodium, which likely had migrated from the glass often accumulated together with oxygen in the neighbourhood of the grid fingers. This indicated a relationship between oxidation and sodium migration, possible due to the facilitation of the oxidation by the presence of sodium. A possible explanation was given a chemical reaction between SiO_x and sodium species (e.g. NaOH or Na_2O) from the glass. Na_2O was reported to dissolve SiO_2 to generate a liquid sodium silicate ($Na_2O{\bullet}x(SiO_2)$). Therefore, the combination of possible oxidation of the nitride and the presence of sodium is detrimental for the stability of the barrier. It was predicted that mitigation of the sodium migration to the top layer and an improved interface integrity could overcome the observed failure mechanism. This was experimentally confirmed by introducing a 10 nm thin TaN_x layer between ITO and SiN_x thus mitigating Na diffusion. Therefore oxidation of the SiN_x film was prevented, leading to significantly improve of the stability of the samples. When this was applied to CIGS solar cells, 90% of the initial performance could be retained after 1900 hours under damp heat exposure.

2.5.2.1 Summary on grid degradation

Various metal compositions for grids in CIGS solar cells have been exposed to damp heat conditions. Generally Ni/Al based grids degraded under damp heat. This could be overcome by placing a nickel top layer (Ni/Al/Ni) or by using nickel only grids. However, the latter led to mechanical stress in the sample. When silver was used in (screen-printed) grids, shunting occurred due to the presence of pinholes. Additionally, nickel-silver grids could react with SiN_x moisture barriers, which can be prevented by the application of a very thin TaN_x layer.

2.6 Acknowledgements

I would like to thank my co-author Felix Daume as well as Heiko Kempa, Lisa Paller, Andreas Rahm (Solarion), Marius Grundmann (University Leipzig), Miro Zeman (Delft University of Technology), Nicolas Barreau (IMN UMR Nantes), Dorrit Roosen and Zeger Vroon (TNO) for the helpful discussions and advice. Furthermore I would like to thank Ilse Schrauwers (isontwerp.nl) for the design of most images, while Marcel Verheijen (Philips Innovation Services) and Nicolas Barreau (IMN) are acknowledged for their contribution to Figure 2.1.

2.7 References

[1] Makrides, G., Zinsser, B., Schubert, M., Georghiou, G., Solar Energy 103 (2014) p 28-42

[2] Dhere, N., Kaul A., Pethe, S., Proc. of SPIE Vol. 8112 (2011) 81120R

[3] Musikowski, H., Styczynski Z., Proc. 25th EUPVSEC (2010) 3942-3946

[4] Del Cueto, J., Rummel, S., Kroposki, B., Osterwald, C., Anderberg, A., Proc. 33rd IEEE PVSC (2008) 1-6

[5] Jordan, D., Kurtz, S., Proc. 37th IEEE PVSC (2011) 827-832

[6] Myers, D. (2004) NREL Conference Paper NREL/CP-560-36320

[7] Niki, G., Contreras, M., Repins, I., Powalla, M., Kushiya, K., Ishizuka, S., Matsubara, K., Progress in Photovoltaics: Research and Applications 18 (2010) 453–466

[8] Ermer, J., Fredric, C., Hummel, J., Jensen, C., Pier, D., Tarrant, D., Mitchell, K., Proc. 21th IEEE PVSC (1990) 595 - 599

[9] Tarrant, D., Gay, R., Process R&D for CIS-Based Thin-Film PV (2006) NREL/SR-520-38805

[10] Kushiya, K., Kuriyagawa, S., Tazawa, K., Okazawa T., Tsunoda, M., Proc. 4th WCPSEC (2006) 348-351

[11] Radue, C., Van Dyk, E., Physica B 404 (2009) 4449–4451

[12] Jordan, D., Kurtz, S., Progress in Photovoltaics: Research and Applications 21 (2013) 12–29

[13] Coyle, D., Progress in Photovoltaics: Research and Applications 21(2) (2013) 156-172

[14] Osterwald, C., McMahon, T., Progress in Photovoltaics: Research and Applications, 17 (2009) 11–33

[15] McMahon, T., Progress in Photovoltaics: Re-

search and Applications 12 (2004) 235–248

[16] Kang, J., Lee, M., Kim, D., Lim, Y., Seo, W., Choi, H., Current Applied Physics 11 (2011) S333-S336

[17] Xu, J., Yang, Z., Wang, H., Xu, H., Zhang, X., Materials Science in Semiconductor Processing 21 (2014) 104–110

[18] Theelen, M., Tomassini, M., Barreau, N., Steijvers, H., Branca, A., Harel, S., Vroon, Z., Zeman, M., Proc. 38th IEEE PVSC 2 (2012) 1-6

[19] Pern, F., Noufi, R., Proc. SPIE 8472 (2012) 84720J

[20] Hyperphysics Relative Humidity http://hyperphysics.phy-astr.gsu.edu/hbase/kinetic/relhum.html, accessed 18 November 2014

[21] Feist, R., Rozeveld, S., Kern, B., D'Archangel, J., Yeung, S., Bernius, M., Proc. 34th IEEE PVSC (2009) 2359 - 2363

[22] Thompson, C., Hegedus, S., Carcia, P., Scott McLean, R., IEEE Journal of Photovoltaics 3 (1) (2013) 494-499

[23] Theelen, M., Barreau, N., Daume, F., Steijvers, H., Hans, V., Liakopoulou, A., Vroon, Z., Zeman, M., Proc. SPIE 9179 (2014) 91790I

[24] Pern, F., Noufi, R., Proc. DOE SETP Review Meeting 4 (2007) 17-19

[25] Pern, F., To, B., DeHart, C., Li, X., Glick, S., Noufi, R., Proc. SPIE 7412 (2008) 74120K

[26] Theelen, M., Polman, K., Tomassini, M., Barreau, N., Steijvers, H., Van Berkum, J., Vroon, Z., Zeman, M., Surface & Coatings Technology 252 (2014) 157–167

[27] Wennerberg, J., Kessler, J., Stolt, L., Proc. 16th EU-PVSEC (2000) 309-312.

[28] Wennerberg, J., Design and Stability of Cu(In,-Ga)Se_2-Based Solar Cell Modules.
Acta Universitatis Upsaliensis. Comprehensive Summaries of Uppsala Dissertations from the Faculty of Science and Technology 683 (2002) 91 pp. Uppsala

[29] Feist, R., Rozeveld, S., Mushrush, M., Haley, R., Lemon, B., Gerbi, J., Nichols, B., Nilsson, R., Richardson, T., Sprague, S., Tesch, R., Torka, S., Wood, C., Wu, S., Yeung, S., Bernius, M., Proc. 33rd IEEE PVSC (2008) 1-5

[30] Pern, F., Noufi, R., Proc. SPIE 8112 (2011) 81120S

[31] Schmid, D., Ruckh, M., Schock, H., Solar Energy Materials and Solar Cells 41/42 (1996) 281-294

[32] Wang, C., Shih, W., Chen, C., Chen, Y., Hong, S., Tsai, C., Wu, Y., Lai, C., Proc. 35th IEEE PVSC 2 (2010) 2483-2487

[33] Salomé, P., Fjallstrom, V., Hultqvist, A., Szaniawski, P., Zimmermann U., Edoff, M., Progress in Photovoltaics: Research and Applications 22 (1) (2014) 83-89

[34] Hempel, W., Wischmann, W., Aging of Molybdenum back contact and its influence on CIGS solar cells, Visual Presentations at 25th EUPVSEC 2010

[35] Theelen, M., Harel, S., Verschuren, M., Tomassini, M., Hovestad, A., Barreau, N., van Berkum, J., Vroon, Z., Zeman, M., submitted to Surface & Coatings Technology (2015)

[36] Reinhard, P., Buecheler, S., Tiwari A., Solar Energy Materials & Solar Cells 119 (2013) 287–290

[37] Guillemoles, J., Thin Solid Films, Proc Thin Film Materials for Photovoltaics 403-404 (2002) 405-409

[38] Wennerberg, J., Kessler, J., Bodegard, M., Stolt, L., Proc. 2nd WCPEC (1998) 1161-1164

[39] Wennerberg, J., Kessler, J., Stolt, L., Solar Energy Materials & Solar Cells 75 (2003) 47-55

[40] M. Schmidt, M., Braunger, D., Schaffler, R., Schock, H., Rau, U., Thin Solid Films 361-362 (2000) 283-287

[41] Deibel, C., Dyakonov, V., Parisi, J., Zeitschrift für Naturforschung, 58 (2003) 691-702

[42] Guillemoles, J., Kronik, L., Cahen, D., Rau, U.,

Jasenek, A., Schock, H., Journal of Physical Chemistry B 104 (20) (2000) 4849-4862

[43] Guillemoles, J., Thin Solid Films, 361-362 (2000) 338-345

[44] Pern, F., Egaas, B., To, B., Jiang, C., Li, J., Glynn, S., DeHart C., A study on the humidity susceptibility of thin-film CIGS absorber, Proc. 34th IEEE PVSC (2009) 287-292

[45] Britt, J., Kanto, E., Lundberg, S., Beck, M., Proc. 4th WCPEC 1 (2006) 352-355

[46] Metzger, W., Repins, I., Romero, M., Dippo, P., Contreras, M., Noufi, R., Levi, D., Thin Solid Films 517 (2009) 2360–2364

[47] Würz, R., Meeder, A., Fuertes Marrón, D., Schedel-Niedrig, T., Lips, K., Proc. MRS 865 (2005) 243-248

[48] Heske, C., Groch, U., Weinhardt, L., Fuchs, O., Holder, B., Umbach, E., Bostedt, C., Terminello, L., Zweigart, S., Niesen, T., Karg, F., Appl. Phys. Lett., 81 (2002) 4550-4552

[49] Braunger, D., Hariskos, D., Schock, H., Proc. 2nd WCPEC 1 (1998) 511-514

[50] Daume, F., Puttnins, S., Scheit, C., Zachmann, H., Rahm, A., Braun, A., Grundmann, M., Materials 6 (12) (2013) 5478-5489

[51] Sakurai, K., Hunger, R., Tsuchimochi, N., Baba, T., Matsubara, K., Fons, P., Yamada, A., Kojima, T.,Deguchi, T., Nakanishi, H., Niki, S., Thin Solid Films 431-432 (2003) 6–10

[52] Naghavi, N., Abou-Ras, D., Allsop, N., Barreau, N., Bücheler, S., Ennaoui, A., Fischer, C., Guillen, C., Hariskos, D., Herrero, J., Klenk, R., Kushiya, K., Lincot, D., Menner, R., Nakada, T., Platzer-Björkman, C., Spiering, S., Tiwari, A., Törndahl, T., Progress in Photovoltaics: Research and Applications 18 (2010) 411–433

[53] Ramanathan, K., Contreras, M., Tuttle, J., Keane, J., Webb, J., Asher, S., Niles, D., Dhere, R., Tennant, A., Hasoon, F., Noufi, R., Proc. 25th IEEE PVSC (1996) 837-840

[54] Allsop, N., Niesen, T., Gledhill, S., Krüger, M., Köhler, T., Lux-Steiner, M., Fischer, C., Proc. 34th IEEE PVSC (2009) 680-684

[55] Spiering, S.; Hariskos, D.; Schröder, S., Powalla, M., Thin Solid Films, 480-481 (2005) 195-198

[56] Lee, D., Cho, W., Song, J., Kwon, O., Lee, W., Park, C., Park, K., Lee, H., Kim, Y., Progress in Photovoltaics: Reseach and Applications 23 (7) (2015) 829-827

[57] Sharma, K., Williams, B., Mittal, A., Knoops, H., Kniknie, B., Bakker, N., Kessels, W., Schropp, R., Creatore, M., International Journal of Photoenergy (2014) 253140

[58] Shunsuke, K., Nakada, T., Applied Physics Express 1 (2008) 075002

[59] Pern, F., Noufi, R., Li, X., DeHart, C., To, B., Proc. 33rd IEEE PVSC (2008) 1-6

[60] Selin Tosun, B., Feist, R., Gunawan, A., Mkhoyan, K., Campbell, S., Aydil, E., Solar Energy Materials & Solar Cells 101 (2012) 270–276

[61] Selin Tosun, B., Feist, R., Campbell, S., Aydil, E., Journal of Vacuum Science & Technology A 30 (2012) 04D101

[62] Greiner, D., Papathanasiou, N., Pflug, A., Ruske, F., Klenk, R., Thin Solid Films 517 (2009) 2291–2294

[63] Greiner, D., Gledhill, S., Köble, C., Krammer, J., Klenk, R., Thin Solid Films 520 (2011) 1285–1290

[64] Ando, E., Miyazaki M., Thin Solid Films 392 (2001) 289-293

[65] Ando, E., Miyazaki M., Thin Solid Films 516 (2008) 4574–4577

[66] Ando, E., Miyazaki M., Thin Solid Films 351 (1999) 308-312

[67] Minami, T., Kuboi, T., Miyata, T., Ohtani, Y., Phys. stat. sol. (a) 205 (2) (2008) 255–260

[68] Minami, T., Miyata, T., Ohtani, Y., Kuboi, T., Phys.

stat. sol. (RRL) 1 (1) (2007) R31–R33

[69] Zhan, Z., Zhang, J., Zheng, Q., Pan, D., Huang, J., Huang, F., Lin, Z., Crystal Growth & Design, 11 (1) (2011) 21-25

[70] Tohsophon, T., Hüpkes, J., Calnan, S., Reetz, W., Rech, B., Beyer, W., Sirikulrat, N., Thin Solid Films 511 – 512 (2006) 673 – 677

[71] Theelen, M., Boumans, T., Stegeman, F., Colberts, F., Illiberi, A., van Berkum, J., Barreau, N., Vroon, Z., Zeman, M., Thin Solid Films 550 (2014) 530–540

[72] Hüpkes, J., Owen, J., Wimmer, M., Ruske, F., Greiner, D., Klenk, R., Zastrow, U., Hotovy, J., Thin Solid Films 555 (2014) 48-52

[73] Pern, F., To, B., Glick, S., Sundaramoorthy, R., DeHart, C., Glynn, S., Perkins, C., Mansfield, L., Gessert, T., Proc. SPIE 7730 (2010) 77730R

[74] Sundaramoorthy, R., Pern, F., DeHart, C., Gennett, T., Meng, F., Contreras, M., Gessert, T., Proc. SPIE 7412 (2009) 74120J

[75] Lin, W., Ma, R., Xue, J., Kang, B., RF magnetron sputtered ZnO:Al thin films on glass substrates: A study of damp heat stability on their optical and electrical properties, Solar Energy Materials & Solar Cells 91 (2007) 1902–1905

[76] Owen, J., Hüpkes, J., Nießen, L. Zastrow, U., Beyer, W., Damp-heat treatment effects on sputtered Al-doped ZnO films, Proc. 24th EUPVSEC (2009) 2774-2778

[77] Hamasha, M., Dhakal, T., Vasekar, P., Alzoubi, K., Lu, S., Vanhart, D., Westgate, C., Solar Energy 89 (2013) 54–61

[78] Kim, J., Lee, H., Choi, S., Bae, K., Park, J, Thin Solid Films 547 (2013) 163–167

[79] Steinhauser, J., Meyer, S., Schwab, M., Faÿ, S., Ballif, C., Kroll, U., Borrello, D., Thin Solid Films 520 (2011) 558–562

[80] Illiberi, A., Scherpenborg, R., Theelen, M., Poodt, P., Roozeboom FJ. Vac. Sci. Technol. A 31 (2013) 061504

[81] Klenk, R., Chalcopyrite Solar Cells and Modules, in Transparent Conductive Zinc Oxide, Springer Series in Material Science 104, edited by K. Ellmer, A. Klein, B. Rech (2007) 415-437

[82] Liu, H., Avrutin, V., Izyumskaya, N., Ozgur, U., Morkoc, H., Superlattices and Microstructures 48 (2010) 458-484

[83] Beyer, W., Breuer, U., Hamelmann, F., Hüpkes, J., Stärk, A., Stiebig, H., Zastrow, U., Mater. Res. Soc. Symp. Proc. 1165 (2009)

[84] Arzel, L., Theelen, M., Leornard, E., Barreau, N., Impact of degradation on optical and electrical properties of sputtered aluminium doped zinc oxide ZnO:Al, Visual presenation e-MRS Spring meeting (2014)

[85] Theelen, M., Dasgupta, S., Vroon, Z., Kniknie, B., Barreau, N., van Berkum, J., Zeman, M., Thin Solid Films 565 (2014) 149–154

[86] Frost, R., Hales, M., Journal of Thermal Analysis and Calorimetry 91(3) (2008) 855-860

[87] Ntinas, V., Damp heat stability and comparison of sputtered Al:ZnO film deposited on Sodium Rich and Sodium Free substrate, master thesis, TNO report (2013) 50-55

[88] Guillen, C., Herrero, J., Surface & Coatings Technology 201 (2006) 309–312

[89] Mei-Zhen, G., Ke, X., Fahrner, W., Journal of Non-Crystalline Solids 355 (2009) 2682–2687

[90] Menner, R., Powalla, M., Proc. workshop TCO für Dünnschichtsolarzellen und andere Anwendungen III (2005) 71-78

[91] Klaer, J., Klenk, R., Boden, A., Neisser, A., Kaufmann, C., Scheer, R., Schock, H., Proc. 31st IEEE PVSC (2005) 336-339

[92] Malmström, J., Wennerberg, J., Stolt, L., Thin Solid Films 431-432 (2003) 436-442

[93] Kirchartz, T., Helbig, A., Reetz, W., Reuter, M., Werner, J., Rau, U., Progress in Photovoltaics: Research and Applications 17 (2009) 394-402

[94] Daume, F., Rahm, A., Braun, A., Grundmann, M., Proc. 28th EUPVSEC (2013) 2192-2198

[95] Yanagisawa, T., Kojima, T., Solar Energy Materials & Solar Cells 90 (2006) 1353–1360

[96] Theelen, M., Hans, V., Barreau, N., Steijvers, H., Vroon, Z., Zeman, M., Progress in Photovoltaics: Research and Applications (2015)

[97] Fjällström, V., Salomé, P., Hultqvist, A., Edoff, M., Jarmar, T., Aitken, B., Zhang, K., Fuller, K.,Kosik Williams, C., IEEE Journal of Photovoltaics 3 (3) 23 (2015) 537-545

[98] Mack, P., Ott, T., Walter., T., Hariskos, D., Schäffler, R., Proc 25th EUPVSEC (2010) 3337-3340

[99] Ott, T., Mack, P., Trudel, F., Schulz, Y., Walter, T., Hariskos, D., Schäffler, R., Proc. 26th EUPVSEC (2011) 2421-2424

[100] Ott, T., Walter, T., Hariskos, D., Kiowski, O., Schäffler, R., IEEE journal of Photovoltaics 3 (1) (2013) 514 – 519

[101] Daume, F., Flexible CIGS: Research & Production, 5th IW-CIGSTech Workshop in Berlin, 2 April 2014

[102] Coyle, D., Blaydes, H., Northey, R., Pickett, J., Nagarkar, K., Zhao R., Gardner., J., Progress in Photovoltaics: Research and Applications 21 (2) (2013) 173-186

[103] Coyle, D., Blaydes, H., Pickett, J., Northey, R., Gardner, J., Proc. 34th IEEE PVSC (2009) 1943-1947

[104] Westin, P., Neretnieks P., Edoff, M., Proc. 21st EU-PVSEC (2006) 2470-2473

[104] Sundaramoorthy, R., Pern, F., Gessert, T., Proc. SPIE 7773 (2010) 77730Q

[106] Olsen, L., Gross, M., Kundu, S., Shafarman, W., Proc. 33rd IEEE PVSC (2008) 1-3

[107] Yanagisawa, T., Kojima, T., Koyanagi, T., Microelectronics Reliability 44 (2004) 229–235

[108] Kempe, M., Terwilliger, K., Tarrant, D., Proc. 33rd IEEE PVSC (2008) 1-6

[109] Hegedus, S., Carcia, P., McLean, R., Culver, B., Proc. 35th IEEE PVSC (2010) 1178-1183

[110] Allsop, N., Hänsel, A., Visbeck, S., Niesen, T., Lux-Steiner, M., Fischer, C., Thin Solid Films 511 – 512 (2006) 55 – 59

[111] Theelen, M., Tomassini, M., Steijvers, H., Vroon, Z., Barreau, N., Zeman, M., Proc. 39th IEEE PVSC (2013) 2047 – 2051

[112] Sols, K., Simulation of solar cell losses depending on cell design. Master's thesis, Chalmers University of Technology, Göteborg, Sweden (2010)

[113] Wennerberg, J., Kessler, J., Stolt, L., Solar Energy Materials and Solar Cells, 67 (2001) 59-65

[114] De Groot, M., Elowe, P., Stempki, M., Proc. 35th IEEE PVSC (2010) 1172-1177

[115] Elowe, P., Stempki, M., Rozeveld, S., DeGroot, M., Chemistry of Materials 23 (2011) 3915-3920


I don't feel well

CHAPTER 3

In-situ monitoring of the degradation of CIGS solar cells

This chapter has been published earlier in the following publications:

M. Theelen, M. Tomassini, H. Steijvers, Z. Vroon, N. Barreau and M. Zeman,
In-situ Analysis of the Degradation of Cu(In,Ga)Se$_2$ Solar Cells,
Proc. 39th IEEE PVSC (2013) 2047-2051

M. Theelen, H. Steijvers, Z. Vroon, M. Tomassini, N. Barreau and M. Zeman,
A unique hybrid degradation setup for CIGS solar cells,
Proc. 9th ICCG (2012) 161-164

M. Theelen, N. Barreau, F. Daume, H. Steijvers, V. Hans, A. Liakopoulou, Z. Vroon and M. Zeman,
Accelerated performance degradation of CIGS solar cells determined by in-situ monitoring,
Proc. SPIE (2014) 91790I

A. Kuypers, R. Knaapen, M. Theelen, M. Meuris, M. van der Vleuten and W. Zijlmans,
Cost-efficient equipment for CIGS production,
Photovoltaics International 20 (2013) 61-69

M. Theelen, H. Steijvers, N. Barreau, M. Buffière, G. Brammertz, M.G. Flammini, R.J. van Vugt,
Z. Vroon, M. Zeman,
In-situ monitoring of the accelerated performance degradation of thin film solar cells,
Proc. 42th IEEE PVSC (2015)

Abstract

We have designed and constructed a 'hybrid' degradation setup that can expose CIGS solar cells and modules to humidity, elevated temperatures and illumination, while the illumination also allows in-situ monitoring of the solar cells and modules. This setup consists of a climate chamber, which can vary temperature and humidity. Within this chamber, an area of 80x80 cm^2 is illuminated, which allows both the study of combined illumination and damp heat induced degradation as well as the in-situ measurement of the current voltage (IV) curves of the CIGS solar cells and mini-modules during the test. The 40x40 cm^2 in the center of the illuminated area was calibrated BAA according to IEC norm 60904-9. In this setup, the current-voltage output of solar cells and minimodules is automatically logged and characteristic parameters like efficiency, currents, voltages, ideality factor and resistances can be extracted. Up to twelve of these solar cells or minimodules can be degraded and measured in-situ at the same time. Therefore, the degradation behaviour and the temperature dependency of solar cells and modules can be observed.

The CIGS solar cells and minimodules used in this thesis are described in this chapter. This chapter also introduces the procedure for the extraction of the electrical parameters from the current voltage curves.

3.1 Introduction

The main goal of this thesis is to obtain better understanding about the long term stability of CIGS solar cells and modules and to use this knowledge to optimise CIGS solar cells and modules regarding their stability. As described in chapter 2, CIGS cells and modules often fail due to exposure to moisture and elevated temperatures. Furthermore, it was observed that light as well as electrical loads influence the behaviour of CIGS cells, although these effects are not always detrimental.

Therefore, a setup has been designed in which we have exposed CIGS solar cells and modules to humidity, elevated temperatures and illumination, while the illumination also allows in-situ monitoring of the samples (Figure 3.1). The setup has been used for various types of studies, aimed at a better understanding of the performance and the degradation of CIGS solar cells and modules. The results of the degradation experiments as obtained with this setup can be found in chapter 7. Furthermore, the setup has been used to determine temperature dependency (chapter 4).

In this chapter, the CIGS solar cells as prepared for this setup and the setup itself are described. Furthermore, the theory used in order to determine the solar cell parameters in this setup is included.

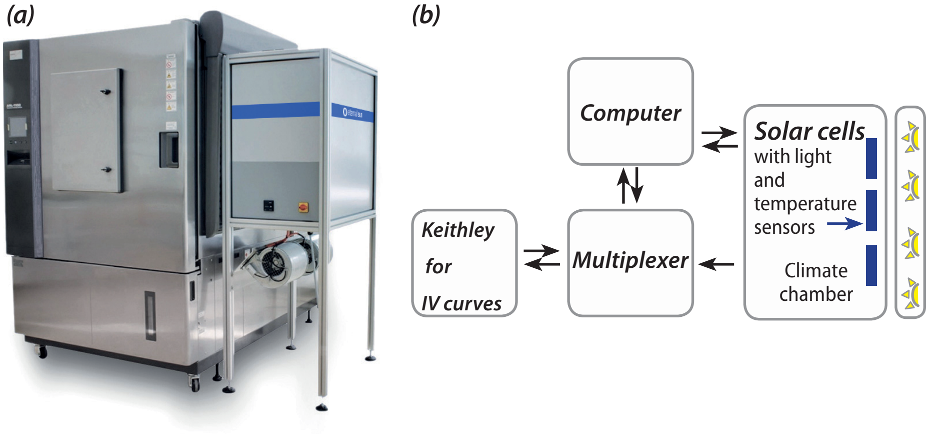

Figure 3.1:

(a) Photograph of the hybrid degradation setup (climate chamber plus illumination grid) (b) Schematic overview of the hybrid degradation setup including the measurement system.

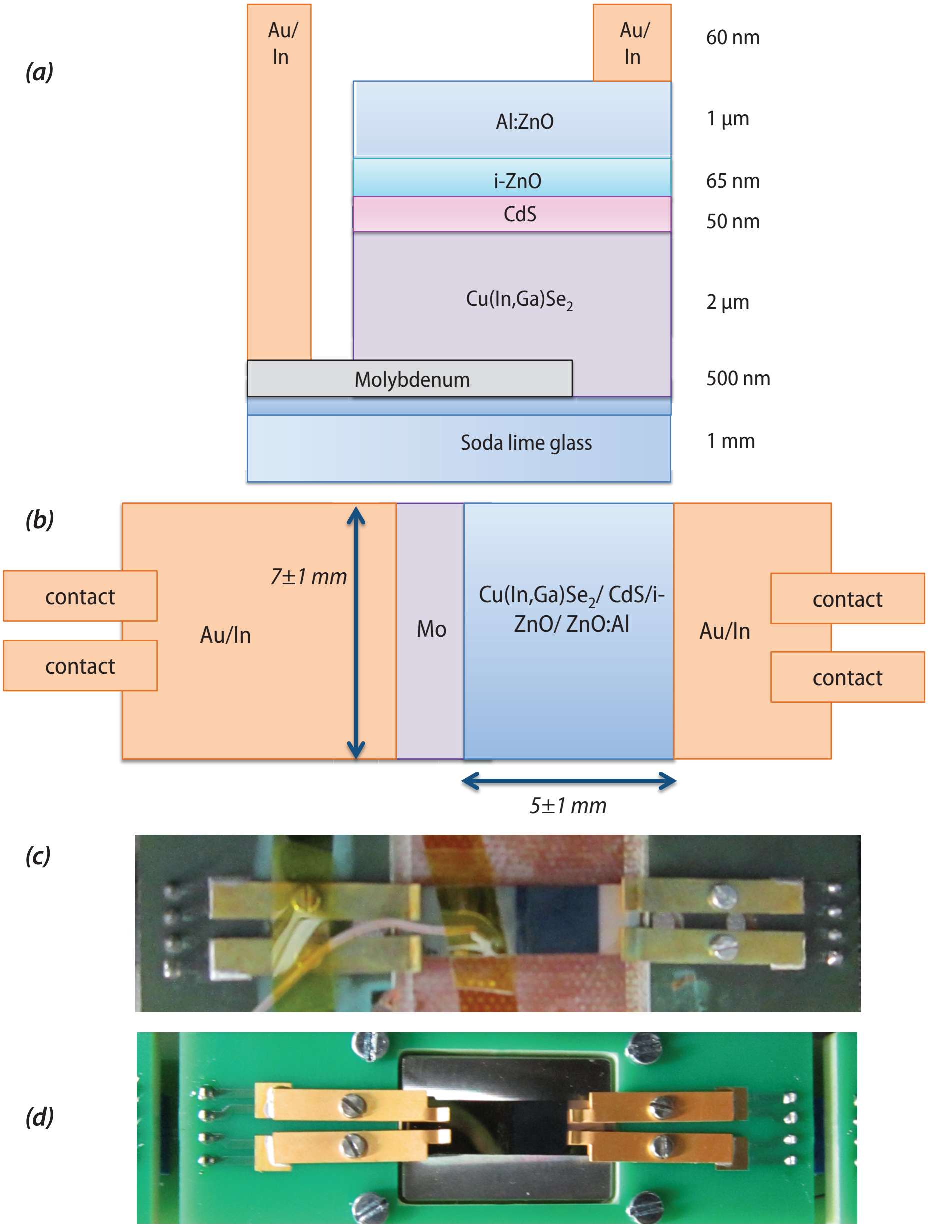

Figure 3.2:

CIGS cells and cell holders as used in this study:

(a) Schematic cross-section of the CIGS test structure (not to scale) (b) Schematic representation of the top view of the CIGS cells combined with the positioning of the contacts to the sample holder (c) CIGS solar cell in the standard sample holder, including thermocouple attached with kapton tape (d) CIGS solar cell in new and improved sample holder.

3.2 CIGS solar cell preparation

Most samples used in the experiments have a relatively standard CIGS stack as described in chapter 1.3 and shown in Figure 3.2a. This stack consists of Soda Lime Glass (SLG)/molybdenum (Mo)/CIGS/cadmium sulfide (CdS)/intrinsic zinc oxide (i-ZnO)/aluminium doped zinc oxide (ZnO:Al). The general deposition conditions are as described by Couzinie-Devy with the exception of the ZnO:Al layer thickness, which has been increased to $1\ \mu m$ [1]. This results in ZnO:Al layer with a sheet resistance under $10\ \Omega/\square$ which is required for the use of relatively long cells (5 mm) without grids. These choices were made in order to optimally simulate the cells in CIGS modules, while the relatively large cell size was also chosen to prevent the dominance of the edge degradation on the output of the complete sample. These design choices result in an initial efficiency loss of approximately 2% points compared to reference samples with a standard cell design based on thin ZnO:Al combined with grids. In order to prevent shadowing, the contacts of the samples are not above the actual cell, but on either sides of the active area (Figure 3.2b). The back and front contacts were covered with evapourated gold, which is stable under damp heat. Figure 3.2c and Figure 3.2d depict the sample holders with a solar cell as used in the experiments described in this thesis and the new designed sample holder respectively.

3.3 The hybrid degradation setup

The hybrid degradation setup (Figure 3.1) consists of a climate chamber for humidity and temperature control with a large window in the side wall. Outside of the window, a steady-state solar simulator is placed allowing the light to enter the climate chamber in a controlled manner. All relevant parameters are logged and controlled by a measurement system, that can also supply external loads. More information about the setup can be found in Video 3.1, which shows the climate chamber, solar simulator, sample holders and the measurement system. For the thesis on paper, this movie can be found on https://www.youtube.com/watch?v=Zmy5tb-2NK8.

☞ Video 3.1: The hybrid degradation setup

For temperature and humidity control, a modified Espec Temperature Chamber model ARL-1100 was utilised (Hielkema Testequipment, Uden, the Netherlands). The right side of the chamber was removed and replaced by a window system. This window system consists of two high transmission glass slides combined with a polymer slide covered with Eternal Sun optical foil. This combination was chosen to obtain an optimal combination of thermal isolation and spectral filtering of the light. A shutter was installed on the climate chamber, so the samples can also be exposed to damp heat in darkness.

The climate chamber should be able to control the temperature between -45°C and +180°C and relative humidity between 10% to 98% (for a temperature range of 10°C - 95°C). Cooling and heating rates can be up to 4.4 °C/min and 4.7 °C/min respectively. However, due to introduction of an illumination source, the real cooling capacity is lower.

For the illumination, a solar simulator of 80x80 cm^2 was obtained from Eternal Sun (Delft, The Netherlands). The solar simulator contains two types of cost-effective lamps, which are homogenised with the help of mirrors to get a homogeneous illumination field. Ventilators and additional cooling elements were installed chamber to remove redundant heat produced by the solar simulator.

Since the current test samples are relatively small, only the inner 40x40 cm^2 are used and calibrated. This area was calibrated BAA according to IEC 60904-9 [2], thereby judging spectral match, uniformity and stability. Figure 3.3 shows the solar simulator spectrum inside the climate chamber at the sample positions. The spectrum is measured inside the chamber to account for the filtering by the window system.

When this spectrum is compared with the AM 1.5 spectrum, most areas show a good spectral match. However, the average intensity of the wavelengths between 900 and 1100 nm is too high, therefore the spectrum has the 'B' qualification. The fluctuation

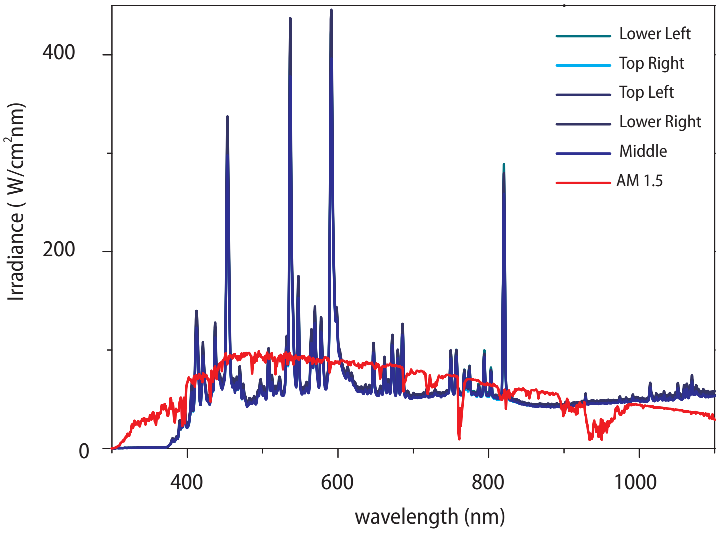

Figure 3.3

Spectrum of the solar simulator at five positions in the climate chamber (spiked blue spectra – not all visible, since they are very similar) compared to AM 1.5 (red spectrum).

of the intensity of the light as a function of time and position were both below two percent, which corresponds to the A qualifications.

The solar cells as described in the previous section are placed in samples holders to allow electrical contact with the measurement system. Contacting between the cells and the sample holder is obtained by gold plated contact pens connected on a Printed Circuit Board (PCB). Figure 3.2c and d show the standard sample holder, as is used for the reported measurements and the new, improved sample holder respectively. These contacts allow measurements in a four point probe configuration. This approach was chosen to minimise the effect of increasing contact resistance on the measurement due to degradation. Up to twelve holders are then placed on a sample grid, which is positioned in front of the light source. On the sample grid, twelve thermocouples and three photodiodes are also present. Figure 3.4 shows this grid with twelve soda lime glass samples.

A data collection system is positioned outside of the degradation setup to measure and log IV curves. The system is schematically depicted in Figure 3.1b. The IV curves are measured by a Keithley 2440 5A source meter. From these data, many characteristics of the cells or modules can be determined. Since up to twelve cells or modules can be placed in the chamber simultaneously, a National Instruments PXI-1011 chassis with multiplexers is connected, allowing all the samples to be measured in turn. Labview software allows automated logging of the temperature, relative humidity and light intensity based on three photodiodes, as well as calculation of the electrical

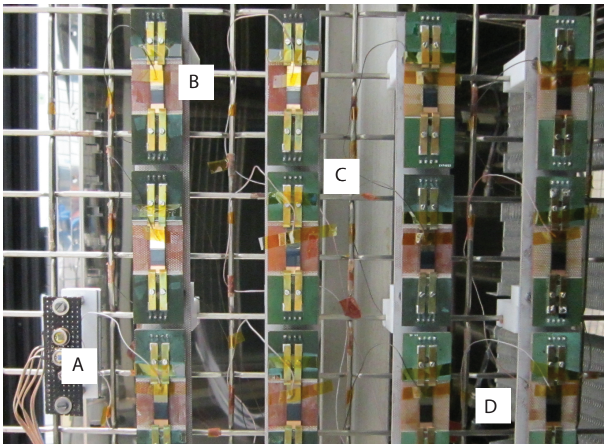

Figure 3.4

The sample grid facing the illumination from the solar simulator: A. Photodiode for monitoring of the light intensity B. Twelve cell holders to measure twelve solar cells simultaneously C. CIGS solar cells with thermocouple D. Wires for connection with the measurement system parameters. With this software, the short circuit current density (J_{sc}), open circuit voltage (V_{oc}), fill factor (FF), series (R_s) and shunt (R_{sh}) resistances, saturation current density (J_o), photogenerated current density (J_{ph}) and ideality factor (n) are obtained following the theory described in chapter 3.4. The output of the logging system is shown in Figure 3.5. The temperature of the cells or modules is higher than their direct surroundings. This temperature difference is caused by the direct radiation from the solar simulator, which heats the thermal mass of the samples and their holders. Therefore, the real sample temperature during experiments conducted at 85°C and 85% RH is over 100°C. The system also continuously logs the temperature by the thermocouples attached to the samples (Figure 3.4), so the correct values are always recorded. In the periods when the current-voltage curves are not measured, which is estimated to be 90-98% of the time, the solar cells are at open circuit conditions.

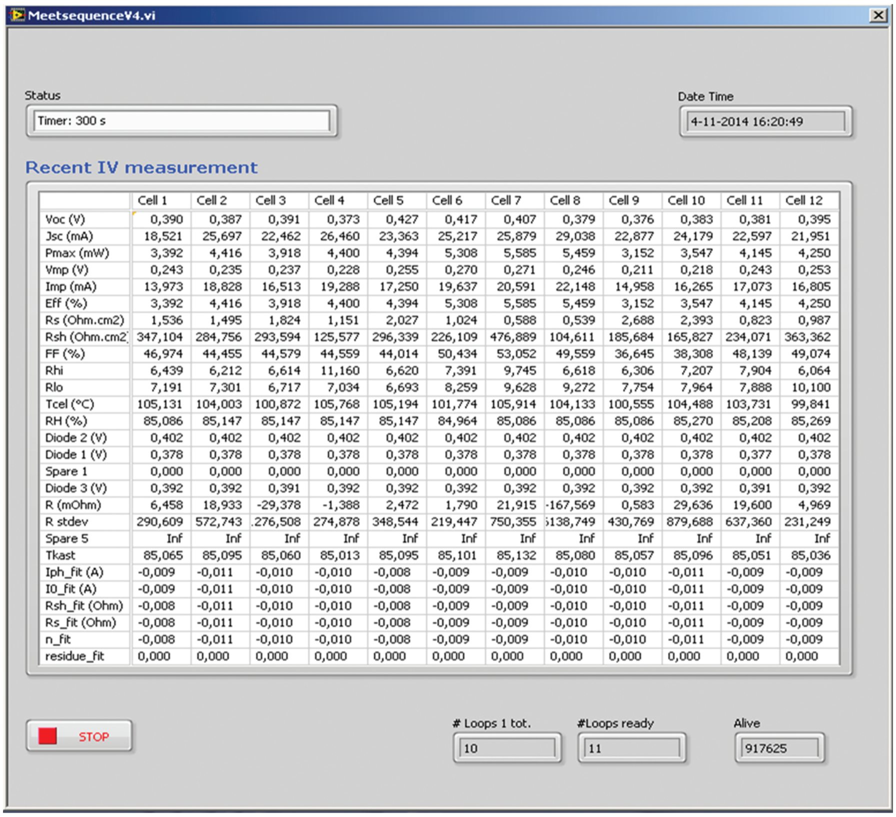

Status: Timer: 300 s

Date Time: 4-11-2014 16:20:49

Recent IV measurement

	Cell 1	Cell 2	Cell 3	Cell 4	Cell 5	Cell 6	Cell 7	Cell 8	Cell 9	Cell 10	Cell 11	Cell 12
Voc (V)	0,390	0,387	0,391	0,373	0,427	0,417	0,407	0,379	0,376	0,383	0,381	0,395
Jsc (mA)	18,521	25,697	22,462	26,460	23,363	25,217	25,879	29,038	22,877	24,179	22,597	21,951
Pmax (mW)	3,392	4,416	3,918	4,400	4,394	5,308	5,585	5,459	3,152	3,547	4,145	4,250
Vmp (V)	0,243	0,235	0,237	0,228	0,255	0,270	0,271	0,246	0,211	0,218	0,243	0,253
Imp (mA)	13,973	18,828	16,513	19,288	17,250	19,637	20,591	22,148	14,958	16,265	17,073	16,805
Eff (%)	3,392	4,416	3,918	4,400	4,394	5,308	5,585	5,459	3,152	3,547	4,145	4,250
Rs (Ohm.cm2)	1,536	1,495	1,824	1,151	2,027	1,024	0,588	0,539	2,688	2,393	0,823	0,987
Rsh (Ohm.cm2	347,104	284,756	293,594	125,577	296,339	226,109	476,889	104,611	185,684	165,827	234,071	363,362
FF (%)	46,974	44,455	44,579	44,559	44,014	50,434	53,052	49,559	36,645	38,308	48,139	49,074
Rhi	6,439	6,212	6,614	11,160	6,620	7,391	9,745	6,618	6,306	7,207	7,904	6,064
Rlo	7,191	7,301	6,717	7,034	6,693	8,259	9,628	9,272	7,754	7,964	7,888	10,100
Tcel (°C)	105,131	104,003	100,872	105,768	105,194	101,774	105,914	104,133	100,555	104,488	103,731	99,841
RH (%)	85,086	85,147	85,147	85,147	85,147	84,964	85,086	85,086	85,086	85,270	85,208	85,269
Diode 2 (V)	0,402	0,402	0,402	0,402	0,402	0,402	0,402	0,402	0,402	0,402	0,402	0,402
Diode 1 (V)	0,378	0,378	0,378	0,378	0,378	0,378	0,378	0,378	0,378	0,378	0,377	0,378
Spare 1	0,000	0,000	0,000	0,000	0,000	0,000	0,000	0,000	0,000	0,000	0,000	0,000
Diode 3 (V)	0,392	0,392	0,391	0,392	0,392	0,392	0,392	0,392	0,392	0,392	0,391	0,392
R (mOhm)	6,458	18,933	-29,378	-1,388	2,472	1,790	21,915	-167,569	0,583	29,636	19,600	4,969
R stdev	290,609	572,743	.276,508	274,878	348,544	219,447	750,355	5138,749	430,769	879,688	637,360	231,249
Spare 5	Inf	Inf	Inf	Inf	Inf	Inf	Inf	Inf	Inf	Inf	Inf	Inf
Tkast	85,065	85,095	85,060	85,013	85,095	85,101	85,132	85,080	85,057	85,096	85,051	85,036
Iph_fit (A)	-0,009	-0,011	-0,010	-0,010	-0,008	-0,009	-0,009	-0,010	-0,010	-0,011	-0,009	-0,009
I0_fit (A)	-0,009	-0,011	-0,010	-0,010	-0,008	-0,009	-0,009	-0,010	-0,010	-0,011	-0,009	-0,009
Rsh_fit (Ohm)	-0,008	-0,011	-0,010	-0,010	-0,008	-0,009	-0,009	-0,010	-0,010	-0,011	-0,009	-0,009
Rs_fit (Ohm)	-0,008	-0,011	-0,010	-0,010	-0,008	-0,009	-0,009	-0,010	-0,010	-0,011	-0,009	-0,009
n_fit	-0,008	-0,011	-0,010	-0,010	-0,008	-0,009	-0,009	-0,010	-0,010	-0,011	-0,009	-0,009
residue_fit	0,000	0,000	0,000	0,000	0,000	0,000	0,000	0,000	0,000	0,000	0,000	0,000

Loops 1 tot.: 10

#Loops ready: 11

Alive: 917625

Figure 3.5:

Logging system for the external parameters of the solar cells, as well as the cell and chamber temperature, the relative humidity, the contact resistances and the diode output.

3.4 IV measurements

In this chapter, the basic theory for the interpretation of the current voltage measurements, as used in the setup, are shown. The parameters as described in this chapter are logged in the setup.

The electrical parameters are determined from current-voltage (IV) curves, which are taken when solar cells are exposed to illumination (normally 1000 W/m^2, AM 1.5 spectrum). A known voltage is then applied between the front and back contact of the solar cell and the corresponding current is measured. By measuring the current for a continuous range of voltage, one can obtain an IV-curve (Figure 3.6). In this figure, the short circuit current (I_{sc}), open circuit voltages (V_{oc}) and maximum power point (MPP) can be distinguished. The maximum power point is the position where the current voltage product is maximal and is thus the operational point of the solar cell. The voltage and current density at the maximum power point are named the voltage and current densityat the maximum power point respectively (V_{MPP} and I_{MPP}) [3].

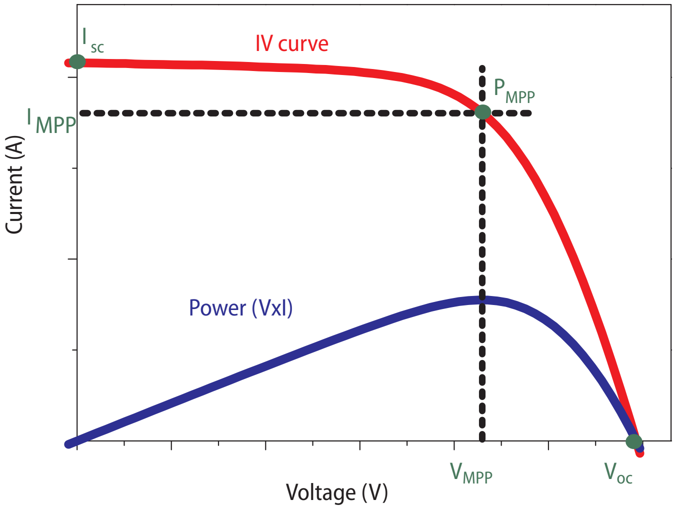

Figure 3.6:

Typical current voltage curve as well as the power curve, showing the open circuit voltage (V_{oc}), short circuit current (I_{sc}) and the power, voltage and current at maximum power point (P_{MPP}, V_{MPP}, I_{MPP}). The curves have been flipped over the x-axis for clarity.

Since the total output current is dependent on the area of the solar cell, often the short circuit density (J_{sc}) is used:

$$J_{sc} = \frac{I_{sc}}{A} \tag{3.1}$$

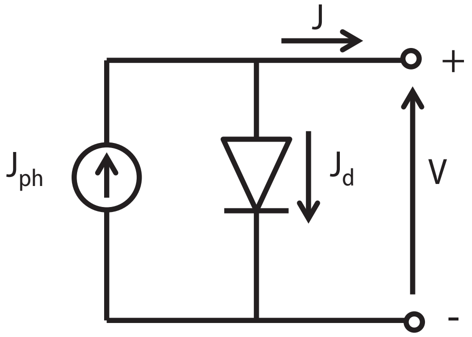

Figure 3.7

Electrical circuit of an ideal solar cell.

where A is the solar cell area. Analogously, other current densities (below) can also be derived from their corresponding current.

Since a solar cell can also be considered a diode, an electrical equivalent circuit of an ideal solar cell under illumination is depicted in Figure 3.7.

In the circuit in Figure 3.7, the current density–voltage (J-V) characteristics of p–n junction solar cells under steady state illumination is:

$$J = -J_{ph} + J_d \tag{3.2}$$

where J is the current density, while J_{ph} and J_d represent photogenerated and diode current density respectively. Additionally, the following relation exists [4]:

$$J = -J_{ph} + J_o\left(e^{\frac{qV}{kT}} - 1\right) \tag{3.3}$$

where J_o is the saturation current density, V is the terminal voltage T is the temperature, q is the elementary charge, k is the Boltzmann constant.

This ideal diode equation (3.3) assumes that all the recombination occur via band-to-band or recombination via traps in the bulk of the device. In reality, there are other modes mode of recombination so solar cells do not follow the ideal diode equation. In order to take this drift from the ideal behaviour into account, the ideality factor (n) is added to equation (3.3), leading to:

$$J_d = J_0\left(e^{\frac{qV}{nkT}} - 1\right) \tag{3.4}$$

In the case of a non-ideal solar cell, the ideality factor will be larger than 1.

To complete the model, some resistive effects should be included: R_s the series

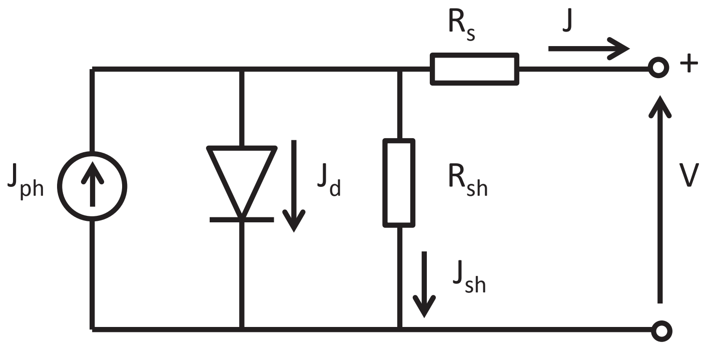

Figure 3.8

Single diode model: equivalent circuit of a non-ideal solar cell showing the impact of series and shunt resistances.

resistance, represents the resistance encountered by the current flowing in the solar cell. The major part of this resistance is due to the resistivity of the front and the back contact. The other resistive effect is R_{sh}, which is the shunt or parallel resistance. This parameter describes how easily the current can cross the pn-junction instead of flowing in the external circuit. When these resistances are included in the circuit, we obtain the single diode model (Figure 3.8), in which the voltage and current are linked by equation (3.5) [4]:

$$J = -J_{ph} + J_0 \left(e^{\frac{q(V - R_s J)}{n k T}} - 1 \right) + \frac{V - R_s J}{R_{sh}} \tag{3.5}$$

In order to show the impact of the resistances as well as other recombination effects, the fill factor (FF) is derived from current voltage curves. The fill facor is the ratio of the maximum output power to the product of J_{SC} and V_{OC} and is a measure of the ´squareness´ of the J-V curve.

$$FF = \frac{V_{MPP} \times J_{MPP}}{V_{oc} \times J_{sc}} \tag{3.6}$$

Finally, the efficiency is the ratio between the maximum output power and the incident power:

$$\eta = \frac{P_{MPP}}{P_{incident}} = \frac{V_{MPP} \times I_{MPP}}{P_{incident}} = \frac{V_{oc} \times I_{sc} \times FF}{P_{incident}} \tag{3.7}$$

where η is the efficiency and $P_{incident}$ is the incident power of the illumination, which is often taken as 1000 W/m^2.

In this study, the efficiency (η), short circuit current density (J_{sc}), open circuit voltage

(V_{oc}), fill factor (FF), as well as the series (R_s) and the shunt (R_{sh}) resistances were directly determined from the current voltage curve. Since the PI samples did gave unstable measurements at negative voltages, the determination of the shunt resistance should be treated with care and is only included at temperatures below 80°C. It should be noted that the setup cannot execute External Quantum Efficiency (EQE) measurements, so the current density is indicative and can be used for comparison as a function of time, but not as absolute value. However, before degradation, the current density values obtained from EQE and the setup are mostly close.

Furthermore, a fitting procedure based on the single diode model is used to calculate the photogenerated current density (J_{ph}), ideality factor (n), saturation current density (J_o) and series and shunt resistance. The fitting procedure consists of an estimation of every parameter, obtained by simplifying and manipulating equation (3.5), as described in reference [5]. An algorithm was used in order to find the best combination of parameters fitting the IV-curve, starting from the estimation fed to the fitting program. It should be noted that regardless of these precautions, fitting of the IV curve can result in unreliable results and depends on the estimations on which the first fits are based. In this study, we judged that the fitting resulted in reasonably reliable values for non-degraded samples on soda lime glass, but becomes less trustworthy when the solar cell is degraded and its electrical behaviour differs strongly from an ideal diode. Therefore, the validity of all data is still under discussion and data of degraded cells is not shown in this thesis.

Figure 3.9

Photograph of the commercial hybrid degradation setup.

3.5 Commercialisation

A spin-off of this thesis is the commercialisation of this setup, due to extensive market interest. A Dutch consortium, consisting of Eternal Sun, Hielkema Testequipment, ReRa Solutions and Solliance partners ECN and TNO has begon to develop a commercial variant of setup. The first commercial version will be in operation in 2015 and will have a 1x1 m^2 AAA calibrated illumination area (Figure 3.9). In comparison to the setup as designed, built and used in this thesis, the following five general improvements are implemented:

1. The intensity of the lamps can be controlled individually in order to obtain the desired spectra and irradiance.
2. The test area is enlarged to 1x1 m^2 in order to be able to test more cells at the same time and thus increase the accuracy of the measurements, or to accommodate larger PV products.
3. A faster shutter is added to be able to rapidly perform ´dark´ measurements between illuminated measurements.
4. Irradiance ranges have been programmed in order to be able to test with low irradiance (200 W/m^2), or with irradiance used for Nominal Operating Cell Temperature (NOCT) measurements (800 W/m^2).
5. The setup is designed in such a way that the climate chamber and the solar simulator can also be used separately.

3.6 Acknowledgements

For this chapter, I would really like to thank Henk Steijvers for all his contributions. Furthermore, I would like to thank all employees of Eternal Sun, Hielkema Testequipment and ReRa Solutions, and especially Stefan Roest, Robert-Jan van Vugt, Peter Hielkema and Erik Haverkamp for the nice collaboration and their excellent support.

3.7 References

[1] F. Couzinie-Devy, E. Cadel, N. Barreau, L. Arzel, P. Pareige, Applied Physics Letters 99 (2011) 232108

[2] IEC norm 60904-9, Photovoltaic devices – Part9: Solar simulator performance requirements

[3] PVeducation http://www.pvcdrom.org/ accessed on 5 November 2014

[4] P. Singh, N. Ravindra, Solar Energy Material & Solar Cells 101 (2012) 36-54

[5] S. Hegedus, W. Shafarman, Prog. Photovolt: Res. Appl. 12 (2-3), (2004 155–176)


P

CHAPTER 4

Temperature dependency of the electrical parameters of CIGS solar cells

This chapter has been submitted as the following publication:

M. Theelen, A. Liakopoulou, V. Hans, F. Daume, H. Steijvers, N. Barreau, Z. Vroon and M. Zeman

Determination of the temperature dependency of the electrical parameters of CIGS solar cells

Submitted to Progress in Photovoltaics: Research and Applications (2015)

Abstract

Two types of CIGS solar cells, both designed for implementation in CIGS modules, were subjected to temperatures between 25ºC and 105ºC. Simultaneous exposure to AM1.5 illumination allowed the measurement of their electrical parameters at these temperatures. These two types of solar cells, deposited with different procedures on soda lime glass (SLG) and polyimide (PI) substrates, showed large variations in temperature dependency of these parameters.

It was shown that the temperature dependency of the open circuit voltage (V_{oc}) was dependent on its room temperature value: a high V_{oc} at 25oC leads to a slower loss of V_{oc} when the temperature is increased. For the V_{oc}, the normalised temperature dependency varied between -0.28%/ºC and -0.47%/ºC, which is in agreement with literature. The temperature dependency of the short circuit current density (J_{sc}) showed more surprising results. While the PI samples had the expected positive temperature dependency (0.03 to 0.32 %/°C) the SLG samples showed a small negative impact of increasing temperature (-0.01 to -0.05 %/°C). A correlation between the temperature dependencies of the J_{sc} and the ideality factor n was observed. Therefore, this difference could be caused by increased recombination for the SLG samples.

Furthermore, the temperature coefficients of the fill factor (negative), efficiency (negative), as well as the series (slightly negative) and shunt (negative) resistances were extracted.

4.1 Introduction

When solar modules, including CIGS, are exposed to elevated temperatures, their conversion efficiency is influenced negatively. The efficiency of CIGS modules with respect to temperature is of great relevance, for example for promising space applications where panels are subjected to temperatures varying from -160 to 100 ^{0}C within a few minutes after eclipse [1], but also in terrestrial applications where they could be subjected to environmental temperatures as high as 70^{0}C [2]. Additionally, modules heat up faster than their surroundings, so the temperatures at the back of modules as high as 71^{o}C have been measured, even at moderate climate [3]. There have been extensive studies in literature [4-9] for the temperature dependency of crystalline silicon PV as well as for other types of thin film solar cells like amorphous silicon or CdTe. However, the temperature dependency of CIGS solar cells and modules has not been studied extensively. It should be noted that module producers often only give a single value for the temperature dependency of their module [10-13]. Within other studies, the values for the temperature dependency of mostly the current, voltage and efficiency dependency are incidentally shown [1, 7, 14-17], but no systematic studies are available.

The main goal of this study was to systematically investigate the impact of exposure to temperatures varying from room temperature (25^{o}C) to elevated temperatures (105^{o}C) on the electrical parameters of CIGS solar cells and modules. For this purpose, we have produced multiple types of CIGS solar cells, following cell designs that are applicable in CIGS modules. These samples were placed in a temperature controlled chamber combined with 1.5 AM illumination. This setup allowed the slow increase of the temperature of the solar cells (0.1 to 0.2 ^{o}C/minute) combined with the continuous measurement of the current voltage (IV) curves of the samples. The temperature coefficients for the main electrical parameters were then calculated from the IV curves.

CIGS photovoltaics is not yet a standardised technology with respect to both substrates and deposition processes. Additionally, it is well known that all the different types of CIGS solar cells and modules have different electrical behaviour. In order to get a good idea of the temperature dependency of different types of CIGS solar cells and modules, in total 42 samples of two types of clearly different CIGS solar cells for modules were tested. One type of samples was deposited on soda lime glass substrates by the relatively standard three stage coevapouration process, while the second batch has been deposited on flexible polyimide substrate by ion-beam assisted coevapouration at relatively low temperatures. Apart from these differences, these two types of CIGS solar cells have different topologies for the collection of the current, which has an impact on the electrical output of the solar cells. Within the two batches, small modifications were also introduced, including variations in the contact material, the alkali content, and the addition of a second cell with monolithic interconnection, in order to study the impact of these modifications.

In this study, we show the temperature dependencies of the efficiency, open circuit voltage, fill factor, ideality factor, series and shunt resistances and photo-, saturation and short circuit current density. Additionally, we propose background theory behind these dependencies. This will also help the estimation of the temperature dependency of CIGS solar cells and modules not included in this study.

4.2 Experimental

4.2.1 CIGS solar cells

In this study, both CIGS solar cells deposited on soda lime glass and polyimide were used. The general structure of these solar cells is shown in Figure 4.1, while the general structure of a CIGS solar cell is extensively described in chapter 1.3.

The samples used in this study were made following these procedures:

- The SLG samples are depicted in Figure 4.1a, b, c and g. The back and front contacts of the test samples were covered with soldered indium or evapourated gold, allowing contact with the measurement system. More information about these samples can be found in see chapter 3.2. Alongside with the single cells, also monolithically interconnected cells or 'minimodules' were used in order to simulate the behaviour of a module with a scribe zone (Figure 4.1g).

  Additionally, small differences between the samples was obtained by the control of the sodium and potassium contents. This was obtained by the modification of the molybdenum back contact or by the introduction of a SiN_x barrier, leading to differences in sodium and potassium concentrations between the samples. Examples of this variation are shown in chapter 7 and reference [18]. It should be noted that the cells that are very low in sodium and potassium have a low initial efficiency (10-11% at room temperature). In the rest of the chapter, we refer to the sodium content, but it should be noted that the potassium content also varied between the samples.
- The CIGS cells on polyimide substrates were also tested (Figure 4.1d, e and f). These samples were deposited via a semi-industrial process and also have the substrate/Mo/CIGS/CdS/i-ZnO/ZnO:Al stack sequence. The CIGS layer is deposited via ion-beam assisted coevapouration. These cells were covered by a screen-printed

metallic grid for a better collection of the current, which is also used for cells in full scale modules. Sodium was added via co-evapouration in a late stage of the CIGS deposition process. The amount of sodium was controlled by tuning the NaF crucible temperature.

In the rest of the chapter, the samples are divided into three global categories, based on substrate and interconnection technology, as is shown in Table 4.1.

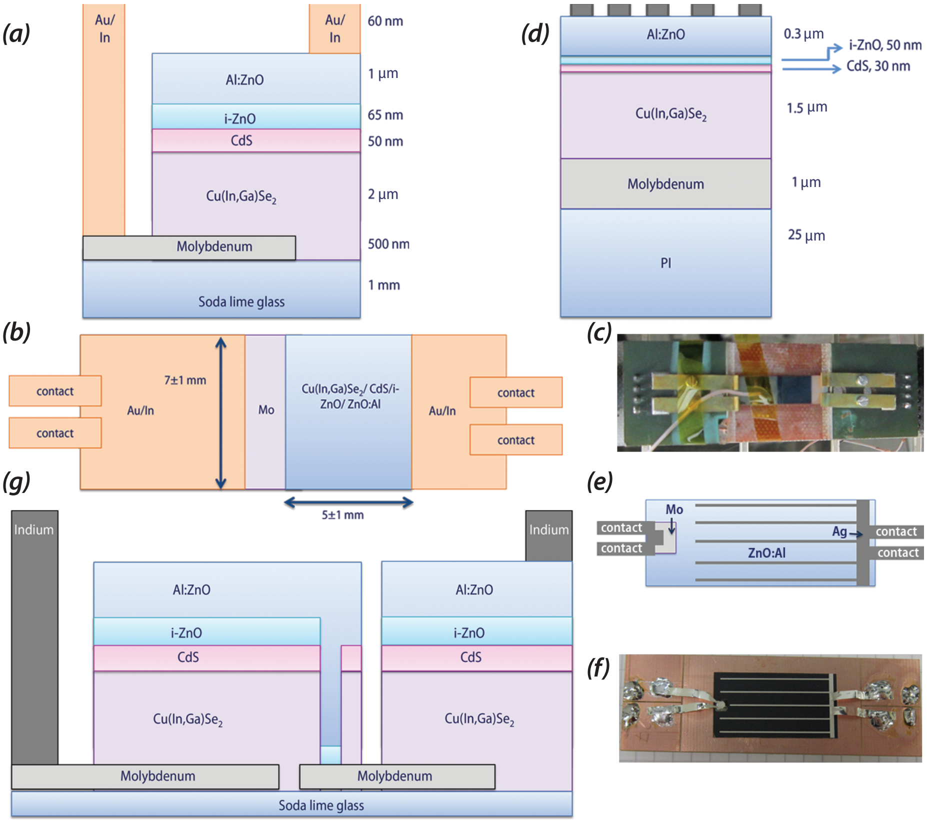

Figure 4.1

CIGS cells and cell holders as used in this study: schematic representation of the cross-section of the CIGS test structures (not to scale) of (a) soda lime glass samples (d) polyimide samples (g) SLG sample for two interconnected cells -Schematic representation of the top view of the CIGS cells combined with the positioning of the contact to the sample holder of: (b) soda lime glass sample with a surface area of 0.32±0.02 cm^2 *for the SLG cells with gold contacts and 0.48±0.04* cm^2 *for the SLG samples with indium contacts (e) polyimide sample with a surface area of 5.1±0.1* cm^2 *- Photograph of the top view of a CIGS cell in a cell holder of (c) soda lime glass sample, including thermocouple attached with kapton tape (f) polyimide sample (depicted without thermocouple).*

Table 4.1 Overview of the experimental parameters of the different batches as used in this chapter.

Name	Substrate	Contacts	Deposition technique	Design	Number of samples	Alkali concentration	Picture in Figure 4.1
SLG Au	Soda Lime Glass	Gold	Coevaporation	Single cells	23	High, normal and very low (Na and K)	a, b, c
SLG In	Soda Lime Glass	Indium	Coevaporation	Single and interconnected cells	7	Normal (Na and K)	a, b, c, g
PI	Polyimide	Silver	Ion-beam assisted coevaporation	Single cells with grid	12	Three concentrations of Na	d, e, f

4.2.2 Analysis of solar cell parameters and temperature

In order to increase the temperature of the samples and to measure the current voltage characteristics, the solar cells were placed in the experimental setup, which is described in chapter 3.3. During these experiments, the relative humidity was set to the minimal value. The samples were placed in sample holders, as is shown in Figure 4.1c and Figure 4.1f. These holders were used to allow electrical contact with the measurement system. Contacting between the cells and the sample holder was obtained by gold plated contact pens or silver plated copper contacts (Figure 4.1c and Figure 4.1f respectively). These contacts allowed measurements in a four point probe configuration. This approach was chosen to minimalize the effect of contact resistance on the measurement. Up to twelve holders were then placed on a sample grid (Figure 3.2 (SLG) and Figure 4.2 (PI)), which is positioned facing the light source of the setup.

In the setup, the samples were heated to maximum 105°C with heating rates of 0.13°C/min for the SLG In samples, 0.19°C/min for SLG Au samples and 0.12°C/min for the PI samples. With the setup, the electrical parameters as a function of temperature were determined as is described in chapters 3.3 and 3.4. The depicted series and shunt resistances were obtained by the determination of the slope of the curves, while the fitted values are not shown. Since the PI samples showed minor fluctuations in the current at negative voltages, the determination of the shunt resistance needs to be treated with care and is only included until 80°C. The ideality factor, saturation current density and photocurrent density is shown in this chapter are determined from

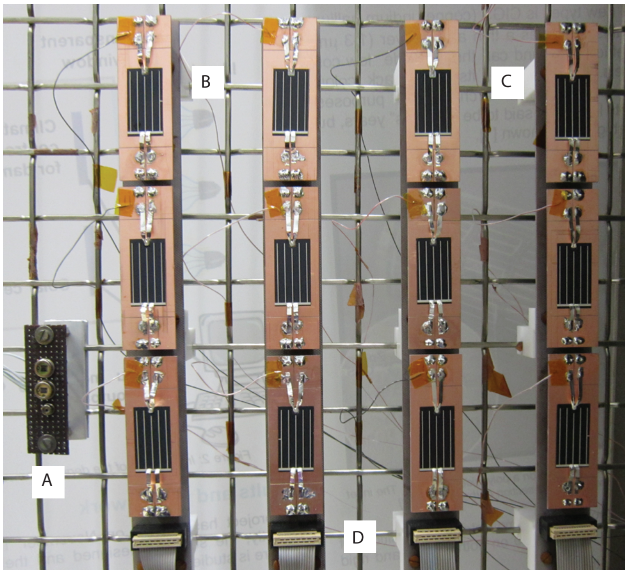

Figure 4.2

The sample grid facing the illumination from the solar simulator with the twelve PI samples.

A. Photodiodes for monitoring of the light intensity ***B.*** *Twelve cell holders to measure twelve solar cells simultaneously*

C. Thermocouples on all solar cells ***D.*** *Wires for connection with the measurement system.*

fitting. Since the values of the shunt resistance were also used as first estimation for the fitting procedure, the exact magnitude of the other values as obtained by fitting can also be unreliable.

4.3 Results

The temperature dependency of the electrical parameters of 42 CIGS cells and minimodules has been determined. The samples were divided into three global categories, based on the substrate (SLG and PI) and deposition method (coevapouration and ion-beam assisted coevapouration). Twelve PI samples are included in this study. The SLG samples can be further divided based on the material used for contacting with the measurement tools: this is indium for 7 cells and minimodules, 23 single cells have gold contacts.

The temperature dependencies of the efficiency, as well as the J_{sc}, V_{oc}, fill factor, R_s and R_{sh}, J_o, J_{ph} and the n as a function of temperature for one solar cell per batch are depicted in Figure 4.3. Since the calculation and fitting procedure was slightly different for the PI and SLG samples, the absolute comparison of the resistances, J_o, J_{ph}

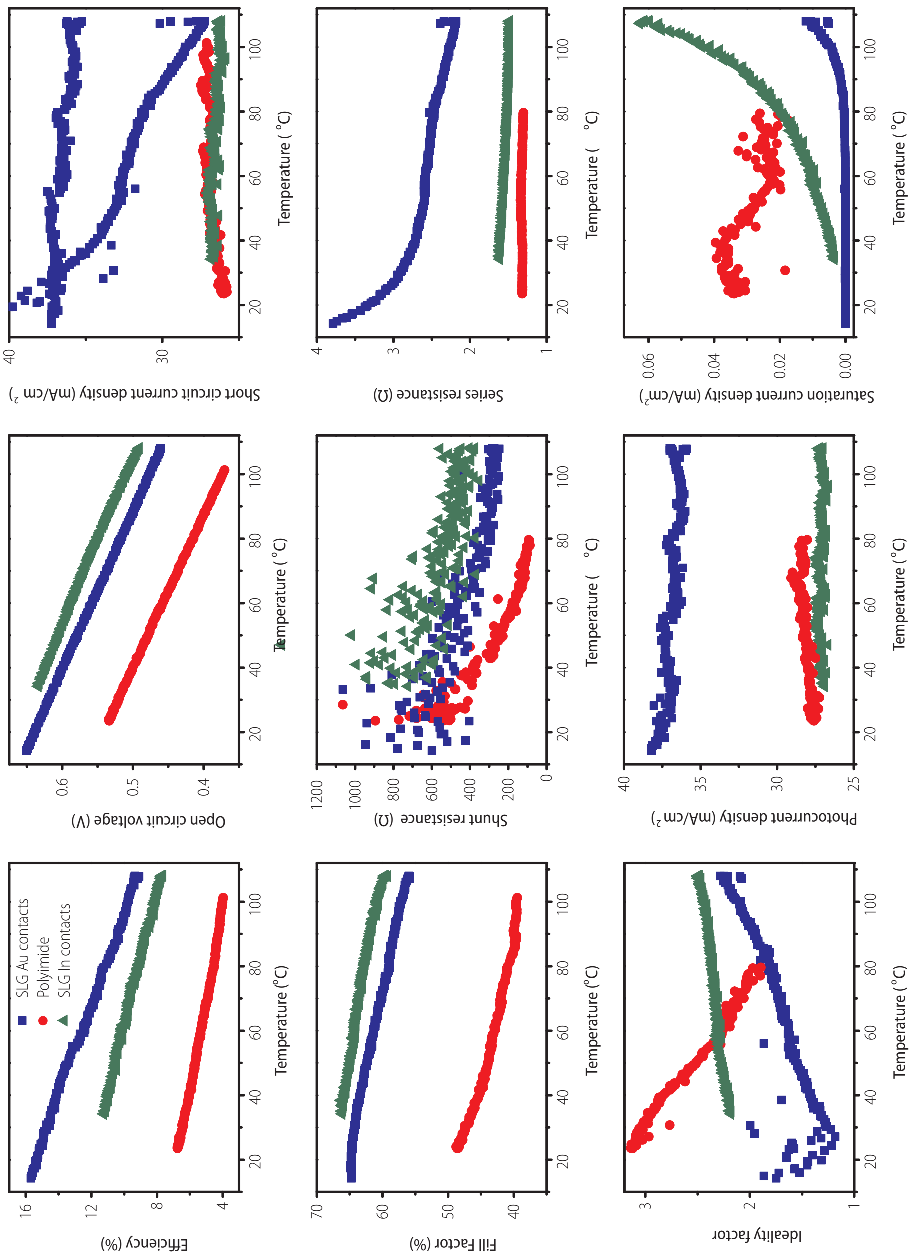

Figure 4.3 ↺

Temperature dependency of the open circuit voltage (V_{oc}), short circuit current density (J_{sc}), fill factor (FF), efficiency (η), series resistance (R_s) and shunt resistances (R_{sh}, with logarithmic axis), photocurrent density (J_{ph}), saturation current density (J_0) and ideality factor (n) for one single cell from all three batches. SLG Au: blue squares - SLG In: green triangles – PI: red circles and n, should be executed with care. Additionally, the resistances are calculated over different areas, so comparison of the absolute values of the resistances is not possible. The temperature dependencies as shown in Figure 4.3 give a representative picture for most measured samples. Next to the trend (negative or positive) and the magnitude of the change, these figures also shows how precisely the temperature dependency can be determined for the PV parameters: While the temperature – open circuit voltage relationship is completely linear with a very high correlation factor ($R^2>0.998$ for all samples) in this temperature zone, other relationships like temperature - series resistance are less linear. It was observed that the series resistance can in most cases be better fitted with a quadratic (aT^2+bT+c) than a linear function ($aT+b$), while the saturation current can be best fitted with an exponential curve. The shunt resistance showed a linear decrease for all samples, although the PI samples in some cases showed an increase for temperature between 20 and 40°C. Based on these observations, the temperature dependency of all 42 samples were determined by fitting of the curves.

In most cases, a linear relationship was assumed, thereby calculating the temperature coefficient (a) following:

$$X(T_{cell})=aT_{cell}+b \tag{4.1}$$

where X can be any of the electrical parameters of the cell and T_{cell} is cell's temperature. When an quadratic or an exponential function is assumed, then a and b are shown following:

$$X(T_{cell})=aT^2_{cell}+bT_{cell}+c \text{ (used for series resistance)} \tag{4.2}$$

$$X(T_{cell}) = a \times e^{bTcell} \text{ (used for saturation current density)} \tag{4.3}$$

For the linear fits, the average temperature coefficient a plus the standard deviation per batch are shown in Table 4.2. For the quadratic and exponential fits, both a and b and their standard deviations are depicted. For the series resistance, parameters based on both a quadratic and a linear fit are shown. For this parameter, both fits are purely empirical and since we cannot determine the physical relevance of the fit, so we cannot judge which fit is better.

The temperature dependencies of the efficiency, open circuit voltage, short circuit current density and fill factor plotted against their values at room temperature are depicted in Figure 4.4.

Based on Figure 4.3, Table 4.2 and Figure 4.4, it can be concluded that reproducible and reliable trends can be observed for the temperature coefficients of the open

Table 4.2 Average absolute temperature coefficients plus standard deviations of 42 single or interconnected solar cells of the three batches.

		Open circuit voltage	Short circuit density	Efficiency	Fill factor	Series resistance	Series resistance		Shunt resistance	Ideality factor	Photo-current	Saturation current	
		aT	aT	aT	aT	aT	aT^2	bT	aT	aT	aT	aT	exp (bT)
		[mV]/°C	[mA/ cm^2]/°C	%/°C	%/°C	(mΩ)/°C	(mΩ)/°C		Ω/°C	Unit/°C	(mA/ cm^2)/ °C	(mA/ cm^2)/°C	
SLG Au	Average	-2,1	-0,006	-0,06	-0,09	-9,0	0,09	-20	-16	-0,004	-4,0E-03	1,E-04	0,1
	Standard deviation	0,2	0,005	0,01	0,03	9,3	0,15	26	7	0,011	1,1E-02	2,E-04	0,1
PI	Average	-2,3	0,02	-0,043	-0,18	0,1	-0,03	4	-3	-0,011	1,7E-02	0,02	0,03
	Standard deviation	0,1	0.02	0,004	0,04	0,7	0,02	2	2	0,017	-0,006	0,02	0,02
SLG In	Average	-1,9	-0,01	-0,049	-0,08	-2,0	0,023	-5	-4	0,002	0,007	0,01	0,08
	Standard deviation	0,04	0,005	0,003	0,01	1,4	0,005	1	4	0,009	0,009	0,01	0,06

The V_{oc} coefficient is shown in mV/°C, all current densities coefficients in mA/cm²/°C, while the fill factor and efficiency coefficients are shown in unit / °C. The series and shunt resistances coefficients are shown in m Ω/°C and Ω/°C respectively, while the ideality factor coefficient is given in unit/°C.

circuit voltage, fill factor and efficiency, which all show a negative trend with increasing temperature. The short circuit current density goes up with increasing temperature for the PI samples, while it decreases for almost all SLG samples. The temperature dependency of the series resistance on the SLG has a low linear correlation coefficient in many cases, but the temperature dependency of these values is in most cases clearly negative.

However, in this study, we have shown that the temperature dependency shunt resistance is mostly strongly negative for the SLG samples, while it is slightly negative for the PI samples. For the two SLG samples that show a slight positive shunt resistance temperature dependency, the initial shunt resistance was very low. For the PI samples, this story is slightly more complicated: While some samples showed a linearly decreasing trend for the shunt resistance, other samples showed a steady increase between 20°C and 40°C-50°C, followed by a decrease at higher temperatures. Therefore, the linear fits do not always give reliable values. A multiple stage temperature dependency can also be observed for the series resistance of the PI samples, which have a maximum around 50°C.

As can be observed in the 'Supplementary information', it was noticed that the sodium

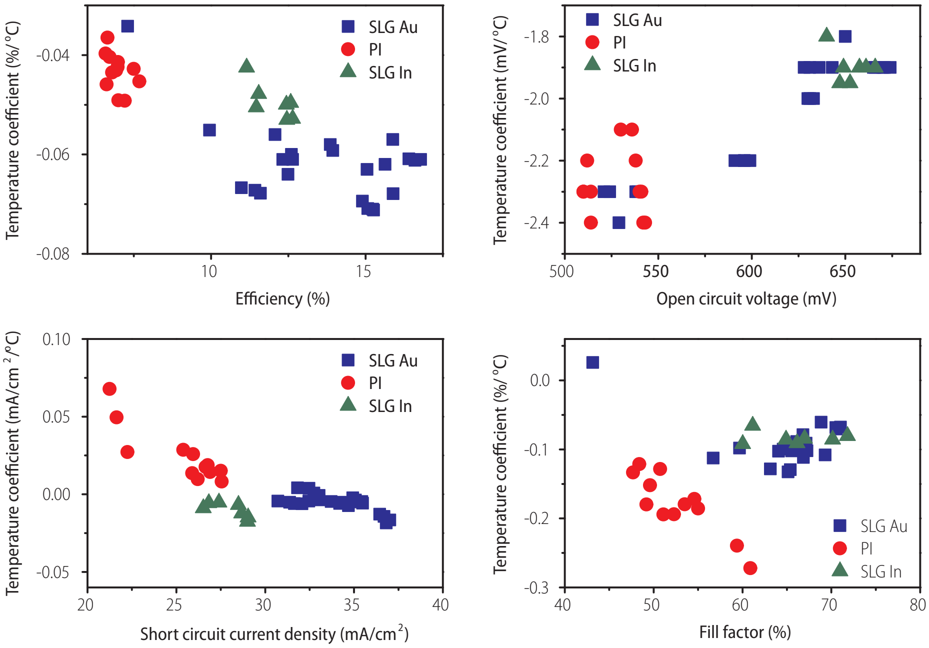

Figure 4.4:

Temperature coefficients of the efficiency, open circuit voltage, short circuit current density and fill factor as a function of these parameters at room temperature.

content slightly influenced the temperature dependency of the V_{oc}. However, no linear relation between the V_{oc} coefficient and the sodium content could be observed, since the lowest decrease number was observed for SLG samples with an average sodium content.

4.3.1 Normalised degradation coefficients

In order to compare the values with other types of solar cells, the temperature coefficients need to be normalised. A different open circuit voltage or short circuit current density at room temperature, which vary greatly between the different PV technologies, does in this approach not directly affect the number in the table. The following formula was followed in order to extract normalised temperature dependency from Table 4.2 or literature:

$$a\,(\text{norm}) = \frac{dX}{dT} \text{x} \frac{1}{X_{25C}} \text{x} 100 \qquad (4.4)$$

where a (norm) is the temperature dependency of any of the parameters $V_{oc,}$ $J_{sc,}$ η or fill factor, while the amount dX / dT was extracted for parameters $V_{oc,}$ $J_{sc,}$ η or fill factorfrom Table 4.2. $X_{25°C}$ is the reference value for this parameter for this sample at 25°C.

It should be noted that the CIGS on SLG, only SLG Au samples with sodium are included into Table 4.3, since the absence of sodium as well as the use of soldered contacts will not occur in real life panels. Since their electrical parameters at room temperature as well as their temperature dependencies can be deviating from standard cells, this would hinder the comparison. In order to include all measurements from this study, an additional line including all samples can be found in Table 4.3. In general, this table should be handled with care, since the temperature coefficients are influenced by a

Table 4.3 The normalised temperature coefficients of different types of solar cells based on this work and references [1,4,7,10,11,12,13,14,15,16,17]

	η (%/°C)	V_{oc} (%/°C)	J_{sc} (%/°C)	FF (%/°C)
c-Si [4,7]	-0.37 to -0.52	-0.25 to -0.55	+0.02 to +0.08	-0.19
a-Si [4,7]	-0.1 to -0.29	-0.19 to -0.5	+0.12	+0.1
CdTe [4,7]	-0.18 to -0.36	-0.22 to -0.43	+0.02 to +0.08	-0.01
CIGS [1]	-0.65 to -0.72	-0.48 to -0.51	-0.03 to -0.04	
CIGS [7]	-0.36	-0.31	+0.02	-0.08
CIGS [16]	-0.6	-0.5		
CIGS [14,15]	-0.26 to -0.6			
CIGS [17] with CdS	-0.39	-0.26	0	-0.10
CIGS [17] with ZnS	-0.41	-0.31	-0.02	-0.10
CIGS [10,11]	-0.38, -0.39			
CIGS [12,13]	-0.31	-0.29, -0.30	0.01	
CIGS (this work)	-0.36 to -0.70	-0.28 to -0.47	+0.32 to -0.05	+0.06 to -0.45
CIGS (this work, SLG Au)	-0.36 to -0.47	-0.28 to -0.32	-0.01 to -0.05	-0.09 to -0.20
CIGS (this work, PI)	-0.55 to -0.70	-0.39 to -0.47	+0.03 to +0.32	-0.25 to -0.45

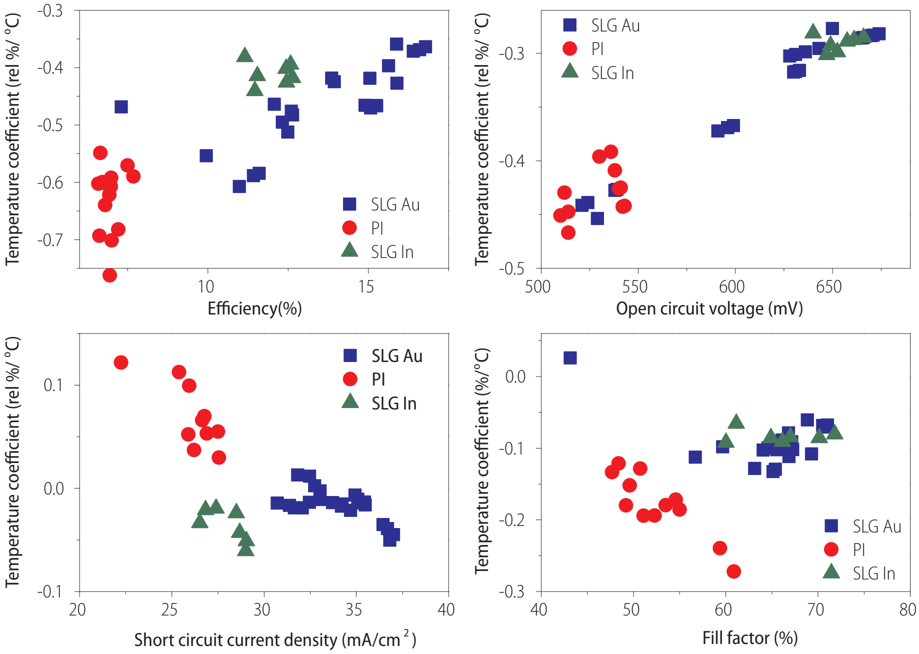

Figure 4.5

Normalised temperature coefficients of the efficiency, open circuit voltage, short circuit current density and fill factor as a function of these parameters at room temperature.

large number of factors.

Additionally, Figure 4.5 shows the normalised temperature coefficients of the efficiency, V_{oc}, J_{sc} and fill factor as a function of their values at room temperature.

4.4 Discussion

In this chapter, an overview about the physical explanations of the temperature dependency is given. For more in-depth information, the reader is referred to reference [19].

Reference [6] has reported that it is commonly expected that a temperature rise leads to an open circuit voltage and fill factor drop and a slight increase in the short circuit current. As a result, this leads to a reduction in the efficiency. The decrease of open circuit voltage, as well as fill factor and efficiency was observed, while the short circuit current showed a less expected picture. In Tables 4.2 and 4.3 and Figure 4.3, the most surprising observation is the behaviour of the short circuit current density. The CIGS on PI has a positive temperature dependency for the short circuit current density,

while this number is negative for the CIGS on SLG.
Furthermore, it is observed that the thermal performance of PI samples is worse due to the relative large decline of the fill factor as a function of temperature (see Figure 4.3). This was not caused by a high dependence of the fill factor with temperature, but on a low fill factor at room temperature partly based on the design of the samples used in these measurements. Therefore, this number as well as the temperature dependency of the efficiency are more strongly negative than expected for optimised samples. Additionally, Figure 4.4 and Figure 4.5 show that it should be taken into account that the normalised temperature dependency is greatly influenced by their values at room temperature.

This chapter shows that the temperature dependency of CIGS solar cells is comparable to crystalline silicon solar cells, but it should be noted that the variation within and between the batches of CIGS samples is large. This is even the case for the samples deposited on PI, which have been produced on a semi-industrial pilot line. The variation is also larger than described in reference [4]. This can imply that large differences between small scale produced CIGS samples exist, but also that differences in cells are levelled out between modules, which contain a large number of cells. In this chapter, the impact of the temperature on the various electrical parameters is studied and described in more detail.

4.4.1 Temperature dependence of the open circuit voltage

In this study, all samples show a steady decrease of open circuit voltage with increasing temperature. The temperature coefficient is -2.1±0.2 mV/°C for all samples, regardless of the type, substrate and open circuit voltage at room temperature. This is in agreement with the values found in reference [1], which is -2.4±0.1 mV/°C.
When the temperature dependencies of the V_{oc} of these 42 samples are plotted versus the V_{oc} at room temperature (Figure 4.4 and Figure 4.5), it can be seen that the absolute temperature dependency is slightly decreasing with an increasing V_{oc} at room temperature. When the V_{oc} is considered, a solar cell with a high V_{oc} is therefore not only preferable at room temperature, but even stronger at higher temperatures. This automatically implies that the normalised temperature coefficient is even more strongly dependent on the V_{oc} at room temperature.

4.4.2 Temperature dependency of the short circuit current

It was noted that the short circuit current response of the PI simples is different from the one deposited on SLG (Figure 4.3, Table 4.2 and Table 4.3): most cells on PI follow the classic theory for temperature dependence since they show a small rise on

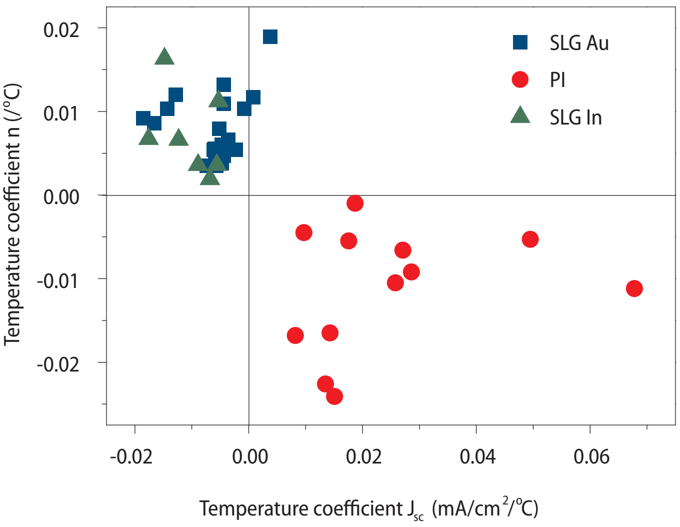

Figure 4.6

The relationship between the temperature coefficients of the ideality factor and of the short circuit current density.

short circuit current with a temperature increase. This is expected since the band gap energy E_g (T) decreases slightly with temperature and more photons therefore have enough energy to create electron hole pairs leading to a higher J_{ph}. This has a minor positive effect on the efficiency of the cell [20].

However, this is not the case for all samples: the short circuit current density of the cells on SLG declined with strongly varying numbers, which can be as low as $\frac{dJ_{sc}}{dT}$ =-0.019 mA/cm²/°C. This negative temperature dependency for the J_{sc} of CIGS modules was also detected in another study, giving $\frac{dJ_{sc}}{dT}$ = -0.007 mA/cm²/°C [1].

It is proposed [19] that the negative temperature coefficient for the SLG samples is caused by enhanced recombination. When the electrical parameters influencing this factor are compared between the PI and SLG samples, the strongest effect can probably be seen in the evolution of the ideality factor. The temperature coefficients of the short circuit current density and the ideality factor are shown in Figure 4.6. This figure shows that the samples with a positive trend for the ideality factor have a negative trend for the current density. This can be explained by the fact that a higher ideality factor negatively impacts the current density, since every inefficient recombination corresponds to an electron which will not contribute to the output current.

Additionally to this clear trend of the ideality factor, it was also concluded that for the PI samples that the photocurrent and saturation current densities have different trends with temperature than the SLG samples. The PI samples have shown an increase in photocurrent density and a relatively stable saturation current, instead of the exponential growth presented by the SLG samples. For the PI samples, the evolutions of n, J_o and J_{ph} are all in favour of an increase of J_{sc} when the temperature increases, while the opposite is true for the SLG samples.

When the relationship between the temperature coefficients and the short circuit current at room temperature, as is shown in Figures 4.4 and 4.5, are studied, no relationship can be observed. It therefore seems that various factors influence the current density at high temperature [20], but the room temperature values do not have a strong impact on the temperature dependency.

4.4.3 Temperature dependency of the fill factor and resistances

In the past the temperature dependence of the series and shunt resistance was only considered to have a minor impact on the efficiency change for increasing temperature [19]. In this study, measurements have shown that there is a dependency between these resistances and temperature. These changes impact on the fill factor and thus on the overall efficiency of the cells.

When the series resistance is considered, an increase of the temperature led to a slight decrease of the series resistance, which should lead to a small improvement the fill factor of the cells. If the series resistance of most cells is studied in more detail, it is visible that they generally do not decrease linearly, but via multiple stages, which can for example be better fitted with a quadratic function. It is proposed that multiple factors are playing a role its temperature dependency, which are all dominant at other temperatures. In general, the impact of the series resistance change on the efficiency is probably relatively small. It was also observed that the shunt resistance $R_{sh\backslash}$ is decreasing rapidly with temperature.

Since the magnitude of the decrease of the shunt resistance as well as the open circuit voltage decrease is a lot larger than the decrease of series resistance, the fill factor has a clear negative trend with increasing temperature. One exception was observed for a sample with a low fill factor, which actually had a positive shunt resistance trend. This again shows that a large variation between the samples can exist. When the relationship between the fill factor at room temperature and its temperature coefficients is studies (Figure 4.4 and Figure 4.5), no clear trend can be obtained from these data points.

4.4.4 Temperature dependency of the efficiency

Since the open circuit voltage and fill factor decrease strongly with increasing temperature, while the short circuit current density either decreases or increases slightly, the efficiency decreases strongly with temperature. The temperature coefficient of the efficiency as described in Table 4.2 and Table 4.3 show a wide range of values. For these samples, the absolute temperature dependency varies from -0.034 until -0.071 absolute %/°C. When this number is divided by the efficiency at room temperature, normalised temperature dependencies of -0.36 to -0.70 relative %/°C are obtained.

Figure 4.4 and Figure 4.5 both show the relative and the normalised temperature coefficients of the efficiency as a function of their efficiency at room temperature. Solar cells with a high efficiency have a slightly higher absolute temperature dependence, but because of their high efficiency, the normalised temperature dependency is lower. Extrapolation of these data points would imply that the temperature dependency of high efficiency CIGS solar cells and modules is therefore less severe than low efficiency CIGS samples, but since the various electrical parameters all react different on temperature increase, part of this difference can be explained by the different compositions.

4.5 Conclusions

The temperature dependency of 42 CIGS solar cells on a soda lime glass and polyimide substrate was determined. It was observed that the open circuit voltage declinesas a function of temperature with an absolute value similar for all cells (-2.1±0.2 mV/°C), regardless of substrate and V_{oc} at room temperature. The short circuit current density showed the expected increase with temperature for PI samples, while it decreased for most SLG samples. We propose that this decrease is largely caused by enhanced recombination. Additionally, a small decrease in the series resistance was observed for most cells, while the shunt resistance showed a large decrease with increasing temperature. The fill factor (-0.12±0.05%/°C) and efficiency (-0.05±0.01%/°C) also showed a decrease with temperature. It is proposed that although the absolute temperature dependency of the efficiency is higher for high efficiency CIGS solar cells and modules, the normalised temperature dependency is lower.

4.6 References

[1] S. Liu, E. Simburger, J. Matsumoto, A. Garcia, J. Ross, J. Nocerino, Progress in Photovoltaics: Research and Applications 13 (2005) 149-156

[2] D. Mildrexler, M. Zhao, S. Running, EOS, 87 (43) (2006) 461-467

[3] T. McMahon, Progress in Photovoltaics: Research and Applications 12 (2004) 235–248

[4] H. Mohring, D. Stellbogen, Proc. 23rd EUPVSEC (2008) 2781-2785.

[5] M. Nikolaeva-Dimitrova, R. Kenny, E. Dunlop, Proc. 21st EUPVSEC (2006) 2565-2569

[6] H. Müllejans, A. Burgers, R. Kenny, E. Dunlop, Proc. 19th EUPVSEC (2004) 2455–2458.

[7] A. Virtuani, D. Pavanello, G. Friesen, Proc. 25rd EU-PVSEC (2010) 4248-4252

[8] J. Wysocki, P. Rappaport, Journal of Applied Phys-

ics 31 (1960) 571–578

[9] Fan, J., Solar Cells 17 (1986) 309-315

[10] Solibro, Datasheet Solibro SL2 module; http://solibro-solar.com/en/product/modules/ accessed on 10 March 2015

[11] AVANCIS, Datasheet Powermax Smart module http://www.avancis.de/en/cis-solar-modules/powermax-smart/, accessed 10 March 2015

[12] TSMC, Datasheet TS CIGS Series, http://www.tsmc-solar.com/Assets/downloads/en-GB/TS_CIGS_Series_Datasheet_EU_05-2013.pdf, accessed 10 March 2015

[13] Solar Frontier, Datasheet SF150-170-S Series http://www.solar-frontier.com/eng/solutions/modules/S002210.html, accessed 10 March 2015

[14] R. Feist, M. Mills, S. Rozeveld, C. Wood, K. Thomson, Proc. 35th IEEE PVSC (2010) 3411–3416

[15] D. Meneses-Rodriguez, P. Horley, J. Gonzalez-Hernandez, Y. Vorobiev, P. Gorley, Solar Energy 78 (2005) 243-250

[16] T. Yanagisawa, T. Kojima, Solar Energy Material & Solar Cells 77 (2003) 83-87

[17] M. Contreras, T. Nakada, M. Hongo, A. Pudov, J. Sites, Proc. 3rd WCPEC (2003) 570-573

[18] F. Couzinie-Devy, E. Cadel, N. Barreau, L. Arzel, P. Pareige, Applied Physics Letters 99 (2011) 232108

[19] M. Theelen, A. Liakopoulou, V. Hans, F. Daume, H. Steijvers, N. Barreau, Z. Vroon, M. Zeman, Determination of the temperature dependency of the electrical parameters of CIGS solar cells, submitted to Progress in Photovoltaics: Research and Applications (2015)

[20] P. Singh, N. Ravindra, Solar Energy Material & Solar Cells 101 (2012) 36-54


AtTack

CHAPTER 5

Degradation mechanisms of the molybdenum back contact

This chapter is based on the following publications:

M. Theelen, M. Tomassini, N. Barreau, H. Steijvers, A. Branca, S. Harel, Z. Vroon and M. Zeman,
The impact of selenisation on damp heat degradation of the CIGS back contact molybdenum
Proc. 38th IEEE PVSC (2012) 1-6

M. Theelen, K. Polman, M. Tomassini, N. Barreau, H. Steijvers, J. van Berkum, Z. Vroon and M. Zeman, Influence of deposition pressure and selenisation on damp heat degradation
of the $Cu(In,Ga)Se_2$ back contact molybdenum
Surface & Coatings Technology 252 (2014) 157–167

M. Theelen, S. Harel, M. Verschuren, M. Tomassini, A. Hovestad, N. Barreau,
J. van Berkum, Z. Vroon and M. Zeman,
Degradation mechanisms of the molybdenum back contact for CIGS solar cells,
submitted to Surface & Coatings Technology (2015)

Abstract

Sputtered polycrystalline molybdenum films on glass with or without a $MoSe_2$ top layer was exposed to damp heat. All molybdenum films already showed degradation effects which were visible by naked eye after only several hours of damp heat exposure. The exposure resulted in large volume expansion due to the formation of a thick non-conductive molybdenum oxide layer consisting of various oxides and suboxides on top of the metallic molybdenum. This MoO_x layer showed cracks and the appearance of needle-like structures, maybe existing of Na_2CO_3.

The degradation effect was most severe for layers with the highest sputter pressure and thus the most porous microstructure. It was less severe for bilayer molybdenum films, which largely oxidised in the more porous bottom layer. The effect of selenisation was observed in the visual and optical characteristics: dense selenised molybdenum layers retained the highest reflectance. Likely, thereaction of molybdenum and selenium, which led to $MoSe_2$ formation, prevented rapid oxidation of the film. These results show that a dense selenised molybdenum is the most stable type.

The oxidised surface of molybdenum was further studied by XPS measurements, which showed that the MoO_x material was mostly MoO_3 with intercalated Na^+, which led to the formation of Na_xMoO_3 (molybdenum bronze) following this redox reaction :

$$MoO_3 + xNa^+ + xe^- \rightarrow Na_xMoO_3$$

Intercalation of Na^+ can explain both the high mobility of sodium in the grain boundaries and the important role this element play in the degradation process. It is thus proposed that both the grain boundaries as well as the degraded molybdenum contains MoO_3 which is intercalated with Na^+. Finally the intercalation of Na^+ in MoO_3 is a key point in the understanding of the evolution of cell performance under damp heat exposure in presence of Na. While the MoO_3 is an insulator, Na_xMoO_3 molybdenum bronze exhibits occupied states near the Fermi level, making this material conductive. Therefore, intercalation of Na^+ in the MoO_3 can greatly influence the band alignment in CIGS cells, while the formation of non-conductive MoO_3 can completely destroy the solar cell.

5.1 Introduction

While all other layers within Cu(In,Ga)Se_2 (CIGS) photovoltaics (PV) are varied in composition and deposition processes, sputtered molybdenum (Mo) is used in almost all CIGS solar cell and module designs as back contact (see chapter 1.3). Mo films show good conductivity, acceptable adhesion and are reasonably smooth. Furthermore, sputtered Mo can withstand the temperatures required for CIGS production processes, allows beneficial sodium diffusion and while it is inert to the metals in CIGS, it reacts with selenium. This results in the beneficial formation of molybdenum diselenide ($MoSe_2$) layers, which function as an ohmic contact between molybdenum and CIGS [1]. The composition of the Mo/CIGS interface has a large impact on the performance of the solar cell. It has also been shown that the grain structure of the molybdenum back contact influences the structure and thus on the efficiency of the CIGS layers [2,3]. The main drawback of molybdenum is the relatively low reflectance compared to other metals.

However, the characteristics of molybdenum are not stable with time. It was shown by reference [4] that storage of molybdenum in an inert atmosphere led to a change in cell parameters, but the impact of humidity is even larger.

It has been observed that damp heat exposure leads to degradation of molybdenum, which has been observed in two locations of CIGS modules [5,6]:

- Scribe P3 – Corrosion of molybdenum in scribe P3 can become significant when the electrical connection between neighboring cells is completely destroyed. (chapter 2.5.1.3)
- Scribe P2: Corrosion can occur in this scribe, which is filled with zinc oxide and molybdenum and allows the transport of current. The surface area of this scribe is relatively small and reduction in conductivity might influence the module greatly (chapter 2.5.1.2). Wennerberg et al. [6] reported an increase in the contact resistance in P2 from 1.5×10^{-3} to $5.5 \times 10^{-2} \Omega cm^2$, corresponding to a fill factor decrease from 74% to 57%.

Molybdenum degradation occurs mainly at places in CIGS solar cells with strong damage – these include scratches from zinc oxide particles due to scribing and scratches from sand blasting during edge preparation. However, extensive knowledge about the stability of molybdenum and the impact of the deposition conditions on the degradation stability is still largely unknown, while this is required to obtain more stable and cost-effective CIGS modules. For more a more extensive overview on the literature about molybdenum degradation, the reader is referred to chapter 2.3.1. To our knowledge, the first systematic studies on the stability of (selenised) molybdenum are described in references [7-9] and this thesis.

Additionally, in this chapter, we present two systematic studies about the impact of deposition conditions on the stability of molybdenum under damp heat conditions. We also present the reaction mechanisms involved in the degradation of molybdenum. The first study ('Selenisation and pressure experiment') [8] has focussed on the identification of the influence of film morphology and selenisation on molybdenum stability and the relationship of these factors with changes in conductivity and reflectivity.

The aim of the second study ('Lift-off experiment') [9] was the identification of the degradation mechanisms of a molybdenum layer which has the exact composition and morphology as this film in an actual CIGS module. Therefore, molybdenum films were produced by deposition and lifting off of a CIGS layer, on order to get the $MoSe_2$ layer (see Figure 5.1). Furthermore, the molybdenum film has a bilayer structure in order to optimize adhesion and conduction.

The degradation behaviour of these films under damp heat conditions was monitored and the changes in film properties were determined. In this paper, we use this information to propose the chemical reactions that are occurring during molybdenum degradation.

5.2 Experimental

5.2.1 Sample preparation

molybdenum thin films have been deposited on soda-lime glass (SLG) substrates by direct current (DC) magnetron sputtering of a 99.95% pure molybdenum target. The base pressure within the chamber before the deposition process was about $7.5\text{x}10^{-4}$ m Torr. The substrates used are 76 mm × 26 mm × 1 mm SLG microscope slides from RS France Company. These substrates have been cleaned in an ultrasonic bath containing detergent and were rinsed with de-ionised water.

5.2.1.1 Selenisation and pressure experiment

Before the deposition, the target was pre-sputtered for 5 minutes; the target-substrate distance was 55 mm and the sputtering power was 1 kW (power density: 3.1 W/cm^2). Films have been grown at three different argon sputtering pressures (2, 10 and 15 mTorr), while the deposition time was 24 minutes for all samples. For all deposition processes, the substrate was not heated intentionally. The DC sputtering parameters of molybdenum are summarised in Table 5.1.

Samples were either used as-prepared or placed in a selenium containing atmosphere

Table 5.1 Summary of deposition parameters of direct current sputtering of molybdenum.

Deposition parameters	Mo2	Mo10	Mo15	Mo2Se	Mo10Se	Mo15Se
Argon pressure (mTorr)	2	10	15	2	10	15
Argon flow (sccm)	11	69	110	11	69	110
Current (A)	3.00	3.35	3.55	3.00	3.35	3.55
Selenised	no	no	no	yes	yes	yes

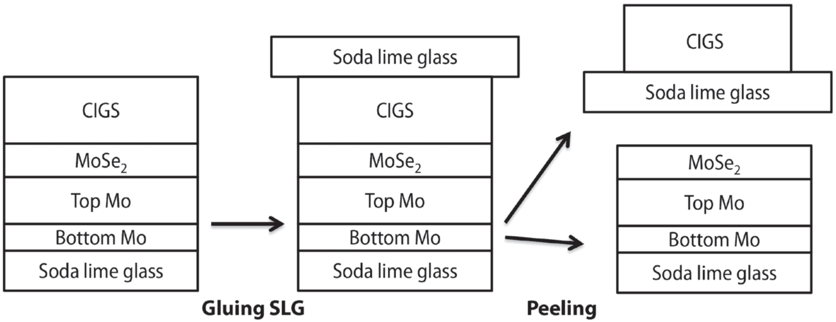

Figure 5.1

The lift-off procedure for the preparation of the 'lift-off' films used for degradation.

at 580°C for 30 minutes, to simulate the $MoSe_2$ formation that is expected to occur while depositing CIGS on top of Mo. This selenisation process offered the same conditions as during CIGS coevapouration, but without the heating of the metal sources.

5.2.1.2 Lift-off experiment

Before the deposition, the target was pre-sputtered. On both samples, a bottom layer of molybdenum was first deposited an argon pressure of 25 mTorr. The top layer had a different sputter pressure for the two samples: The sputter pressure for the dense sample (´Mo25/2´) was 2mTorr, while the porous sample (´Mo25/15´) was deposited at 15 mTorr. More information about the deposition conditions can be found in Table 5.2. The higher sputter pressure for the top layer (Mo25/15) leads to the formation of a film with more porous structure and therefore a higher sheet resistance [10].

After molybdenum deposition, a CIGS layer was deposited on both types of molybdenum by a three stage coevapouration process at 580°C [11,12].

A piece of soda lime glass was glued on top of the CIGS layer with EPO-TEK 353 ND glue. After the drying of the glue (30 minutes at 120°C), the second piece of glass was used to lift off the CIGS layer. The lift-off process resulted in separate CIGS and

Table 5.2 Summary of deposition parameters in the lift-off experiment.

Deposition parameters	Mo25/2	Mo25/15
Both		
Technique	DC sputtering	DC sputtering
Temperature	Room temperature	Room temperature
Target distance (mm)	55	55
Bottom layer		
Argon pressure (mTorr)	25	25
Argon flow (sccm)	200	200
Current (A)	1.5	1.5
Power (kW)	0.4	0.4
Power density (W/cm^2)	1.2	1.2
Deposition time (min)	14.5	14.5
Thickness (μm)	0.1	0.1
Top layer		
Argon pressure (mTorr)	2	15
Argon flow (sccm)	11	110
Current (A)	3	3.55
Power (kW)	1.0	1.0
Power density (W/cm^2)	3.1	3.1
Deposition time (min)	23.3	22.7
Thickness (μm)	0.9	0.6
Full film		
Sheet resistance (Ω/□)	0.27	1.54
Thickness (μm)	1.0	0.7

molybdenum layers a separate Mo layer. Therefore, the molybdenum film had the exact composition of molybdenum in a CIGS solar cell (Figure 5.1) .
This lift-off process was also described in reference [12], which also reports on the composition of the non-degraded interface of similar samples, which have also been deposited with different molybdenum sputter pressures. Extensive information about similar non-degraded samples can be found there.

5.2.2 Sample degradation

The samples were submitted to a damp heat test, according to certification standard IEC 61646 [13], which specifies 1000 hours exposure to damp heat (85°C and 85% RH). The damp heat tests were performed in a temperature and humidity controlled chamber (Espec Humidity Cabinet LHU-212).

Due to the rapid degradation reported in literature [6], initial degradation periods of one and two hours were chosen for both degradation studies. Later the exposure time to 85°C/85% RH was increased to 24 or 32 hours. This allowed excellent study of the initial degradation mechanisms, but also induced many rapid warm-cold transitions, thereby introducing an additional weak form of the 'thermal cycling' load [13] to the samples. These temperature transitions combined with 85°C/85% RH will be more representative for molybdenum that is exposed in the field than continuous exposure to damp heat.

The samples were characterised by various analysis techniques (see section 2.3) before, during and after the degradation periods. When the samples were not in the climate chamber or being measured, they were stored in an inert atmosphere or wrapped in a container that was evacuated to low pressure.
During the 'selenisation and pressure' experiment, the samples were placed in the climate chamber at 85°C/85% RH for varying intervals accumulating to 105 hours. The degradation periods were 2/2/1/1/1/2/4/4/8/8/8/16/24/24 hours.

During the 'lift-off' experiment, the samples were placed in the climate chamber at 85°C/85% RH for varying intervals accumulating to 105 hours. The degradation periods were 1/1/1/1/2/2/4/4/8/8/8/16/32/30/32 hours.

5.2.3 Characterisation of film properties

A Jandel Engineering Cylindrical Probe four-point was used to determine the sheet resistance of the films. The optical properties were determined by a Shimadzu UV-3600 UV-VIS-NIR, which allowed analysis of the reflectance of the molybdenum samples. A Leica Wild M400 microscope and a digital camera were used to determine the optical characteristics.

The morphological and structural properties of the films were determined by a FEI Quanta 600 Scanning Electron Microscope (SEM) combined with Energy Dispersion X-ray (EDX) EDAX Genesis 4000 and a Philips X'pert 5068 powder diffractometer, equipped with a Cu Kα source (λ=0.154 nm) in the 5° to 95° 2θ range with a step size of 0.02°. No internal standard was used. Raman spectra were taken with a Renishaw Raman spectrophotometer using a 514 nm laser.

Time-Of-Flight Secondary Ion Mass Spectrometry (TOF-SIMS) depth profiling was performed in the negative mode using an Ion-Tof TOF-SIMS IV instrument, with a beam of 50x50 μm^2 of 2 keV Cs^+.

The X-ray photoemission measurements were performed on a Kratos AXIS Ultra spectrometer using a monochromatic Al K_α X-ray source at 150 W for core levels and valence band. The analyzed area was 700×300 μm^2. The energy scale was calibrated using Au $4f_{7/2}$ at 83.97 eV and Cu $2p_{3/2}$ peaks at 923.63 eV measured from sputter-cleaned gold and copper films. The overall energy resolution, as determined from the Fermi edge of a silver reference, was 0.47±0.03 eV at 20 eV pass energy. The Kratos charge neutralizer system was used during all the experiments. The wide spectra and detailed spectra (core levels and valence band) were obtained using a 160 eV and 40 eV pass energy respectively. All high-resolution spectra were analysed and fitted with CasaXPS (N. Fairley, Copyright 2005 Casa Software Ltd). The photoemission contributions were fitted using a Shirley function for the background. For the Mo 3d-Se 3s signal, the spectrum of the non-degraded Mo2 in Figure 5.27 has been used to create a Line Shape (LS), which has been used for further fitting. Then pseudo-Voigt functions for the Mo 3d doublets relative to Mo^{5+} and Mo^{6+} have been used with a 3.14 eV spin-orbit-splitting and an area ratio for the 3d5/2 / 3d3/2 peaks of 1.5.

Unless mentioned otherwise, the results of degradation in this article are shown after the damp heat treatment.

5.3 Results

In these studies, two important deposition parameters for molybdenum in CIGS modules have been taken into account, which are the sputter pressure and the presence of selenium.

Sputter pressure

When molybdenum is deposited by DC magnetron sputtering, a correlation is observed between the sputter gas pressure and the stress in the film [10,14]. Under low argon pressure, molybdenum films become tightly packed and have a relatively low resistivity.

On the other hand, at high pressures, the number of collisions of sputtered atoms with argon atoms increase, hereby decreasing the energy of the sputtered atoms when they reach the substrate. Molybdenum films then get a more porous columnar molybdenum grain growth with larger intergranular areas [3], probably containing a mixture of MoO_3 and $Na_2MoO_4•2H_2O$ as reported in reference [15] and shown in Figure 5.2a. This intergranular material causes a higher resistivity. However, since the arriving atoms do not reorganise during the sputtering process, the adhesion is good.

When film porosity does not increase with sputter power, this can be attributed to compressive forces which might be associated with absorption of impurities like O, H and OH on the increased grain surface, but this was not observed in this study.

Since both good adhesion and low resistivity are required, often a molybdenum bilayer or multilayer is used. The first layer is sputtered at high pressure for good adhesion, while the second layer is sputtered at low pressure in order to obtain a low resistivity.

For the ‘selenisation and pressure’ study, three sputtering pressures were chosen: low (2 mTorr), medium (10 mTorr) and high (15 mTorr). For the ‘lift-off’ experiment, the first layer of the bilayer was deposited at very high pressure (25 mTorr), while the top stacks were deposited at either low pressure (2 mTorr) or high pressure (15 mTorr)

Presence of selenium

Molybdenum dichalcogenides, like $MoSe_2$ [1] are often observed in CIGS type solar cells, since the molybdenum reacts with selenium during the deposition process. This material functions as an interlayer and influences the adhesion of the absorber to the molybdenum. It is a layer compound consisting of a molybdenum layer embedded between two selenium layers. While the individual selenium and molybdenum layers

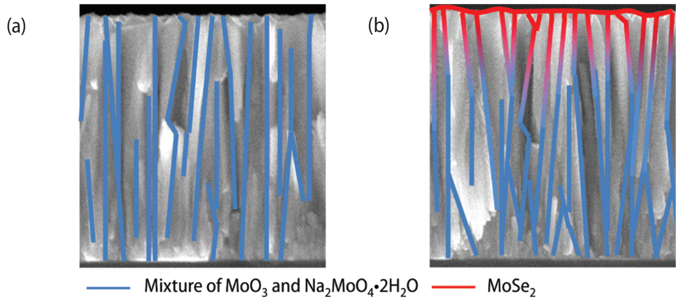

Figure 5.2

Schematic figure of sputtered molybdenum layers before degradation used as back contact for CIGS deposition (a) as deposited molybdenum layer (b) selenised molybdenum layer - The blue lines indicate the presence of a mixture of MoO_3 *and* $Na_2MoO_4•2H_2O$ *and the red lines represent* $MoSe_2$*. These samples were deposited for 47 minutes at 15 mTorr, and have a thickness of: 1.8 µm (not further described in this thesis).*

are covalently bonded, the Se/Mo/Se triple layers are bound together by weak Van der Waals forces.

A CIGS/Mo contact without $MoSe_2$ is a Schottky-type contact, while the introduction of $MoSe_2$ leads to a change into a beneficial ohmic-type contact. $MoSe_2$ may be incorporated in a molybdenum matrix is through its presence in the intergrain area, as shown in Figure 5.2b. A similar structure was reported in reference [16] for MoS_2.

Since this $MoSe_2$ layer is present in CIGS solar cells, it should also be taken into account for the degradation of CIGS. In the 'selenisation and pressure' study, half of the samples were selenised with a recipe resembling the selenisation conditions in a typical coevapouration process.

In the 'lift-off' study, a CIGS layer was first deposited on the molybdenum, creating a SLG/Mo/$MoSe_2$/CIGS stack. After this, the CIGS layer was removed, so a SLG/Mo/$MoSe_2$ layer remained.

5.3.1 Selenisation and pressure experiment

5.3.1.1 Initial layer properties

The initial properties of the samples are shown in Table 5.3. It was observed that the thickness and especially the resistivity of the sample were influenced by the sputter pressure: an increasing sputter pressure leads to a large increase of resistivity as well as a slight decrease in thickness. Furthermore, selenisation also leads to an increase in initial resistivity. These values can be compared with the resistivity of bulk molybdenum, which is 5.3×10^{-6} Ωcm (http://nl.wikipedia.org/wiki/Molybdeen)

Table 5.3 Characteristics of the molybdenum layers in the 'selenisation and pressure' experiment.

	Thickness (nm)	Sheet resistance (Ω/☐)	Resistivity ($\times 10^{-5}$ Ωcm)	Thickness after degradation bottom/top layer (nm)
Mo2	880	0.180±0.003	1.6	850/310
Mo10	740	0.437±0.010	3.2	580/350
Mo15	770	0.737±0.021	5.7	520/530
Mo2Se	910	0.214±0.003	2.0	940/170
Mo10Se	870	0.606±0.019	5.3	830/200
Mo15Se	620	1.439±0.031	9.0	540/130+520*

** This indicates the formation of two distinguishable layers, as visible in Figure 5.6*

5.3.1.2 *Visual degradation*

The visual degradation of molybdenum occurs quickly and follows different paths for the selenised and non-selenised samples. Photographs of the surface were taken after each degradation step to see the visible changes on the surface of the samples. The photographs taken after 17, 33 and 105 hours are depicted in Figure 5.3, Figure 5.4 and Figure 5.5 respectively.

Before degradation, no visual difference could be observed between the six samples, except for a discolouration at the edge of the selenised samples. This discolouration was caused by the sample holder used during selenisation, which covered the edge of the samples, so these regions are not selenised. These regions therefore degraded different from the rest of the samples, as can be seen in Figure 5.3 and are not representative for the degradation of selenised molybdenum.

After 17 hours of degradation of 85°C/85% RH exposure, a clear difference could be observed between the selenised and the non-selenised samples (Figure 5.3). The non-selenised samples had large degraded areas with layered colours, while the selenised samples had only small spots on the surface and some larger coloured spots at the edge. On the Mo15Se sample, dark spots from four point probe (4PP) measurements could be seen, indicating this porous material was very easily damaged by mechanical loads. This damage was not observed for the non-selenised Mo15 samples.

After 33 hours under 85°C/85% RH conditions (Figure 5.4), the samples still showed two distinctly different degradation patterns. The non-selenised samples showed the layers of coloured molybdenum oxide surrounded by large grey areas on the edges,

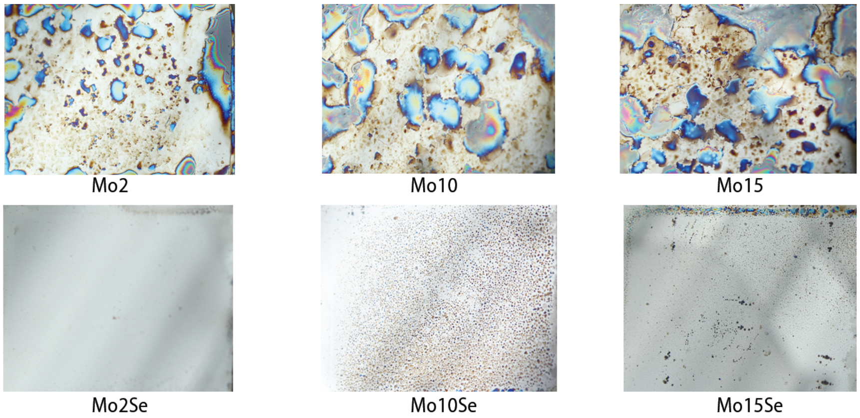
Mo2 Mo10 Mo15

Mo2Se Mo10Se Mo15Se

Figure 5.3

Photographs of the samples (30x25 mm) after 17 hours exposure to 85°C/85% RH.

while the selenised samples only showed small spots in the middle section. At the edges of the selenised samples some more coloured spots had appeared, especially on Mo10Se. This sample, which was deposited under the middle argon pressure, has degraded the most out of the three selenised samples.

In comparison, the non-selenised samples showed a clear relation between argon sputter pressure and degree of degradation. The sample with the highest sputter pressure has the highest degree of degradation.

After 105 hours, the non-selenised samples had degraded further, leading to the coverage of a large part of the surface of the samples with a greyish material (Figure 5.5). This material easily flaked off the surface: small flakes were found in the sample

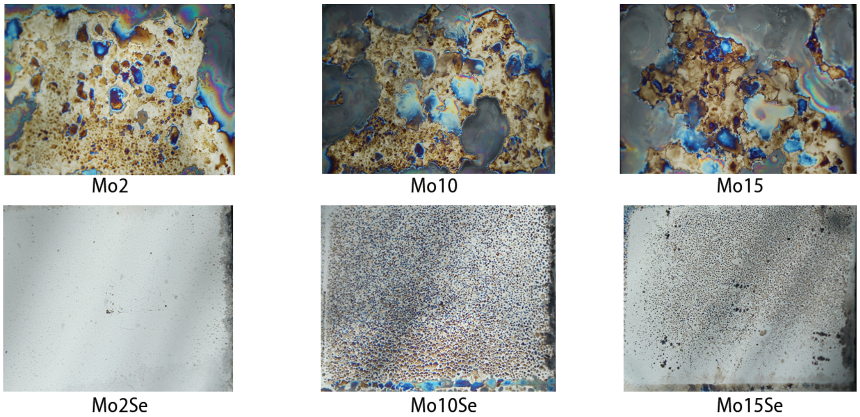
Mo2 Mo10 Mo15

Mo2Se Mo10Se Mo15Se

Figure 5.4

Photographs of the samples (30x25 mm) after 33 hours exposure to 85°C/85% RH.

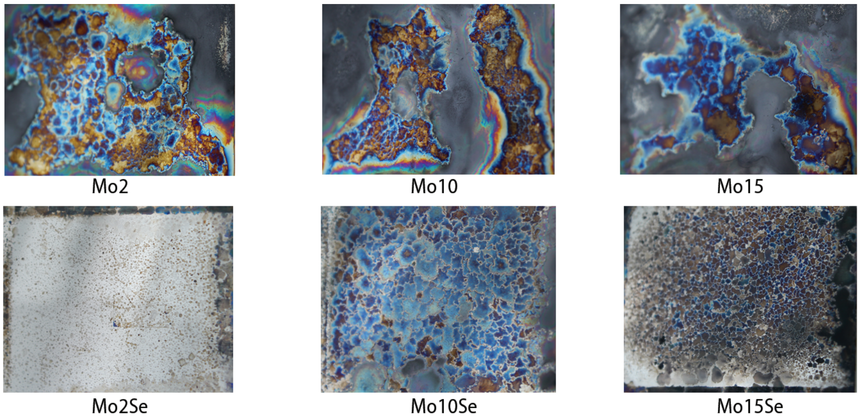
Mo2 Mo10 Mo15

Mo2Se Mo10Se Mo15Se

Figure 5.5

Photographs of the samples (30x25 mm) after 105 hours exposure to 85°C/85% RH.

holder. On Mo15, the material in the upper right corner of the sample had even delaminated. The selenised samples had changed severely in the last degradation steps. The coloured spots on the edge of the selenised samples changed into dark grey patches after 105 hours of degradation. The small spots in the middle area of Mo10Se and Mo15Se had grown larger and formed a mosaic-like layer. The spots on Mo10Se were mostly blue, while the spots on Mo15Se were mostly brown. Mo2Se seemed to have retained its reflective surface, though if this sample was studied under reflective lighting, the surface is also covered with spots.

The samples were further studied by optical microscopy in which the above observations were confirmed.

5.3.1.3 Structural changes

Scanning Electron Microscopy (SEM) gave more insight into the structural changes of the samples. Figure 5.6 shows the cross-section pictures of Mo2 and Mo15 before and after degradation as well as the selenised samples after degradation.

As was already mentioned in reference [7], a clear multilayer structure combined with volume expansion was formed due to damp heat exposure. It was observed that the bottom layer still resembled the structure of the original Mo layer, while the top layer showed a different structure and possibly also a different composition. The changes of the layer thickness due to exposure to 85°C/85% RH is shown in table 5.3. The total layer thickness after degradation is the sum of the bottom and the top layer. It should be noted that the change in thickness of the complete layer can change in magnitude

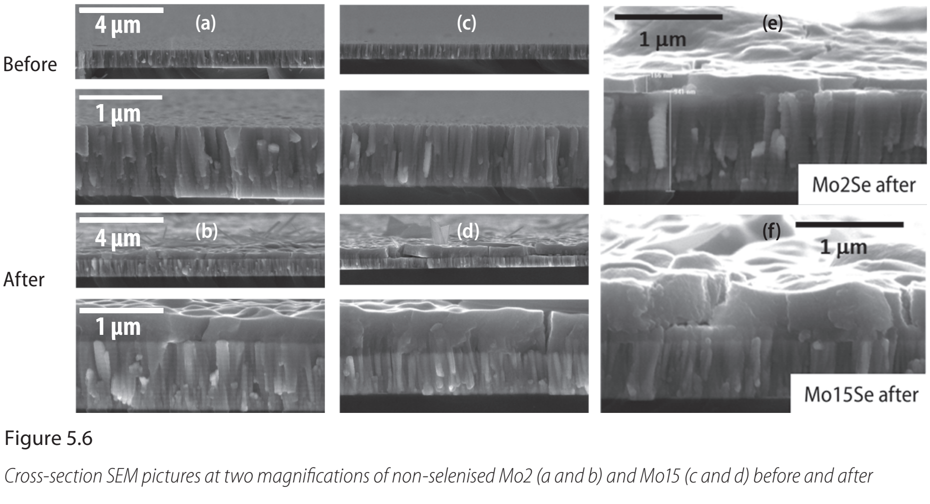

Figure 5.6

Cross-section SEM pictures at two magnifications of non-selenised Mo2 (a and b) and Mo15 (c and d) before and after 105 hours exposure to 85°C/85% RH. Cross-section SEM pictures of the selenised Mo2Se (e) and Mo15Se (f) after 105 hours exposure to 85°C/85% RH.

between different but comparable experiments. Various experiments (carried out, not reported in this thesis) also showed large volume expansion, but no unambiguous correlation between the absolute numbers of the volume change and the deposition parameters could be observed. Therefore, no conclusions can be drawn for the volume expansion as a function of selenisation and sputter pressure. However, an increase of the total layer thickness of at least 20% is observed in all cases.

A correlation between the ratio between the top and the bottom layer and the sputter pressure was observed: more porous layers showed thicker top layers.

The composition of the top layer was studied with EDX. The main elements measured after degradation were molybdenum and oxygen, while sodium, nitrogen and carbon as well as elements from the glass were present in small quantities. For the selenised samples, selenium was naturally also found. The oxygen content in the top layer was very high, leading to Mo/O ratios that varied between 0.36 and 0.66. This indicates that the top layer consists of molybdenum oxide. Other SEM figures showed the cracking of the top layer, exposing a new metallic molybdenum surface layer to a degrading environment, as is shown in Figure 5.7.

Another phenomenon observed by the SEM is the appearance of needle-like structures on the surface. Their lengths vary from hundreds of nanometres to tens of micrometres, as is shown in Figure 5.8.

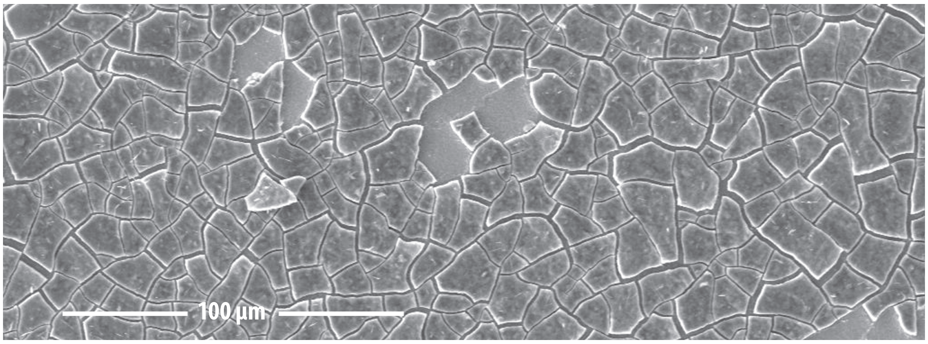

Figure 5.7

SEM pictures of the cracked surface of non-selenised Mo15 after 105 hours exposure to 85°C/85% RH.

When the needle-like structures were studied separately, molybdenum, oxygen and nitrogen were measured in these structures and in similar concentrations in the background material. Carbon and sodium, on the other hand, were found in these structures in higher concentrations than in the surroundings, indicating that the needle-like structures are rich in this element. This might indicate the formation of a carbonate, for example Na_2CO_3.

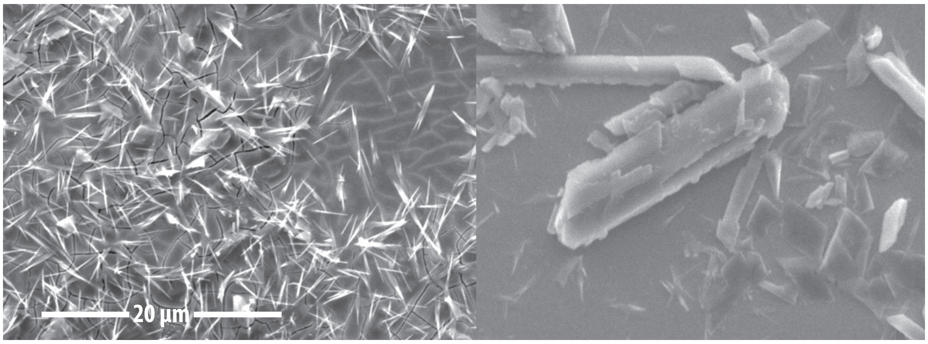

Figure 5.8

SEM pictures of the non-selenised Mo2 (left) and selenised Mo15Se (right) after 105 hours exposure to 85°C/85% RH.

5.3.1.4 Raman analysis

The samples were measured by Raman spectroscopy to further analyse their chemical composition. Molybdenum before degradation did not give peaks, since molybdenum is not a Raman-active compound. For the selenised samples, $MoSe_2$ modes around 172, 244, 293, 364, 443, 520 and 590 cm^{-1} were expected and observed [17].

After degradation, molybdenum oxide peaks of both MoO_2 and MoO_3 and various suboxides occurred. These molybdenum oxide modes were compared with the literature values [18-22] for assignment. The spectra were fitted with a baseline, $MoSe_2$ peaks and various types of molybdenum oxide peaks, as can be seen in Figure 5.9 and Figure 5.10.

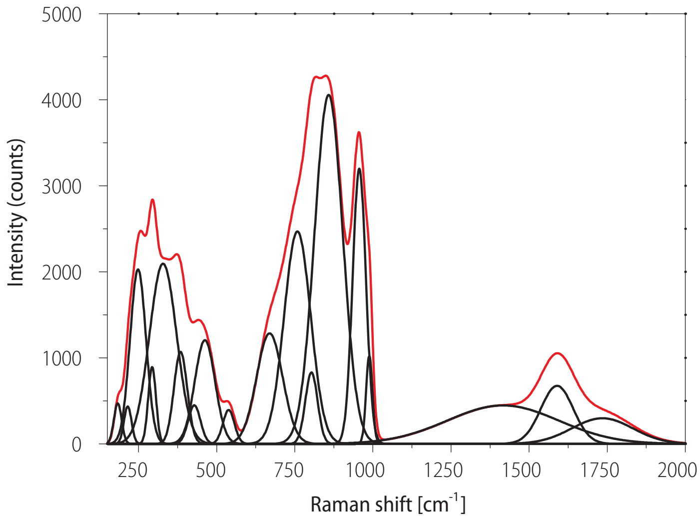

Figure 5.9

Raman spectrum of Mo2 on a blue spot after 5 hours of exposure to 85°C/85% RH. In this figure, the smoothed measured spectrum is shown in red, while the fitted modes are shown in black.

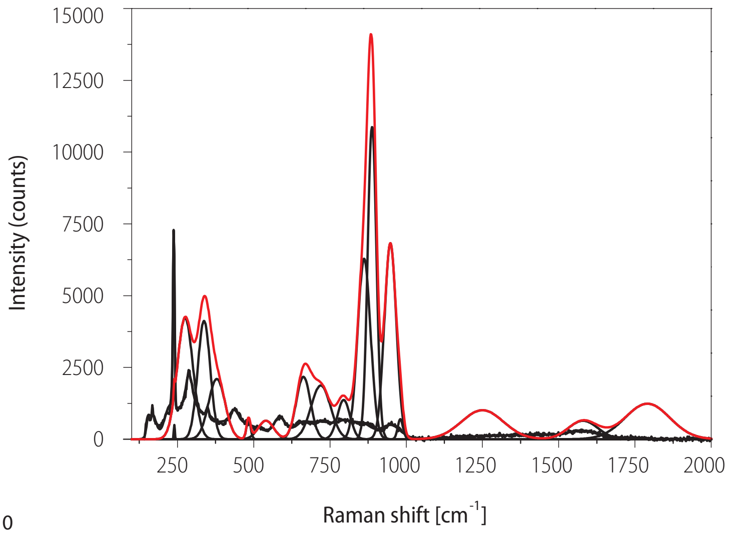

Figure 5.10

Raman spectrum of Mo10Se on a blue spot after 105 hours of exposure to 85°C/85% RH. In this figure, the smoothed measured spectrum is shown in red, while the fitted modes are shown in black.

After 5 hours of degradation, $MoSe_2$ modes were visible in the spectra of the selenised samples, providing the dominant modes. Very locally and in small quantities, molybdenum oxide peaks also started to appear, for example on a degraded spot on Mo10Se.

On the non-selenised samples, visual inspection showed large spatial difference. However, these local differences were not observed by Raman, since spectra taken on the blue spots and on the shiny background are similar. An example of the spectra after 5 hours of exposure to 85°C/85% RH is depicted in Figure 5.9. These spectra consist mostly of MoO_3 modes, with a few MoO_2 modes. The observed Raman signals after 5 hours of exposure are shown in Table 5.4.

There was also a set of modes around 1100 to 1800 cm^{-1} that increased in intensity as the samples degraded, similar to the molybdenum oxide modes, but these cannot be assigned to molybdenum oxides. In this region, signals of amorphous carbon with or without nitrogen and hydrogen can be observed [23,24]. This is supported by the high carbon and nitrogen content measured with SEM-EDX and might indicate that a thin layer of carbon-based materials is formed on the surface.

After 17 hours of degradation, the spectra of the non-selenised samples have not changed significantly except for an increase in absolute intensities. The selenised samples now have molybdenum oxide peaks in the spectra but no amorphous carbon peaks. An interesting difference in the molybdenum oxide peaks is now observed.

Table 5.4 Raman spectroscopy signals in cm^{-1} after 5 hours exposure to 85°C/85% RH, for the non-selenised samples taken on blue spots.

Mo2	Mo10	Mo15	Mo2Se	Mo10Se	Mo15Se	Assignment [14-24]
					154	A_g-$\delta(O_2Mo_2)_n$
			157	159	160	A_g-$\delta(O_2Mo_2)_n$
			172	172	171	$MoSe_2$
185	192	192	185	185	192	
217		217				A_g-$\delta(OMo_2)$
			228	228		MoO_2
			243	243	242	$MoSe_2$
250	246	246	250	250	246	A_g-$\delta(OMo_2)$
			291	291	291	$MoSe_2$
295	295	300	293	295	295	B_{2g}-$\delta(O{=}Mo)$
330	337		333	333	337	A_g-$\delta(OMo_2)$
		346	350	350		A_g-$\delta(OMo_2)$
			354	354	354	$MoSe_2$
		361				A_g-$\delta(O{=}Mo)$
386	380			380		A_g-$\delta(O{=}Mo)$
430	440	440	444	444	445	MoO_2
464	480					B_{1g}-$\nu(OMo_3)$
			520	513	515	$MoSe_2$
540						
			588	588	591	$MoSe_2$
671		660				B_{3g}-$\nu(OMo_3)$
					700	
	740	745				m-MoO_2
760				764		β–MoO_2
805	810	810				B_{1g}-$\nu(OMo_2)$
860	864	860				β–MoO_3
958	953	955				Mo_8O_{23}
990	985	985				A_g, B_{1g}-$\nu(O{=}Mo)$
	1207	1203				carbohydrites
1418			1419	1416		carbonitrides
1591	1595	1601	1556	1575	1529	carbon
1736		1802				carbonitrides
		2332	2331			carbohydrites

The non-selenised samples have mainly 660, 739, 810, 860 and 958 cm^{-1} peaks with 810 cm^{-1} as the dominant peak, which are MoO_3, MoO_2 and Mo_8O_{23} modes, while the selenised samples also show a 881 cm^{-1} peak, which could be assigned to Mo_4O_{11} [20]. After 105 hours there is no further significant change in the non-selenised samples, while the selenised samples do show a change. The spectra from the places on the samples where no degradation has taken place still show only $MoSe_2$ peaks. The spectra from spots on the surface show the Mo_4O_{11} peak around 881 cm^{-1} with a high intensity, some MoO_3 peaks and the amorphous carbon broad bands. In the case of Mo10Se, the $MoSe_2$ modes are barely observable in the spectrum taken at the blue spot, while in the case of Mo15Se, the amorphous carbon broad peaks are very large and of the same intensity as the main $MoSe_2$ and Mo_4O_{11} peaks. In Figure 5.10, the spectrum taken on a blue spot on the Mo10Se sample is depicted. More information can be found in Table 5.5, which shows all the Raman signals as measured after 105 hours of exposure to 85°C/85% RH as well as their assignment.

It can be concluded that the top layer of the degraded samples consists of MoO_x with 3>x>2. Furthermore, on the selenised samples, the specific Mo_4O_{11} composition is present.

Table 5.5 Raman spectroscopy signals in cm^{-1} after 105 hours exposure to 85°C/ 85% RH, taken on spots

Mo2	Mo10	Mo15	Mo2Se	Mo10Se	Mo15Se	Assignment [14-24]
			155		155	A_g-$\delta(O_2Mo_2)_n$
			170		169	$MoSe_2$
		175				
	192	192			189	
217		217			209	A_g- $\delta(OMo_2)$
228	228				225	MoO_2
			240	240	238	$MoSe_2$
246	246	246				A_g- $\delta(OMo_2)$
			285	275	288	$MoSe_2$
296	296	296	290			B_{2g}- $\delta(O{=}Mo)$
	328		337	337		A_g- δ (OMo_3)
	346		350		348	A_g- δ (OMo_2)
369		365			364	A_g- δ $(O{=}Mo)$

Table 5.5 Continued

Mo2	Mo10	Mo15	Mo2Se	Mo10Se	Mo15Se	Assignment [14-24]
379	379		379	379	437	A_g- δ (O=Mo)
			437			$MoSe_2$
445	445	440				MoO_2
477	477	477	483	483		B_{1g}- ν(OMo_3)
520		515	529			
				540		
565						MoO_2
			588		585	$MoSe_2$
660	648	666	661	663	687	B_{3g}- ν(OMo_3)
739	728	739	720	720		m-MoO_2
806	806	810	795	795		B_{1g}- ν(OMo_2)
860	860	873	860	862	845	β-MoO_3
			890	888		Mo_4O_{11}
					902	Mo_4O_{11}
956	950	955	951	948	968	Mo_8O_{23}
971	985	985	985	981		A_g, B_{1g}- ν(O=Mo)
					995	A_g, B_{1g}- ν(O=Mo)
1206	1220	1220	1250	1250		carbohydrites
1496	1496	1496	1430		1400	carbonitrides
1592	1592	1592	1580	1580	1585	carbon
1748	1721	1721	1791	1791	1740	carbonitrides
					2750	carbohydrites

5.3.1.5 X-Ray Diffraction

More information about the composition of the top layers was obtained by analysis with X-Ray Diffraction. Before degradation, all the samples gave similar diffractograms, with (110) signals as the dominant orientation next to the (200), (211) and (220) signals of molybdenum [25]. Besides the molybdenum peaks, several minor signals were observed on the samples before degradation. These peaks were located at the 2θ positions 43.6°, 63.8° and 81.3°. The most likely candidates for the identification of these signals are MoN_2 and MoO_xH_y. The latter might have been present as an impurity in the molybdenum target, which contained up to 40 weight ppm oxygen and 2 weight ppm hydrogen. The intensity and position of these minor signals does not change significantly during degradation. The graphs of Mo10 and Mo10Se are depicted as an example in Figure 5.11.

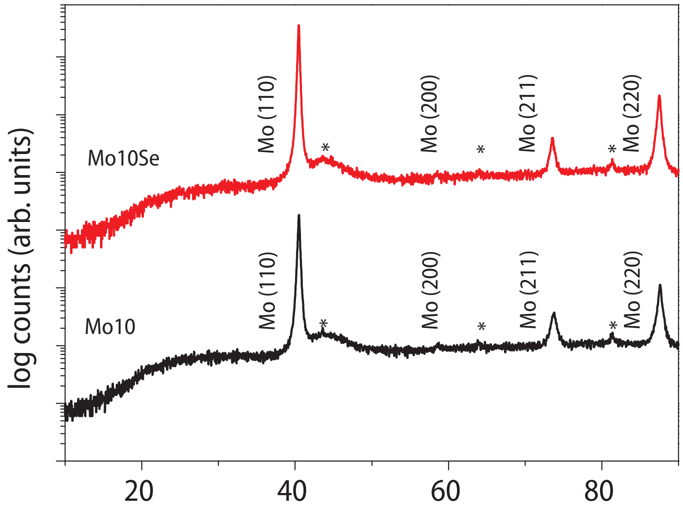

Figure 5.11

XRD patterns of the molybdenum orientations of Mo10 and Mo10Se before degradation on a logarithmic scale. The minor signals indicated with a star might be attributed to small quantities of MoN_2 *or* MoO_xH_y *of which the hydroxide is the most likely.*

During degradation, the molybdenum signals did not show a change in position. However, a steady decrease of the intensity of the (110) and (220) signals could be observed during exposure to 85°C/85% RH. The intensity of the other two minor peaks did not change significantly, which indicates that simple absorption of the radiation by the top layer of MoO_x cannot explain this intensity decrease. Therefore, this is another hint that all the molybdenum layers became thinner during degradation, as was also observed by cross-section SEM measurements. Since the (110) and (220) signals were selectively disappearing, these orientations were probably dominant in the top layer of the molybdenum.

Furthermore, new signals were observed due to exposure to 85° C/85% RH: after 20 hours, an extra signal at a 2θ position of 8.6° (*) became visible in the diffractograms of the selenised samples. This peak is believed to be the (200) reflection from $Mo_{17}O_{47}$, also known as molybdenum χ-oxide with a composition close to $MoO_{2.78}$. It later also occurred for the non-selenised sample, which only had a few other new peaks after 105 hours of degradation. An overview of the XRD spectrum of the area where new peaks are observed after 105 hours exposure to 85°C/85% RH is depicted in Figure 5.12.

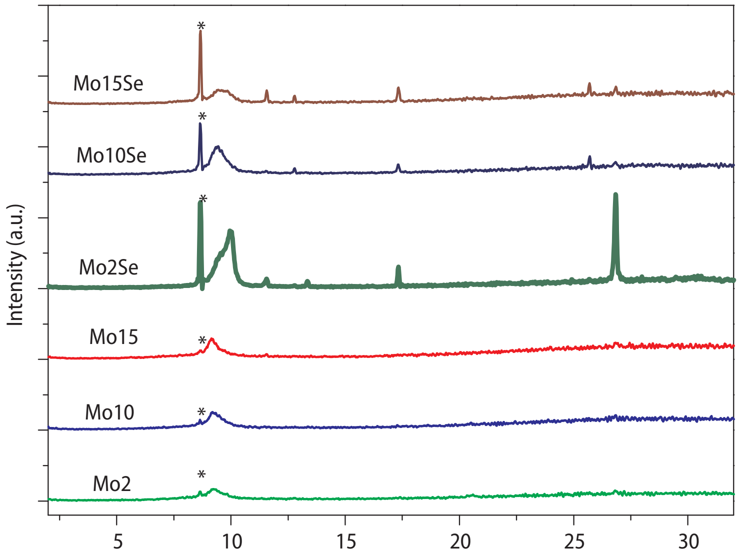

Figure 5.12

XRD patterns of the six samples after 105 hours exposure to 85°C/85% RH.

This figure shows signals around a 2θ position of 9.6° for all samples and signals varying in size at 2θ positions of 11.5° (Mo15 + selenised samples) and 26.8° (Mo10 + selenised samples). The compounds that are responsible for the 9.6° and 11.5° peaks are unknown, but the third peak is believed to be the $(0\bar{2}5)$ reflection of Mo_9O_{26}, also known as ζ-oxide with a composition close to $MoO_{2.89}$ [22]. The selenised samples have more extra signals, including signals at 12.8° and 25.7°, probably belonging to o-MoO_3 and m-MoO_3. Other signals have not been identified. Due to the large amount of relatively unknown molybdenum oxide compounds, they might be other suboxides, but sodium and selenium based materials might also be present. It should be noted that the absolute intensity of these signals is small – the highest oxide signal has an intensity of approximately 4% of the molybdenum (110) orientation. Since the intensity of these signals is still very modest compared to the molybdenum signals, while a thick layer of molybdenum oxide is observed by cross-section SEM, it is concluded that the molybdenum oxide is partly amorphous.

5.3.1.6 Compositional changes

The composition as a function of the depth was measured by SIMS in the negative mode before and after degradation. The negative mode is very sensitive to electronegative elements (fluorine, chlorine, oxygen, sulphur and also carbon and hydroxide), but there is little information on metal contamination.

The depth profiles of Mo10 and Mo10Se before and after 105 hours exposure to 85°C/85% RH are shown in Figure 5.13. These values show the difference in concentration of various important ions within the layers as well as due to degradation. It should be noted that the concentrations depend on the ionisation probability of the atoms and molecules, which varies per species and per background material. Therefore, no absolute concentrations were obtained by these measurements. Furthermore, the sputter depth has been calibrated based on the thickness of the molybdenum as determined by cross-section SEM, while the layer of molybdenum oxide has been scaled according to the same rate. In reality, MoO_3 and molybdenum probably have a different erosion rate, so the thickness of the top layers is only indicative.

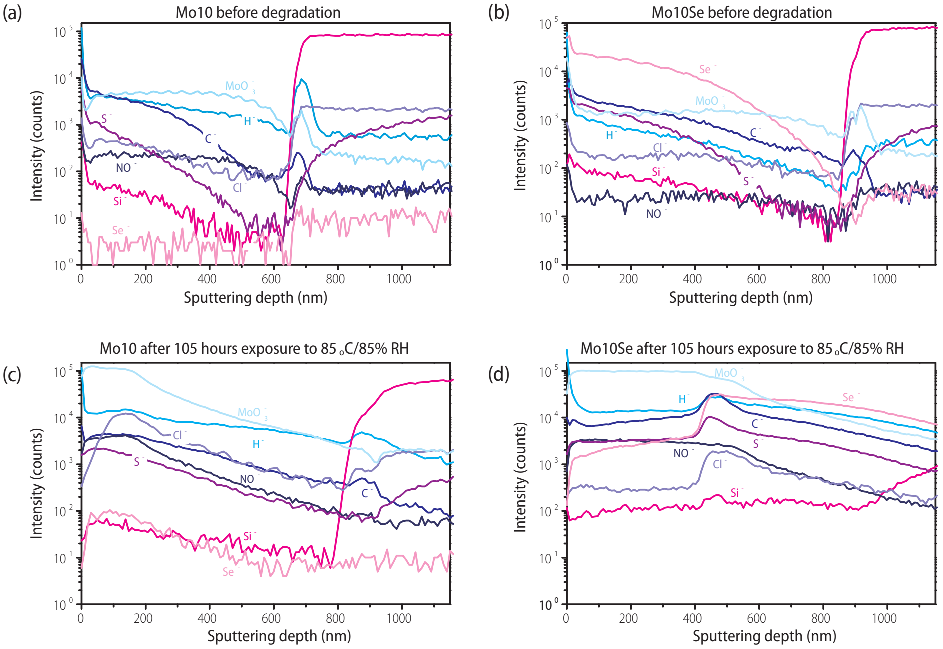

Figure 5.13

SIMS depth profiling of Mo10 and Mo10Se before and after 105 hours exposure to 85°C/85% RH.

Before degradation, small quantities of MoO_3, carbon, sulphide and hydroxide were measured in the non-selenised layer. These species might have been present in the target. In the selenised layer, high concentrations of selenium were naturally also present, mainly in the top 400 nm. Before degradation, the selenised sample showed a gradient in selenium concentration, which indicated that $MoSe_2$ is present as well as molybdenum. This can be explained by the presence of $MoSe_2$ as well as MoO_3 in the intergrain area as shown in Figure 5.2b.

The SIMS measurement on the non-selenised sample showed a large increase in MoO_3 concentration near the surface due to damp heat exposure. The top 100 nm layer mainly contained MoO_3, which was also present in the whole layer at a decreasing concentration to the bottom of the layer. Small quantities of chloride were found at the Mo/MoO_3 interface, while carbon, nitride-like materials and sulphide were present in the MoO_3 layer. These species were also present before degradation, but their concentration near the surface had increased. These elements might originate from the air or the vapourised demineralised water.

For the selenised sample, a clear two-layer structure was also formed after degradation. The top layer consisted mainly of MoO_3 with increased amounts of hydrogen and nitrate. The selenium content was very low in this layer, indicating that the selenium was not incorporated in the molybdenum oxide layer. Approximately 300 nm from the surface, an intermediate layer was formed. This layer had an increased content of hydrogen, carbon, sulphur and to a lesser extent chloride. The selenium content at this position was comparable to the initial selenium content at the surface.

5.3.1.7 *Changes in electrical properties*

The main requirement on molybdenum in a CIGS solar cell is a low sheet resistance. Figure 5.14 shows the development of the sheet resistance of the molybdenum samples as a function of exposure time to 85°C/85% RH. In general, no large changes in conductivity were observed, although an increase was observed for the porous

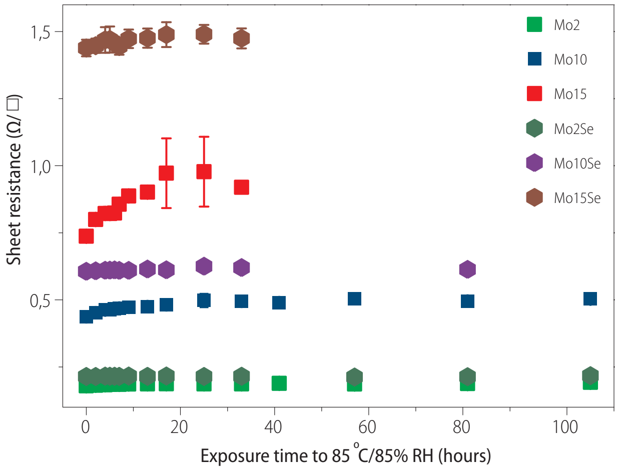

Figure 5.14

Development of the sheet resistance of the molybdenum layers as a function of exposure time to 85°C/85% RH. All data points are averages with standard deviation of the initial five measurements spots, but the number of spots decreased with degradation time. When no data point is depicted, none of the selected spots could be measured.

non-selenised samples (Mo10 and Mo15). However, this figure also shows that many data points are not depicted for Mo10Se, Mo15 and Mo15Se, indicating that the layer had become non-conductive. This already started after 13 hours and is explained by the formation of an isolating MoO_x layer which separates the conductive molybdenum from the measurement pins. This layer slowly covers the complete surface. Here, the impact of the sputtering pressure was observed. The porous samples (Mo15, Mo10Se, Mo15Se) had already largely lost their conductivity after 41 hours at 85°C and 85% RH, while the more dense samples still showed conductivity after 105 hours.

5.3.1.8 Changes in reflectance

Before and after each degradation step, the reflectance of the samples was measured with a UV-VIS spectrophotometer, as depicted in Figure 5.15. A wavelength range of 300 to 1200 nm is depicted, since most CIGS absorbers absorb in this range. The CIGS solar cells described in this thesis generally show absorption between approximately 340 and 1150 nm. Before degradation, there is a clear trend visible: the samples with a higher argon sputter pressure had a lower reflectance in this wavelength range. Next to that, the selenised samples have a lower reflectance than the non-selenised samples. Therefore, the sample with the lowest argon sputter pressure without selenisation has the highest initial reflectance.

After 57 hours of degradation, not shown here, the reflectance of Mo10Se, Mo10 and Mo15 has decreased to around 10%. Mo2 and Mo15Se vary between the 10% and 30%

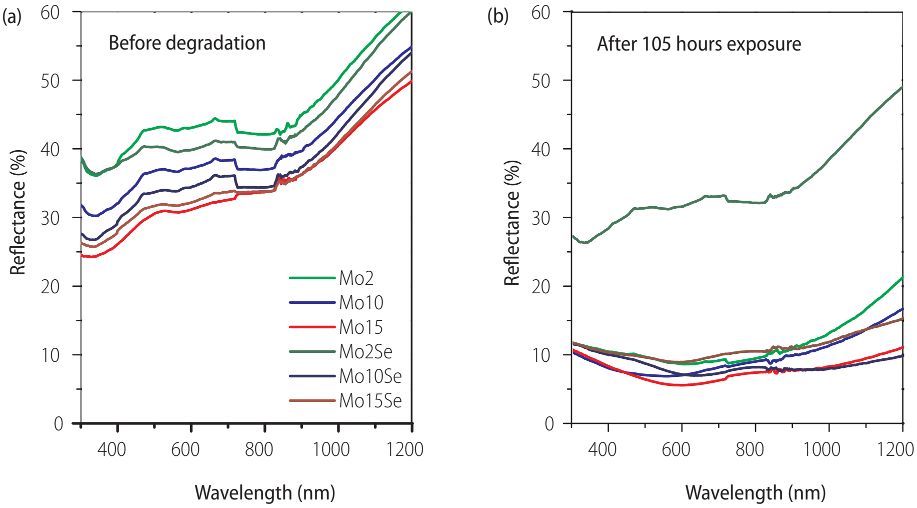

Figure 5.15

Reflectance of the samples plotted against the wavelength of the incident light before and after 105 hours exposure to 85°C/85% RH.

reflectance, while the Mo2Se sample has a slightly decreased reflectance. The Mo2Se sample also showed less severe degradation on the photographs. After 105 hours of degradation, the reflectance of all samples except Mo2Se has decreased to around 10%, as seen in Figure 5.15. The low pressure sample with selenide is thus the only sample which largely retains its reflective properties.

5.3.2 Lift-off experiment

5.3.2.1 Visual changes

Damp heat exposure of the samples lead to the appearance of black and blue spots as is shown in Figure 5.16 and Figure 5.17. This effect is stronger for Mo25/15, which is likely caused by the high porosity of this sample, obtained due to the higher deposition pressure. The changes are similar to the ones for the Mo/MoSe$_2$ samples in the 'selenisation and pressure' experiment, but it should be noted that the degradation characteristics of the previous samples occurred faster than observed in the 'lift-off experiment'.

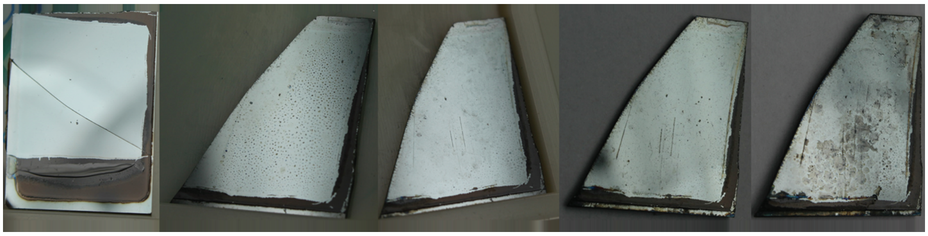

Figure 5.16

Photographs of Mo25/2 before and after 8, 32, 88 and 150 hours exposure to 85°C/85% RH. The width of the samples is 21 mm. The first pictures shows both the sample for degradation and the reference sample.

Figure 5.17

Photographs of Mo25/15 before and after 8, 32, 88 and 150 hours exposure to 85°C/85% RH. The width of the sample is 25 mm.

The degraded area was studied more thoroughly with a microscope as is shown in Figure 5.18 and Figure 5.19. It was observed that the visual degradation of both samples globally occurred in a similar way. The following steps can be distinguished

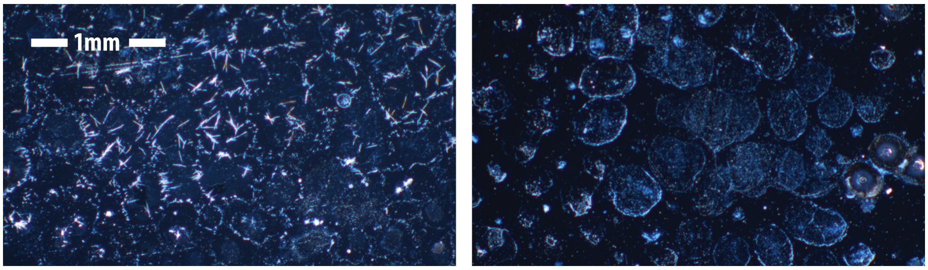

Figure 5.18

Microscopy photos of Mo25/2 (left) and Mo25/15 (right) after 8 hours of damp heat exposure.

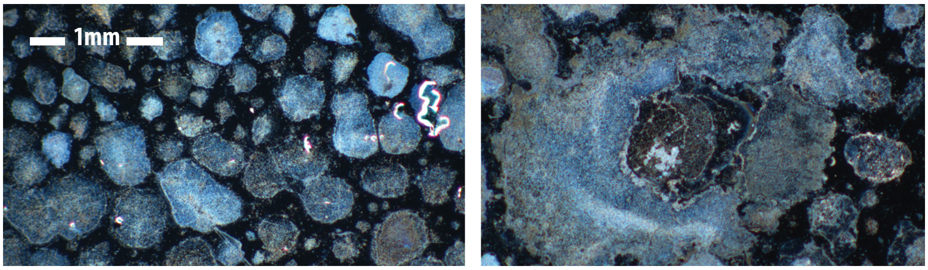

Figure 5.19

Microscopy photos of Mo25/2 (left) and Mo25/15 (right) after 150 hours of damp heat exposure.

during the degradation process:

1. The formation of bluish circular spots
2. These spots grow out and can become several hundreds of micrometres in size
3. Needles are formed on the surface (see chapter 5.3.2.4.1). It is observed that these needles are more prominently present on Mo25/2 (already after 8 hours) than on Mo25/15. It cannot be determined whether this difference is reproducible. Surprisingly, the needles were less prominently present after 150 hours exposure, indicating they can have grown together or be covered by another layer
4. The blue spots in Mo25/15 obtained brown rims and grow very large

In general, it can be observed that the degradation occurs faster for Mo25/15 than for Mo25/2.

5.3.2.2 *Changes in reflectance*

The average reflection (not weighted) before and after degradation was determined for a wavelength range from 340 to 1120 nm, which is the relevant range for CIGS solar cells (Table 5.6). On average, the reflectance of Mo25/15 was initially slightly higher. The non-degraded samples showed some difference in the shape of the reflectance curves: Mo25/2 reflected better at wavelengths below 500 nm, while the porous Mo25/15 reflected better above 500 nm. This difference is not yet explained.

As expected, the formation of spots and needles on the surface influenced the reflectance of the molybdenum. The reflectance decreased due to damp heat treatment. As expected based on the visual changes, the decrease was larger for the more porous Mo25/15 sample, which is in agreement with the results in the 'selenisation and pressure' study.

Table 5.6 Average reflectance of the Mo25/2 and Mo25/15 samples iin the wavelength range between 340 and 1120 nm at different exposure times to 85°C/85% RH

Time at 85°C/85% RH (hours)	Average reflectance Mo25/2 (%)	Average reflectance Mo25/15 (%)
0	29.0	36.1
8	24.8	31.9
16	24.2	31.9
32	25.1	31.5
56	25.3	33.5
88	23.2	27.6
118	24.1	21.9
150	20.7	14.3

5.3.2.3 Electrical effects

The main requirement for molybdenum in a CIGS solar cell is a sufficiently low sheet resistance. Figure 5.20 shows the development of the sheet resistance as a function of exposure time to 85°C/85% RH. Initially, Mo25/2 showed a lower sheet resistance than Mo25/15, which is due to the higher sputter pressure of the top layer of Mo25/15, which resulted in a more porous structure.

The sheet resistance of both samples might have increased slightly during the first 118 hours – the Mo25/2 sample showed an increase which is still within the error margin of the measurement, while Mo25/15 showed an increase of 33% over 118 hours. After 150 hours, the samples did not give any measurable values anymore, indicating the formation of a non-conductive top layer. This layer might already have formed in earlier hours, but the thickness is after 150 hours is apparently too high for 'piercing' by the probes of the measurement tools.

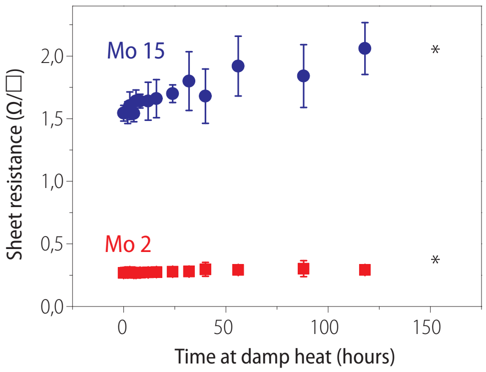

Figure 5.20

*Sheet resistance of Mo25/2 and Mo25/15 as a function of exposure time to 85°C/85% RH. Every data point represents five measurements on different positions of the samples. * Another measurement was executed after 150 hours, but the layers did not show any conductivity after this duration.*

5.3.2.4 Compositional changes

The compositional changes have been studied with SEM-EDX, SIMS and XPS, as described in this chapter. Furthermore, Raman spectroscopy and XRD were utilised, which gave results similar to the selenised samples in the 'selenisation and pressure' study: Raman spectroscopy showed the presence of $MoSe_2$, MoO_2, Mo_4O_{11} and MoO_3 type bonds, while very low signals for carbon and carbon hydrides or carbon nitrides were likely also present. XRD indicated the presence of a low amount of crystalline molybdenum oxide species, which can partly be identified by molybdenum suboxides, with compositions in between MoO_2 and MoO_3.

5.3.2.4.1 SEM-EDX

In optical microscopy, changes of morphology on the surface were already detected after several hours of damp heat treatment. Various SEM pictures (Figure 5.21) show examples of the morphology on Mo25/2 and Mo25/15. The SEM pictures revealed the occurrence of among others needles, stains and crystalline bars. EDX measurements were taken on the surface of non-degraded and degraded samples after various degradation times in order to globally determine the composition of the different regions. Table 5.7 shows the EDX analysis before and after damp heat exposure – it should be noted that the penetration depth is likely similar to the sample thickness, so perfect analysis of the particle composition is not possible.

Before damp heat exposure, molybdenum and selenium as well as low concentrations of oxygen and carbon were found in EDX measurements. After exposure, measurements were executed both on the 'clean' area and on areas with different types of needles and

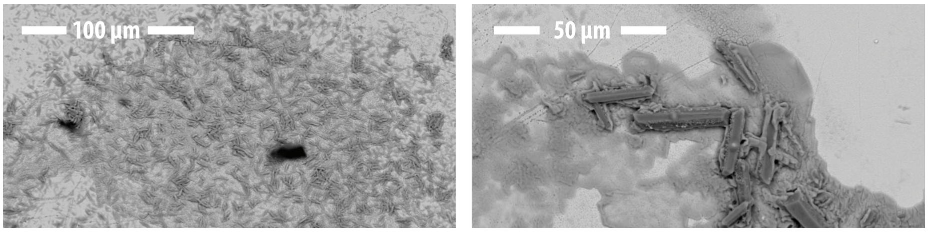

Figure 5.21

Backscattered SEM images of Mo25/2 (left) and Mo25/15 (right) taken at 15 kV after 150 hours exposure to 85°C/85% RH.

Table 5.7 Atomic percentages (%) obtained with EDX analysis with an acceleration voltage of 15 kV of the molybdenum samples before and after 150 hours of exposure to 85°C/85 RH.

	Mo25/2	Mo25/2	Mo25/2	Mo25/15	Mo25/15	Mo25/15	Mo25/15	Mo25/15	Mo25/15
		Light area	Spot*		Light area	Particle	Stain	Edge stain	Bar*
Exposure time to 85°C/85 RH	0h	150 h	150 h	0 h	150 h	150 h	150 h	150 h	150 h
Se	5	5	3	8	7	2	6	1	
Mo	79	66	41	77	69	27	50	28	12
Na		1	2			2	1	2	<0.5
O	8	19	39	9	15	44	32	59	39
C	7	8	11	6	7	11	7	4	18
Si		<0.5	<0.5	1	1	<0.5	1	1	
N		2	5		2	14	4	5	31
Ti						1			

The positions with the stars (*) are shown on the SEM photographs. It should be noted that the real composition can deviate several percent from the values measured by EDX, so these values are only indicative.

stains.

The 'clean' spots still contained molybdenum and selenium, but the oxygen concentration had increased. When the various 'needle' and 'bar' rich areas were studied, the oxygen concentrations was even higher. Furthermore, sodium and nitrogen were also measured.

It should be noted that the content varied greatly per location of the sample, but it was certainly concluded that exposure to damp heat leads to an increased oxygen

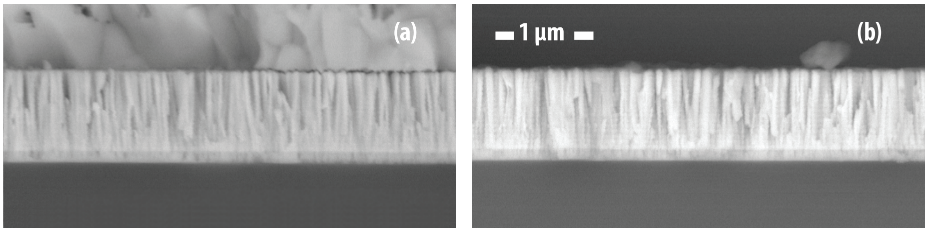

Figure 5.22

SEM cross-section image of Mo25/2 with CIGS before lift-off and degradation (left) and lifted Mo25/2 after 150 hours of damp heat exposure (right). The size bars represent 1 micrometres.

content, while the various particles also seem to contain higher concentrations of sodium and nitrogen. The molybdenum and selenium content naturally decreased. It should be noted that the nitrogen concentrations varied greatly and were mostly found after 150 hours, while shorter degradation times did not show high concentrations of nitrogen.

Cross-section SEM images were used to determine the thickness and the morphology of the samples. Figure 5.22 shows the Mo25/2 sample with the CIGS layer still attached before degradation as well as the lifted Mo25/2 sample after damp heat exposure. Similar pictures were obtained for Mo25/15. These figures show that the initial molybdenum film clearly consisted of two layers: The bottom 100 nm was deposited at 25 mTorr for adhesion, while the top layer was deposited at lower pressure (2 mTorr for this figure). The pictures also show that the morphology did not change significantly due to damp heat. This is a clear difference with the monolayer molybdenum in the 'selenisation and pressure' study in which the formation of a thick layer of molybdenum oxide on top of the metallic molybdenum was reported. After 105 hours of damp heat exposure, these oxide layers formed on selenised molybdenum had thicknesses from 170 nm to 650 nm.

5.3.2.4.2 SIMS

SIMS analysis was used in order to determine the composition of the sample as a function of depth. Since the measurements were executed in the negative mode, it is very sensitive to electronegative elements (for example fluorine, chlorine, oxygen and sulphur), but there is little information on metal contamination and the presence of sodium and potassium. It should be noted that no absolute concentrations can be determined with SIMS, since the intensity is not calibrated for these measurements.

Two depth profiles taken on the degraded Mo25/15 sample are shown in Figure 5.23,

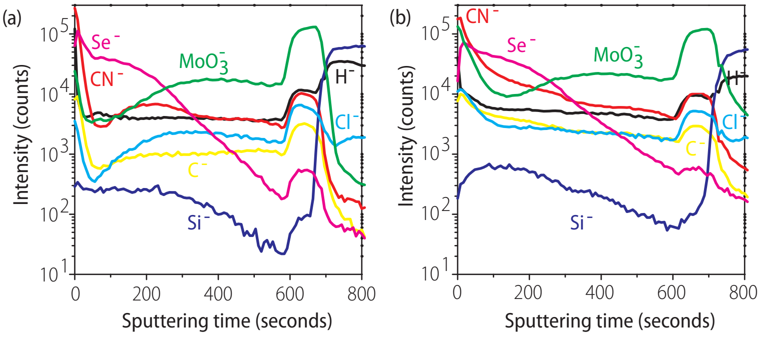

Figure 5.23

SIMS intensity depth profiles of sample Mo15 in two different regions after 150 hours exposure to 85°C/85% RH. (a) represents a shiny area, while (b) shows a dark grey region.

while Mo25/2 (not depicted) roughly showed the same effects. The profiles are taken on a 'shiny' area and on a dark grey 'degraded' area. As expected, the selenium content is especially high at the surface and is rapidly decaying after about one third of the molybdenum layer thickness. As described above, this probably indicates that $MoSe_2$ is present both as a surface layer and in the grain boundaries. A decreased selenium concentration is observed for the top zone of the dark grey region, indicating that $MoSe_2$ has disappeared from the surface layer. The high concentration of MoO_3 indicates that oxygen has replaced the selenium. Furthermore, on the dark grey area, other 'foreign' species, including hydrogen, carbon, cyanide, chlorine and oxygen were also found in higher concentrations. The cyanide signal does not indicate the actual presence of this material, but is probably formed by the reaction of the carbon and nitrogen present in the material. However, the exact determination of the formed molecules is not possible with SIMS.

At the bottom of the molybdenum layer, there is a large increase in oxidised MoO_x, also containing increased concentrations of foreign species as well as selenium. This effect was also observed for the Mo2 sample - this region has a thickness of 15-20% of the total molybdenum thickness, but it should be noted that the erosion rate of Mo and MoO_x might differ, so the absolute thickness of this layer cannot be calculated. However, this thickness can easily be linked with the highly porous bottom layer of the sample (sputtered at 25 mTorr), which is 0.1 micrometres on a total thickness of 0.7 micrometres. Therefore, it can be assumed that the MoO_x content is very high in this highly porous layer. It should also be noted that this bottom MoO_x layer was not observed for the monolayers Mo in the 'selenisation and pressure' experiment in which all the Mo in a sample was deposited at the same sputter pressure.

5.3.2.4.3 XPS measurements

XPS was used to determine the chemical environment of the elements in order to learn the molecular structure of the reaction products. The reported results are only for the surface composition, due to the very low penetration depth of XPS.

The survey spectra of Mo25/2 before and after degradation and Mo25/15 after degradation are displayed in Figure 5.24.

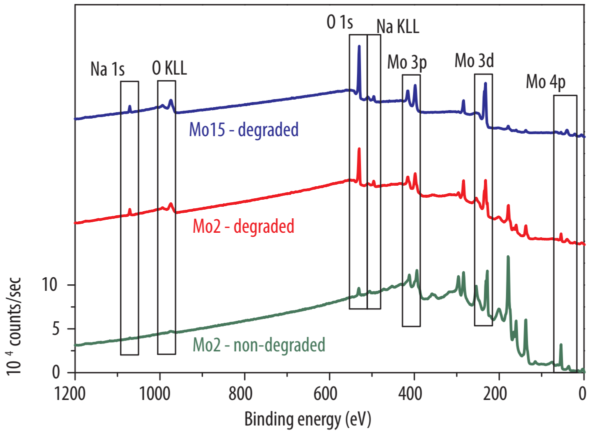

Figure 5.24

The survey XPS spectra of the non-degraded Mo25/2 and Mo25/2 and Mo25/15 after 150 hours exposure to 85°C/85% RH.

The non-degraded molybdenum sample as obtained by the lift-off process exhibits molybdenum and selenium signals pointing out the presence of $MoSe_2$, which is formed during the CIGSe growth. Furthermore, sodium and oxygen signals with a very low intensity are observed. These elements were expected, since sodium was also present on the molybdenum side after the CIGSe layer lift-off process on other samples, while the oxygen is rapidly incorporated due to air exposure. Indium and gallium were not detected on the molybdenum side, which is unlike results obtained in a previous study [12].

Figure 5.25 and Table 5.8 show more in-depth information about the sodium signals as measured by XPS. After damp heat exposure, the sodium signal intensity increased due to diffusion of sodium through the molybdenum layer. The surface of the degraded molybdenum samples contained the same amount of sodium, while the chemical environment of the sodium for both the degraded and the non-degraded samples were similar, since they all showed the same binding energy and line shape.

The similar binding energy and shape indicated that the sodium must be in the same chemical environment before and after degradation. The modified Auger parameter value α* is used to determine the composition of the sodium containing species.

$$\alpha^* = E_b(\text{Na 1s}) + E_k(\text{Na KLL}) \quad (5.1)$$

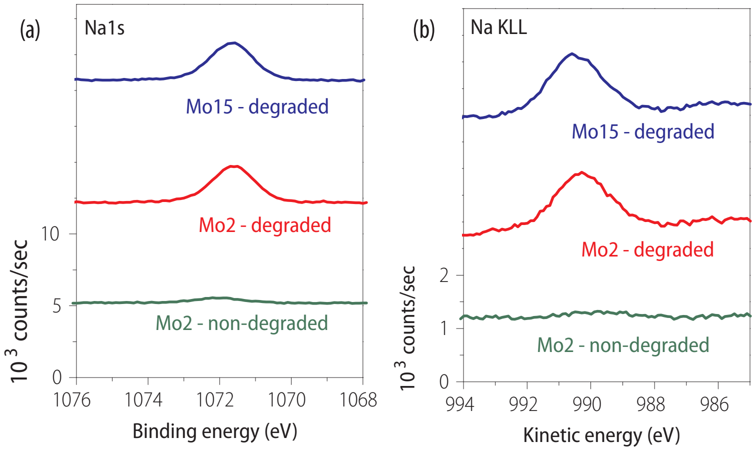

Figure 5.25

XPS spectra of both the sodium signals for the non-degraded Mo25/2 and Mo25/2 and Mo25/15 after 150 hours of exposure to 85°C/85% RH. (a) Na 1s signal (b) Na KLL signal.

Table 5.8 Overview of the binding energies and areas of the sodium signals as obtained for non-degraded Mo25/2, degraded Mo25/2 and degraded Mo25/15.

	Na 1s		Na KLL	α*
	E_b (eV)	area (cps)	E_k (eV)	
Mo25/2 non-degraded	1072.0	548	989.8	2061.8
Mo25/2 degraded	1071.6	3850	990.4	2062.0
Mo25/15 degraded	1071.7	4012	990.5	2062.1

In this case, the modified Auger parameter value α* is approximately 2061.9 eV, which is close to the range 2061.0-2061.6 eV which is defined to be an ‘oxide environment’, indicating the presence of for example Na_2O, Na_2SeO_3 or Na_2CO_3 [26].

Due to damp heat, the oxygen 1s signal (528-534 eV, not shown) had increased greatly, indicating the presence of oxides. It should be noted that the oxide component had a higher intensity for the degraded Mo25/15 than for Mo25/2, which confirmed the higher state of oxidation for Mo25/15 than for Mo25/2, as can be expected based on the information shown in chapter 5.3.1.

When the selenium signals were considered (Figure 5.26), it was concluded that the signal for the dense Mo25/2 is significantly higher than the for Mo25/15 signal. This indicated that the oxidation seems to be more effective for the porous Mo25/15 than for the dense Mo25/2. This difference can be explained by the morphology difference of the two layers.

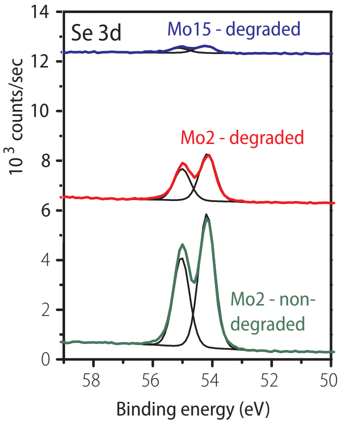

Figure 5.26

XPS spectra of selenium (Se 3d) signals for the non-degraded Mo25/2 and Mo25/2 and Mo25/15 after 150 hours of exposure to 85°C/85% RH.

More information about the oxidation process can be obtained in the Mo 3d-Se 3s XPS profiles (Figure 5.27 and Table 5.9). For the non-degraded dense Mo25/2, the obtained doublet can be resolved with a Mo $3d^{5/2}$ binding energy which is characteristic for $MoSe_2$ [27-29] and a 3.14 eV spin-orbit splitting. After degradation, the signal undergoes a marked evolution: these new spectra have been fitted with the Line Shape signals of

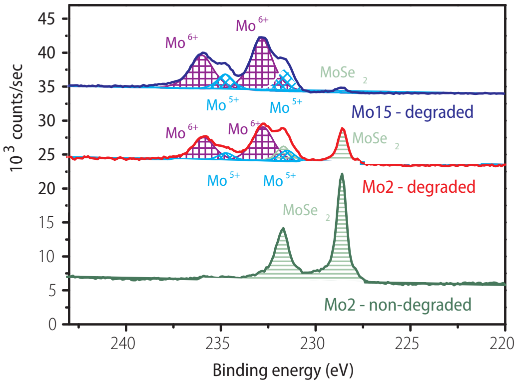

Figure 5.27

XPS spectra for the overlapping Mo 3d and Se 3s signals for the non-degraded Mo25/2 and Mo25/2 and Mo25/15 after 150 hours of exposure to 85°C/85% RH.

Table 5.9 Overview of the binding energies and areas of the Mo signals as obtained for non-degraded Mo25/2, degraded Mo25/2 and degraded Mo25/15. The error on the binding energy is 0.1 eV. r = $Mo^{5+}/(Mo^{5+}+Mo^{6+})$

	Mo 3d5/2 $MoSe_2$		Mo 3d5/2 Mo^{6+}		Mo 3d5/2 Mo^{5+}		r
	E_b (eV)	area (cps)	E_b(eV)	Area (cps)	E_b (eV)	area (cps)	
Mo25/2 non degraded	228.9						
Mo25/2 degraded	228.7	8116	232.8	6935	231.6	2338	0.25
Mo25/15 degraded	228.6	1121	232.9	10780	231.7	4081	0.27

$MoSe_2$ and two other doublets.

This can be fitted with three contributions, as can be seen in Table 5.9. The spectra of degraded samples also contain the Mo 3d-Se 3s signal corresponding to $MoSe_2$, while for the remaining signals, two additional doublets indicating two different Mo oxides are identified. According to literature values the highest binding energy contribution is attributed to Mo^{6+}, while the lowest can be attributed to Mo^{5+} [30].

In order to get a better understanding on the degradation process of the molybdenum back contact, the spectral region from -3 until 26 eV has also been analysed. In this region, the outer core levels (O 2s and Se 4s) and the valence band have been recorded (Figure 5.28a).

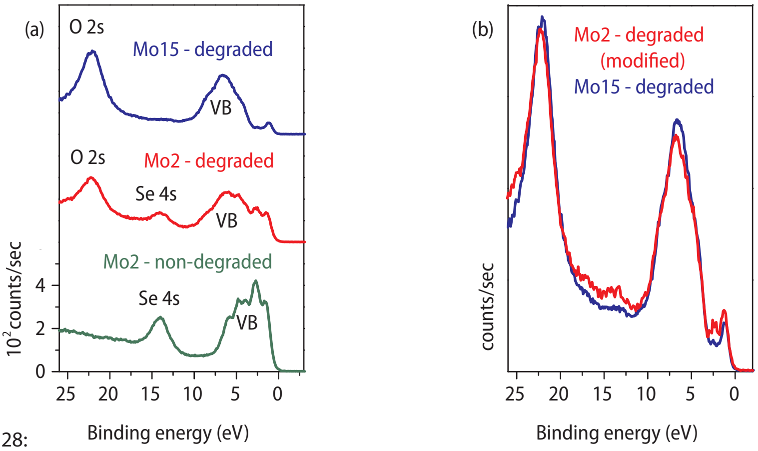

Figure 5.28:

(a) XPS spectra from -3 until 26 eV of the non degraded Mo25/2 and the degraded Mo25/2 and Mo25/15 after 150 hours exposure to 85°C/85% RH. These spectra depict the O 2s, Se 4s and the valence band spectra. (b) Depicts the modified and normalised spectra of degraded Mo25/2 compared with degraded Mo25/15.

In the non-degraded Mo25/2 spectrum, the Se 4s core level is clearly present, as well as an valence band signal (0-10 eV) which is similar to the signals previously recorded for $MoSe_2$ [13]. For the degraded porous Mo25/15, the information from the survey spectrum was confirmed: the Se 4s peak has vanished and the O 2s signal is raised, confirming the almost complete oxidation of the $MoSe_2$ layer. When the dense Mo25/2 is considered after degradation, the Se 4s signal is still detected, which indicates that part of the $MoSe_2$ layer has not been oxidised.

The identification of the valence band part for the degraded samples was more complicated. In order to separate the signal of $MoSe_2$ from the other present species, the $MoSe_2$ signals as obtained from the non-degraded sample were subtracted from these spectra by the following treatment:

1. The contribution of $MoSe_2$ has been determined through the Se 4s area relative to the pure $MoSe_2$ spectrum (non-degraded Mo25/2).
2. Subtraction of the $MoSe_2$ contribution from the full spectra.
3. Normalisation of the spectrum of Mo2 to get similar counts as Mo25/15

The new spectra of Mo25/2 and Mo25/15 are plotted together as shown in the Figure 5.28b. The resulting graphs are very similar for Mo25/2 and Mo25/15, which indicates the reaction products have the same chemical composition. The main part of the valence band between 3 and 10 eV binding energy is built from a mixture of O 2p states with Mo 4d. Since the photoelectric cross-section of the Mo 4d states at Al K_α energy is 16 times greater than that of O 2p states, the valence band spectrum obtained by XPS is largely representative of the Mo 4d admixture into the valence band. The signals between 3 and 10 eV can therefore be attributed to molybdenum and oxygen in molybdenum oxide.

However, it must be highlighted that a small peak is detected at 1 eV, which is near the Fermi level E_F. This indicates the presence of a conductive material. This latter structure cannot be related to MoO_3 or another molybdenum oxide due to their insulating nature. Reference [31] showed that the valence band spectrum of MoO_3 showed no intensity near the Fermi level. Furthermore, it cannot be $MoSe_2$, since the signal for this material has been subtracted. Therefore, it was concluded that another conductive species must also be present in these samples.

5.4 Discussion

5.4.1 Selenisation and pressure experiment

5.4.1.1 Molybdenum oxide formation

The degradation of molybdenum is visible after less than two hours of 85°C/85% RH exposure. After only two hours under these conditions, there were already large stains of molybdenum oxide on the non-selenised molybdenum samples. These areas became larger and thicker, until a thick cracked layer of molybdenum oxides was present on the surface. The cracking allowed further progression of the degradation due to the exposure of new metallic molybdenum located deeper in the bulk of the layer. Furthermore small needle-like structures were observed on the degraded material.

Raman spectroscopy showed MoO_3, MoO_2 and Mo_8O_{23} bonds were present on both selenised and non-selenised samples, while the signal of suboxide Mo_4O_{11} was predominantly observed on the selenised samples. The presence of MoO_x species was confirmed by XRD. Preliminary identification of the formed species by XRD and Raman measurements showed the presence of MoO_3, as well as the suboxides Mo_9O_{26} ($MoO_{2.89}$) $Mo_{17}O_{47}$ ($MoO_{2.78}$), Mo_8O_{23} ($MoO_{2.88}$) and Mo_4O_{11} ($MoO_{2.75}$). These are all MoO_3-like compounds with different amounts of oxygen vacancies.

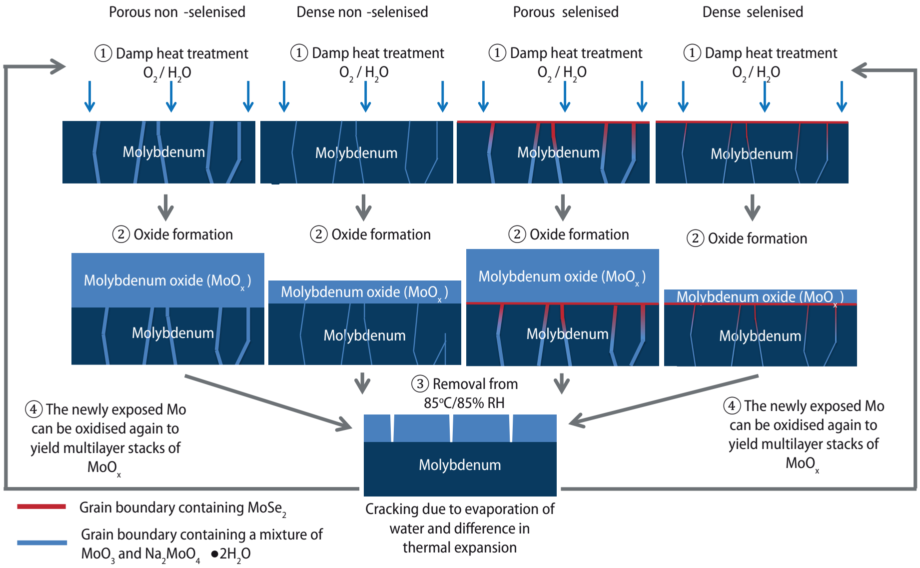

Figure 5.29

Proposed degradation route for different thin film molybdenum layers on soda lime glass. The differences between porous and dense as well as selenised and non-selenised molybdenum films is shown.

These results are in agreement with the results as observed in reference [7], which reported the formation of suboxides with O/Mo ratios between MoO_2 and MoO_3. In this study, XPS measurements have shown that the O/Mo ratio is 2.88±0.01, which is similar to the MoO_3-like compounds as observed here.

The cracked molybdenum oxide on the surface contained small amounts of nitrogen and carbon, indicating the presence of nitrates and carbonates. The small crystalline needle-like structures have a higher content of sodium and carbon than the underlying layer, which might indicate the formation of Na_2CO_3. However, it is not likely that these needle-like structures would also occur in complete CIGS solar cells.

5.4.1.2 Electrical effects

The degradation effects increased with the porosity of the molybdenum material: porous layers resulted in the formation of the thickest oxide layer due to damp heat exposure. This has an effect on the sheet resistance of the most porous molybdenum, which became non-conductive after approximately thirty hours, while the most dense layers still showed conductivity by four point probe after 105 hours exposure to 85°C/85% RH. It can thus be concluded that low sputter pressures lead to the formation of molybdenum layers that retain their conductivity for a longer time.

The presence of selenium did not have an influence of this abrupt loss of conductivity. However, the presence of selenium seemed to lead to a smaller increase in sheet resistance due to damp heat exposure: while selenised samples started with a higher sheet resistance, the increase in sheet resistance as a function of damp heat time is slower.

This is especially important for the conduction in P2 through which a thin column of molybdenum and ZnO:Al has to transport the current. The molybdenum back contact, which still consists of conductive molybdenum and transports the current in the lateral direction will suffer less from the formation of a non-conductive molybdenum oxide layer on top of a still conducting molybdenum layer.

5.4.1.3 Optical properties and visual inspection

The selenised and non-selenised samples showed large differences in degradation behaviour, especially when the visual and optical properties are considered. This indicates that degradation experiments on non-selenised molybdenum layers are not representative for the degradation of the molybdenum layer in CIGS modules. However, degradation experiments on non-selenised samples can show what is happening to stored non-processed molybdenum sheets as well as non-selenised side edges of a CIGS cell. The non-selenised samples already showed visual degradation and a decrease of the reflectance after two hours.

Within the selenised samples, there was also an impact of the sputter pressure on the reflectance. Mo2Se retained only spot-like degradation and was still quite reflective after 105 hours of degradation, while on Mo10Se and Mo15Se the spots grew into a mosaic-like structure on the surface, which led to a decrease in reflectivity. Mo2Se was the only sample that retained a reflectance over 10%. Therefore, considering the optical properties, dense selenised molybdenum layers are also the most suitable for incorporation in CIGS solar cells.

5.4.1.4 Degradation route

Figure 5.29 shows a possible degradation route for molybdenum thin film layers. Due to damp heat exposure of molybdenum (step 1), an oxide layer is formed on top of the molybdenum sample. The same effect might occur in the grain boundaries (step 2).
It was observed in cross-section SEM that porous layers had thicker top layers than dense samples, which indicates that these layers degrade the fastest. This can be attributed to the faster diffusion of water and other molecules like O_2 and CO_2 in molybdenum with a higher volume of intergranular material, since the mobility of for example sodium is faster in MoO_x than through the metallic molybdenum [32]. The formation rate of the molybdenum oxide will depend on the deposition parameters.
It is proposed that the stable character of the dense selenised sample can be explained by the presence of $MoSe_2$ on the surface and in the grain boundaries, which protects the metallic molybdenum from oxidation.

When the samples are removed from the climate chamber and their temperature as well as the humidity is quickly decreased, or just in the climate chamber itself, the oxide layers can crack (step 3). The cracking of the molybdenum oxide layer is proposed to be due to the difference in thermal expansion coefficients between the glass (α_{slg}: $8.6 \cdot 10^{-6}$ K^{-1}) [33], the molybdenum (α_{Mo}: $4.8 \cdot 10^{-6}$ K^{-1}) [33] and the molybdenum oxide (α_{MoO3}: $18\text{-}90 \cdot 10^{-6}$ K^{-1}) [34], which becomes important after a temperature change from 85°C to room temperature. Furthermore, evapouration of water diffused in the molybdenum layers could also lead to breaking of the molybdenum oxide top layer. The cracking of the top oxide layer then allows the exposure of fresh metallic molybdenum to the atmosphere, so the degradation process can start over, leading to a multilayer stack consisting of $Mo/MoO_x/MoO_x$ (step 4). The needles on top of these layers, which may consist of Na_2CO_3 might have resulted from the migration of sodium from the glass through the molybdenum surface, where it then reacted with oxygen and carbon from the air.

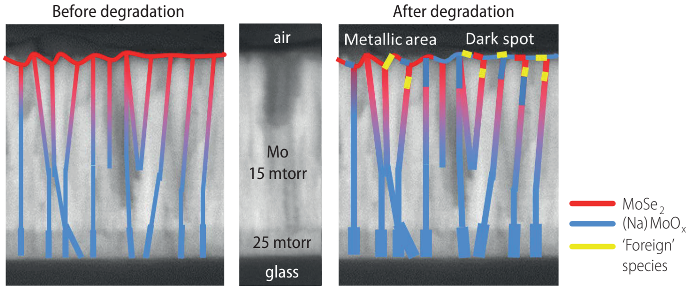

Figure 5.30

Schematic representation of the molybdenum film before and after degradation, drawn on the cross-section SEM photo of Mo25/15. The lines represent the composition of the grain boundaries: The blue lines represent (Na)MoO$_x$*, while the red lines represent MoSe*$_2$*. The yellow spots indicate the presence of foreign species, like carbon, nitrogen, chlorine and sulfur. It should be noted that the only the global position of the colours should be considered, since all materials will be present in some concentration at all indicated positions.*

5.4.2 Lift-off experiment

It has been observed that bilayer molybdenum thin films, which contain small concentrations of MoSe$_2$ as obtained by lifting off of a CIGSe layer, degrade when exposed to damp heat. This exposure led to a complete loss of conductivity after 150 hours, while the reflectivity also decreased. It was observed that the degradation behaviour for both the electrical and optical parameters was less severe for the molybdenum thin film deposited at lower sputter pressure, as was also observed in the 'selenisation and pressure' experiment. However, the degradation process occurred slower for these bilayer Mo samples obtained by the lift-off process than for the standard selenised monolayer molybdenum.

In order to learn more about the degradation process and its products, the samples have been studied with SEM-EDX, XPS and SIMS. Cross-section SEM did not show the formation of a thick MoO$_x$ layer on top of the metallic molybdenum, as reported for the 'selenisation and pressure' experiment but it clearly showed the bilayer structure. SIMS indicated the presence of a bottom layer with a high concentration of molybdenum oxide and 'foreign' species, like carbon, nitrogen and chlorine. The local degradation of this bottom layer is probably due to the porous nature of that molybdenum before damp heat exposure, since it was deposited at a high sputter pressure. This also led to a less degraded top layer: the degrading species diffused towards the bottom layer and did not impact the top layer. It is proposed that the decrease of reflectivity and conductivity is therefore a relatively slow process for the lift-off samples: the oxidation of the bottom layer has less impact on the physical parameters than changes at the Mo/CIGS interface.

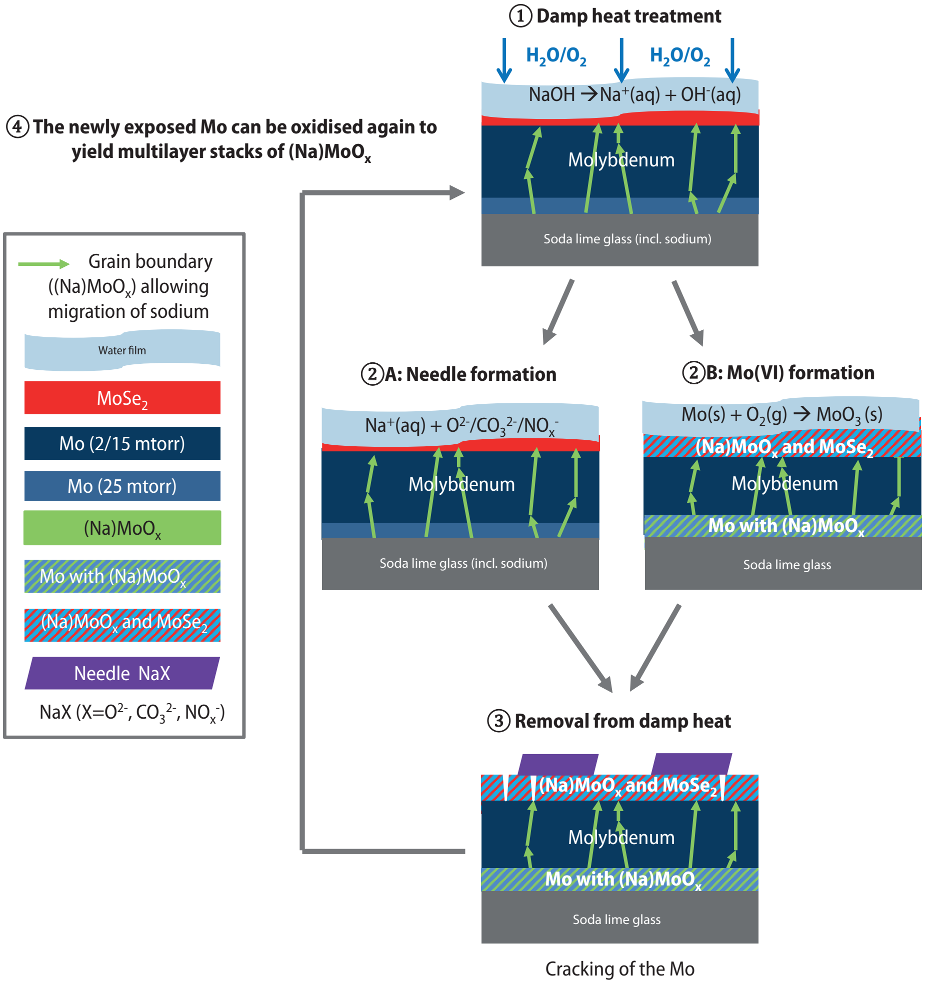

Figure 5.31

Simplified schematic representation of the degradation of a thin bilayer molybdenum film obtained by the lift-off process on soda lime glass

The top layer was divided into multiple regions: the darker ‘spots’, of which the surface was rich in MoO_x and ‘foreign’ species, like hydrogen, carbon, cyanide, sulfur, chloride and oxygen, and poor in $MoSe_2$, while the lighter regions contained more $MoSe_2$. Deeper in the film, foreign species as well as $MoSe_2$ and MoO_x are still present, but in decreasing quantities. Positive species, like sodium, can also be present, but are not detected with SIMS in a negative mode. In order to schematically represent these reactions, Figure 5.30 shows the molybdenum films before and after degradation. This representation is based on SIMS measurements and on references [8,16].

5.4.2.1 Oxide and needle formation

In the presence of H_2O and O_2, a MoO_x layer containing sodium is formed on top of metallic molybdenum. Similar material is probably present on the surface of the grain boundaries, as is described in reference. A schematic representation of the first stages of the degradation is shown in Figure 5.31, while more information about the exact nature of the $(Na)MoO_x$ layer is described in chapter 5.4.2. It should be noted that the information given in Figure 5.30 is not included in this figure in order to improve readability.

It is proposed that the degradation of metallic molybdenum follows these steps:

1. Due to exposure to damp heat, a thin water film is formed on the surface of metallic molybdenum. The Na_2O present in the glass can migrate via the grain boundaries and dissolve in this water film. Furthermore O_2 from the environment is also present.
2. A: The corrosion of metallic molybdenum occurs due to the formation of an oxide film by the reaction between oxygen and molybdenum on the interface between the molybdenum film and surrounding water or air. The exact nature of the formed product depends on the pH and possible potential (not relevant here) of the water film, but in this case, probably MoO_3 is formed via redox reactions as for example defined in reference [35]:

   B: The reaction of Na with various atmospheric species can result in the formation of needles. These needles are likely formed as a drying effect when the samples are removed from the climate chamber and have various geometrical shapes.

Sodium can be built into the MoO_3, as is explained in chapter 5.4.2

3. Cracks occur in the $(Na)MoO_x$, probably due to a different in the Coefficient of Thermal Expansion (CTE) of molybdenum and its oxides [33,34] which leads to vulnerability when samples are removed from the 85°C environment and very quickly cooled to room temperature. The difference in density of the two materials can also play a role in this cracking.
4. Due to cracking or other damage to the $(Na)MoO_x$, the degradation process can start again on new freshly exposed metallic molybdenum.

5.4.2.2 The formation of molybdenum bronze by Na^+ intercalation

It is mentioned above that sodium plays a role in the degradation of metallic molybdenum films via the formation of $(Na)MoO_x$. It is proposed that this occurs via the inclusion of Na^+ in the MoO_3 matrix. This is possible due to the structure of MoO_3, which has a MoO_6 octahedron with molybdenum atom at the center surrounded by six oxygen atoms as its basic element. The MoO_3 is formed by bilayers consisting of two interleaved sheets of MoO_6 piled up along the b direction and held together by weak Van der Waals forces. Ions can be inserted into and extracted from this van der Waals gap by redox reactions with the host MoO_3 matrix:

$$MoO_3 + xA^+ + xe^- \rightarrow A_xMoO_3 \qquad (5.2)$$

With A=H, Li, K, Na, …

This reversible inclusion of a molecule or ion into a compound is called 'intercalation' [35].

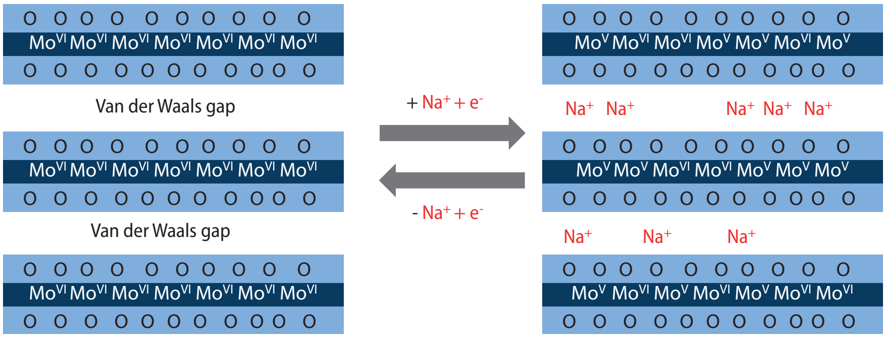

Figure 5.32

Simplified schematic representation of intercalation of Na^+ *into a* MoO_3 *material. The process involves the reduction from* Mo^{6+} *to* Mo^{5+} *[36]. All depicted oxygen atoms have a charge of -2, which is not shown.*

This intercalation process of Na^+ into MoO_3 can lead to the formation of $Na_{0.9}Mo_6O_{17}$, which is often referred as ´purple bronze´, while ´red´ and ´blue´ bronzes with different alkali concentrations also exist [37]. It should be noticed that intercalation of K^+ and Li^+ in the MoO_3 layered structure also leads to the formation of bronzes. We have only found Na in the analyses, so Na^+ is certainly the dominant ion here, but it is possible that a small quantity of K^+ is also present. The physical properties of Na(K) MoO_x purple bronzes as well as the blue bronzes $A_{0.3}MoO_3$ with A= K, Rb, Tl and Cs have been extensively studied because of their charge density wave phenomenon at low temperatures arising from their low-dimensional metallic character [38,39]. As this specific transition is related to the electron properties at room temperature, several studies of the electronic properties of these materials through photoemission measurements of the band structure have been performed [40].

For several molybdenum bronzes, including $K_{0.3}Mo_6O_{17}$ [31], $K_{0.9}Mo_6O_{17}$ [40] and KMo_6O_{17} [41], a small peak near the Fermi level has been detected. This peak has been assigned to the conduction band, more specifically to inserted electrons occupying the otherwise empty Mo 4d and 5s orbitals.

The presence of a non-zero density of states at E_F is a direct evidence of the metallic character of these compounds. Similar structure at E_F to those previously observed for $KMoO_x$ compounds are clearly detected for degraded Mo25/2 and Mo25/15 (Figure 5.28a and b). These occupied states indicate a metallic behaviour which is typical for the purple bronze materials. It can be noticed that a comparable structure has been observed for titanium oxide [42]. The wide depleted region lying between the conduction and valence bands is also typical for these transition metal oxides and has already been detected in other molybdenum and tungsten bronzes [43]. According to references [41,43], the largest structure extending below 4 eV corresponds to the valence band which is largely representative of the Mo 4d states.
Nevertheless, a valence band signal corresponding to the insulator MoO_3 oxide could overlap the $NaMoO_x$ one. In order to determine the fraction of Na^+ intercalated MoO_3, one can consider the Mo 3d spectra (Figure 5.27). Swiatowska et al. [44] have observed that the intercalation of lithium in MoO_3 leads to a partial reduction of Mo^{6+} to Mo^{5+}. Based on Mo 3d-Se 3s signals (Table 5.9 and Figure 5.27), where a Mo^{5+} signal is clearly detected for both types of degraded molybdenum, it is assumed that a comparable intercalation process takes place, confirming the observation of a conduction band for the degraded molybdenum (Figure 5.27). The average valence state of molybdenum for $Na_{0.9}Mo_6O_{17}$ is closed to 5.5 meaning a $r=Mo^{5+}/(Mo^{5+}+Mo^{6+})$ ratio close to 0.5. Our calculated $Mo^{5+}/(Mo^{5+}+Mo^{6+})$ ratio is ~ 0.25. This r-value would indicate that the samples do not have the standard structure, but contain less Na^+. This would imply that the formation of a material with the composition $NaMo_4O_{23}$ occurred. However, another more likely explanation is that only a part of MoO_3 is intercalated. Therefore, we propose that the degradation product is MoO_3 with and without intercalated Na^+. As the r values are similar for both molybdenum degraded samples (Mo25/2 and Mo25/15), the formed intercalated molybdenum oxides have the same average composition. is present in both samples.

It should be noted that conductivity measurements showed the disappearance of conductivity after 150 hours at 85°C/85% RH. This can be explained by either a low Na^+ content in the complete or part of the molybdenum oxide layer: since XPS is very sensitive for the material on the top nanometers and does not measure the bulk material, the bulk might contain higher quantities of MoO_3 which is not or only slightly intercalated. Finally it should be also highlighted that the bronze electrical properties show a large two-dimensional anisotropy. This leads to a difference in the electrical conductivity along different axes: For $K_{0.9}Mo_6O_{17}$, the resistivity is a 1000 times higher along the b axis than along the layers [45]. The non-conductive behaviour could also, partly, related to the orientation of the Na^+ intercalated MoO_3 layer.

5.4.2.3 Influence of molybdenum density

The optical and electrical measurements showed that Mo25/15 degraded faster than Mo25/2. It was also observed that the black and blue spots, associated with the oxidation of the molybdenum, occurred faster for Mo25/15. Therefore, it can be assumed Mo25/2 is more stable, as can be expected based on the 'selenisation and pressure' experiment.

XPS measurements also confirmed the presence of higher concentrations of oxides for Mo25/15, therefore indicating the formation of a higher amount of molybdenum oxide. The faster decrease for the selenium content also confirms this. However, it was observed that the sodium concentration was the same for both samples. Therefore, it is assumed that sodium migrates through the samples during the damp heat exposure, independently of the oxidation of the molybdenum. Likely the sodium is thus also present in the non-degraded $MoSe_2$ regions.

5.4.3 Influence of molybdenum degradation on CIGS solar cell performance

It can be concluded that the slowest degradation with respect to reflectance, conductivity and volume expansion can be obtained for molybdenum samples with a low argon sputter pressure and a selenised surface. The former can be explained by the dense structure with a small volume of intergrain material, which would allow migration of the degrading species, like O_2 and H_2O as well as sodium. The influence of selenisation might be explained by the presence of $MoSe_2$ in the intergrain space, preventing either the diffusion of degrading species or preventing the oxidation of the molybdenum.

Most molybdenum back contacts are obtained by the deposition of a bilayer of molybdenum, of which the bottom layer is sputtered under high argon pressure, while the top layer is deposited under low argon pressure. This is positive for the stability of the molybdenum layer in CIGS solar cells, since the water and oxygen migrate into the bottom layer, therefore degrading the top layer less and maintaining a high conductivity for the layer. Therefore, the conditions used for the deposition of the 'standard' molybdenum layers in CIGS solar cells are similar to the deposition conditions of the slowly degrading sample in these studies.

The vulnerability of molybdenum to damp heat can be a problem in CIGS PV technology. On one hand, degradation of the back contact itself is probably not a big risk, since this will probably not lead to the complete loss of the lateral conductivity of molybdenum. The most likely degradation point is the molybdenum-zinc oxide interface in P2 by the formation of an oxide layer between the molybdenum and zinc oxide [6]. This would break down the monolithic connection, which would have a destructive effect on CIGS modules. Another risk can be found in the volume expansion, which can lead to delamination between the CIGS and the molybdenum layers or the disappearance of the ohmic contact.

It is therefore recommended to use bilayer (or multilayer) molybdenum film with a dense top layer, which can prevent the formation of a top later of molybdenum oxide.

A last remark concerns the storage of molybdenum films. In research environments, molybdenum is often deposited and then stored, instead of direct further processing. Exposure to humid air for several days can already lead to molybdenum oxide formation, which can be detrimental for quality of the later processed solar cells. It should be noted that the storage of molybdenum layers can also influence the electrical parameters of a solar cell in a positive way, but since the impact is not known, this can reduce experimental reproducibility and disturb the interpretation of the obtained results.

5.5 Conclusions

All molybdenum layers already showed degradation effects which were visible by naked eye after only several hours of damp heat exposure. The exposure resulted in large volume expansion due to the formation of a thick non-conductive molybdenum oxide layer consisting of various oxides and suboxides on top of the metallic molybdenum. This MoO_x layer showed cracks and the appearance of needle-like structures, maybe existing of Na_2CO_3.

The degradation effect was most severe for layers with the highest sputter pressure and thus the most porous microstructure. It was less severe for bilayer molybdenum films, which largely oxidised in the more porous bottom layer. The effect of selenisation was observed in the visual and optical characteristics: dense selenised molybdenum layers retained the highest reflectance. Likely, the presence of $MoSe_2$ prevented rapid oxidation of the molybdenum. These results show that a dense selenised molybdenum is the most stable type.

The surface oxidation of molybdenum was further studied by XPS measurements, which showed that the MoO_x material is mostly MoO_3 with intercalated Na^+, leading to the formation of Na_xMoO_3 ‘molybdenum bronze’ following this redox reaction:

$xNa^+ + MoO_3 + xe^- \rightarrow Na_xMoO_3$

Intercalation of Na^+ can explain both the high mobility of sodium in the grain boundaries and the important role this element play in the degradation process. It is thus proposed that both the grain boundaries as well as the degraded Mo contains MoO_3 which is intercalated with Na^+. Finally the intercalation of Na^+ in MoO_3 is a key point in the understanding of the evolution of cell performance under damp heat exposure in presence of Na. While the MoO_3 is an insulator, Na_xMoO_3 molybdenum bronze exhibits occupied states near the Fermi level, making this material conductive. Therefore, intercalation of Na^+ in the MoO_3 can greatly influence the band alignment in CIGS cells, while the formation of non-conductive MoO_3 can completely destroy the solar cell.

5.6 Acknowledgements

We would like to thank Harmen Rooms, Emile van Veldhoven and Arthur Eijk (TNO), Bertil Okkerse (Philips Innovation Services), Klaas Bakker (ECN) for their assistance with deposition, measurements or analysis or the fruitful discussions.

5.7 References

[1] T. Wada, N. Kohara, S. Nishiwaki, T. Negami, Thin Solid Films 387 (1-2) (2001) 118-122.

[2] D. Fisher, I. Repins, J. Schaefer, M. Beck, W. Batchelor, M. Young, S. Asher, Proc. 31st IEEE PVSC (2005) 371-374

[3] P. Bommersbach, L. Arzel, M. Tomassini, E. Gautron, C. Leyder, M. Urien, D. Dupuy, N. Barreau, Progress in Photovoltaics: Research and Applications 21 (2013) 332-343

[4] P. Salomé, V. Fjallstrom, A. Hultqvist, P. Szaniawski, U. Zimmermann, M. Edoff, Progress in Photovoltaics: Research and Applications 22(1) (2014) 83-89

[5] M. Powalla, B. Dimmler, Thin Solid Films 387 (2001) 251-256

[6] J. Wennerberg, J. Kessler, L. Stolt, Proc. 16th EU-PVSC (2000) 309-312

[7] M. Theelen, M. Tomassini, N. Barreau, H. Steijvers, A. Branca, S. Harel S, Z. Vroon, M. Zeman, Proc. 38th IEEE PVSC 2 (2012) 1-6

[8] M. Theelen, K. Polman, M. Tomassini, N. Barreau, H. Steijvers, J. van Berkum, Z. Vroon, M. Zeman, Surface & Coatings Technology 252 (2014) 157–167

[9] M. Theelen, S. Harel, M. Verschuren, M. Tomassini, A. Hovestad, N. Barreau, J. van Berkum, Z. Vroon, M.Zeman, submitted toSurface and Coatings Technology

[10] J. Scofield, A. Duda, D. Albin, B. Ballard, P. Predecki, Thin Solid Films 260 (1995) 26-31

[11] F. Couzinie-Devy, N. Barreau, J. Kessler, Progress in Photovoltaics: Research and Applications 19 (2011) 527–536

[12] S. Harel, M. Tomassini, L. Arzel, E. Gautron, N. Barreau, Proc. 40th IEEE PVSC (2014) 425-430

[13] International Electrotechnical Commission IEC 61646 ed. 2, International Standard, Geneva, Switzerland, 2008

[14] P. Salomé, J. Malaquias, P. Fernandes, A. da Cunha, J. Phys. D: Appl. Phys. 43 (2010) 1-7

[15] E. Gautron, M. Tomassini, L. Arzel, N. Barreau, Surface & Coatings Technology 211 (2012) 29–32

[16] J. Sandino, E. Romero, J. Oyola, G. Gordillo, H.Lichte, Solar Energy Materials and Solar Cells 95 (2011) 2006–2009

[17] T. Polcar and M. Evaristo, Surface & Coatings Technology 202 (2008) 2418-2422

[18] M. Camacho-López, L. Escobar-Alarcón, Optical Materials, 33 (2011) 480-484.

[19] L. Seguin, M. Figlarz, Spectrochimica Acta part A 51 (1994) 1323-1344

[20] M. Dieterle, G. Mestl, J. Jäger, Y. Uchida, H. Hibst, R. Schlögl, Journal of Molecular Catalysis A: Chemical 174 (2001) 169–185

[21] A. Bollero, L. Kaupmees, Thin Solid Films 520 (2012) 4163-4168

[22] R. Sharma, G. Reddy, AIP ADVANCES 3, 092112 (2013)

[23] A. Chowdhury, D. Cameron, M. Hashmi, Thin Solid Films 332 (1998) 62-68

[24] M. Veres, M. Füle, S. Tóth, M. Koós, I. Pócsik, Diamond and Related Materials 13 (2004) 1412–1415

[25] ICDD JCPDS cards 00-042-1120 (cubic molybdenum), 00-029-0914 (hexagonal $MoSe_2$), 00-032-0671 (monoclinic MoO_2) 00-005-0508 (orthorhombic MoO_3), 00-047-1081 (monoclinic MoO_3), 00-047-1320 (monoclinic MoO_3), 00-012-0753 (anorthic Mo_9O_{26}) and 00-013-0345 (orthorhombic $Mo_{17}O_{47}$)

[26] X. Song, R. Caballero, R. Felix, D. Gerlach, C. Kaufmann, H.-W. Schock, R.Wilks, M. Bär, Journal of applied physics 111 (2012) 034903

[27] J. Assmann, J. Bernede, J. Drici, C. Amory, E. Halgand, M. Morsli, Surf Sci. 246 (2005) 159-166.

[28] C. Wagner, W. Riggs, L. Davis, J. Moulder, Handbook of X-ray photoelectron spectroscopy, Eden Prairie: Perkin-Elmer (1979)

[29] M. Bär, L. Weinhardt, C. Heske, S. Nishiwaki, W. Shafarman, Physical Review B - Condensed Matter and Materials Physics, 78 (7) (2008) 075404

[30] D. Schmid, M. Ruckh, H.W. Schock, Solar Energy Materials and Solar Cells 41/42 (1996) 281-294

[31] M. Sing, R. Neudert, H. von Lips, M. Golden, M. Knupfer, J. Fink, R. Claessen, J. Mücke, H. Schmitt, S. Hüfner B. Lommel, W. Aßmus, C. Jung, C. Hellwig, Physical review B, 60 (12) (1999) 8559-8568

[32] M. Bodegard, K. Granath, L. Stolt, A. Rockett, Solar Energy Materials and Solar Cells 58 (1999) 199-208

[33] D. Brémaud, Investigation and development of CIGS solar cells on flexible substrates and with alternative electrical back contacts, Thesis Zürich, 2009

[34] Collaboration: Authors and editors of the volumes III/17G-41D: O. Madelung, U. Rössler, M. Schulz, ´MoO_3: thermal expansion, density´ Springer Materials - The Landolt-Börnstein Database (http://www.springermaterials.com).

[35] V. Saji, C. Lee, Chem Sus Chem 5(7) (2012) 1146-1161

[36] D. Thomas, E. McCarron, Materials Research Bulletin 21 (8) (1986) 945–960

[37] K. Eda, K. Chin, N. Sotani, M. Stanley Whittingham, Journal of Solid State Chemistry 178 (2005) 158–165

[38] X. Xu, A. Bangura, C. Niu, M. Greenblatt, S. Yue, C. Panagopoulos, N. Hussey, Physical Review B - Condensed Matter and Materials Physics 85 (2012) 195101

[39] K. Smith, Solid State Sciences. 4 (3) (2002) 359-378

[40] H. Guyot, H. Balaska, P. Perrier, J. Marcus, Surf Sci. 600 (18) (2006) 3860-3864.

[41] X. Qin, J. Wei, J. Shi, M. Tian, H. Chen H, D. Tian, Modern Physics Letters B. 10 (14) (1996) 653-660.

[42] T. Cottineau, A. Rouet, V. Fernandez, L. Brohan, M. Richard-Plouet, Journal of Materials Chemistry A, 2 (29) (2014) 11499-11508.

[43] H. Guyot, N. Motta, J. Marcus, S. Drouard, B. Balaska, Surf Sci. 482-485 (2001) 759-763.

[44] J. Swiatowska-Mrowiecka, S. De Diesbach, V. Maurice, S. Zanna, L. Klein, E. Briand, I. Vickridge, P. Marcus, Journal of Physical Chemistry C 112 (29) (2008) 11050-11058

[45] H. Vincent, M. Ghedira, J. Marcus, J. Mercier, C. Schlenker, Journal of Solid State Chemistry. 47 (1) (1983) 113-121


TeAmWORK
H
O
H
O
C
O
ZnO:Al
ZnO:Al

CHAPTER 6

Degradation mechanisms of the aluminium doped zinc oxide front contact

This chapter is based on the following publications:

M. Theelen, T. Boumans, F. Stegeman, F. Colberts, A. Illiberi, J. van Berkum,
N. Barreau, Z. Vroon and M. Zeman,
Physical and chemical degradation behaviour of sputtered
aluminum doped zinc oxide layers, for Cu(In,Ga)Se_2 solar cells,
Thin Solid Films 550 (2014) 530–540

M. Theelen, S. Dasgupta, Z. Vroon, B. Kniknie, N. Barreau, J. van Berkum and M. Zeman,
Influence of atmospheric species water, oxygen, nitrogen and carbon dioxide
on the degradation of aluminum doped zinc oxide layers,
Thin Solid Films 565 (2014) 149–154

M. Theelen, Z. Vroon, N. Barreau and M. Zeman,
Degradation studies of aluminum doped zinc oxide,
Photovoltaics International (2014) Edition 23

M. Theelen, C. Foster, S. Dasgupta, Z. Vroon, N. Barreau and M. Zeman,
The influence of atmospheric species on the degradation of
aluminum doped zinc oxide and Cu(In,Ga)Se_2 solar cells,
Proc. SPIE (2014) 91790K

Abstract

Sputtered thin ZnO:Al films on borosilicate glass were exposed to 85°C/85% RH and to various combinations of atmospheric gases, which led to changes in the optical and especially electrical properties of the films. For the damp heat exposed samples, it was observed that the bulk structure did not change, which was confirmed by the stable carrier concentration. However, the Hall mobility and thus the overall resistivity decreased, which implied the increase of the height of the potential barriers, which are likely located at the grain boundaries. Furthermore, white spots appeared, containing elements that might have migrated from the glass, like silicon and calcium, which did react with elements from the environment, including oxygen, carbon and chloride.

Treatment with atmospheric species helped the identification of the species most detrimental to ZnO:Al. It was shown that the driving force behind ZnO:Al degradation is the combined presence of H_2O *and* CO_2*. Individually, gaseous* CO_2 *did not impact the degradation at all during the tested period, while the individual impact of* H_2O *is minor: the latter leads to slow diffusion of water down the grain boundaries, where it reacts, possibly resulting in the formation of* $Zn(OH)_2$*, which led to a decrease in mobility. However, in the presence of* CO_2*, the electrical and optical properties changed very quickly. Depth profiling showed that the concentration of hydroxide increased with factors as high as 20 in the bulk due to* H_2O *and* CO_2 *exposure, while carbon, hydrogen, chlorine and sulphur were also observed. Exposure to* H_2O *and* CO_2 *also led to local dissolution of the ZnO:Al at the ZnO:Al/glass interface. Additionally, it was observed that the influence of oxygen and nitrogen on ZnO:Al stability was very small.*

Together, these experiments showed that exposure of ZnO:Al the atmospheric conditions mostly led to a decrease in mobility, likely caused by an increased potential barrier at the grain boundaries. This effect on the mobility is limited when only H_2O/OH*-diffuses down, which can lead to the formation of* $Zn(OH)_2$ *or adsorption of* OH^-*. In the presence of* CO_2*, the effect on the mobility is larger, probably due to the formation of a* $Zn_x(OH)_y(CO_2)_z$ *compound, like* $Zn_5(OH)_6(CO_3)_2$ *in the grain boundaries. Furthermore, chlorine and sulphide were found in the top layer of the degraded samples, so equivalent molecules containing these elements might also have formed.*

6.1 Introduction

Zinc oxide (ZnO) has been investigated extensively because of the increasing number of possible industrial applications. Being a wide band gap semiconductor, zinc oxide is emerging as a prospective material for gas sensors, transparent electronics and thin film solar cells. For chalcopyrite based thin film solar cells, like $Cu(In,Ga)Se_2$, aluminium doped ZnO (ZnO:Al) is used as a front contact, since it is a non-toxic, inexpensive and abundant material. Furthermore, ZnO:Al is very attractive for CIGS solar cells, since sputtering allows room temperature deposition, which prevents exposure of the underlying layers to elevated temperatures.

In the Photovoltaic (PV) market, producers give out warrantees that panels will still yield 80% of the starting power after 25 years. Therefore, CIGS modules should be reliable for at least this time, but it was observed in field testing that CIGS modules often degrades too fast. It was observed that zinc oxide is one of the key parameters in the panels' degradation, indicating that ZnO:Al is not stable for 25 years in the field. From accelerated lifetime testing [1] it has been shown that the water ingress leads to an increase in lateral sheet resistance of the ZnO:Al, hereby increasing the series resistance in the solar cell. This will decrease the fill factor and consequently the efficiency.

Proper encapsulation can protect the solar cells against water ingression. For rigid modules, glass is an excellent encapsulation material, while for flexible modules often expensive inorganic/organic multistack materials are chosen. A CIGS solar cell with a more stable ZnO:Al front contact can contribute to lower energy costs and accelerate the introduction of flexible CIGS modules to the market. Therefore, it is necessary to understand and improve the degradation behaviour of ZnO:Al under water ingression. Several studies [2-6] have already tried to simulate the field exposure, by placing the samples under 'damp heat' conditions, as defined according to the International Electrotechnical Commission (IEC) module testing procedure 61646. These studies [2,3] have led to an increased insight in the changes in optical and electrical properties due to degradation. Relations between these properties and the surface roughness of the substrate [2], deposition temperatures [4], crystallinity [4] and aluminium content [3] have been described in literature.

However, the environmental factors leading to ZnO:Al degradation are mostly still unknown. This can be a problem, since it is expected that other atmospheric species like O_2 or CO_2 might also play a role in the degradation, but this has not been studied thoroughly for solar applications. The exact nature of the environmental molecules that are playing a role in the relevant degradation processes in ZnO:Al are proposed in literature, but have not been studied thoroughly. A suggestion for the main degrading species include oxygen and water molecules [7] and water and CO_2 [8].

Knowledge about the species playing a role in ZnO:Al degradation is very important, because it can be used to optimise the product design and the accelerated tests for ZnO:Al containing products. This can for example be useful in the design of encapsulation materials in which the water and oxygen barrier properties (water vapour transmission rate and oxygen transmission rate respectively) are optimised, while the penetration of other atmospheric species is not defined at all.

Furthermore, information in the literature about the chemical mechanisms leading to the change in optical and electrical properties during degradation is limited. It is suggested that the presence of oxygen and water promotes zinc oxide degradation [7], while Greiner, Feist and Pern [2,9,10] suggest that the formation of $Al(OH)_3$ [2,10] and $Zn(OH)_2$ [2,9,10] plays a role in the degradation, since these materials are non-conductive. The presence of a hydroxide in degraded ZnO:Al was also shown in reference [10]. An overview about the literature on this topic can be found in chapter 2.3.4.1.

In general, literature (see chapter 2.3.4.1) gives an excellent picture on the electrical and optical aspects, but the chemical behaviour is underexposed and does not yield an unambiguous picture for the influence of layer composition on the film properties. Therefore, we aimed to identify the chemical and physical failure mechanisms.

In this study, ZnO:Al samples were therefore exposed to a damp heat test as well as to a test to learn more about the impact of atmospheric species (including H_2O, CO_2, N_2 and O_2). The electrical, optical and compositional characteristics were analyzed before, during and after exposure. This information is used to determine the impact of various degradation conditions on ZnO:Al and to identify the relationship between the chemical and physical degradation phenomena for this material. This information is used to propose the possible chemical and physical failure mechanisms. The impact of these mechanisms on CIGS solar cell performance are discussed.

6.2 Experimental

6.2.1 Sample preparation

6.2.1.1 Damp heat treatment

ZnO:Al films were deposited by radio frequency (RF) magnetron sputtering using a Lesker sputtering tool. The films were sputtered on 0.7 mm thick Eagle 2000 Corning glass substrate from a circular (7´) high purity ZnO ceramic target with 2% Al_2O_3 from the company Processmaterials. The target to substrate distance was fixed to 110 mm and the flow of pure Ar gas was set to 15 standard cubic cm^2 per minute (sccm). The chamber pressure was 0.26 Pa, while the RF power was 400 W, which corresponds to a power density of 1.61 W/cm^2. The deposition time was 50 minutes for both samples. The samples varied in deposition temperature: one sample was not intentionally heated as is mostly observed for CIGS cells (labeled 'RT', this sample heated slightly due to the sputtering process, the highest reached temperature was 49°C) while another samples were heated to 200°C (labeled sample '200°C'), hereby reaching the maximal temperature acceptable for deposition on top of a CIGS/CdS stack (see chapter 2.3.4). These samples allowed us to look at a broad possible deposition spectrum, so the optimal conditions can be selected for further CIGS production.

6.2.1.2 Atmospheric species treatment

ZnO:Al layers were deposited by radio frequency (RF) magnetron sputtering using a MRC 643 vertical batch sputtering tool. The layers were sputtered on a 10x10 cm^2 0.7 mm thick Eagle 2000 Corning glass substrate from a rectangular 5"x17" high purity ZnO ceramic target with 2% Al_2O_3. The flow of pure Ar gas was set to 15 sccm. The chamber pressure was 0.42 Pa, while the RF power was 800 W, which corresponds to a power density of 1.46 W/cm^2. The deposition time was 35 minutes and was executed in 14 passes. The deposition was executed at room temperature.

6.2.2 Sample degradation

6.2.2.1 Damp heat treatment

The samples were submitted to a damp heat test, according to certification standard IEC 61646, which describes 1000 hours exposure to damp heat (85°C and 85% RH). The damp heat test was performed in a temperature and humidity controlled chamber (Espec Humidity Cabinet LHU-212). The samples were kept up to 2876 hours at 85°C/85% RH. Of both types, four individual samples have been degraded and analyzed. The reported results are representative for the results of various other similar experiments. The samples were characterised by different analysis techniques before, during and after the degradation test (see section 6.2.3). Unless mentioned otherwise, the measurements on degraded samples in this article are taken after the damp heat treatment. When the samples were not in the climate chamber or measured, they were stored in an inert atmosphere or wrapped in a container that was evacuated to low pressure. A small number of samples were kept in the climate chamber for 1000 hours with only a few interruptions. These were used as reference samples to exclude the effect of continuous removal from the setup.

6.2.2.2 Atmospheric species treatment

All samples in this study were obtained from one 10x10 cm^2 substrate with a ZnO:Al coating, which was cut into smaller samples. The initial thickness and sheet resistance

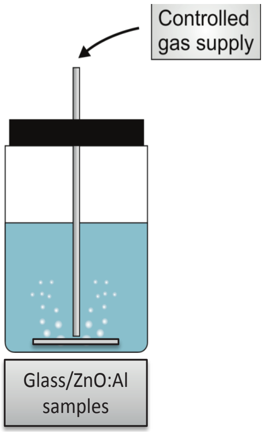

Figure 6.1

Schematic representation of the degradation setup for the degradation with atmospheric species.

measured over the complete sample had standard deviation of 5%. The water samples were placed in closed vessels, which were filled with 150 mL ultrapure water (demineralised water further treated by a Synergy Millipore tool). One vessel only contained water in an open connection to the atmosphere, while the other vessels contained water that was purged with the gases O_2 (purity: 99.995%), N_2 (purity: 99.99995%), CO_2 and compressed air (Figure 6.1). It is expected that purging the water with the gases will lead to the presence of only water and the gas, while no additional species are present, except for species that might have dissolved from the glass or the ZnO:Al layer. For water without purging, it is expected that all species present in the atmosphere are dissolved in the water in small quantities.

The gas samples were placed in CO_2 and O_2 atmospheres, while reference samples were kept in an argon glovebox (MBraung lovebox Unilab). All the samples were removed from the vessels at set times and analysed. For the samples in the water vessels, these degradation periods were 4/4/4/4/4/4/6/6/6/6/6/6/17/17/17/17/17/17/17 /17/17/17/17/20/20/20/20 hours, which counted up to 310 hours. The pH of the water in the vessels was checked before the removal of the samples, to observe whether the pH has changed. The samples in the gaseous O_2 and CO_2 were kept up to 1000 hours under these conditions.
In Table 6.1, sample abbreviations used in this article to refer to the ZnO:Al samples and the conditions of the degradation experiments of the samples are summarised.

Table 6.1 Degradation conditions for the ZnO:Al samples cells and the sample abbreviation used in this chapter.

Conditions	Name
H_2O	H_2O
H_2O purged with CO_2	H_2O/CO_2
H_2O purged with O_2	H_2O/O_2
H_2O purged with N_2	H_2O/N_2
H_2O purged with compressed air	H_2O/air
CO_2 gas	CO_2
O_2 gas	O_2
Argon gas (glovebox)	Argon

6.2.3 Characterisation of film properties

The samples in both experiments were characterised by a number of techniques before, during and after degradation.

A PhysTech RH2010 Hall effect measurement tool, a Jandel Engineering Cylindrical Probe four-point and a Dektak 8 advanced development profiler were used to determine the electrical properties and the thickness of the film respectively. The optical properties were determined by a Shimadzu UV-3600 UV-VIS-NIR, which allowed analysis of the transmittance and reflectance of the ZnO:Al samples including the glass. From these data, the absorption was calculated. A Leica Wild M400 macroscope and a digital camera were used to determine the visual changes.

The morphological and structural properties of the films were determined by a FEI Quanta 600 Scanning Electron Microscope (SEM) combined with Energy Dispersion X-ray (EDX) EDAX Genesis 4000, and a Zeiss Orion plus Helium Ion Microscope (HIM) with a Everhart-Thornley detector. The He ions had a voltage of 25kV with a current of 0.5 to 2 pA. A Philips X'pert 5068 powder diffractometer, equipped with a $CuK_α$ source ($λ$=0.154 nm) in the 5° to 95° 2θ range with a step size of 0.02 ° was also used to determine the structural properties.

In the damp heat experiment, the grain sizes as described in the introduction have been determined from Helium Ion Microscopy (HIM) images. This required additional sample preparation of the ZnO:Al layers by helium etching. The active helium species were introduced in the layer, causing the weaker spots of the layer, in this case the grain boundaries, to crack.

Since the current has to be transported millimeters in the lateral direction, against less than a micrometer in the vertical direction, the grain size was determined only in the horizontal direction. Since most of the grains have a columnar structure, the average grain size was obtained by measuring only the cross-section at the surface. The axis of the grains perpendicular to the surface has thus not been taken into account.

It was observed that not all the samples crack in a similar way. This can partly be explained by etching conditions, but it was noted that the 200°C sample broke in a burst-like fashion, while the RT sample broke more homogeneously. This difference might be caused by difference in grain size.

Time-Of-Flight Secondary Ion Mass Spectrometry (TOF-SIMS) imaging was performed using an Ion-Tof TOF-SIMS IV instrument, operated in positive and negative mode, using a high current 25 keV Bi^+ beam of ~3 μm diameter. Depth profiling was only performed in negative mode, using 2 keV Cs^+ ions for sputtering. The depth scale calibration was based on the thickness of the RT sample as determined by HIM.

Determination of the water content was executed by a Prodigy High Dispersion Induced Coupled Plasma – Mass Spectrometer (ICP-MS).

6.3 Results

6.3.1 Damp heat treatment

6.3.1.1 Structural properties

ZnO:Al films were deposited by radio frequency (RF) magnetron sputtering for 50 min by room temperature (RT) and 200°C. These samples were studied and recorded before, during and after degradation by camera, optical microscope, SEM-EDX and HIM. In Table 6.2, the deposition conditions and the initial material properties are summarised. The grain sizes and thicknesses are obtained from the HIM photographs shown in Figure 6.2 and Figure 6.3. These measurements showed that before degradation, the thickness of the 200°C sample (490 nm) was smaller than the RT sample (620 nm). The grain size of the 200°C sample was larger than for the RT sample. The roughness of the films was similar within the error margin.

The decreased deposition rate and increased grain size for the elevated deposition temperature can be explained by the influence of the substrate temperature on the mobility of the adsorbed atoms and therefore on the resulting structural development of the film: a substrate with a low temperature has a low adatom (adsorbed atom) mobility and tends to form crystallite structures that are highly porous, low in density and have rough surfaces. Higher substrate temperatures on the other hand enhance

Table 6.2 Summary of deposition conditions and initial material properties of the sputtered ZnO:Al layers.

Sample	Deposition time	Thickness	Grain size (surface)	Length scale grains	Roughness (R_a^*)
RT	50 min	620 nm	0.009 μm^2	97 nm	1.8±0.6 nm
200°C	50 min	490 nm	0.013 μm^2	113 nm	2.6±1.2 nm

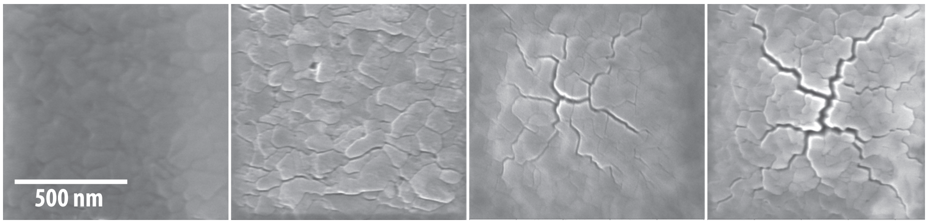

(a) (b) (c) (d)

Figure 6.2

HIM pictures of helium etched samples ; (a) RT sample before degradation; (b) RT sample after degradation; (c) 200°C sample before degradation; (d) 200°C sample after degradation.

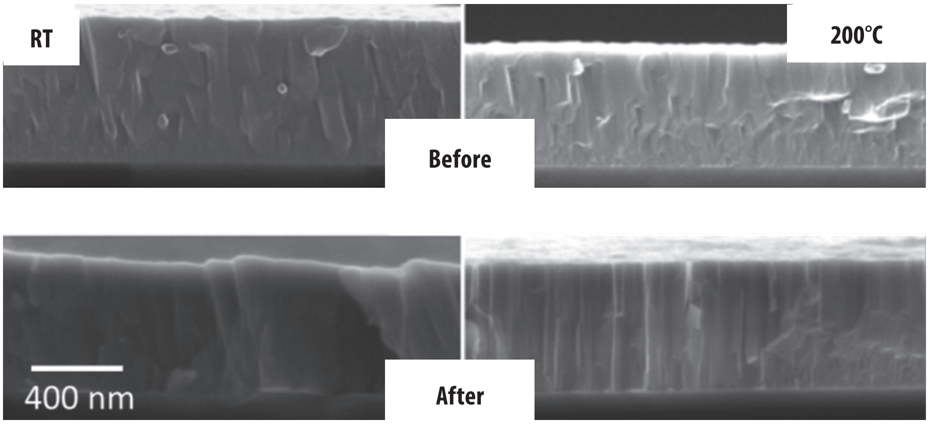

Figure 6.3

HIM pictures of the cross-sections of RT and 200°C samples before and after exposure to 85°C/85% RH.

atom mobility and cause re-evapouration of poorly combined structures. Therefore, higher deposition temperatures in general result in a lower deposition rates (thickness/time) and more dense films [11].

During degradation, no change in shape or size of the grains was observed. Similarly, the thickness of the samples did not change significantly, which is in contrast to results reported in reference [9], which reported that exposed zinc oxide films were five to ten times thicker than their originals, as a result of damp heat induced degradation.

X-Ray Diffraction (XRD) showed that the ZnO:Al samples have a polycrystalline wurtzite structure and consist of hexagonal crystallites with a preferred orientation in the (002) directions along the c-axis perpendicular to the substrate as shown in Figure 6.3. For the 200°C sample (Figure 6.4b), only the (004) orientation was further observed, while for RT sample (Figure 6.4a), the secondary (101), (102), (103) and (112) plane reflections were also present.

When the RT sample was considered, all diffraction lines were shifted to the lower diffraction angles. When looking at the dominant (002) orientation, it was clear that the signal shifts from 34.59° (200°C) to 34.37 ° (RT), thereby showing that the RT samples likely had more internal stress. The Full Width at Half Maximum was respectively 0.14° and 0.21°±0.03°, which indicate that the grain size of the RT sample is smaller than the 200°C sample, as was already shown by HIM measurements. Further quantification was not undertaken, since the structure of the grains was not fit for calculations based on the Scherrer equations.

The shift in position can have many explanations. One of the most likely causes in this case is of compressive stress in the thin film. This might be caused by the bombardment of the growing film by energetic ions (especially by oxygen ions) during the sputtering

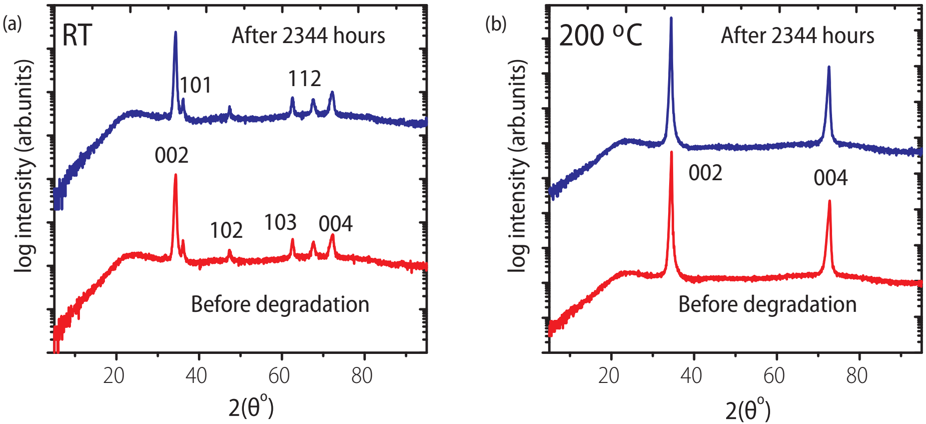

Figure 6.4

XRD patterns before (red) and after (blue) exposure to 85°C/85% RH of the (a) RT and (b) 200°C sample.

process. Oxygen has a small atomic diameter and creates interstitial alloys with many materials, which can expand the lattice structure.

Furthermore, the (002) and (004) lines are asymmetric, which is somewhat unusual. This asymmetry can be caused by presence of a second phase with a different structure or composition. It is suggested that this effect is observed when the substrate is located directly below the erosive zone of the target in magnetron sputtering unit, where the concentration of negative oxygen ions is the highest. Those ions are accelerated on the substrate and are implanted into the film and occupy the interstitial positions. This asymmetry effect could probably be countered by post-deposition heating, but this is probably not possible for CIGS cells, which cannot stand temperatures above approximately 200°C.

After degradation, the number and general position of the orientation did not change, which indicated that structural properties were constant. The position and intensity changed slightly but this change is within the measurement variation of the XRD.

6.3.1.2 Surface evaluation

While measurements by HIM did not show large differences in appearance due to degradation, the SEM and microscope revealed the occurrence of small dots and larger stains on the surface. The size and quantity of these spots increased with time, as is shown on the microscope photos in Figure 6.5a. After approximately 2000 hours, the circle-like dots have diameters up to 100 micrometres, while the stains, with less defined shapes, have diameters up to 1 mm. After 2182 hours, these dots and stains cover approximately 6±1% of the surface, but do not influence the transmission of the ZnO:Al layers in the relevant region for CIGS, as is described in the 'Optical properties' chapter. However the absorption at wavelengths above 1600-1700 nm increases with time, while the reflection decreases. This indicates that these spots and stains absorb near-infrared light.

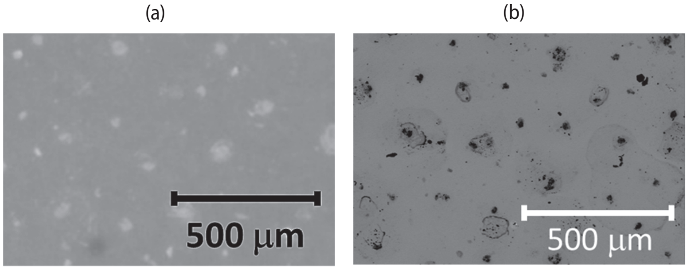

Figure 6.5

(a) Optical microscope picture of the surface of the RT sample after 2182 hours exposure to 85°C/85% RH

(b) Backscattered SEM image of the RT sample after 2344 hours exposure at 85°C/85% RH.

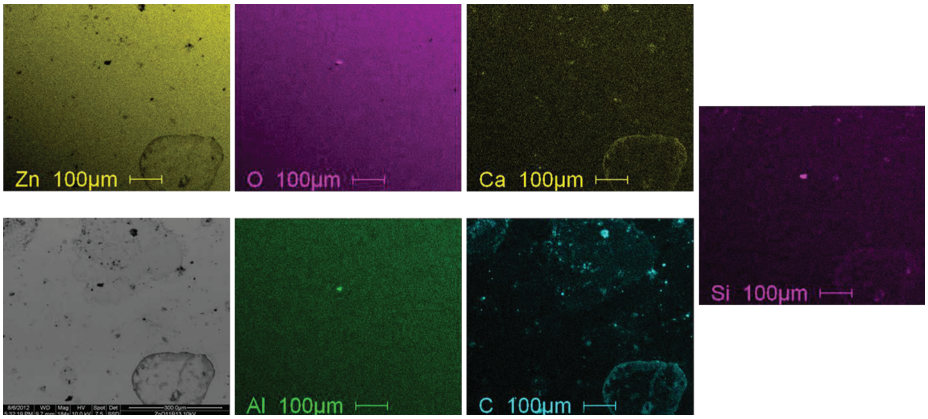

Figure 6.6

The backscattered and secondary EDX mapping at 10kV of the surface of the 200°C sample after exposure to 85°C/85% RH.

White spots were also reported in reference [3], who looked at the damp heat degradation of ZnO:Al/Ag/ZnO:Al low emissivity (low-e) coating. They observed that the size was mainly influenced by the aluminium content in the film, but the individual spots were not chemically analyzed. Very high aluminium concentrations (10%) in ZnO:Al lead to hazy samples, while the largest spots were obtained for samples without any aluminium. In this case, the quantity or size of these spots is not significantly different for the RT and 200°C samples.

In backscattered SEM, it was observed that these spots contain lighter elements than ZnO:Al (Figure 6.5b). The nature of these spots was studied by EDX mapping at 10 kV (Figure 6.6). Naturally, the elements zinc, oxygen and aluminium were encountered, but the presence of carbon, silicon and calcium was less expected, but also observed. The spots and stains seem to consist of mostly calcium and carbon, but oxygen, silicon and aluminium were certainly also present, while the zinc has disappeared from these spots. The origin of the unexpected elements was studied. One possible source was the destilled water in the climate chamber. This water was therefore checked by ICP-MS on residual cations and 0.55 mg/l Na and 0.35 mg/l Si were found. However, no aluminium and calcium were detected. It is known that aluminium, silicon and calcium are present in the glass, so it is likely that the calcium has migrated from the glass, which might also be possible for the aluminium and silicon. It can be expected that these migrating cations will react with H_2O, CO_2 or O_2 from the air to form carbonates or hydrates. It is proposed that the spots and stains occur when the samples are removed from the climate chamber. The thin water film on the surface can then dry-out and form little dots or coffee stains and leave salts behind.

It should be noted that the zinc oxide film is in these experiments in direct contact

with the glass, allowing direct migration of the cations. However, in CIGS cells, the glass cations have to travel through multiple layers to reach the zinc oxide, which will slow down this process. Furthermore, stain formation on top of the zinc oxide is probably hindered by the encapsulation materials, like Ethylene-Vinyl Acetate (EVA).
Another difference with CIGS solar cells is the presence of sodium, which was not present in the Corning XG type glass. However, during the deposition of the CIGS layer, sodium is present. In some cases, this element is obtained from the substrate soda lime glass, which contains a high concentration of sodium, while other producers choose to add the sodium in a controlled way, for example by NaF deposition. In either cases, sodium is present in the CIGS layer, which is located close to the zinc oxide layer and can play a role in the degradation process. More information about this topic can also be found in the chapter 7.

6.3.1.3 Optical properties

The optical properties were studied by UV-VIS and are depicted in Figure 6.7. Initially, the samples including glass transmit 81% and 84% of the light for the RT and the 200°C samples respectively. During degradation, the average transmission barely changes with time in the measured wavelength region (240 – 2400 nm). The constant plasma frequency and the constant transmission in both the near infrared and the UV region imply that the carrier concentration is constant in the bulk of the film [12].
However, a small drop in reflection and a small increase in absorption was observed in the near infrared region. This can be explained by the small white spots, which might absorb a part of the near infrared light. A similar trend in absorption and reflection was also observed during damp heat treatment in [13], although it is not known whether this might be caused by the formation of surface spots.

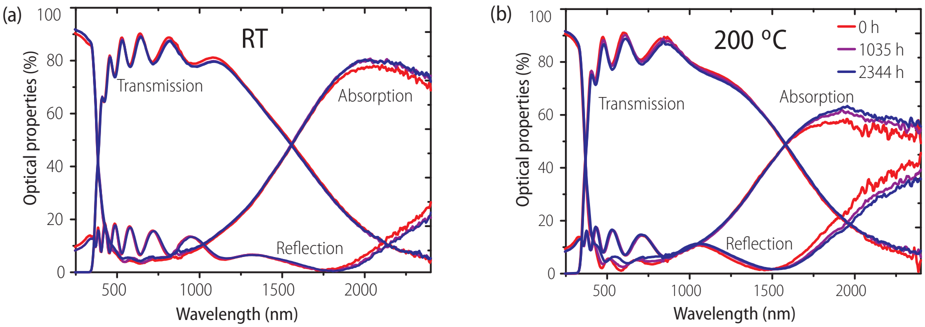

Figure 6.7

Optical properties of the (a) RT and (b) 200°C samples before damp heat exposure (red) and after 1035 hours (purple) and 2344 hours (blue) exposure to 85°C/85% RH.

Within the highly transparent region, the measured spectra show an oscillatory behaviour that is caused by interference effects due to multiple internal reflections of the incoming light in the zinc oxide layer. The degradation has not influenced this behaviour, so no texturing or reduction of zinc oxide to zinc has occurred.

6.3.1.4 Electrical properties

The electrical properties were determined by Hall Van der Pauw and four point probe measurements. Both films exhibited an n-type behaviour, which is in conformity with the type of conduction mechanism associated with these ZnO:Al semiconductors. Figure 6.8 depicts the development of resistivity of the two samples with degradation time as obtained by Hall measurements. The resistivity data obtained by the four point probe have the same shape with a small offset and are not shown. It was observed that the 200°C sample has an initial resistivity of $6x10^{-4}\Omega$cm, which is a factor two lower than the RT sample. After exposure to 85°C/85% RH, the detoriation was also faster for the RT sample. The RT sample is therefore more vulnerable to damp heat.

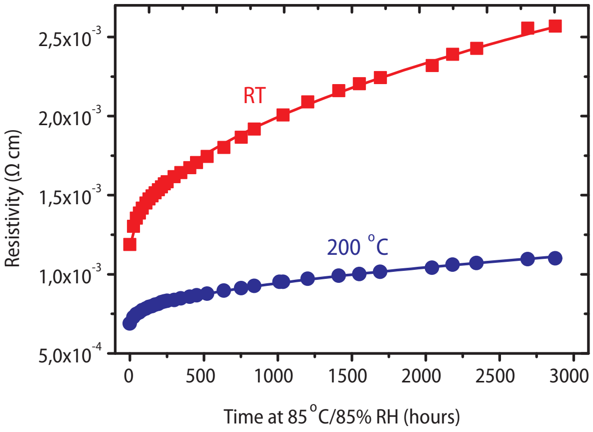

Figure 6.8

Resistivity of the RT (red) and 200°C(blue) ZnO:Al samples as a function of time at 85°C/85% RH.

This is a different conclusion than drawn in reference [4], in which no influence of sputtering temperature in a similar deposition temperature range was reported. However, in that case, samples obtained with a different deposition technique (Pulsed Laser Deposition) and a different thickness range (20-200 nm) were studied.

The increase in resistivity of both samples can be fitted with a square root function, following:

$$y = a * \sqrt{(bt)} + c \qquad (6.1)$$

As can be seen in Figure 6.8, the resistivity is higher for the RT sample, indicating a higher initial resistivity as well as a faster degradation. Since the resistivity increase can be fitted with a square root function, the conductivity automatically follows a $1/\sqrt{(t)}$ trend. Therefore, the resistivity change can be linked with a diffusion-like process, in which a species from an infinite reservoir diffuses into a semi-porous material. The diffusion of the species in the sample will thus be the rate-determining step, while the reaction between the diffusion species and the grain boundary atoms inside the sample is a quicker process.

In literature, it has been observed that thick samples have a lower degradation rate than thin samples [4,7,9]. This is explained by either a diffusion based degradation process that starts from the surface and gradually deepened into the layer [9] or by a difference in grain sizes or structures for different thicknesses [7]. In this case, we confirm that diffusion controls the resistivity increase.

The difference in resistivity increase between the 200°C and RT samples cannot be explained purely by the difference in thickness, since the samples were respectively 490 and 620 nm thick, which cannot account for the large difference in the rate of resistivity increase. We therefore propose that the diffusion rate is explained by the number of diffusion channels present, for example grain boundaries.

Alongside with the resistivity, the Hall mobility and carrier concentration were measured (Figure 6.9). The initial values of both parameters were higher for the 200°C sample than for the RT sample. The initial carrier concentration for the 200°C sample was approximately 4.5×10^{20} cm^{-3}, while this was around 3×10^{20} cm^{-3} for the RT sample. For the mobility, values of 20 cm^{2}V^{-1}s^{-1} and 16 cm^{2}V^{-1}s^{-1} were measured respectively. These values are in line with literature values [14].

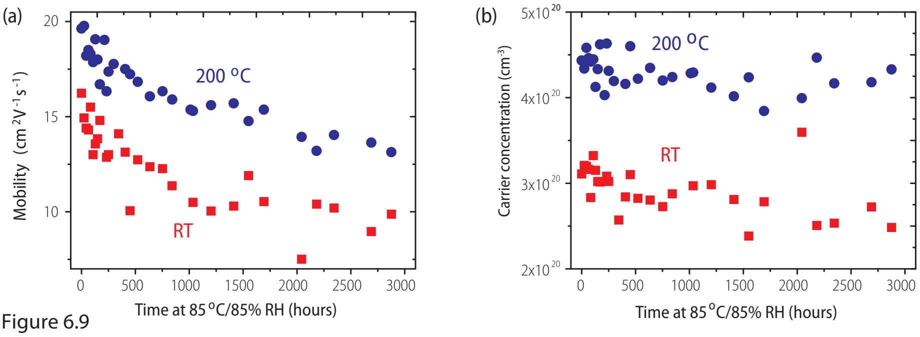

Figure 6.9

(a) Hall mobility and (b) carrier concentration of the RT (red) and 200°C (blue) ZnO:Al samples as a function of exposure time to 85°C/85% RH.

When the influence of damp heat exposure was studied, the carrier concentration showed variation as a function of exposure time, but did not show a clear trend. The initial and final values of the carrier concentrations only show a very small decrease, which is within the error margin.

From these data, it can be concluded that the change in carrier concentration cannot be a major source for resistivity increase, which indicates that the bulk of the zinc oxide grains has a constant composition. This does not completely agree with the small changes in carrier concentrations as reported in literature [4,15], but it should be noted that these films were thinner (100-240 nm) than our films.

The Hall mobility decreased the first 1000 hours, while afterwards, the decline slowly continues. This decrease cannot be explained by the small white dots as described above, since these mainly occur at the top of the ZnO:Al layer, which will not block lateral electron movement. Furthermore, the size of the spots is a factor 1000 larger than the grain size, so any influence on the electrical properties would also affect the carrier concentration. Therefore the reason for the mobility decrease should be found within the zinc oxide layer itself. Figure 6.10 shows the dominant electron scattering mechanisms in zinc oxide limiting the mobility: potential barriers at the grain boundaries and ionised impurity scattering in the grain. In the case of the Hall effect measurements, electrons travel macroscopic lengths and cross several grain boundaries, so the grain boundary density can be a limiting factor on the value of Hall mobility [16].

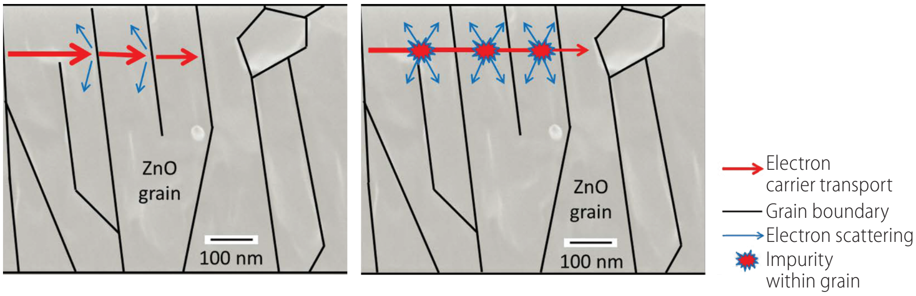

Figure 6.10

Possible scattering mechanisms in zinc oxide samples based on reference [13].

Based on the stable carrier concentration and the decreasing mobility, it can be expected that the formation of detrimental compounds in zinc oxide occurs at the grain boundaries and not in the bulk material.

This important role for the grain boundaries in the electrical properties of zinc oxide is also confirmed in reference [17]. It was reported that neon cannot effuse in or out of the bulk material of sputtered zinc oxides for temperatures as high as 1000°C. However, transport through the grain boundaries was possible. Therefore, the transport of molecules like large molecules like oxygen, carbon dioxide and water is only possible through the grain boundaries.

This important role of grain boundaries in the degradation process was also concluded by various references [6, 7, 10]. Reference [16] also concludes this, based on experimental work where the decrease of electrical properties of optical measurements (intra grain) and electrical measurements (inter grain) were compared. Calculations based on these experiments allowing the barrier width and height, are explained further in reference [16].

As reported in references [2,13] and chapter 2.3.4.3, stronger degradation of ZnO:Al electrical properties will occur when the films are grown on rough substrates, due to the formation of 'extended grain boundaries'. These are local perturbations of the ZnO:Al morphology, which also allow fast diffusion of environmental species into the material. Generally stated, it is proposed that the extended grain boundaries are the most likely to be prone to degradation, followed by the grain boundaries. If both these elements are not present or are stable, then the grain will probably become the next problem.

A high number of grain boundaries thus leads to a low probability for the electrons to travel through the material. This makes zinc oxide with larger grains more stable.

The probability of electrons travelling through the grain boundaries naturally decreases as the number of grain increases, so large grains reduce the grain boundary scattering [18]. Since the 200°C grains are larger than RT grains, it is expected that an increase in grain boundary scattering is larger for the RT sample. Therefore, the larger mobility decrease can be explained by a difference in grain size between the RT and 200°C sample, which is shown in Table 6.2.

Additionally, the difference in grain orientation could also have played a role. It is possible that the grain boundary surface of the small grains that do not have the (002) and (004) orientations are more sensitive for degrading species.

6.3.1.5 Composition

The composition as a function of the depth was measured by SIMS through the layer before and after degradation. The depth profiles taken in the negative mode of the RT sample are shown as graphs (Figure 6.11) and as cross-sections maps (Figure 6.12). These values show the difference in concentration of various important ions within the layers as well as due to degradation. It should be noted that the concentrations depend on the ionisation probability of the atoms and molecules, which varies per species and per background material. Therefore, no absolute concentrations are obtained in this study.

It is immediately clear that the damp heat test introduces hydroxides, chlorine, sulphur and carbon concentrations in the film. The hydroxyl profile decays by about an order of magnitude in 300-500 nm and is everywhere higher than before degradation. When comparing the RT sample with the 200°C sample, it was observed that the hydroxyl profile has a slightly higher maximum value for the RT film, which indicates more water has been taken up by this sample. This can be explained by the higher number of grain boundaries.

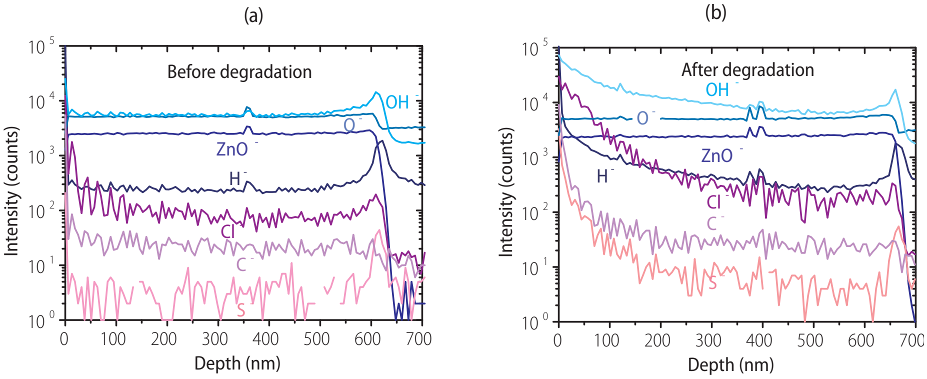

Figure 6.11

SIMS depth profiles taken in the negative mode of a (a) RT sample before and (b) after exposure to 85°C/85% RH.

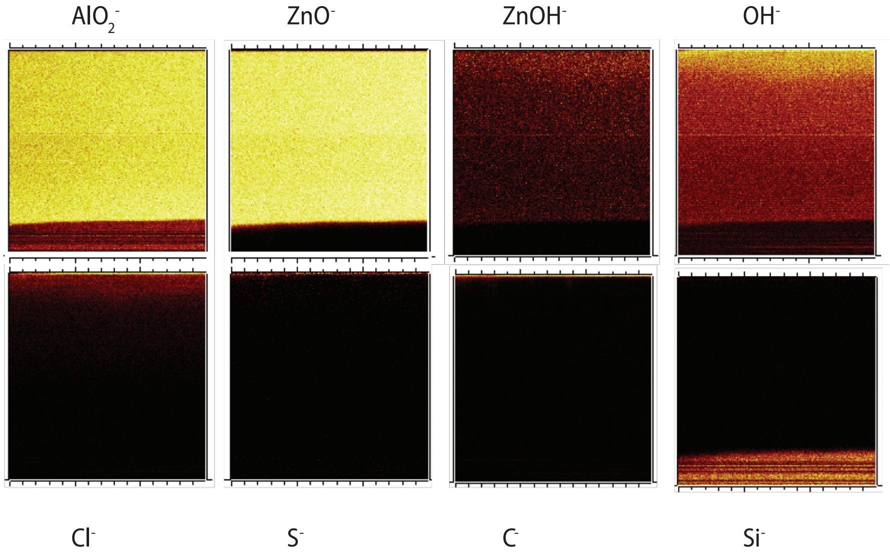

Figure 6.12

SIMS depth profiles of the RT sample after exposure to 85°C/85% RH visualised as cross sections: the top of each image is the surface, the bottom ~20% is the substrate. The total width of the pictures is 300 µm.

Looking at the bottom 300 nm of the layer, the hydroxide and hydrogen concentrations are lower than in the top layer, indicating that the diffusion and thus the degradation can still develop further. In addition, there is a large amount of chlorine in the films after degradation, which decreases an order of magnitude for 100-200 nm. In the region near the surface, the concentration is probably comparable to the hydroxide concentration, assuming that the ionisation probabilities of hydroxide and chlorine in ZnO are similar. Degradation thus induces relatively high concentration of chlorine in the top layers of the samples. Similarly, there is a slightly increased sulphur signal in the top 200 nm after degradation, which is visible in the cross-section mappings as a very thin surface layer. The sulphur is probably present as sulphite or sulphate (SO_3^{2-} or SO_4^{2-}). It should be noted that these SIMS measurements do not provide absolute concentration values. Since chlorine and sulphur were barely detected by EDX, the total amount of these species in ZnO:Al is probably very low. The treatment thus only induces these species near the surface of degraded ZnO:Al.

The carbon signal is only significantly raised by damp heat testing in the top 100 nm of the film. The carbon concentration is difficult to estimate, because the carbon ionisation probability is usually much lower than that of hydroxide and chlorine, but the concentrations are likely low in the bulk. The chemical state of the carbon cannot be determined easily from a depth profile in an oxide film, but it might be (bi-) carbonate.

The oxygen concentration did not change due to degradation and is completely stable as a function of depth, so it is unlikely that adsorption of O_2 is the main reason for ZnO deterioration.

Looking at the spots on top of the samples, higher concentrations of sulphur, chloride, carbon and hydroxide were found. On the other hand, the ZnO, ZnOH and AlO_2 concentrations were very low, indicating the absence of ZnO:Al. TOF-SIMS measurements were also executed in the positive mode, in order to map the positive ions in the atomic layers near the surface. The most striking cations were Zn^+, Al^+, Na^+, K^+, H^+, Si^+ and Ca^+, which confirms the presence of silicon and calcium in the white spots.

Since the complete thickness of the ZnO:Al layer is used for lateral transport of the electrons, it can be assumed that the impact of the surface elements on the electrical properties is small. Therefore, chlorine and especially sulphur, carbon, calcium and silicon, which are mainly present at the surface, will not be the main reasons for decreased conductivity. Since ZnOH and OH are present in the complete layer, these will have the largest influence.

6.3.2 Atmospheric species treatment

6.3.2.1 Structural properties

From cross section HIM and SEM pictures, it was concluded that the non-degraded ZnO:Al layer has a columnar structure and a thickness of 480-520 nm. It was observed that the structure of the columns was not completely straight, but showed a wavy structure. This wavy structure can be caused by the movement of the substrate during deposition on the semi-industrial tool, which slowly moves the substrate back and forth during the deposition.

During degradation, the most striking observation was complete dissolution of the sample that was placed in H_2O purged with CO_2, which occurred within hours. No further results of this sample are therefore given in this article. The other samples did not dissolve and their compositional, optical and electrical properties were followed for 310 hours.

After exposure to most treatments, no differences in structural properties could be observed. The structure of the H_2O/N_2 sample is shown in Figure 6.13 as example. However, an unexpected change in morphology was observed for the H_2O/air sample, in which gaps occurred in the ZnO:Al layer at the glass interface (Figure 6.13), indicating local dissolution of the ZnO:Al. It was observed that only the bottom 200 nm was affected, while the top part of the ZnO:Al still looked intact. This was not expected, since the water and other reactive species are initially only present at the top of the ZnO:Al layer. This effect was not unambiguously shown for the non-purged

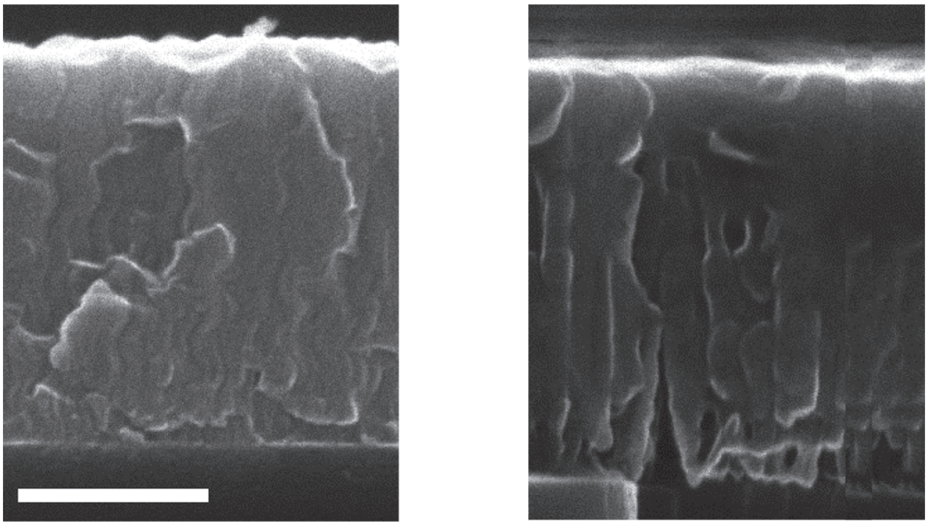

Figure 6.13

Cross section HIM pictures after degradation: Left: ZnO:Al H_2O/N_2 sample; Right: ZnO:Al H_2O/air with gaps near the glass/ZnO:Al. The scale bar indicates 250 nm.

H_2O, but probably also occurred.

When the samples were studied by eye or by light microscope, it was observed that most samples did not look significantly different after degradation, although the H_2O/air sample looked less homogeneous.

X-Ray Diffraction (XRD) measurements showed that the ZnO:Al samples before degradation had a polycrystalline wurtzite structure and consisted of hexagonal crystallites with a strong preferred orientation in the (002) directions along the c-axis perpendicular to the substrate. The (004) orientation was also observed. Apart from the dissolved sample exposed to H_2O/CO_2, the degradation neither led to the introduction of any additional signals nor led to a significant change in position or shape of the signals. Furthermore, the structural properties of the all the ZnO:Al samples did not change.

6.3.2.2 Electrical properties

Hall measurements showed that before degradation, all samples had a sheet resistance of 10.0±0.5 Ω/□, corresponding with a resistivity of 4.5-5 x 10^{-4} Ωcm. Clear differences in the evolution of the resistivity as a function of exposure time were observed for the samples exposed to different atmospheric gases (Figure 6.14). During exposure, no change in resistivity was observed for the samples stored under an argon or a gaseous O_2 or CO_2 atmosphere, while the samples exposed to water purged with nitrogen and oxygen showed a very slow increase. This was especially visible during the first thirty hours, and continued very slowly for the following 300 hours. A larger impact was observed for the samples that were stored in water without purging, therefore naturally containing some atmospheric gases. This sample showed a twofold increase over 210 hours of exposure time. The H_2O/air showed the largest increase, which resulted in a sheet resistance of over 80 Ω/□ or 4x10^{-3} Ωcm after 310 hours.

The main reason for the increase in resistivity could be found in the electron mobility

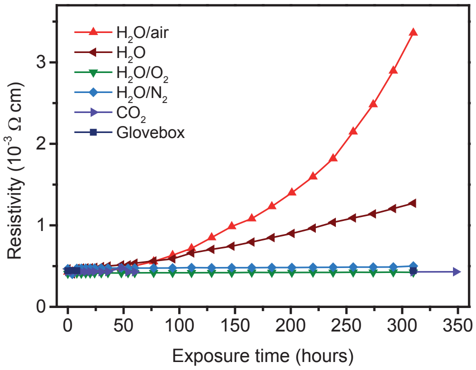

Figure 6.14

Development of the resistivity of ZnO:Al as a function of exposure time to the various species.

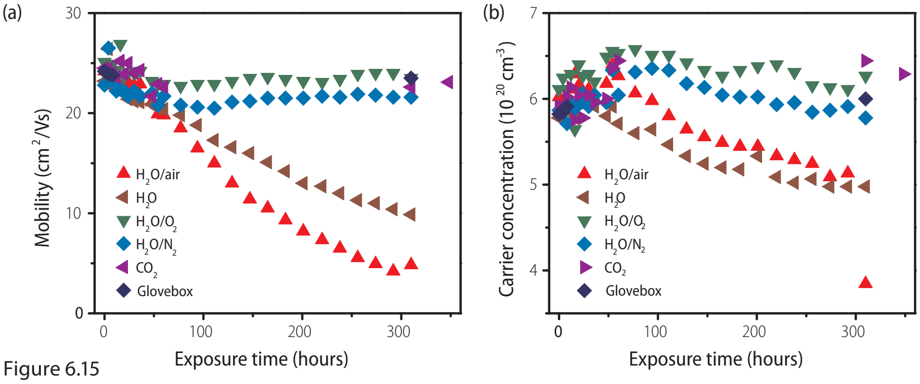

Figure 6.15

Development of (a) the mobility and (b) the carrier concentration as a function of exposure time to the various species.

(Figure 6.15). For the samples stored in CO_2 and in water purged with N_2 and O_2, a small initial decrease in the first 100 hours was observed, followed by a stable electron mobility. The samples exposed to water with or without compressed air showed a very large decrease in this electron mobility.

A minor change in electrical properties was also visible in the carrier concentration of the samples in water and water purged with compressed air (Figure 6.15). This effect was small compared to the change in electron mobility. The samples stored in water purged with nitrogen and oxygen as well as the samples stored in a CO_2 atmosphere did not show any decrease in the carrier concentration.

6.3.3 Optical properties

In Figure 6.16, the optical properties determined by UV-VIS measurements of the samples after exposure to H_2O/O_2 and H_2O with and without air purging are shown. The optical properties of the H_2O/N_2 are very similar to the H_2O/O_2 sample. In these graphs, it can be observed that the optical parameters of the H_2O/O_2 sample barely changed with time in the measured wavelength region (240 – 2400 nm). For these samples, the constant plasma frequency and the constant transmission in both the near infrared and the UV region imply that the carrier concentration is constant in the bulk of the film, as is also observed in Hall measurements. The samples exposed to the gases (CO_2, O_2) are not depicted but barely showed any change.

However, for the H_2O and H_2O/air samples, large changes in the optical properties were observed. For the H_2O sample, the fringes get a little bit weaker, while the transmission in the IR region slightly increases. In the region above 1500 nm, the reflection decreases while the absorption increases. For the H_2O/air sample, these effects became stronger: the fringes have completely disappeared, the transmission in the IR region has increased, while the reflection in this region decreased.

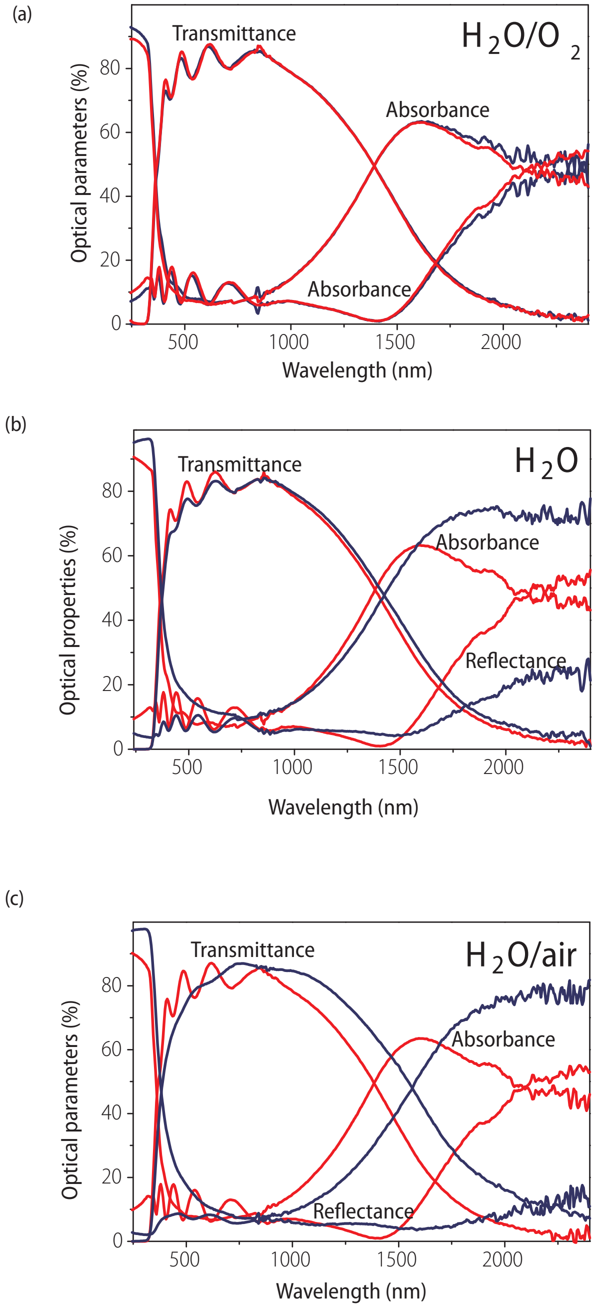

Figure 6.16

Optical properties before (red) and after 310 hours exposure to various conditions (blue) which are (a) H_2O/O_2 *(b) non-purged* H_2O *(c)* H_2O*/air.*

6.3.4 Compositional changes

The change of composition as a function of the sample depth was determined by ToF-SIMS measurements. The intensity depth profiles of the most relevant ions of various ZnO:Al layers (non-degraded, H_2O/O_2 and H_2O/air) are shown in Figure 6.17. We observed that the reference sample showed completely flat profiles of the matrix species AlO_3, ZnO and Oxygen. Furthermore, it has mostly flat profiles of the 'foreign' species hydroxide, hydrogen, carbon, sulphur, chlorine and PO_x, where part of the signals may be due to instrumental background. However, in this sample, and less visible in the H_2O/O_2 sample, the OH and H content shows a 14-cycle periodic variation, as if the layer consists of 14 sub-layers. It was checked under different conditions and concluded that was not an instrumental effect. Since the samples were deposited in 14 passes in the sputtering tool, it can be concluded that H_2O or similar species are incorporated in small quantities during the deposition process.

Exposure to H_2O/O_2 seems to lead to the smoothening of the OH and H profiles in the bulk and near the glass. Furthermore, small signal increases of most 'foreign' species (hydroxide, hydrogen, carbon, sulphur, chlorine and PO_x) were observed near the top of the sample. The largest concentration increase was observed for hydroxide.

The sample exposed to H_2O/air showed a completely different composition profile: Much higher signals for hydroxide, hydrogen, carbon, sulphur, chlorine and PO_x were observed (20 fold increase of hydroxide in the bulk). These species are even more enhanced near the ZnO:Al/glass and the air/ZnO:Al interfaces. For the newly observed species sulphur and copper, the gradient near the interface was even steeper. At the interface regions, where the foreign species have a very high concentration, the matrix materials oxygen, ZnO and AlO_3 show a decrease.

6.3.5 Acidity measurements

Since it was expected that the presence of CO_2 would impact the pH, this value was measured for the water based experiments before the removal of the samples from the H_2O vessels for analysis. The pH of the H_2O purged with CO_2 showed a pH value of 4.7. It was noticed for all other vessels that the pH showed a small initial increase (an average from 7.9 to 8.4) followed by a slow and steady increase over the duration of the experiments, on average from 8.4 to 9.2. This effect was the strongest for the N_2 purged vessel and the smallest for the O_2 purged vessel. Another control experiment did show a small initial increase, but it did not show any later effect on the pH. The small observed changes might have resulted from the measurement error of the pH measurement tool. It can be concluded that the pH did not change more for the H_2O/air and H_2O vessels than for the H_2O/N_2 an H_2O/O_2, so large global fluctuations of the pH were not the cause of the difference in degradation behaviour.

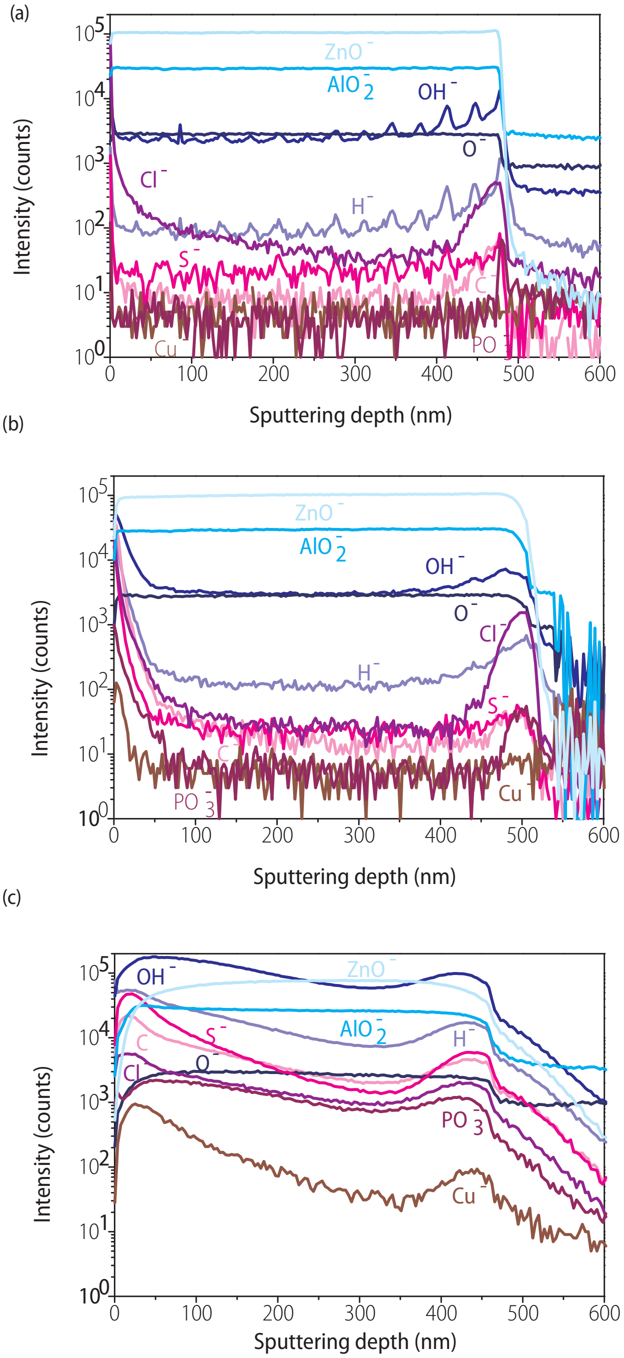

Figure 6.17

SIMS depth profiling of the ZnO:Al (a) non-degraded (b) 310 hours exposure to H_2O/O_2 (c) 310 hours exposure to H_2O/air.

6.4 Discussion

In this discussion session, first the observations and discussions for both the experiments are summarised, while a general degradation mechanism for ZnO:Al degradation is also introduced.

6.4.1 Damp heat treatment

When considering the observed results, the following conclusions on physical and chemical changes in ZnO:Al due to damp heat treatment can be drawn:

1. The three dimensional structure of the samples stayed intact. The grain sizes and the thickness of the layers did not change.
2. The main visual change was the appearance of white spots, containing elements which migrated from the glass, like calcium and silicon, and reacted with elements from the environment, including oxygen and carbon. These spots have a small influence on the absorption of light in the IR region, but do not have an influence the electrical properties or the overall transmission.
3. The resistivity increases, mainly driven by a large drop in the Hall mobility, while the carrier concentration showed fluctuations, but did not change significantly. This implies the formation of a potential barrier in the grain boundaries.
4. Chlorine, sulphur and carbon are present near the surface of degraded ZnO, while hydroxide is present in the volume of the whole samples.

6.4.1.1 Physics of grain boundary degradation

When the chemical mechanisms for the degradation of ZnO:Al are considered, the relevant degradation reactions are most likely to occur at the grain boundaries. These grain boundaries thus have a changed composition, but the volume of the degraded material is very small, so techniques like XRD and UV-VIS do not show direct evidence for material change. The nature of the changes in the material and the relationship with the mobility drop (Figure 6.8) can be found in the structure of the grain boundaries: these are complex structures, usually consisting of a few atomic layers of disordered atoms, representing a transitional region between two neighbouring crystallites.

The diffusion of environmental gases (e.g. oxygen, carbon dioxide and/or water vapour) through these grain boundaries in doped ZnO films can lead to a reaction between the atoms at grain boundaries and these species. This can result in the accumulation of negatively charged trap states at the crystallite interface. This local increase in the density of these states leads to a higher potential barrier, which hinders the mobility of the carriers among the grains [12]. It is proposed that the carriers flow across the grain boundaries via thermionic emission and tunneling increases with the

Fermi level [19]. Therefore films with higher carrier concentration, in which the carriers have a higher probability for thermionic emission, are typically found to have more stable electrical properties in a harsh environment.

6.4.1.2 Reaction mechanisms in the grain boundaries

It was observed in the 'atmospheric species' experiment that H_2O in combination with CO_2 lead to ZnO:Al degradation, while nitrogen and oxygen only have a minor impact on the stability of this layer. Since chlorine and sulphur were also encountered in the degraded zinc oxide, we also propose a role for these materials.

The diffusion of species into the grain boundaries can influence the resistivity in two ways, which are not easy to distinguish:

- Molecular adsorption (physical reactions)
- Chemical reactions

A combination of those two is the most likely scenario. This can also be expected based on the reversibility experiments in reference [6], where a change in resistivity was reported when annealing at 150°C as well as effusion of water, CO_2 and H_2 at higher temperatures (around 500°C), indicating two different phenomena were involved.

6.4.1.3 Molecular Adsorption

The adsorption of molecules would occur in the grain boundaries or at the surface and is considered to result in the formation of electron traps. Zinc oxide is known to have great absorptivity for H_2, CO and CO_2 after being cleaned of absorbed H_2O and CO_2 by vacuum heating [20]. We propose H_2O can be adsorbed at the grain boundaries, based on the fact that OH^- and H^- were encountered.

6.4.2 Degradation due to chemical reactions

The other possibility for degradation is chemical degradation and begins with presence of unbound zinc, oxygen or aluminium species. These species can either be present due to dangling bonds or defects or occur due to the dissolution of ZnO:Al in the thin water film present at the surface and possible in the grain boundaries. Looking at the dissolution of zinc oxide, both chemical and electrochemical dissolution can result in the formation of a Zn^{2+} cation. Electrochemical reactions depend on the electrode potential which regulates the absorption of protons to the surface. This is not expected for these experiments, but might occur in solar cells, which are electrically active.

Zinc oxide is an amphoteric material and the chemical stability of zinc oxide in aqueous solution is a function of the pH. It is thermodynamically stable in the pH between 6 and 12, however in solutions with a high or low pH zinc oxide, zinc oxide can react [20]:

$ZnO (s) + 2H^+ (aq) \rightarrow Zn^{2+} (aq) + H_2O(l)$ (chemical dissolution) (6.2)

Another route to the dissolution of zinc oxide is due to the impact of light under some conditions:

$2 ZnO (s) + 4h\nu \rightarrow 2Zn^{2+} (aq) + O_2 (g) + 4e^-$ [21] (6.3)

After formation, this Zn^{2+} can either wash away with the water or react into other species. In this case, the layers keep the same structural characteristics, so it is not likely that Zn^{2+} has disappeared from the samples.

More information about the nature of the species formed in the grain boundaries was found in literature and by calculations. The first hint for possible stable reaction products of zinc oxide degradation can be found in nature. In exposed deposits, most of the mined zinc compounds are sulphides, carbonates and hydrocarbonates.

The reaction products of zinc compounds in nature were already described in literature [20]. This shows the large amount of reaction products that occur in nature, and the possibility that multiple corrosion products can be present at the same place. Although aluminium doped zinc oxide is naturally a different material then pure zinc, it can be assumed that various of the reaction products should be similar for ZnO:Al.

The corrosion products of zinc in the presence of only carbon, oxygen and hydrogen are ZnO, $Zn(OH)_2$, $ZnCO_3$, $Zn_5(CO_3)_2(OH)_6$ and $Zn_4CO_3(OH)_6{\bullet}H_2O$. In addition to these predominantly found oxides, hydroxides and carbonates, various sulphur or chloride based compounds were also detected. These products include $Zn_4SO_4(OH)_6{\bullet}nH_2O$ (basic zinc sulphate), $Zn_4Cl_2(OH)_4SO_4{\bullet}5H_2O$ (zinc chlorohydroxysulphate), $(Zn,Cu)_4SO_4(OH)_6{\bullet}4H_2O$, $NaZn_4Cl(OH)_6 SO_4{\bullet}6H_2O$, $Zn_5(OH)_8Cl_2{\bullet}H_2O$ (zinc hydroxychloride), $ZnSO_4$ and $ZnSO_4{\bullet}nH_2O$ (zinc sulphate). This indicates that sulphur and chloride based reaction products also occur in nature.

In nature, the relative amount of chlorine in the corrosion products is usually low due to the high solubility of the chloride containing compounds. However, while in the nature rain is omnipresent, no large quantities of liquid water have been in contact with our samples in this damp heat experiment, so these molecules can still be present in this case. Therefore, chlorine species might be found less in CIGS panels in the field, but might still play an important role in their degradation.

It was also found that the corrosion products are often not uniform with depth. ZnO was found in the outer 15 nm of the surface layer, while $Zn(OH)_2$ or $ZnCO_3$ were found deeper in the film. Chlorine and sulphur based species were present as surface contaminants in the outer 1 nm. These soluble salt ions may also penetrate into the bulk material through cracks and defects. This might of course also occur in the grain boundaries.

The effect of the temperature and CO_2 on Zn^{2+} in thermodynamic equilibrium is described in reference [22]. Under standard CO_2 concentrations and at 85°C, zinc oxide should be the most stable reaction product of zinc. However, at lower temperatures, $Zn_5(OH)_6(CO_3)_2$ (hydrozincite) and $ZnCO_3$ (smithsonite) are the most stable materials.
The formation of hydrozincite from zinc hydroxide follows this reaction:

$$Zn(OH)_2\ (s) + 4Zn^{2+}\ (aq) + 4OH^-\ (aq) + 2CO_3^{2-}\ (aq) \rightarrow Zn_5(CO_3)_2(OH)_6\ (s) \qquad (6.4)$$

Analogue reactions can occur in the presence of Cl^- and SO_4^{2-} ions, resulting in the above mentioned chlorides or sulphates.
Furthermore, reference [23] showed experimentally that $Zn(OH)_2$ is kinetically favoured at low temperatures (under 34°C) and can thus also be formed according to:

$$Zn^{2+} + 2OH^- \rightarrow Zn(OH)_2 \qquad (6.5)$$

At higher temperatures, ZnO formation was observed, which is explained by dehydration. This might also have occurred to our samples due to long storage in an inert atmosphere. It is expected that the compounds mentioned above might be formed during field operation of CIGS modules.

Since these results are mainly based on zinc corrosion, this reaction matrix was expanded further by basic thermodynamical calculations with the program Medusa [24] on the degradation of ZnO:Al, so a rough idea could be obtained about the expected reaction products. These results served as a guideline for further studies, but are not per se valid for this case, which is a situation without thermodynamic equilibrium in a crystal lattice instead of an aqueous solution. In this calculation, the reaction products of Zn^{2+} in an aqueous solution were determined under the following conditions:

- pH: 6.5
- CO_3^{2-} concentration: 5×10^{-6} mol/liter
- Al^{3+} concentration: 10^{-3} mol/liter

Under these circumstances, $Al(OH)_3$ (aluminium hydroxide), $Zn(OH)_2$ (zinc hydroxide) and $Zn_5(OH)_6(CO_3)_2$ (hydrozincite) came out as the most likely reaction products. Other calculations indicate that the CO_3^{2-} concentration has a large impact on the $[Zn(OH)_2]/[Zn_5(OH)_6(CO_3)_2]$ ratio. The concentration of CO_2 is very important in the consideration whether the less stable hydroxide is converted in the more stable hydrozincite.

6.4.3 Atmospheric species treatment

6.4.3.1 Gases

The impact of exposure of ZnO:Al to different kinds of gases (pure CO_2, O_2 and argon) was minimal. Both the electrical and the optical properties did not change significantly. In general, it can be stated that ZnO:Al seems to be stable for middle long term exposure (for hunderds of hours) to these conditions.

6.4.3.2 Water purged with nitrogen or oxygen

When the H_2O/N_2 and H_2O/O_2 samples are considered, a minor increase in resistivity during the first 100 hours was observed. The electrical changes could majorly be attributed to changes in mobility, while the carrier concentration did not change significantly.

Reference [15] describes the dominant electron scattering mechanisms in zinc oxide limiting the electron mobility for ZnO:Al: potential barriers at the grain boundaries and ionised impurity scattering in the grain. For the H_2O/N_2 and H_2O/O_2 samples, based on the stable carrier concentrations and the decreasing mobility, it can be expected that the formation of detrimental compounds in zinc oxide occurs mainly at the grain boundaries and not in the bulk material.

This is supported by the observation in reference [16], which shows that neon cannot effuse through the bulk of the grains, while it can migrate through the grain boundaries. Therefore, the transport of molecules like oxygen, nitrogen and water is likely also only possible through the grain boundaries. Since the effects for H_2O/N_2 and H_2O/O_2 on both the electrical and the optical parameters are minor and nitrogen is known for its inertia, it is not expected that oxygen plays a large role in the degradation of ZnO:Al. Therefore, it is expected that the main component leading to ZnO:Al degradation under these conditions is H_2O. We therefore propose that a reaction between Zn^+ and OH^- occurs, leading to the formation of $Zn(OH)_2$ according to reaction (6.5). Due to the relatively stable carrier concentration, it is likely that also in this case, degradation of the grain boundaries is the driving force behind the observed mobility decrease.

6.4.3.3 Water purged with CO_2

The sample in H_2O/CO_2 dissolved directly, which is caused by the decreased pH (4.7), that occurred due to the dissolution of CO_2 in water.

$$H_2O\ (l) + CO_2\ (g) \rightarrow 2H^+\ (aq) + CO_3^{2-}\ (aq) \qquad (6.6)$$

The chemical stability of zinc oxide in an aqueous solution is a function of the pH. It is thermodynamically stable in the pH between 6 and 12, outside this pH range, zinc oxide dissolves [19]. In an acidic environment, the reaction (6.2) occurs, leading to Zn^{2+} formation.

6.4.3.4 *Water and water purged with air*

The effect for the H_2O/air and H_2O samples is more severe than the degradation of the H_2O/N_2 and the H_2O/O_2 samples. When considering non-purged water as well as water purged by compressed air, it can be assumed that the gases found in air will be present in the water. A standard air mixture contains N_2 (~78% volume), O_2(~21%), Ar (~1%) and CO_2 (0.03% volume) plus other constituents (e.g. H_2, Ne, He, Kr) in concentrations under 20 ppm. Since ZnO:Al appears to be inert for N_2 and O_2, while Ar is known to be very inert, it is expected that the main reactive species in air is CO_2. A possible reaction product, as also described above, is hydrozincite ($Zn_5(CO_3)_2(OH)_6$) as described in reaction mechanism (6.4).

The formation of a carbonate and hydroxide containing material is also supported by the observation of large quantities of hydrogen, hydroxide and carbon in SIMS analysis. Furthermore, sulphur and chlorine were also present. As presented in reference [19], various natural degradation products of zinc contain chlorides and sulphates. These products are formed the presence of Cl^- and SO_4^{2-} ions. The formation reaction are analogue to reaction (6.4), and are expected to result in the formation of e.g. $Zn_5(OH)_8Cl_2{\bullet}H_2O$ (zinc hydroxychloride) and $Zn_4SO_4(OH)_6{\bullet}nH_2O$ (basic zinc sulphate). The origin of the 'foreign' elements was not shown, but these must have resulted either from the compressed air or the glass (vessel or substrate).

Another observation for the H_2O/air samples was the appearance of gaps in the ZnO:Al layer near the glass/ZnO:Al interface. This can be explained by preferred dissolution of the ZnO:Al near the interface. This indicates that ions from the glass have played a catalytic role in the etching of the ZnO:Al, for example by a local change in pH. As mentioned above, especially silicon and calcium can migrate through the grain boundaries from borosilicate glass. Possible candidates for ions with a catalytic role are therefore for example basic SiO_3^{2-} or Ca^{2+}. ZnO:Al dissolves both under basic conditions (pH>12) and acidic conditions (pH<6), while it is stable in a pH between 6 and 12 [19], but it cannot be distinguished which reaction is more likely. However, since CO_3^{2-} is probably involved, an acidic reaction is the most likely.

A significant pH change was not observed, but the volume of formed H^+ or OH^- has been very small compared to the total volume of the H_2O. Therefore, a local change in pH is possible even when no significant pH shift in the H_2O has been observed.

The changes in optical properties of the H_2O/air sample compared to e.g. H_2O/O_2 can be explained by two phenomena:

1. An increased transmission from 1000-2400 nm: this can be explained by a decrease of the carrier concentration. This is supported by the change in carrier concentration as observed in the electrical measurements.
2. The disappearance of the fringes (350-950 nm) as well as decreased reflection (1700-2400 nm): this can be explained by increased scattering caused by increased void formation of the ZnO:Al at the glass/ZnO:Al interface, due to the dissolution of the ZnO:Al.

6.4.3.5 Proposed reaction products

Reference [25] proposes the formation of the major corrosion products of zinc under sheltered conditions and shows a reaction sequence from zinc hydroxide to the chlorides and sulphates. It is suggested that $Zn(OH)_2$ is not very stable and reacts to hydrozincite. In the presence of sulphur or chlorine, the hydrozincite can be replaced. Next steps might lead to the formation of sodium containing compounds and products containing both sulphate and chlorine. Since it is concluded that $Zn(OH)_2$ can form from ZnO, Figure 6.18 shows a possible reaction scheme for the degradation of the grain boundaries in zinc oxide.

Since carbon and sulphur are mainly found in the top of the samples in the SIMS measurements, it is expected that the hydroxycarbonate and the hydroxysulphate are surface compounds. However, the chloride-compounds and the hydroxide will be present in a larger piece of the sample and therefore have a larger impact on the change in the electrical parameters.

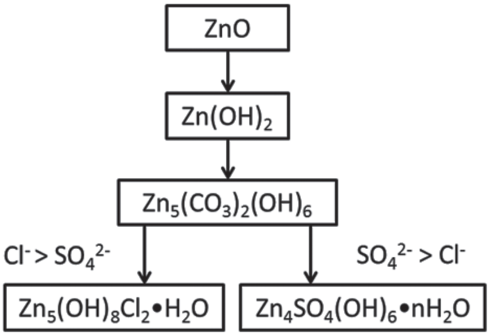

Figure 6.18

General reaction scheme for the degradation of zinc oxide based on reference [25].

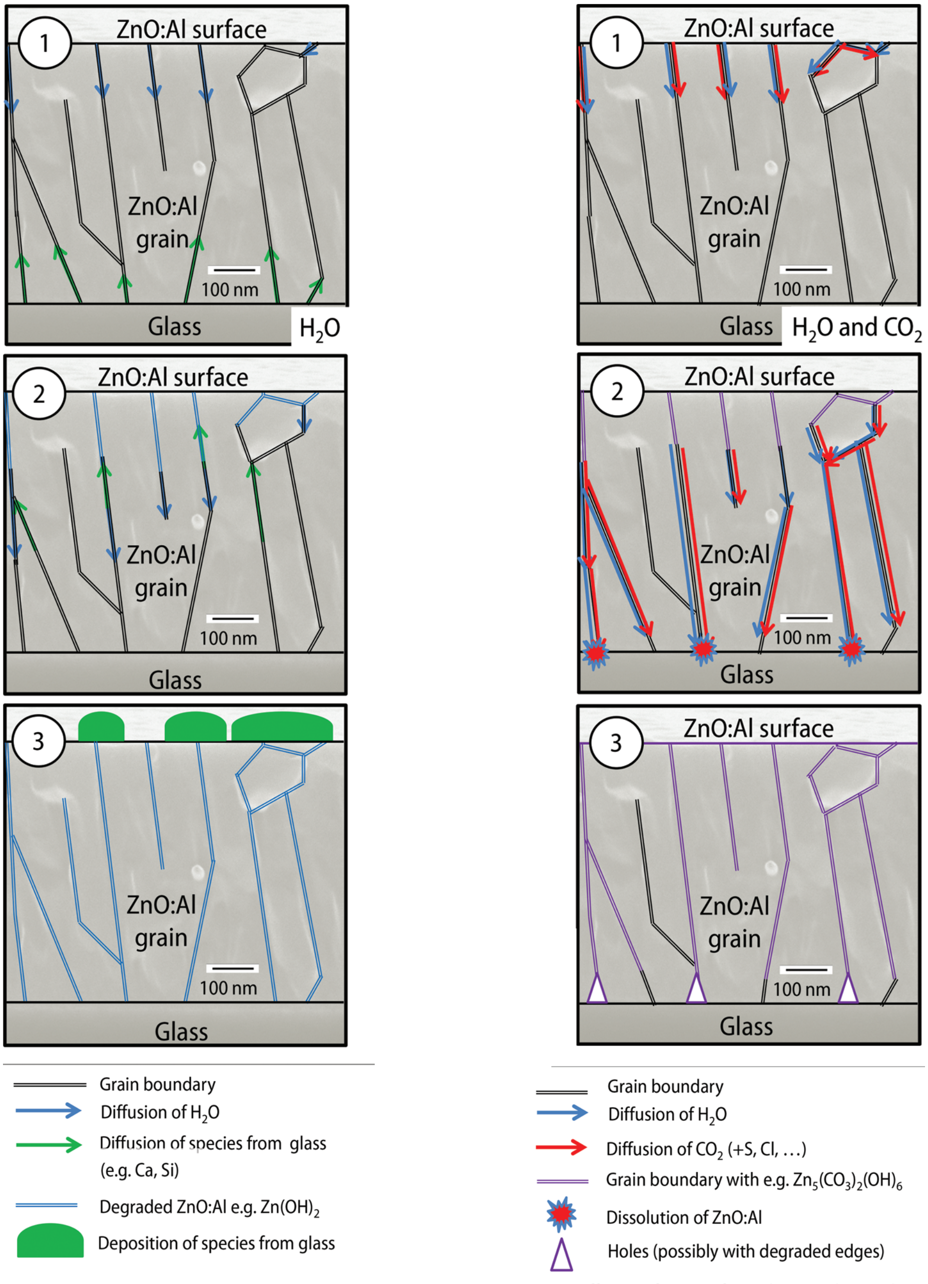

Figure 6.19

Proposed degradation mechanism for thin film ZnO:Al in the presence of (top) H_2O *and (bottom)* H_2O *and* CO_2*. In the latter case, the diffusion of species from the substrate is omitted for clarity. Stain formation is only observed when these reaction products cannot directly dissolve.*

6.4.4 Degradation mechanism based on diffusion of species

Based on the knowledge that diffusion of both small elements from glass and small atoms or molecules from the environment occur, we propose that diffusion occurs in two directions. The reaction down leads to an increased resistivity or even dissolution, while the upward diffusion (green) does not seem to influence the electronic properties. However, this upward diffusion has a minor impact on the optical properties (Figure 6.19).

1.
- Small molecules, like water, carbon dioxide as well sulphur and chlorine species diffuse from the environment into the grain boundaries.
- Small elements, like calcium, silicon and aluminium leach from the glass and enter the grain boundaries.

2
- The small molecules react with the grain boundaries, which results in the increased potential barriers and thus decreased mobility. The rate of this reaction is determined by diffusion and is different per element. The hydroxide and CO_2 based elements have a higher diffusion rate than sulphur and chlorine species. The elemental species arrive in the grain boundaries, where they react, leading to the formation of e.g. $Zn(OH)_2$ or $Zn_5(CO_3)_2(OH)_6$, the complete dissolution of the material, or to adsorption of these species.
- Calcium, silicon and aluminium reach the zinc oxide surface. When soda lime glass is used, this likely also happens with sodium

3
- When reactions or adsorption occur, the grain boundaries can be saturated, leading to a slower decrease in mobility.
- Spots and stains can form due to reactions of calcium, silicon and aluminium with carbon and oxygen. When the samples are removed from the climate chamber, drying stains are formed due to the evapouration of residual moisture at the surface, while in solution these species do probably dissolve directly.

6.5 Conclusions

Sputtered thin ZnO:Al films on borosilicate glass were exposed to damp heat (85°C/85% RH) and to various combinations of atmospheric gases. This led to acceleration of the physical and chemical degradation behaviour. Damp heat treated samples were studied by XRD and optical measurements, which showed that the crystal structure and transmission in the range 300-1100 nm do not change, hereby confirming that the bulk structure stayed constant. It was also observed that the carrier concentration stayed constant, while the Hall mobility and thus the overall resistivity decreased. This implies the increase of potential barriers, which are likely located at the grain boundaries.

Furthermore, white spots appeared, containing elements that migrated from the glass, like silicon and calcium, which reacted with elements from the environment, including oxygen, carbon and chlorine.

Treatment with atmospheric species helped the identification of the species most detrimental to ZnO:Al. We have shown that the driving force behind ZnO:Al degradation is the combined presence of H_2O and CO_2. Individually, gaseous CO_2 does not impact the degradation at all during the tested period, while the individual impact of H_2O is minor: the latter leads to slow diffusion of water down the grain boundaries, where it reacts, possibly resulting in the formation of $Zn(OH)_2$. This leads to a decrease in the electrical mobility. However, in the presence of CO_2, the electrical and optical properties change very quickly. Depth profiling showed that the concentration of hydroxide is a factor 20 higher in the bulk, and even higher at the air/ZnO:Al and the ZnO:Al/glass interface, while carbon, hydrogen, chlorine, sulphur were also observed. Exposure to H_2O and CO_2 also led to local dissolution of the ZnO:Al at the ZnO:Al/glass interface. Additionally, it was observed that the roles of oxygen and nitrogen in ZnO:Al degradation are very small.

Together, these experiments shown that ZnO:Al degradation mostly led to a decrease in mobility, likely caused by an increased potential barrier at the grain boundary. This effect on the mobility is limited when only H_2O/OH^- diffuses down, which can lead to the formation of $Zn(OH)_2$ or adsorption of OH^-. In the presence of CO_2, the effect on the mobility is larger, probably due to the formation of $Zn_5(OH)_6(CO_3)_2$ or a similar molecule in the grain boundaries. Furthermore, chlorine and sulphide were found in the top layer of the degraded samples, which suggest that e.g. $Zn_5(OH)_8Cl_2 \cdot H_2O$ and $Zn_4SO_4(OH)_6 \cdot nH_2O$ can also be present.

6.6 Acknowledgements

I would like to thank Henk Steijvers, Linda van de Peppel, Harmen Rooms, Arthur Eijk, Hans van der Veer, Emile van Veldhoven and Ester de Vrees (TNO) and Bertil Okkerse (Philips Innovation Services) for their assistance by the measurements, analysis and the building of the setup. I would also like to thank Arjan Hovestad and Paul Poodt (TNO) for the fruitful discussions.

6.7 References

[1] J. Wennerberg, J. Kessler, L. Stolt, Proc. 16th EU-PVSEC (2000) 309–312

[2] D. Greiner, S. Gledhill, C. Köble, J. Krammer, R. Klenk, Thin Solid Films 520 (2011) 1285–1290

[3] E. Ando, M. Miyazaki, Thin Solid Films 516 (2008) 4574–4577

[4] T. Minami, T. Miyata, Y. Ohtani, T. Kuboi, Phys. Status Solidi: Rapid Res. Lett., 1 (2007) 31–33

[5] Z. Zhan, J. Zhang, Q. Zheng, Da. Pan, J. Huang, F. Huang, Z. Lin, Crystal growth and design, 11 (2011) 21-25

[6] T. Tohsophon, J. Hupkes, S. Calnan, W. Reetz, B. Rech, W. Beyer, N. Sirikulrat, Thin Solid Films 511 – 512 (2006) 673 – 677

[7] W. Lin, R. Ma, J. Xue, B. Kang, Sol. Energy Mater. Sol. Cells 91 (2007) 1902–1905

[8] I. Hüpkes, J. Owen, M. Wimmer, F. Ruske, D. Greiner, R. Klenk, U. Zastrow, J. Hotovy, Damp heat stable doped zinc oxide films, Thin Solid Films 555 (2014) 48-52

[9] R. Feist, S. Rozeveld, M. Mushrush, R. Haley, B. Lemon, J. Gerbi, B. Nichols, R. Nilsson, T. Richardson, S. Sprague, R. Tesch, S. Torka, C. Wood, S. Wu, S. Yeung, M. T. Bernius, Proc. 33rd IEEE PVSC (2008) 1-5

[10] F. Pern, B. To, C. De Hart, X. Li, S. Glick, R. Noufi, Proc. SPIE 7048 (2008)

[11] K. Sundaram, A. Khan, Thin Solid Films 295 (1997) 87-91

[12] K. Ellmer, A. Klein, B. Rech, Transparent Conductive Zinc Oxide, basics and applications in Thin Film Solar Cells, Springer-Verlag: Berlin, Germany (2008)

[13] D. Greiner, N. Papathanasiou, A. Pflug, F. Ruske, R. Klenk, Thin Solid Films 517 (2009) 2291–2294

[14] H. Liu, V. Avrutin, N. Izyumskaya, U. Ozgur and H. Morkoc, Superlattices and Microstructures 48 (2010), 458-484

[15] J. Kang, M. Lee, D. Kim, Y. Lim, W. Seo, H. Choi, Current Applied Physics 11 (2011) S333-S336

[16] J. Steinhauser, S.Meyer, M. Schwab, S. Faÿ, C. Ballif, U. Kroll, D. Borrello, Thin Solid Films 520 (2011) 558-562

[17] W. Beyer, U. Breuer, F. Hamelmann, J. Hüpkes, A. Stärk, H. Stiebig, U. Zastrow, Mater. Res. Soc. Symp. Proc. 1165 (2009) 209-214

[18] F. Warkusz, Electrocomponent Science and Technology, 5 (1978) 197-199

[19] J. Seto, J. Appl. Phys. 46 (1975) 5247-5254

[20] X. Zhang, Corrosion and electrochemistry of Zinc, Springer (1996)

[21] H. Gerischer, Journal of Electrochemical society 113 (1966) 1174-1182

[22] W. Preis, H. Gamsjäger, Monatshefte für Chemie 132 (2001) 1327-1346

[23] A. Goux, T. Pauporté, J. Chivot, D. Lincot, Electrochimica Acta 50 (2005) 2239-2248

[24] Puigdomenech, I.,MEDUSA: Make Equilibrium Diagrams Using Sophisticated Algorithms. HYDRA: Hydrochemical Equilibrium-Constant Database. http://www.kemi.kth.se/medusa

[25] I. Odnevall, C. Leygraf, Reaction sequence in atmospheric corrosion of zinc ASTM STP 1239, American Society for Testing and Materials, Philadelphia, 1994

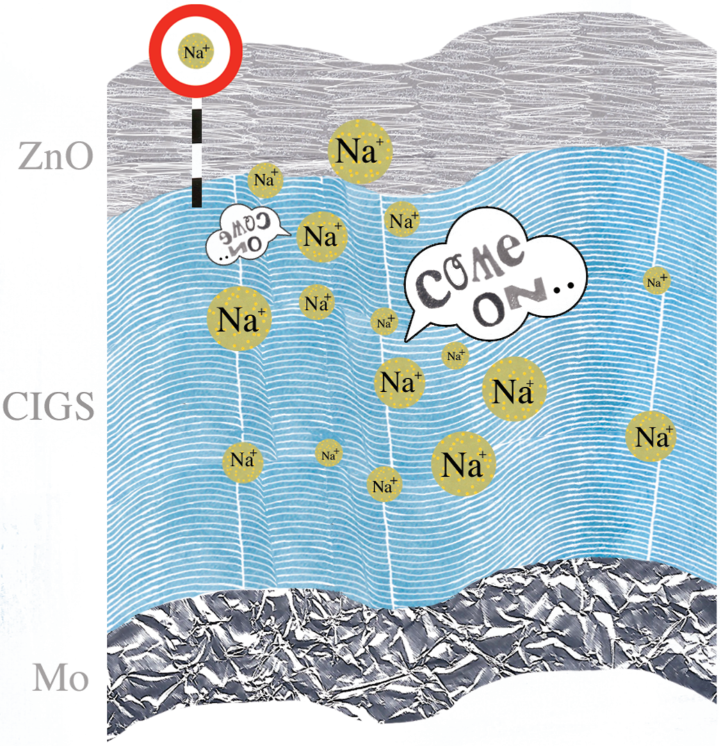
Na^+
ZnO
Na^+
Na^+
COME ON..
Na^+
Na^+
COME ON..
Na^+
Na^+
Na^+
Na^+
Na^+
CIGS
Na^+
Na^+
Na^+
Na^+
Na^+
Na^+
Na^+
Mo

CHAPTER 7

The impact of alkali elements on the degradation of CIGS solar cells

This chapter is based on the following publication:
M. Theelen, V. Hans, N. Barreau, H. Steijvers, Z. Vroon and M. Zeman,
The impact of alkali elements on the degradation of CIGS solar cells,
Accelerated publication in Progress in Photovoltaics: Research and Applications 23 (2015) 537–545

Abstract

Cu(In,Ga)Se$_2$ based thin film solar cells require incorporation of a small amount of especially sodium and potassium into the absorber layer to obtain high efficiencies. However, the influence of these elements on CIGS solar cell stability is not yet known. Therefore, unencapsulated CIGS solar cells with high and low contents of sodium (Na) and potassium (K) were exposed to damp heat and illumination. The solar cells with a high alkali (Na, K) content exhibited higher initial conversion efficiencies, but degraded severely within 100 hours, while the alkali-poor samples kept relatively stable performance under damp heat and illumination.

The degradation of the samples with a high alkali content resulted in the formation of sodium rich spots on the top ZnO:Al surface of the samples. This is likely caused by light-induced Na^+ migration via the grain boundaries in the absorber to the depletion region, accumulation of Na^+ at the depletion region and subsequent transport through the depletion region due to the lowering of the internal electric field caused both by the Na^+ accumulation and illumination. The migration resulted in the formation of shunt paths, which reduced the shunt resistance and open circuit voltage and can even lead to the formation of cracks in the solar cell. Furthermore, ingression of water into the ZnO:Al is expected to be responsible for a slow but steady increase in series resistance for both high and low alkali solar cells. Additionally, sodium migration led to a severe increase of the series resistance in case of alkali-rich samples.

7.1 Introduction

This chapter focuses on the identification of the mechanisms that are involved in CIGS solar cell degradation. More information about long term stability of CIGS absorbers and solar cells can be found in chapters 2.3.2 and 2.4 respectively. The impact of the alkali elements sodium and potassium on the degradation behaviour of CIGS solar cells was studied. These elements are used in CIGS solar cells in order to obtain high conversion efficiencies [1,2]. However, earlier studies demonstrated that either or both elements could have a negative impact on the long-term stability of CIGS modules [3-6]. More information can be found in chapter 2.3.2.4.

7.1.1 Impact of sodium and potassium

$Cu(In,Ga)Se_2$ based thin film solar cells require incorporation of a small amount of especially sodium and potassium into the absorber layer to obtain high efficiencies. This increase in efficiency is obtained by an increase in hole carrier density, which results in the improvement of p-type conductivity and therefore an improved open circuit voltage (V_{oc}) and fill factor (FF). Several models have been proposed to account for the increase in the hole carrier density. The models proposed in the literature are, for example:

(i) Minimisation of compensating antisite In_{Cu} donor defects by sodium.
(ii) Increase in acceptor density due to antisite Na_{In} defects.
(iii) the neutralisation of donor-like selenium vacancy defects by oxygen atoms accompanied by the presence of sodium during the growth [7].

Furthermore, sodium is also known to affect the CIGS growth orientation and enhance (112) texture formation. It is also reported that sodium addition leads to enhanced grain size [8], although in this work, the opposite effect has been observed.

Similar effects have been observed from other alkali elements including potassium, but knowledge about the effect of this element is even more limited. However, recent efficiency records have been obtained [2] by the introduction of potassium. The main reason for enhanced efficiency was the possibility to add more gallium to the CIGS layer when potassium is present, thereby allowing higher bandgap CIGS. This again allows the deposition of CIGS material with a higher V_{oc}.

The average concentration of sodium in CIGS films is approximately 0.1%. Recent studies [9,10] have shown that the concentration varies a lot within the CIGS layer: sodium contents are very high at the grain boundaries (around 1%) compared to the CIGS bulk (30-150 ppm) (Figure 7.1).

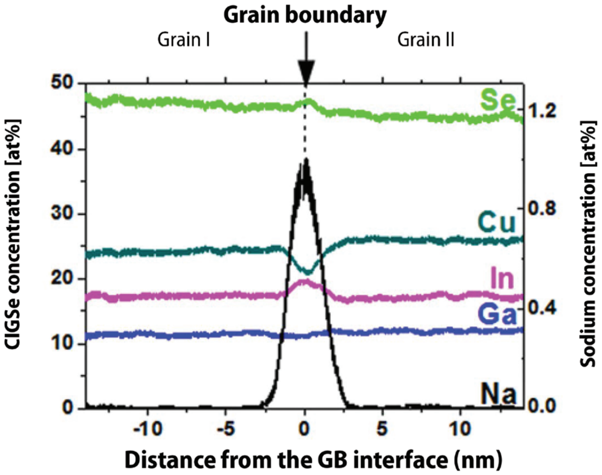

Figure 7.1

Copper, indium, gallium, selenium and sodium concentration profiles perpendicularly to the grain boundary interface in a CIGS layer on the end of the three stage coevapouration process [9].

7.1.2 Sodium introduction

Sodium can be applied in various ways: When soda lime glass is used as a substrate, sodium and potassium are often supplied during the growth process by diffusion from the substrate through the molybdenum back electrode into the CIGS layer. For substrates that do not contain the required amount of sodium or for more controlled sodium addition, alternative methods such as deposition of a sodium containing back contact layer (Mo:Na) or the use of NaF as sodium source. The latter can be used by deposition of a precursor layer, co-evapouration during the CIGS growth process or evapouration of NaF after the CIGS growth in a post-deposition treatment (PDT) [8]. In this case, the sodium and potassium have only been obtained from the soda lime glass substrates.

This study focuses on the impact of damp heat and illumination on unencapsulated CIGS solar cells with high and low concentrations of the alkali elements. The impact of these elements on the stability performance of the solar cells is evaluated. The mechanisms which might be responsible for the degradation of CIGS solar cells under simultaneous damp heat and illumination conditions are proposed.

7.2 Experimental

CIGS solar cells were deposited as described in chapter 3.2. Alkali-rich solar cells were produced following the standard deposition procedure, while alkali-poor solar

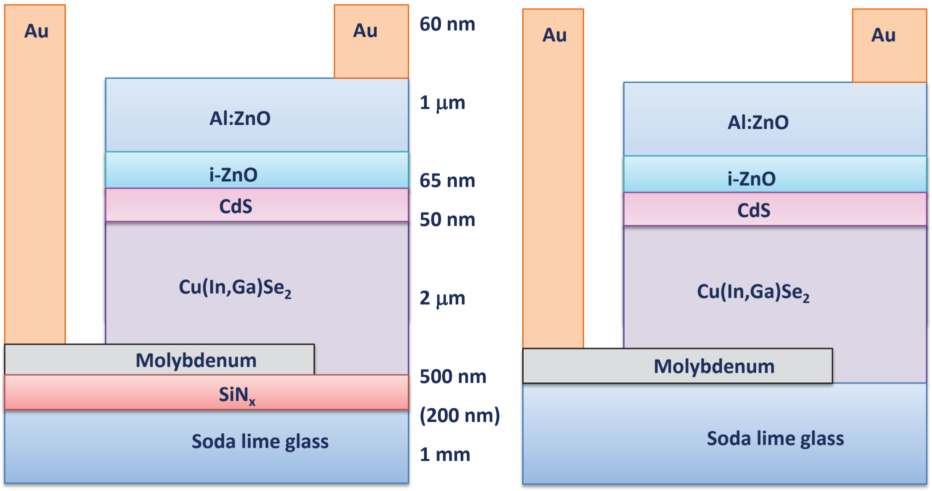

Figure 7.2

Schematic cross-section of the alkali-poor CIGS solar cells with a SiN_x *barrier as used in this study (left) and the alkali-rich sample (right) (not to scale).*

cells were deposited on a soda lime glass substrate with a SiN_x barrier in the same deposition runs under exactly the same conditions. A schematic cross-section of the samples is shown in Figure 7.2.
Six samples from both solar cell types were placed in the hybrid degradation setup, which is described in chapter 3.3. There they were exposed to an atmosphere of 85°C and 85% RH combined with 1000 W/m^2 AM 1.5, which allowed the in-situ monitoring of the degradation behaviour. Two samples were kept in a glovebox as reference samples. The samples were degraded as is described in chapter 3.3. IV curves of all solar cells were measured every 3 or 8 minutes. The temperature of all cells was measured individually, since the cells are heated by the illumination: the actual sample temperature was 107±1°C.

In order to study the progress of the degradation process, the degraded samples were progressively removed from the setup. The first samples were removed after 165 hours (one sample per type), next samples after 365 hours (one sample per type), then after 525 hours (one sample per type) and finally after 778 hours (three samples per type). One sample showed strange results, including a very rapid increase of series resistance and a relatively slow increase of the open circuit voltage, and was omitted from this study. The alkali-poor solar cells in this study have a cell size of 0.33±0.03 cm^2, while the alkali-rich samples are 0.31±0.01 cm^2.

7.2.1 Sample analysis

The samples were analysed before and after damp heat-illumination exposure with optical microscopy, current-voltage (IV) measurements, current voltage measurements as a function of temperature, spectral response (SR) measurements and Secondary Ion Mass Spectroscopy (SIMS).

Optical microscopy was carried out using a Leica Wild M400 microscope, primarily used at 8x and 64x magnification, coupled with a Leica DFC 320 camera and Leica Application Suite software, version 4.3.0.

Ex-situ (IV) measurements were obtained using an OAI TriSol Solar Simulator attached to a KeithleySourceMeter 2400 and controlled using IV runner software, version 1.4.0.6. The series and shunt resistances are obtained by the determination of the steepness at the end of the current voltage curves. The SR and therefore also of the external quantum efficiency (EQE) spectra, were taken using a SR setup. No bias illumination is used during EQE measurements.

Current voltage measurements as a function of temperature were taken in a Cryostat Janis VPF-100 with sample holder controlled by a Lake shore 332 temperature controller. Current voltage curves are obtained with a Keithley Source Meter 2600A using software in LabView 7.1.

Cross-section scanning electron micrographs were recorded with the FEI XL40 FEG microscope using backscatter electrons. SEM-EDX measurements in top view were performed using a JEOL JSM-6010LA IntouchScope.

SIMS depth profiles were performed using a magnetic sector Cameca IMS 7F instrument in the positive mode, the primary beam intensity was 57nA with 5keV acceleration and it was rastered by 200x200 μm^2. As a guide for the eye, several SIMS spectra of sodium, potassium and hydroxide before and after degradation have been multiplied with a factor close to one along the x-axis to provide better comparison of the spectra.

7.3 Results

7.3.1 Visual changes

Photography and optical microscopy were used in order to study the visual changes of the surface of the samples. Before degradation, the top surface of all samples exhibited a homogeneous blue area, as is shown for an alkali-poor sample in Figure 7.3. Due to damp heat and illumination exposure, small grayish spots occurred on the top surface of all alkali-rich samples already after 165 hours, while later also white spots were observed. The spots were ranging in size from about 10 to 150 micrometres. The top surface of these samples is shown in Figure 7.3.

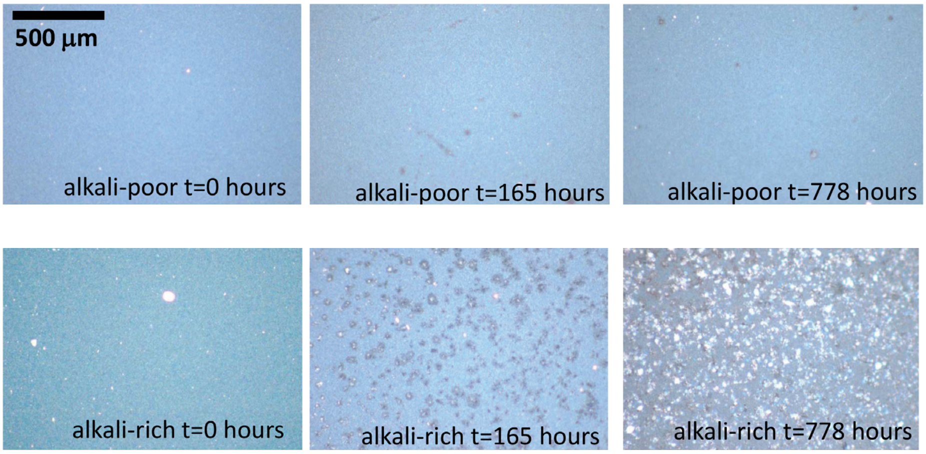

Figure 7.3

Microscopy picture of the surface of alkali-poor samples at t=0 hours, t=165 hours and t=778 hours, and of alkali-rich samples at t=0 hours, t=165 hours and t=778 hours. The size bar depicts 500 µm.

It should be noted that similar samples exposed to only damp heat (samples at 105°C in a 85°C/85% RH chamber) did not show these spots. Surprisingly, these spots were not detected on the alkali-poor samples, not even after 778 hours of degradation. A small number of spots was detected alongside the edges of these samples, but the cutting of the samples might have damaged the SiN_x barrier layers near the edge.

7.3.2 Development of solar cell parameters

The initial average solar cell parameters of alkali-poor and alkali-rich CIGS solar cells are shown in Table 7.1.

Initially, the alkali-rich solar cell samples had a higher V_{oc}, fill factor and efficiency than the alkali-poor samples. This can be expected, since the presence of sodium and potassium increases the electronic quality of as-deposited CIGS material [1,2].

All solar cell parameters were continuously monitored and logged as a function of degradation time in the setup. The evolution of these parameters is shown in Figure 7.4, while individual current voltage curves of two solar cells are shown in Figure 7.5. It should be noted that the values of the parameters are determined from measurements at elevated temperatures and are thus different (generally lower) than the values given in Table 7.1.

Figure 7.4 demonstrates demonstrate that although the alkali-rich samples had higher initial solar cell parameters, the exposure to damp heat and illumination led to much faster decrease in V_{oc}, fill factor and efficiency.

The decrease in performance of the alkali-rich samples is especially large for the shunt

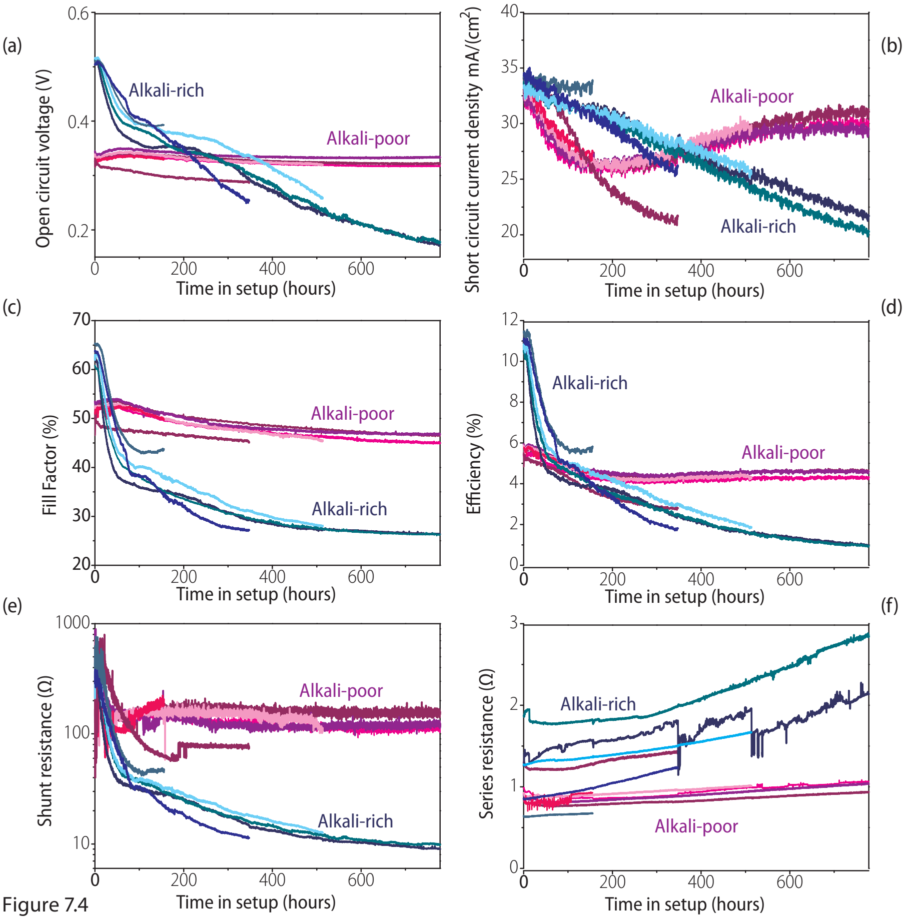

Figure 7.4

Evolution of the electrical parameters (a) Open circuit voltage (b) short circuit current density (c) fill factor (d) efficiency (e) shunt resistance (f) series resistances as a function of time in the setup taken at 107±1°C. The pink and purple lines represent the alkali-poor samples, while the blue lines represent the alkali-rich samples.

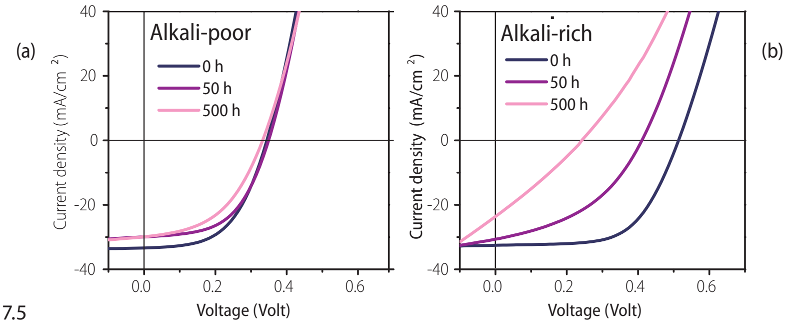

Figure 7.5

Current voltage curves of one (a) alkali-poor and one (b) alkali-rich sample before exposure and after 50 and 500 hours in the setup at sample temperatures of 105.0±0.5 and 106.9±0.5°C respectively.

Table 7.1 The average solar cell parameters of the alkali-poor and alkali-rich solar cells and their standard deviations.

	Alkali-poor			Alkali-rich		
	Before (STC)	Before (107±1°C)	After (107±1°C)	Before (STC)	Before (107±1°C)	After (107±1°C)
V_{oc} (mV)	528±5	331±11	324±9	667±6	513±1	173±0
J_{sc} (mA/cm^2)	29.9±0.1	32.6±0.4	30.0±0.4	30.2±0.2	33.8±0.3	20.9±1.2
FF (%)	63±2	52±2	46±1	71±1	62±1	26.3±0.1
Efficiency (%)	10.0±0.3	5.6±0.3	4.5±0.2	14.3±0.3	10.7±0.3	0.9±0.1
R_s (Ω)	4.3±0.6	0.9±0.1	1.0±0.1	4.6±0.6	1.6±0.4	2.5±0.5
R_{sh} (Ω)	1787±532	323±172	135±23	2505±372	399±20	9±1
$R_{sh\ dark}$ (kΩ)	74±19			23±15		

The first columns show all samples measured under standard test conditions (STC) before degradation. The short circuit current and efficiency in these columns are corrected based on EQE measurements. The other columns are the electrical parameters recorded with the setup at 107±1°C and only include the samples degraded for 778 hours.

resistance, fill factor and open circuit voltage. The decrease is the strongest during the first 100 hours, while from 100 to 778 hours, these parameters still show a decrease, but at a lower rate. The largest decrease can be found for the shunt resistance, which had a final value around 10Ω. This value indicates that the solar cells no longer functioned as diodes. The decrease of the short circuit current did not happen in two phases, but occurred more or less linear as a function of time.

The effect was different for the alkali-poor samples, which demonstrated reasonable stable fill factors and open circuit voltages, while the shunt resistance only showed a small decrease in the first 100 hours. The short circuit current first decreased, but increased later for all measured samples.

The series resistance increased for both types, but the rate was higher for the alkali-rich samples. When the samples degraded for 525 hours and longer are included, the degradation rates are 0.28±0.05 mΩ/h for the alkali-poor samples, while the series resistance increases with 1.0±0.4 mΩ/h for the alkali-rich samples.

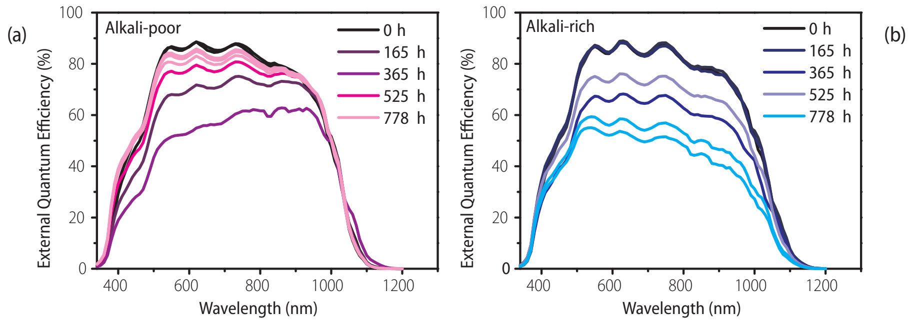

Figure 7.6:

The external quantum efficiency (EQE) curve of the (a) alkali-poor and (b) alkali-rich CIGS solar cells presented for different degradation times

7.3.3 Development of the EQE

More information about the decrease of the current was obtained by External Quantum Efficiency (EQE) measurements. Before degradation, the J_{sc} of the alkali-poor samples was 29.9±0.1 mA/cm^2, while the alkali-rich samples gave 30.2±0.2 mA/cm^2. The EQE curves were also measured after removal from the hybrid degradation setup, thereby showing curves for different degradation times (Figure 7.6). It should be noted that these figures do not depict two samples at different degradation times, but 15 different samples.

When the alkali-poor samples were studied, the EQE measurements confirmed that the short circuit current first decreased, followed by a recovery. This early drop and recovery occurred more strongly for the wavelengths below 850 nm.

The alkali-rich samples did show a more steady decline of the J_{sc} (see Figure 7.4). It showed that the degradation led to a stronger decrease in the high wavelength region. The alkali-poor samples, on the other hand, retained most of their response at this wavelength, but had a reduced EQE around 600 nm after 165 and 365 hours. This difference can indicate that the alkali-rich and alkali-poor solar cells had material changes in different depths in the CIGS absorber, since low wavelength photons are mostly absorbed in the top part of the film, while high wavelength photons are more absorbed in the bottom part, since their absorption occurs at a lower rate in CIGS absorbers. These changes can therefore either indicate that the generation of electron-hole pairs changed differently within different parts of the CIGS absorbers or that electrons obtained at different depths show different recombination behaviour.

In some degraded samples, it was shown that the wavelength range from 350-500 nm increased. If the graphs are normalised, it becomes clear the degradation leads to a relative increase in this region. This phenomenon is likely related to a change in the CdS region. Similar preferential increase in the blue response in EQE was earlier

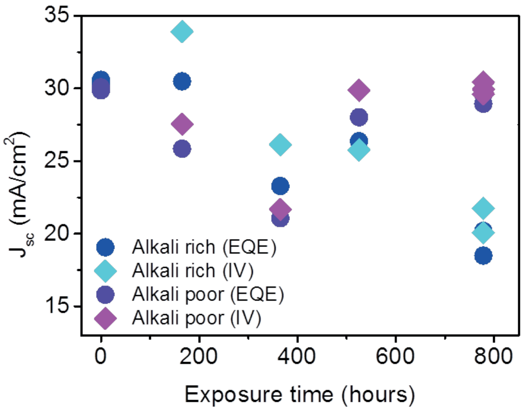

Figure 7.7

Short circuit current density of the alkali-rich and alkali-poor samples as determined by EQE and from the IV measurements as obtained in the hybrid setup.

observed by Ramanathan et al. [11], who observed this due to two minutes annealing at 250°C of CIGS solar cell containing a CdS layer. The reasons for this change are still unclear, but various suggestions were given: they proposed that a reaction between i-ZnO and CdS occurred, resulting in the formation of an intermediate material with a high bandgap. Suggested candidates are $Cd_{1-x}Zn_xS$ and $ZnO_{1-x}S_x$, but no evidence of these new species have been found in this study.

The short circuit current density as measured by both EQE and IV was also compared (Figure 7.7). In this study, these measurements show good similarity for the alkali-poor samples, while the alkali-rich samples can show deviations of up to 3.4 mA/cm^2. In earlier studies, this difference could be as large as 12 mA/cm^2 or 41% of the highest value. In these cases, the EQE values were always higher than the IV values, while in this experiment, the general trend is in the opposite direction. These difference might have been caused by differences in light intensity between IV and EQE, but this theory has not been validated yet.

7.3.4 Development of temperature dependent IV

The temperature dependent current voltage curves (IV(T)) were measured in order to study the defects in the samples. Figure 7.8 and 7.9 show the IV curves as a function of temperature under illumination before degradation and after 165 hours exposure under illumination and in darkness respectively. It was observed that all non-degraded samples, both in light and darkness show losses which cannot be explained as simple series resistance. The alkali-rich sample under illumination also showed a kink at lower temperatures, indicating recombination for majority carriers under forward bias. This difference in electronic transport occurred at temperatures below ~190K, but did not

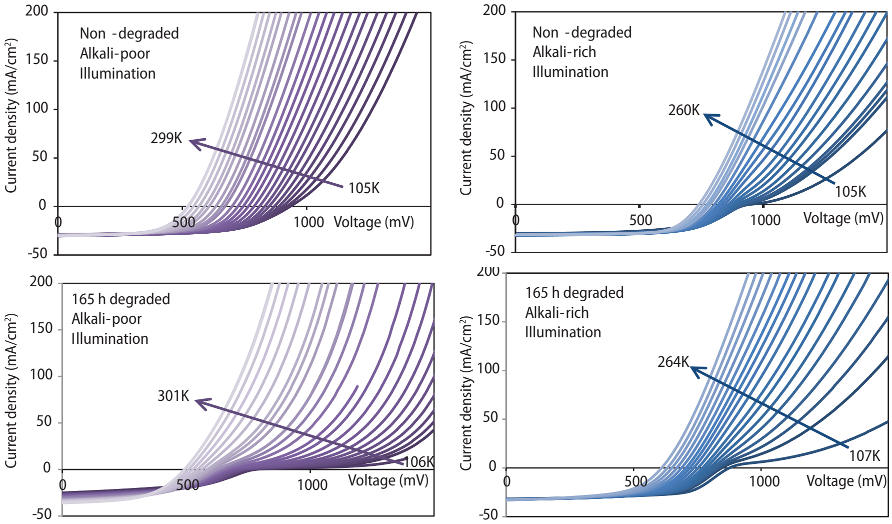

Figure 7.8

Current-voltage curves at different temperatures between 100 and 300/260K for the non-degraded CIGS solar cells and solar cells degraded for 165 hours with barrier (purple) and without barrier (blue) taken under illumination.

seem to prevent the formation of decent solar cell, as is shown in among others Table 7.1. The occurrence of a kink was not observed in the IV(T) spectra of the alkali-poor sample under illumination. Both samples did also not show a kink in darkness.

After 165 hours of degradation, the kink could still be found for the alkali-rich sample under illumination. For this specific sample, the impact of degradation seemed reasonably small, which is surprising since in-situ IV measurements indicated that almost half of the efficiency at 107°C has disappeared. However, at lower temperatures, the relative loss of efficiency might have been smaller. It can be expected that other samples, which are more degraded, show more modifications in the curves.

After degradation, the alkali-poor sample did also demonstrate the appearance of a kink in the illuminated IV curves starting for temperatures as high as ~250K. This was surprising, since this sample did not show large changes in their electrical parameters due to damp heat illumination exposure. This kink is still present after 365 hours degradation (not depicted). The IV(T) of samples degraded for more than 365 hours were not measured.

In darkness, the exposure to damp heat and illumination did not lead to the appearance of kinks for either samples. However, the steepness of these curves at especially low temperature did decrease. Generally, it was concluded that the damp heat illumination exposure did not only affect the series resistance, but also led to a changes in the electrical transport.

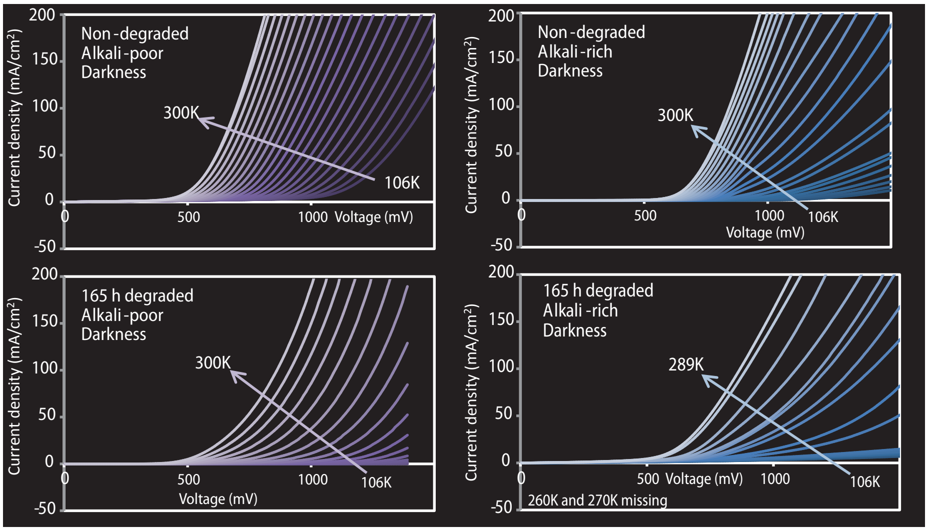

Figure 7.9

Current-voltage curves at different temperatures between 100 and 300K for the non-degraded CIGS solar cells and solar cells degraded for 165 hours with barrier (purple) and without barrier (blue) taken in darkness.

7.3.5 Changes in structure and composition

The samples were also studied by SEM-EDX. Figure 7.10 shows high magnification SEM pictures before, during and after degradation. Before degradation, both the alkali-rich and alkali-poor samples show ZnO:Al grains with some tiny white particles (around 1 micrometres). However, the 'before degradation' pictures were taken after months of storage, mostly in the glovebox, while a fresh sample contained less of these white spots (not shown). Apart from some dust particles and incidental scratches, these samples further both looked mostly homogeneous, as is also shown in Figure 7.3. However, some early degradation spots were already observed on the non-degraded alkali containing samples, so these are also depicted in Figure 7.10. Since these SEM pictures are taken after many other measurements and a long time period, it is expected that these spots occurred during the storage and mostly the measurement process.

As already shown on the optical microscopy pictures, spots occur on the alkali-rich sample after degradation. After 165 hours, these spots are generally round, and often have a nucleus. EDX analysis indicate that the spots are rich in carbon, oxygen and sodium, although the latter is hard to detect due to the overlapping signals of sodium and zinc in EDX. The white nuclei are often rich in cadmium, while they also contain higher contents of either cadmium or bromine, which also have overlapping EDX signals. On the other hand, on the alkali-poor samples, barely any change of the samples can be detected after 165 hours of exposure. After 778 hours of exposure, a small amount

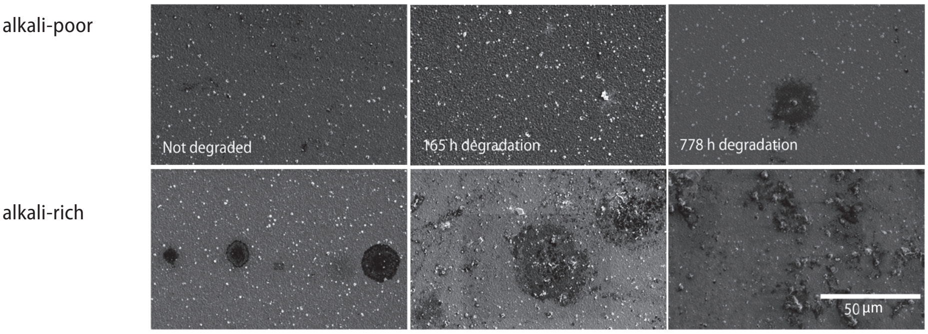

Figure 7.10

SEM pictures at high magnification of the surface of alkali-poor (top) and alkali-rich (bottom) samples before and after 165 and 778 hours of exposure to damp heat and illumination. The pictures were taken at 5kV.

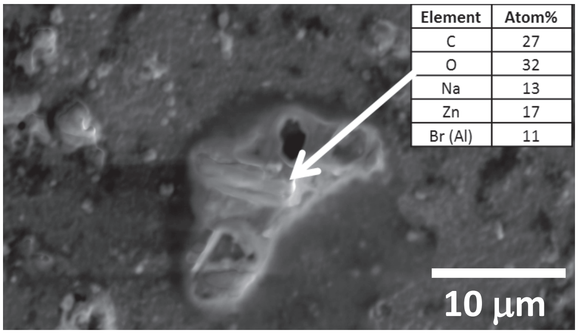

Element	Atom%
C	27
O	32
Na	13
Zn	17
Br (Al)	11

Figure 7.11

SEM picture and EDX values on an alkali-rich sample after 778 hours of exposure to damp heat and illumination

of these degradation spots can also be detected on the alkali-poor samples. One example is shown in Figure 7.10, but it should be taken into account that the majority of the surface is still free of spots. When the alkali-rich samples are taken into account, it is clear that the structure of the sample has been destroyed after very long exposure to damp heat illumination. The well-defined spots have been replaced over the whole surface by figures with holes and small pieces of debris, as is also shown in Figure 7.11. These figures still contain carbon, oxygen, sodium as well as zinc, while bromine as well as aluminium are also present. In some cases, cadmium is also observed.

It is proposed that the carbon originates from the air, while the oxygen can come from the air, but is naturally also present in the ZnO:Al, which is also the case for zinc and aluminium. The sodium likely migrated from the glass, while the cadmium is present in the CdS layer. The most surprising element, bromine, can have originated from the printed circuit boards (PCBs), which have been used as sample holders (see chapter 3). It is possible that volatile bromine species have outgassed from these boards when they were exposed to damp heat and illumination for a very long time.

Additionally, cross-section SEM pictures were also taken, as is shown in Figure 7.12. Although all deposition conditions, except for the introduction of the SiN_x barrier layer, were identical, the samples clearly look different. The molybdenum layer for the alkali-poor sample has a thickness of 0.6 µm, while its thickness is 1.0 µm for the alkali-rich sample, which likely has a more porous structure. Another surprising difference is the CIGS grain size: while it is often stated that the alkali content influences the grain size, an increase in grain size is mostly reported [8]. In this case, the grain size becomes smaller, either due to the present of the alkali content, or due to the changed molybdenum morphology.

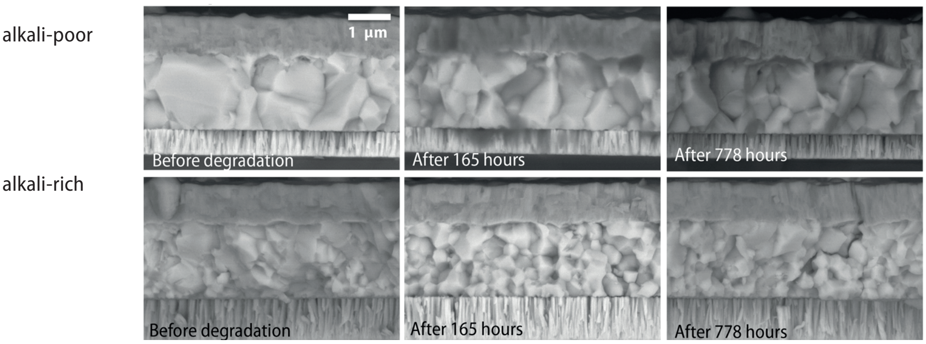

Figure 7.12

Cross-section SEM pictures of the alkali-poor (top) and the alkali-rich (bottom) samples before and after 165 and 778 hours of exposure to damp heat and illumination.

After degradation, no changes in morphology can be detected for either types during the first 165 hours, even though the composition and the electrical properties of the alkali-rich samples had already clearly changed. After 365 hours (not depicted), some small cracks seemed to occur in the alkali-rich sample. However, large impact on the morphology is only visible for this sample after 778 hours, when cracks occurred, as can be seen in Figure 7.12 and Figure 7.13. Additionally, Figure 7.13 shows that the complete structure of the stack has expanded at some positions.

Figure 7.13

Cross-section SEM picture of the alkali-rich sample after 778 hours of exposure to damp heat and illumination.

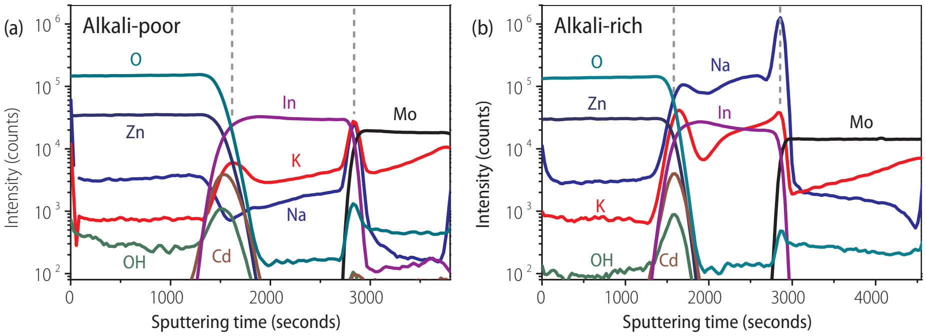

Figure 7.14

SIMS measurements on the (a) alkali-poor and the (b) alkali-rich samples before degradation. For clarity reasons, the elements copper, gallium, selenium and sulphur are omitted. The gray dashed lines indicate the global positions of the zinc oxide, CIGS and Mo layers.

7.3.6 Changes in depth-profiles

The elemental depth profiles of non-degraded and degraded samples were measured by SIMS. It should be noted that no absolute concentrations could be determined with SIMS, since the intensity was not calibrated for these measurements. Since the measured number of counts was largely influenced by the surrounding matrix, no absolute comparison of concentrations between different matrices (e.g. ZnO:Al or CIGS) or different elements could be executed.

The composition of the samples before degradation is shown in Figure 7.14. The width of the cadmium peaks indicate that it is hard to pinpoint exact location For clarity reason, the copper, gallium, selenium and sulphur profiles are omitted. The profiles for these elements as well as indium did not differ significantly between the alkali-poor and rich solar cells.

Figure 7.14 shows the difference in sodium and potassium content between the samples. Before degradation, the sodium is predominantly present at the Mo/CIGS interface and in the CIGS layer. The difference in sodium content between the alkali-poor and alkali-rich samples varies per layer: it differs almost two orders of magnitude in the CIGS bulk, less in the molybdenum layer, while the sodium content in ZnO:Al was similar for both samples. The potassium content followed similar trends, although the difference in magnitude between the alkali-rich and alkali-poor solar cells is smaller. Furthermore, an increase at the pn-junction is very pronounced for this element.

SIMS measurements (Figure 7.15) were executed on the degraded samples, on positions with and without spots (see Figure 7.2). It should be noted that due to the relatively small size and large quantity of the spots, it was hard to probe areas completely free or completely covered with spots with a spot size of 200x200 μm^2.

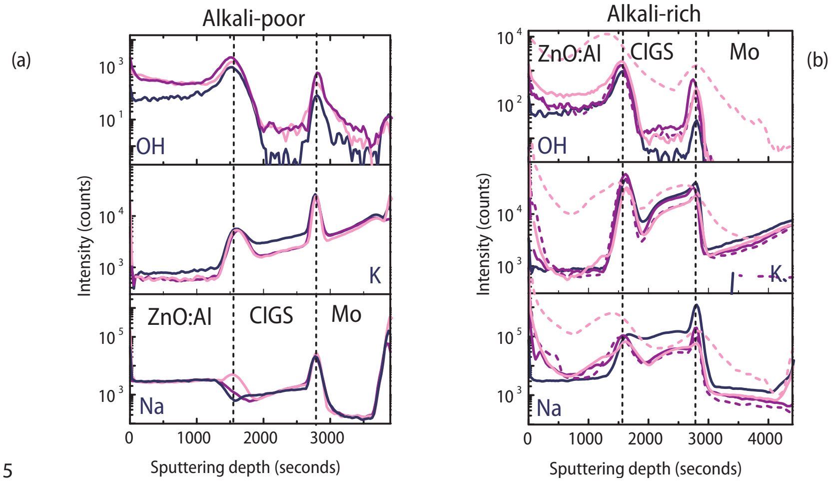

Figure 7.15

Sodium, potassium and hydroxide concentrations as a function of depth in (a) alkali-poor and (b) alkali-rich CIGS solar cells exposed to illumination and damp heat for different periods. The dark blue lines indicate the samples before degradation, the purple lines are the samples after 165 hours of the damp heat illumination exposure, while the light pink colours represent the samples after 778 hours of exposure. The dotted lines represent measurements on a spot, while the continuous line represent spotless area. The left graphs represent the alkali-poor samples, while the right graphs represent the alkali-rich samples.

Due to degradation, the sodium (Na), potassium (K) and hydroxide (OH) distribution in the samples changed (Figure 7.15), while the other species remained more or less constant. An exception should be made for the spots on the alkali-rich samples after 778 hours, where all elements present changed largely, as can be expected based on their completely modified structure (dotted pink lines) (Figure 7.13). It should be noted that no significant changes for the oxygen concentration could be observed, but due to the high concentrations of oxygen in ZnO:Al, any concentration change of oxygen in the pn-region could easily be overlooked. In the spots on the alkali-rich samples after 778 hours, bromine was also detected, while this element was absent before degradation. In shorter degraded samples, and next to the spots, a slight increase of bromine was observed near the ZnO:Al/air interface.

When the hydroxide evolutions were studied, it was observed that this concentration increased equally for both samples. The increase mainly occurred in the ZnO:Al layers, while it also increased in the CIGS layers and at the Mo/CIGS interface.

When looking at the sodium depth profiles, large differences between the two solar cell types were observed: for the alkali-rich samples, the effect of damp heat illumination exposure was very large: within 165 hours damp heat-illumination exposure, sodium migrated from the Mo/CIGS interface and the CIGS bulk to the pn junction region and

the ZnO:Al layer. This effect is stronger within the spots (dotted purple line after 165 hours) than for regions without spots. The sodium migration continued in the same way after 365 hours (not depicted). Migration of potassium also occurred, but was very limited and mainly led to an increase in the top of the ZnO:Al layer.
For the alkali-poor sample, sodium migrated from the Mo/CIGS interface to the pn-junction region. Furthermore, the potassium and sodium profiles were relatively stable.

7.3.7 Reproducibility

Experiments similar to this one have been executed multiple times before on similar samples, as is for example shown in reference [4]. These experiments have shown that the decrease of the solar cell parameters is much slower for samples with a low alkali content. Since several of the earlier samples had spots with a larger size, the SIMS measurements could be executed more precisely. In earlier SIMS profiles, the differences between positions on and next to the spots was therefore even stronger.

7.4 Discussion

The in-situ IV measurements indicated that alkali-poor samples were stable under damp heat-illumination, while the performance of the alkali-rich samples decreased quickly, especially during the first 100 hours. This degradation was accompanied by the appearance of surface spots. SIMS and SEM-EDX measurements in alkali-rich samples indicated that especially sodium and to a lesser account potassium migrated from the CIGS/Mo interface and the CIGS bulk towards the pn-junction and ZnO:Al layer. The sodium migration is stronger on the spots than on spot-free areas. These measurements also indicated that the alkali-rich samples showed a complete change of the sample structureand composition after 778 hours.

The first factor playing a role in the degradation process of the CIGS solar cells is an increase in hydroxide content, which is mainly observed in the ZnO:Al layers in both the alkali-rich and poor samples. This hydroxide increase is likely caused by water and possible CO_2 ingression, which leads to a slow but steady increase of the series resistance for all samples, for example by the formation of hydrozincite in the grain boundaries (see chapter 6) [13]. However, this increase of the series resistance only has a small impact on the performance change and does not explain the differences in degradation behaviour between the samples. We propose that the migration of sodium and possibly potassium has the largest impact on the performance change and leads to the formation of surface spots as well as the decrease of the solar cell parameters.

A negative effect of sodium migration on CIGS solar cells was observed by Fjällström et al. [3]. After the exposure of a 50V bias combined with 85°C on CIGS solar cells, sodium migrated from the glass substrate to the pn-junction, which resulted in a rapid decrease of the conversion efficiency. In this case, the relatively high voltage bias was apparently able to drive sodium from the glass, leading to a potential induced degradation-(PID-)like process, which was also reported by Colli [14].In our work, it is not yet possible to distinguish between the impact of sodium and potassium migration. Because of the limited potassium migration and the results of Fjällström [3], who observed that sodium migration led to degradation, it will be assumed that sodium migration is the most important factor.

7.4.1 Degradation model

In our case the exposure conditions are different since during the damp heat treatment, no voltage bias is applied. The majority of sodium atoms in CIGS are located at the grain boundaries [15], most probably bonded to the adjacent grains dangling bonds. The presence of water likely enables the release of Na^+ ions through the hydrolysis of the bonds between CIGS and sodium. The soda lime glass can also serve as a source of the sodium, but it should be noted that, as far as can be judged from the SIMS spectra, the sodium content in the complete stack does not increase greatly. Therefore, it is likely that the majority of the mobile Na^+ ions originate from the active layer. These Na^+ ions are then free to migrate along the grain boundaries; however, this phenomenon alone can hardly explain the accumulation of sodium at the pn-junction because simple diffusion should rather result in a homogeneous distribution of sodium throughout the layers. The migration of released Na^+ ions is therefore driven by an additional force. In the following, we argue that the driving mechanism is related to illumination.

We consider the energy band diagram in the region of grain boundaries in the CIGS absorber. This band diagram with band bending due to trapped positive charges is shown in Figure 7.16. In the dark, the positive Na^+ should drift from the grain boundaries to the grains due to the internal electric field in the region of the grain boundaries. It is proposed that migration of Na^+ does not occur because of limited solubility of Na^+ in CIGSe compared to that of Cu^+, while it has the same driving force for migration. This hypothesis is supported by the fact that although copper vacancies are certainly present within the grains, allowing the formation of p-type CIGSe, sodium accumulates at the grain boundaries. Therefore, the Na^+ ions are pinned in the grain boundaries. However, the band bending in the region of the grain boundaries is dependent on the density of the photogenerated carriers. Under

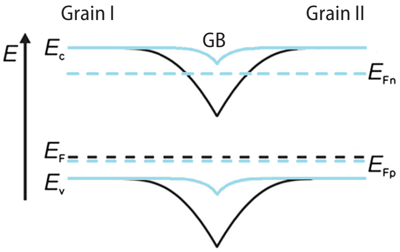

Figure 7.16

Band structure of a grain boundary and two grains in a CIGS absorber with (light blue) and without (black) charge carrier generation caused by illumination (modified after [16]).

illumination a large concentration of charge carriers is generated in the CIGS absorber with a depth profile from a large concentration at the top of the absorber than at the bottom. The trap states related to the defects in the grain boundaries are filled with photogenerated carriers and consequently the band bending at the vicinity of the grain boundaries is reduced. Therefore, the internal field at the grain boundaries decreases. The enhanced concentration of primarily minority carriers contributes to lowering the internal electric field. Under illumination, an upward potential gradient for Na^+ is created that facilitates the migration of ions towards the pn-junction.

Additionally, under open circuit conditions, the build-in voltage at the pn junction is reduced under illumination. Consequently, the electrostatic barrier that the Na^+ ions have to overcome to cross the pn-junction is reduced.

These effects, induced by the illumination and open circuit conditions, favour the migration of Na^+ through the grain boundaries (Figure 7.17, step 1). It is also proposed that the elevated temperature of the samples leads to faster migration.

The positively charged Na^+ ions can then arrive at the pn-junction. Since the internal electric field of the depletion region of the pn junction does not facilitate the drift of the Na^+ ions across the depletion region, they cluster at the depletion region together to form sodium rich spots. Accumulation of the Na^+ ions in clusters counterbalances the internal electric field of the depletion region of the pn-junction (Figure 7.17, step 2). The presence of sodium naturally influences the electrical behaviour of the diode. Analogous to Shin et al. [17], who demonstrated that high concentrations of sodium near the CIGS/CdS interface deteriorated conversion efficiencies, we propose that this has a negative impact on the solar cell performance. The clustering of the positively charged Na^+ can locally reduce the electric field of the depletion region, which both influences the electrical properties of the diode and favours the accumulation of further additional Na^+ ions (no more barrier to overcome). This can lead to the local formation of a shunt path, which are then observed as the formation of spots.

When the shunt path is formed, the Na^+ ions cross the pn-junction and diffuse into the

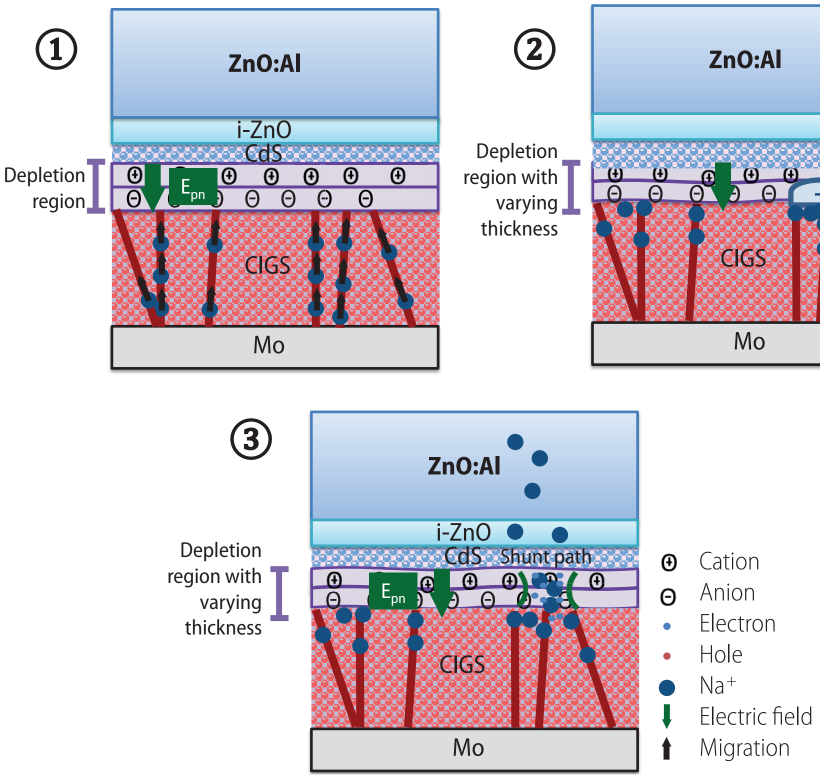

Figure 7.17

Proposed degradation mechanisms for CIGS solar cells containing sodium due to exposure to damp heat and illumination exposure.

top layers, which can explain the occurrence of Na^+ in the ZnO:Al. These shunt paths can function as a tunnel, through which additional Na^+ still present in the CIGS layer, can be transported through the depletion region of the pn junction (Figure 7.17, step 3). This migration into the top solar cell layers can also explain the faster increase in series resistance for the alkali-rich samples.

The occurrence of shunt paths has also been confirmed by SEM and EDX measurements, which show that the degradation spots consist of sodium, carbon and oxygen, but have nuclei which also contain for example cadmium. Cross-section SEM also revealed that after 778 hours, cracks occurred in the layers. We therefore propose that exposure to damp heat and illumination as long as 778 hours even led to structural changes in the regions of the spots. Since the cracks were not detected for solar cells that were degraded for a shorter time, we suggest that the crack formation resulted from severe ion migration.

7.4.2 Diffusion of sodium

In order to study whether the sodium diffusion as described before would actually be possible, both in elevated and room temperatures, indicative theoretical diffusion lengths have been calculated based on a model proposed by Lämmle et al. [10]. In this reference, it was shown that sodium can migrate, which largely happens via the grain boundaries, thereby influencing the properties of the solar cell.

Reference [10] studied the diffusion behaviour of sodium applied via Post Deposition Treatment (PDT) NaF within CIGS cells at increased temperatures (157-400°C): at 157°C, the diffusion coefficient for sodium within a grain was around 4x10^{-13} cm^2/s, while it was 2x10^{-11} cm^2/s in a grain boundary. At 157°C or lower diffusion temperatures, the diffusion along the grain boundaries is therefore the dominant mechanism. The grain boundary diffusivities determined between 157°C and 226°C are about 20 – 50 times higher than the corresponding diffusivities in the CIGS bulk.

The sodium diffusion coefficient for sodium in the grain boundaries was fitted by an Arrhenius equation as a function of temperature:

$$D_{Na}^{GB} = 6.5x10^{9} \exp\left(\frac{-0.21eV}{k_B T}\right) cm^2 s^{-1} \tag{7.1}$$

By extrapolating to 107°C according to this equation, the diffusion coefficient should be around 1.1x10^{-11} cm^2/s. It should be noted that the fit of the diffusion coefficients at high temperatures are empirical, so extrapolating to lower temperatures does not necessary yield correct values.

In order to estimate how far sodium can diffuse at different temperatures, the expected diffusion length for sodium in grain boundaries has been calculated for 10 and 100 hours (Figure 7.18). When 107°C is considered, the expected diffusion lengths are approximately 9 and 28 micrometres for 10 and 100 hours respectively. This would

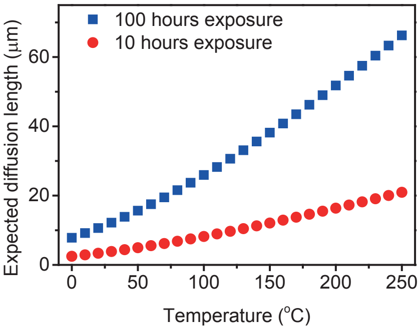

Figure 7.18

Expected diffusion length in micron after 10 and 100 hours for sodium present in the grain boundaries based on the extrapolation of the diffusion coefficients as presented in reference [10].

indicate that diffusion of sodium through the whole CIGS absorber layer can easily occur within 10 hours.

In order to predict how likely sodium diffusion is in the field, the values at 20°C can be considered. Extrapolation indicates a coefficient of 1.6×10^{-12} cm^2/s, which leads to expected diffusion lengths of 3 and 11 micrometres after 10 and 100 hours respectively. Therefore, it can be expected that this also happens for CIGS PV in the field. It should however be noted that extrapolation of an emperical function from 157°C to 20°C can introduce a large error in the result of this calculation.

However, regardless of the limitations and assumptions in these calculations, it is very likely that sodium migration over several micrometres via the grain boundaries can occur both at elevated and room temperatures within several hours.

7.5 Conclusions

CIGS solar cells with a high alkali (sodium, potassium) content exhibited higher initial conversion efficiencies, but degraded rapidly under exposure to both damp heat and illumination. On the other hand, CIGS solar cells with a low alkali content did barely degrade under combined damp heat and illumination.

The degradation of the alkali-rich samples especially impacted the shunt resistance and open circuit voltage and resulted in the formation of sodium rich spots on the top ZnO:Al surface of the samples. This is likely caused by light-induced Na^+ migration through the grain boundaries of the absorber to the depletion region, accumulation of Na^+ at the depletion region and subsequent transport through the depletion region due to the lowering of the internal electric field. The migration resulted in the formation of shunt paths, which reduced the shunt resistance and consequently the open circuit voltage. Calculations showed that sodium can migrate the required distance to cause these effects.

Additionally, ingression of water into the ZnO:Al is expected to be responsible for a slow but steady increase in series resistance for both samples. The alkali-rich solar cells show an additional increase in series resistance, probably due to the ingression of sodium in the ZnO:Al.

7.6 Acknowledgements

I would like to thank Denis Mangin (Université de Lorraine) for the SIMS measurements and Arjan Hovestad (TNO), Guy Brammertz (imec) and Felix Daume (Solarion) for the fruitful discussions.

7.7 References

[1] P. Jackson, D. Hariskos, R. Würz, W. Wischmann, M. Powalla, Phys. Status Solidi RRL 8 (3) (2014) 219–222

[2] A. Chirila, P. Reinhard, F. Pianezzi, P. Bloesch, A. Uhl, C. Fella, L. Kranz, D. Keller, C. Gretener, H. Hagendorfer, D. Jaeger, R. Erni, S. Buecheler, A. Tiwari, Nature Materials 12 (12) (2013) 1107-1111

[3] V. Fjällström, P. Salomé, A. Hultqvist, M. Edoff, T. Jarmar, B. Aitken, K. Zhang, K. Fuller, C. Kosik Williams, IEEE journal of photovoltaics 3 (3) (2013) 1090 – 1094

[4] M. Theelen, N. Barreau, F. Daume, H. Steijvers, V. Hans, A. Liakopoulou, Z. Vroon, M. Zeman, Proc. SPIE 9179 (2014) 91790I

[5] D. Braunger, D. Hariskos, H. Schock, Proc 2nd WCPEC 1 (1998) 511–514.

[6] F. Daume, S. Puttnins, C. Scheit, H. Zachmann, A. Rahm, A. Braun, M. Grundmann, Materials 6(12) (2013) 5478–5489

[7] G. Niki, M. Contreras, I. Repins, M. Powalla, K. Kushiya, S. Ishizuka, K. Matsubara., Progress in Photovoltaics: Research and Applications 18 (2010) 453–466

[8] A. Urbaniak, M. Igalson, F. Pianezzi, S. Bücheler, A. Chirilă, P. Reinhard, A. Tiwari, Solar Energy Materials & Solar Cells 128 (2014) 52–56

[9] F. Couzinie-Devy, E. Cadel, N. Barreau, L. Arzel, P. Pareige, Appl. Phys. Lett. 99 (2011) 232108

[10] A. Lämmle, R. Würz, T. Schwarz, O. Cojoca-ru-Mirédin, P. Choi, M. Powalla, Journal of Applied Physics 115 (2014) 154501

[11] K. Ramanathan, M. Contreras, J. Tuttle, J. Keane, J. Webb, S. Asher, D. Niles, R. Dhere, A. Tennant, F. Hasoon, R. Noufi, Proc. 25th IEEE PVSC (1996) 837-840

[12] M. Theelen, M. Tomassini, H. Steijvers, Z. Vroon, N. Barreau, M. Zeman, Proc. 39th IEEE PVSC (2013) 2047-2051

[13] M. Theelen, T. Boumans, F. Stegeman, F. Colberts, A. Illiberi, J. van Berkum, N. Barreau, Z. Vroon, M. Zeman, Thin Solid Films 550 (2014) 530–540

[14] A. Colli, Renewable Energy 60 (2013) 162-168

[15] E. Cadel, N. Barreau, J. Kessler, P. Pareige, Acta-Materialia, 58 (2010) 2634-2637

[16] S. Schmidt, Microscopic properties of grain boundaries in Cu(In,Ga)Se_2 and $CuInS_2$ thin-film solar cells studied by transmission electron microscopy, thesis Berlin 2011

[17] Y. Shin, D. Shun, J. Kim, B. Ahn, Current Applied Physics 11 (2011) S59-S64


BLUBb
BLUB
BLUB

CHAPTER 8

The impact of atmospheric species on the degradation of CIGS solar cells

This chapter is based on the following publications:
M. Theelen, C. Foster, S. Dasgupta, Z. Vroon, N. Barreau, M. Zeman,
The influence of atmospheric species on the degradation
of aluminium doped zinc oxide and Cu(In,Ga)Se_2 solar cells,
Proc. SPIE (2014) 91790K

M. Theelen, C. Foster, N. Barreau, H. Steijvers, Z. Vroon and M. Zeman,
Influence of atmospheric species on the degradation of CIGS solar cells,
Solar Energy Materials & Solar Cells 141 (2015) 49–56

Abstract

CIGS solar cells were exposed to liquid water purged with the atmospheric gases carbon dioxide (CO_2), oxygen (O_2), nitrogen (N_2) and air in order to investigate their degradation behaviour. The samples were analysed by electrical, compositional and optical measurements before, during and after exposure in order to follow the degradation behaviour of these solar cells in time.

The solar cells showed a rapid decrease in conversion efficiency when exposed to water purged with a combination of CO_2 and N_2 as well as to water purged with air which contains O_2, N_2 ánd CO_2, while their efficiency was slowly reduced in unpurged water and water purged with N_2 or O_2. Cross-section SEM showed that the exposure of samples to H_2O with large concentrations of CO_2 led to the dissolution of the ZnO:Al layer, likely starting from the grain boundaries. This resulted in an increased series resistance, which is likely related to an increase in resistivity of the ZnO:Al layer. It also led to a very rapid decrease of the short circuit current of these samples. Therefore, the conversion efficiency was rapidly lost.

8.1 Introduction

The requirements of flexible barriers and encapsulation for CIGS solar cells are normally only based on water penetration numbers, and in some cases on oxygen penetration, while it is not clear which atmospheric gases are actually involved in the degradation of CIGS solar cells. Since it is known that increased resistance of ZnO:Al is often a reason for CIGS solar cell degradation, in chapter 6, it was shown that ZnO:Al layers undergo a large performance deterioration due to combined water and CO_2 exposure, while these layers were stable under many other conditions.

Based on earlier experiments, it could be expected that CO_2 is important [1,2,3], but this has not been studied yet. Therefore, the impact on complete CIGS solar cells was unknown, but it could be expected that the combined impact of water and CO_2 will be detrimental for the ZnO:Al layer of the solar cells, while other layers might be affected by different combinations. Therefore, we have studied the impact of the exposure of CIGS solar cells to water combined with atmospheric gases (air, N_2, O_2 and CO_2) in order to learn more about the influence of these species and their combination on the degradation.

8.2 Experimental

8.2.1 Sample preparation

Eight similar solar cells as introduced in chapter 3.2 with a width of 6.9±0.4 mm and a length of 4.3±0.1 mm length were cut from one microscopy slide. The total cell area was therefore 30±2 mm^2.

Figure 8.1a and b depict the schematic cross-section and top view of the solar cells

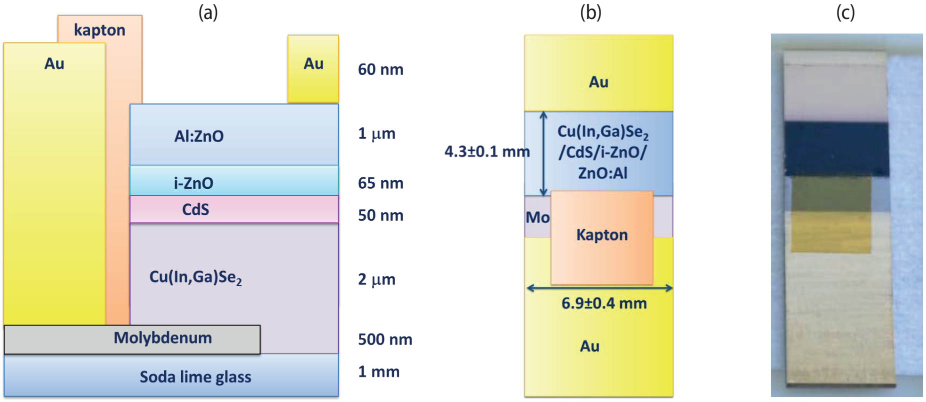

Figure 8.1

Samples as used in the experiments: (a) Schematic cross-section (b) Schematic top view (c) Photograph of the top view.

respectively. Additionally, kapton tape was placed over the molybdenum part exposed to the environment, as shown in Figure 8.1c. This is necessary due to the very rapid degradation of molybdenum in water, especially when purged with oxygen. Therefore, unprotected molybdenum can degrade more quickly than the complete cell, which does not result in relevant measurements.

8.2.2 Sample degradation

Samples were placed in ultrapure water (deionised water further treated with a Synergy Millipore purifier) in high density polyethylene (HDPE) containers, as is shown in Figure 8.2. A schematical representation of this setup is shown in Figure 6.1. The vessels are non transparent, so the samples are kept in dark. The setup is further similar to the one earlier described in reference [3] and chapter 6, which was used to test ZnO:Al layers. Gas purges were fed into the containers, namely air, nitrogen (Air Liquide, 99.99995% purity), oxygen (Air Liquide, 99.995% purity) and a carbon dioxide (Air Liquide, 99.7% purity)/nitrogen mix. Flow rates for the air, nitrogen and oxygen samples were each maintained at about 0.3 L/min with calibrated flow meters (Brooks Instrument).

Carbon dioxide was diluted with nitrogen to avoid acidification of the water, which leads to dissolution of the top ZnO:Al layer (see reference [3] and chapter 6). To provide a nitrogen-diluted carbon dioxide purge, nitrogen and carbon dioxide were provided through mass flow controllers (from Bronkhorst Nederland B.V.). The total flow was approximately 0.7 L/min, and was primarily nitrogen with a carbon dioxide content of 250±80 ppm. This is slightly less than the carbon dioxide content of normal air (400 ppm).

The pH of all vessels was monitored. The global pH of the solutions was above 6.5 for all

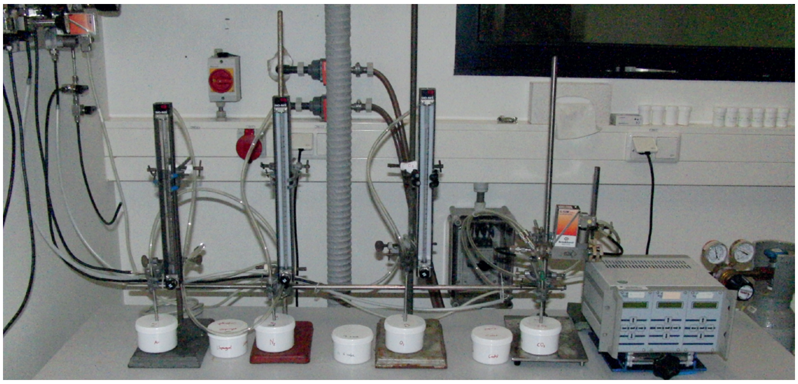

Figure 8.2

Photograph of the complete degradation setup, including the white degradation vessels, and three flow meters to define the O_2*,* N_2 *and air flows. The mass flow controller (right) is used to determine the* CO_2/N_2 *flows.*

vessels at all times, and was not clearly lower for the CO_2 containing solutions than for the N_2 and O_2 based vessels. During the degradation period, the pH of all vessels slowly rose with approximately 0.5 to 1 pH point, but this was observed for most conditions as well as the reference vessel, so it is assumed that this is within the measurement error.

The samples were all exposed to these conditions for 4/16/21/17/41/40/44/88/69 hours, counting up to a total of 340 hours.

Two samples were used as references: One sample was kept in the glovebox in an argon atmosphere, while the other one was exposed to air for approximately 1560 hours. The sample names as used in this chapter are shown in Table 8.1.

Table 8.1 Degradation conditions for the CIGS solar cells and the sample abbreviation used in this article.

Exposure conditions	Sample name
Argon glovebox	Reference
Air	Air
Non-purged H_2O (containing small quantities of air)	H_2O
H_2O purged with N_2	H_2O/N_2
H_2O purged with O_2	H_2O/O_2
H_2O purged with air	H_2O/air
H_2O purged with N_2 and 250 ppm CO_2	$H_2O/CO_2/N_2$

8.2.3 Characterisation of film properties

The optical, structural and electrical properties were determined by a number of techniques before, during and after degradation. The measurements during the degradation period were obtained by removal of the samples from the vessels, after which they were dried and measured. The executed measurements are IV, EQE, SEM, SIMS and lock-in thermopgraphy measurements and photography.

IV (current-voltage) measurements were obtained using an OAI TriSol Solar Simulator attached to a Keithley SourceMeter 2400 and controlled using IV runner software, version 1.4.0.6. The series resistance has been calculated from the last four points of the IV measurement (+0.70 to +0.75 V), instead of at V_{oc}, while the shunt resistances have been determined in a voltage range from -0.3 V to -0.06 V.

The spectral response (SR), and therefore also the external quantum efficiency (EQE), were measured using a home-built SR setup at ECN in Eindhoven. The short circuit current and efficiency were corrected for all degradation times based on the ratios between J_{sc} (IV) and J_{sc} (EQE) as obtained at t=0 h. The mismatch between the Jsc from IV and the EQE measurements was between 15.8 and 16.9%. After degradation, the mismatch was between 15.6 and 17.0% for the non-degraded and the H_2O/O_2, H_2O/N_2 and unpurged H_2O samples. EQE on $H_2O/CO_2/N_2$ and H_2O/air samples did not show any current, while the IV reported very low currents.

A Leica Wild M400 macroscope and a digital camera were used to determine the visual changes. Lock-in thermography (LIT) images were taken using an ImageIR camera and a Sunfilm IR lens from Infratec.

The morphological and structural properties of the layers were determined by a FEI XL40 FEG Scanning Electron Microscope (SEM). Compositional depth profiles were performed by SIMS using a magnetic sector Cameca IMS 7F instrument in the positive mode with Cs^+ ions, the primary beam intensity was 57nA with 5keV acceleration and it was rastered by 200x200 μm^2.

8.3 Results

8.3.1 Structural properties

Figure 8.3 shows microscopy pictures of the surface of the samples before (a) and after 340 hours exposure to the different conditions (b-f). It is shown that all samples looked less homogeneous after exposure, which can be observed as surface patterns. The effect is the largest for the H_2O/air and $H_2O/CO_2/N_2$ samples, while the latter also has a slightly purple red colour after exposure.

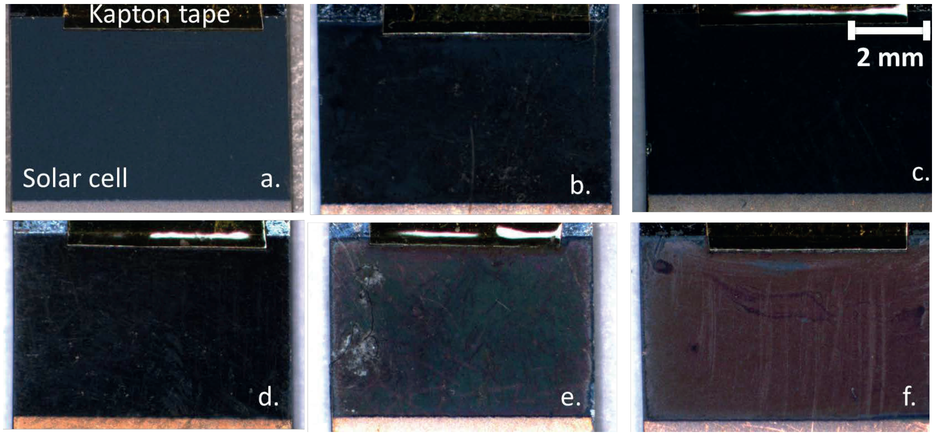

Figure 8.3

Microscopy photos taken on the surface of the (a) H_2O/O_2 *sample before degradation (b-f) after 340 hours exposure to (b)* H_2O *(c)* H_2O/N_2 *(d)* H_2O/O_2 *(e)* H_2O*/air (f)* $H_2O/CO_2/N_2$

Lock in thermography was used to define shunt paths in the solar cells (Figure 8.4). For the H_2O/N_2 samples, shunt paths were observed along the edges of the solar cell, while the other samples did not reveal any shunt paths.

Cross-section SEM was used to determine the structural changes (Figure 8.5). These measurements showed that the morphology of the molybdenum and the bottom part of the CIGS layer remained the same, while large structural changes were found

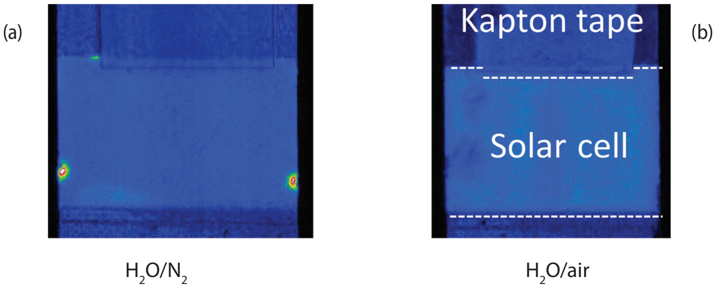

Figure 8.4

Lock in thermography pictures of the surface of the (a) H_2O/N_2 and (b) H_2O/air samples after 340 hours exposure. The white/ green/red dots indicate the position of shunt paths.

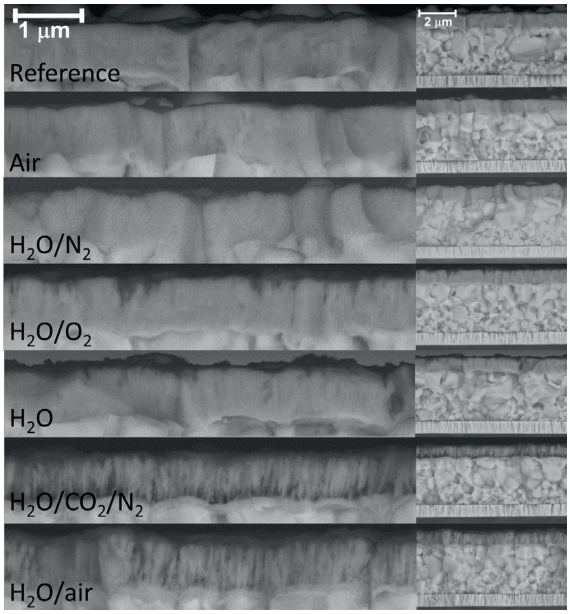

Figure 8.5

Cross-section SEM pictures of CIGS solar cells (right) and zooms to the CIGS/CdS/i-ZnO/ZnO:Al region (left) after exposure to various conditions.

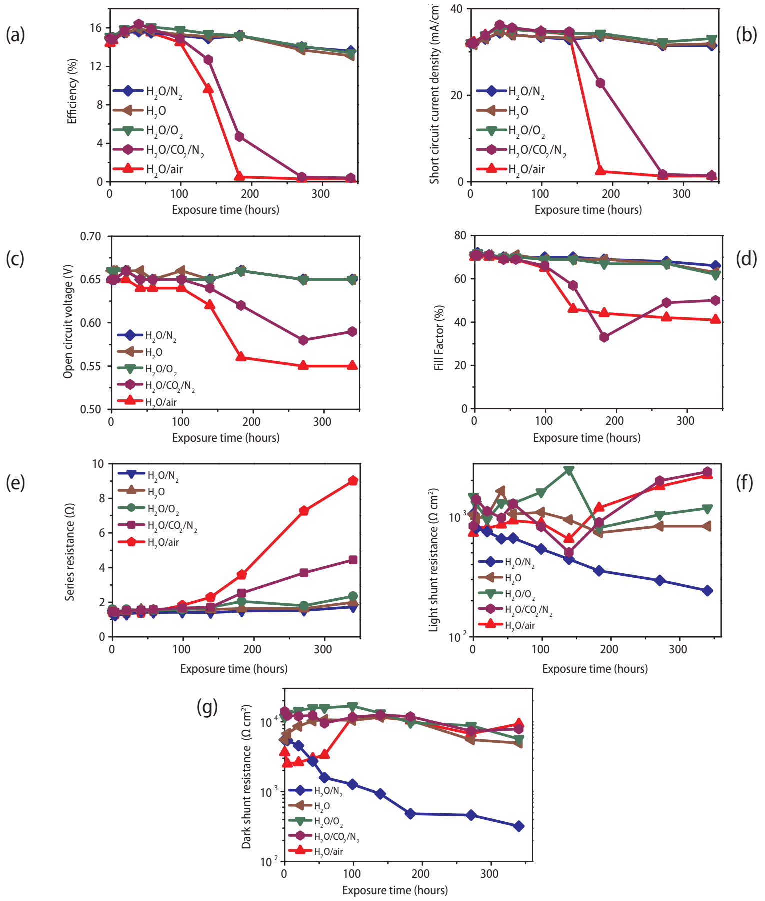

Figure 8.6

Evolution of the solar cell parameters (a) efficiency (b) short circuit current density (c) open circuit voltage (d) fill factor (e) series resistance (f) light shunt resistance (g) dark shunt resistance as a function of exposure time to different conditions.

in the top layer of the CIGS and especially in the zinc oxide layers.

Figure 8.5 also shows a close-up of only the top layers of the solar cell. The reference samples, which have been kept in argon or in air, show a standard dense zinc oxide structure. The samples exposed to unpurged water and H_2O/O_2 show a small number of gaps, which are starting at the top of the layer and seem to follow the grain boundaries. Furthermore, an unidentified layer might have been formed in the CIGS/CdS/ZnO region, since an intermediate film of tens to hundreds of micrometres seems to be visible on the SEM pictures. These effects are stronger for the H_2O/air and $H_2O/CO_2/N_2$ samples, which have large gaps in the ZnO:Al layer, which seem to result from dissolution of the grains starting from the grain boundaries. This dissolution is the strongest at the bottom of the zinc oxide layer, which indicates that the degradation started at least partly at this

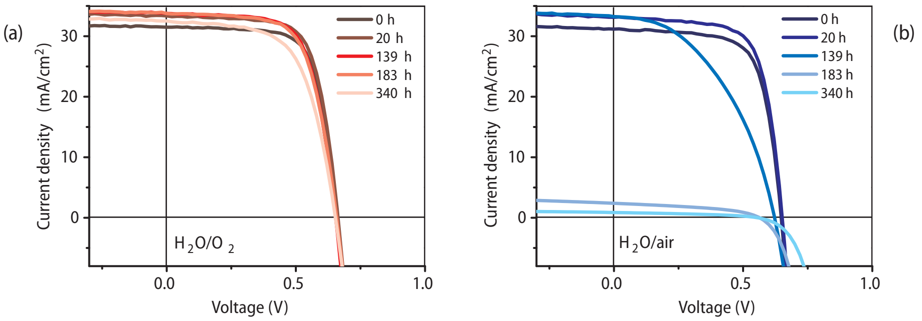

Figure 8.7

Light current voltage curves of the(a) H_2O/O_2 and (b) H_2O/air samples before and after exposure for 20, 139, 183 and 340 hours.

position. Additionally, the ZnO:Al layers of these samples is probably also slightly thinner.

8.3.2 Electrical properties

The electrical properties of the solar cells were followed as a function of time. Before degradation, all samples showed similar efficiencies (Figure 8.6), which increased for all conditions within the first 50 hours. After this, the $H_2O/CO_2/N_2$ and H_2O/air samples showed a very rapid decay, while the other showed a very small decrease, leading to a final efficiency similar to the starting value. For better visualisation of the current voltage curves as a function of time, the curves for the H^2O/air and H_2O/O_2 before and after different exposure times are shown in Figure 8.7.

When considering the $H_2O/CO_2/N_2$ and H_2O/air samples, it was observed that they lost nearly all efficiency within 100 to 150 hours, which indicated that the degradation process occurred very rapidly. It should be noted that in this experiment, the H_2O/air sample degraded the fastest, while in a similar earlier experiment, the rapid decay started after 100 hours for the $H_2O/CO_2/N_2$ sample, while the H_2O/air sample only started degrading after 200 hours. A quantitative comparison between these two conditions should therefore not be made. Apart from this difference, the results obtained in this earlier experiment were similar to the results presented here.

The other solar cell parameters were also monitored (Figure 8.6), which indicated that the main driving forces behind the efficiency decrease were the decrease in short circuit current and, to a lesser extent, the increase in series resistance. A part of the decrease in the efficiency was driven by the steady increase in series resistance, which was especially rapid for the $H_2O/CO_2/N_2$ and the H_2O/air samples. It should be noted that the series resistance is calculated from V=0.70 to V=0.75V and not at V_{oc} in order to remove the impact of the change in current.

Even stronger effects were observed for the short circuit current, which decreased very rapidly and seemed to lead to the 'sudden death' of the solar cells. This complete disappearance of the current was also observed by EQE measurements for the H_2O/air and $H_2O/CO_2/N_2$ samples.

The changes in light shunt resistance were remarkable: for the H_2O/air and $H_2O/CO_2/N_2$ samples, the shunt resistance dropped when the efficiency dropped, but later increased again. This can imply the formation of shunt paths that are later not shunting anymore, but can also result from the disappearance of contact points, thereby decreasing the possibilities for shunt paths. This decrease was not observed for the dark shunt resistance. Another observation for especially the light but also the dark shunt resistances was the decrease for the H_2O/N_2 samples, which also has been observed in similar experiments. Furthermore, the open circuit voltage also changed, but this impact was minor compared to the changes series resistance and current.
When the initial increase during the first 50 hours is considered, it seems that this is mostly caused by enhancement of the short circuit current, while the open circuit voltage also has a small impact. It should be noted that in earlier experiments, the impact of V_{oc} on this efficiency increase was larger (20-30 mV).
When the reference and air samples were measured before and after 1560 hours under argon and air respectively, it was observed that these solar cells showed a slight increase in efficiency (+0.2 and +0.3 percent point respectively). This was mostly driven by small changes in the shunt resistance (glovebox sample) and open circuit voltage (air). However, it is not expected that these changes are significant.

8.3.3 Compositional changes

The elemental depth profiles of non-degraded and degraded samples was measured by SIMS (Figure 8.8). This was operated in positive mode, and the elements zinc, oxygen, aluminium, cadmium, sulphur, copper, indium, gallium, selenium, chlorine, bromine, sodium, potassium as well as the compound hydroxide were measured. It should be noted that no absolute concentrations can be determined with SIMS, since the intensity is not calibrated. Since the measured number of counts is largely influenced by the surrounding matrix, no absolute comparison of concentrations between different matrices (e.g. ZnO:Al or CIGS) or different elements can be executed. Figure 8.8a shows a depth profile of a typical CIGS cell, which has only been exposed to argon. The gallium, indium and selenium profiles are not included, since they do not change significantly during degradation. In these SIMS spectra, the boundaries between the various layers can be distinguished, although the width of the cadmium peak also indicates that the depth resolution is limited. One remarkable observation is the high concentration of sodium, potassium and sulfur in the ZnO:Al layer, but this can be explained by the matrix effects and difference in electronegativity. Similar

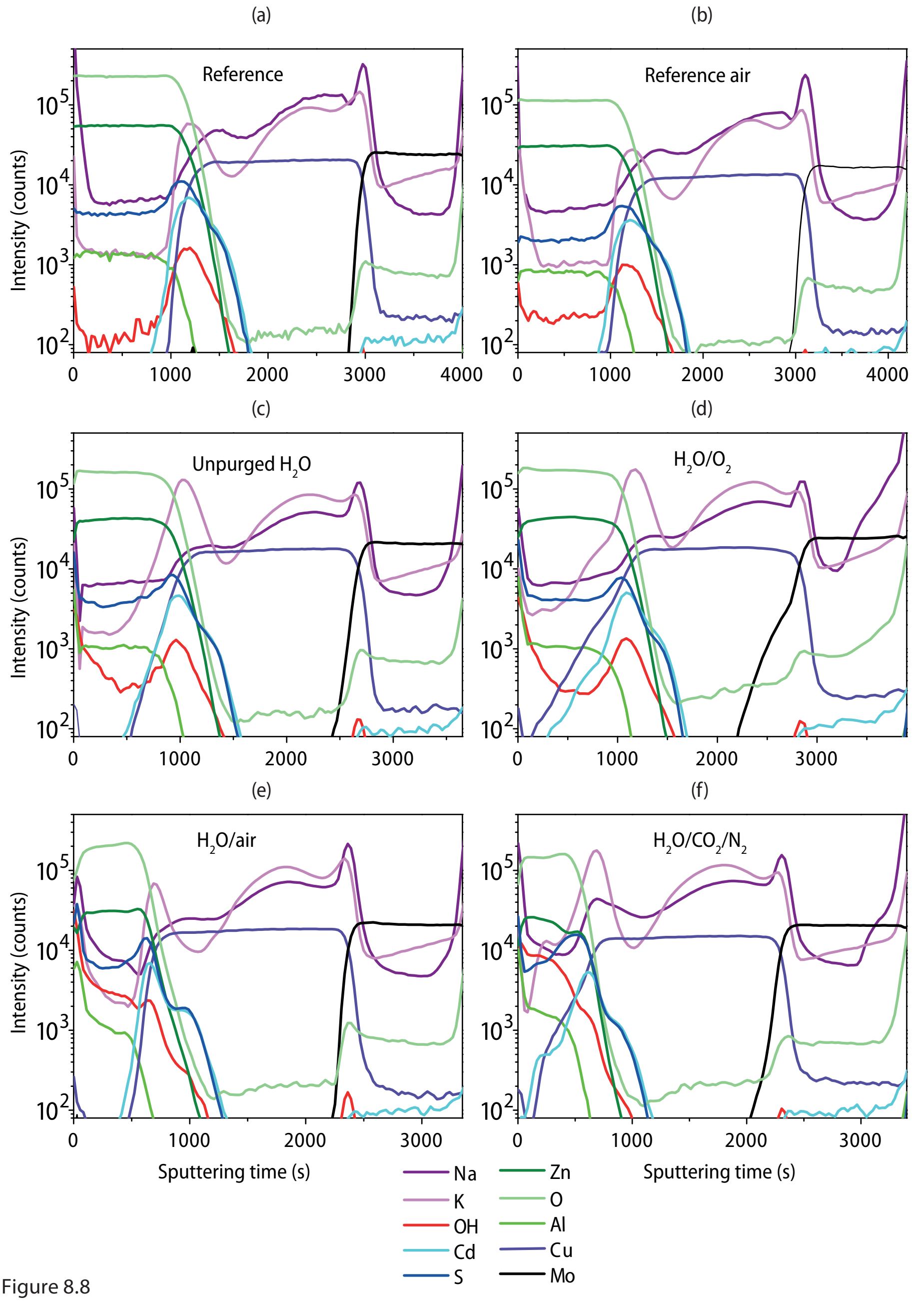

Figure 8.8

Depth profiles as obtained by SIMS measurements of CIGS solar cells: the (a) glovebox and (b) air reference sample as well as the solar cells exposed for 340 hours to (c) H_2O*, (d)* H_2O/O_2*, (e)* $H_2O/CO_2/N_2$ *and (f)* H_2O*/air . The gallium, indium and selenium profiles are not included.*

profiles were detected for the reference air sample (not depicted).
The sample degraded in non-purged water, which contains small quantities of among others nitrogen, oxygen and CO_2, is shown in Figure 8.c. In this figure, it seems that the thickness of the ZnO:Al layer has decreased slightly, while the CIGS and the zinc oxide layer have intermixed slightly. The sodium profile is still the same, but it is possible that the content in the CIGS layer and especially near the pn-junction has decreased. The potassium content might have increased in this region. As is shown in Figure 8.5, the thickness of none of the layers has reduced greatly, while the layers also do not seem intermixed. It is therefore more likely that the reduced sputter time can be explained by the dissolution of part of the zinc oxide, resulting in a very porous material which has an increased average sputter rate compared to the dense original zinc oxide. Since the sputter rate in zinc oxide is locally very high (at the empty grain boundaries) and locally lower (at the still existing grains) and many grains and empty areas are included in the measurement, the intermixing is probably largely an artefact of the SIMS measurement. The intermixing between the CIGS and the molybdenum also becomes larger, which can probably be explained by the same reason.

Additionally, the amount of hydroxide has increased, especially near the ZnO:Al/air interface, while the sulfur and the aluminium content were also higher very close to this surface. A small change was also observed at the CIGS/Mo interface, where the oxygen concentration likely has slightly increased.
The sample degraded in H_2O with O_2 shows an even larger intermixing between the ZnO:Al and CIGS signals, which might indicate less homogeneity or just more dissolution of the zinc oxide. Further trends are similar to the non-purged H_2O sample.

The picture changes greatly when the samples degraded in H_2O/air and $H_2O/CO_2/N_2$ are studied. As expected from the SEM pictures, for the H_2O/air sample, the sputtering time for the ZnO:Al has been reduced even further, while the amount of foreign species near the ZnO:Al/air interface becomes higher. These species include hydroxide, sulfur and to a lesser account chlorine. There seems to be a clear border in between the thinner ZnO:Al and the CIGS layer, while the Mo/CIGS interface is also quite well defined, which might indicate a very homogeneous dissolution. In this sample, the highest increase in oxygen content at the Mo/CIGS interface was found. The sodium profile in this sample is similar to the profiles in the reference samples.
The $H_2O/CO_2/N_2$ gave largely the same picture as the H_2O/air samples, but the border between the CIGS and the ZnO:Al signals is less well defined. Furthermore, the increase in oxygen at the Mo/CIGS interface can barely be observed.

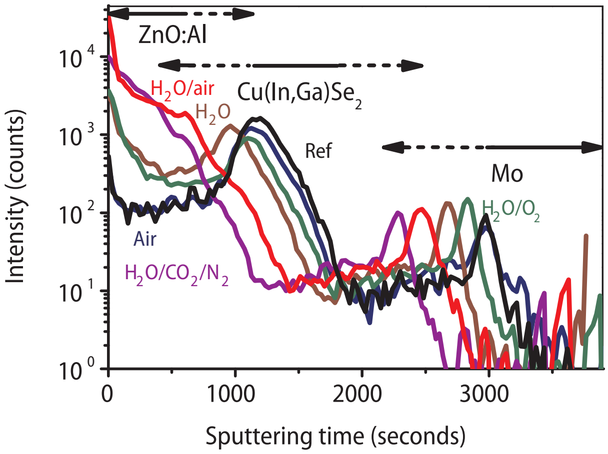

Figure 8.9:

The OH profile for the reference samples (air and glovebox) and for samples exposed for 340 hours to H_2O, H_2O/O_2, $H_2O/CO_2/N_2$ and H_2O/air. Since the morphology and also the thickness of the samples is varying, the start and end points of the ZnO:Al/CIGS/Mo layers is different in this figure for the different samples.

For a better comparison between the samples, the hydroxide signal is shown in Figure 8.9. This figure shows that especially in the ZnO:Al near the surface, the hydroxide has increased one order of magnitude due to H_2O and H_2O/O_2 exposure, while it even increased almost two orders of magnitude for the H_2O/air and $H_2O/CO_2/N_2$ samples. For the last samples, this difference is still very high in the bulk of the ZnO:Al. It can therefore be expected that water or hydroxide is present in the gaps between the grains or less likely, in the grains themselves. When the hydroxide content in the CIGS or molybdenum was studied, no significant changes could be observed.

8.4. Discussion

Complete CIGS solar cells were exposed to ultrapure water at room temperature purged with N_2, O_2, CO_2/N_2 and air (which contains N_2, O_2 and CO_2) and to unpurged water and air. The samples exposed to water with CO_2/N_2 and air showed a quick decrease in conversion efficiency, which was primarily caused by a very rapid decrease in current density as well as an increase in series resistance. Cross-section SEM pictures showed that the ZnO:Al/i-ZnO/CdS region had been greatly impacted by the exposure to these conditions, while the remaining CIGS as well as the molybdenum layer remained largely constant. The zinc oxide layers had dissolved at the grain boundaries, starting from the CdS/i-ZnO interface and likely also from the ZnO:Al/air, while also a new thin, unidentified layer formed around the CdS/i-ZnO interface. SIMS measurements also showed an increase in hydroxide content of one to two magnitudes in the zinc oxide layers in the H_2O/air and $H_2O/CO_2/N_2$ samples. SIMS also indicated that the sodium profiles did not change greatly, while it has been shown to migrate under illumination or bias, leading to degradation of the solar cells [10,11]. Therefore, it is unlikely that similar reactions are occurring under these conditions. Furthermore, these samples also showed a change in colour: initially, they were blue/black, while after degradation, they showed a reddish colour.

When the dissolution of ZnO:Al is taken into account, the changes in series resistance and short circuit current density are not surprising. When part of the zinc oxide has disappeared, the grains are barely connected and the resistivity of the layer increases. Therefore, the transport of the current through this layer becomes very hard, leading to an increase in series resistance and a decrease in short circuit current density. Additionally, the new layer might also play a role in these changes.

For the samples exposed to unpurged H_2O, H_2O/N_2 and H_2O/O_2, some minor gaps in the ZnO:Al were also observed. The gaps started at the ZnO:Al/air interface, while some hydroxide was also present in the ZnO:Al layers. These effects seem to have led to a small increase in series resistance over time, probably also by an increased resistivity of the ZnO:Al layer. For the H_2O/N_2 sample, a decrease in the light and dark shunt resistance was also observed. No effects were observed for the sample exposed to air.

Since the degradation experiments in aqueous solutions took place in darkness, it is not expected that a voltage was formed across the solar cell. Therefore, the reason for the degradation can likely be found in the diffusion of the atmospheric species, followed by chemical or physical reactions with the materials from the solar cells.

8.4.1 Grain boundary dissolution

The impact of the various combinations of water and atmospheric gases was comparable to the observations obtained for ZnO:Al layers on borosilicate glass [3]. In this reference, it was shown that ZnO:Al layers rapidly degraded in the presence of a mixture of H_2O and CO_2. Individually, CO_2 did not impact the degradation at all during the tested period, while the individual impact of H_2O was small. However, when CO_2 was also present, the concentration of OH increases greatly in the ZnO:Al bulk and even more at the air/ZnO:Al and the ZnO:Al/glass interfaces. Carbon based species were then also present, indicating that $Zn_5(OH)_6(CO_3)_2$ was formed at the grain boundaries.

Detailed cross-section pictures obtained by Helium Ion Microscope showed the formation of voids at the ZnO:Al/glass interface, indicating the local dissolution of ZnO:Al, probably due to a reaction of elements from the glass, like calcium or silicon, with water and CO_2 leading to a pH change. Similar to the current experiment, the impact of water purged with N_2 and O_2 on ZnO:Al degradation was very small.

The degradation on complete CIGS cells showed similar effects: the samples exposed to water purged with N_2 and O_2 were more or less stable as a function of time, while the samples exposed to water purged with large quantities of CO_2 degraded quickly. However, unlike the ZnO:Al experiment, the unpurged water sample was also stable in this case. The CO_2 content might have been too low to have a large impact in this case. For the experiments on complete solar cells, it is proposed that the dissolution of part of the ZnO:Al is the driving force behind the loss of efficiency, while the formation of species like $Zn_5(OH)_6(CO_3)_2$ (hydrozincite) will only have played a marginal role. However, hydrozincite formation could still have occurred in case the dissolution was avoided for a longer time, for example for the unpurged water samples. This would have resulted in ZnO:Al layers that still have a closed structure, but have increased potential barriers at the hydrozincite positions, for example at the grain boundaries, leading to increased sheet resistance of the ZnO:Al (see chapter 6 and reference [1]). Naturally, this would have led to an increased series resistance of the complete CIGS solar cell as well.

Since the samples with gaps in the ZnO:Al and the highest hydroxide/water content show the lowest conversion efficiency, it is proposed that these effects are detrimental

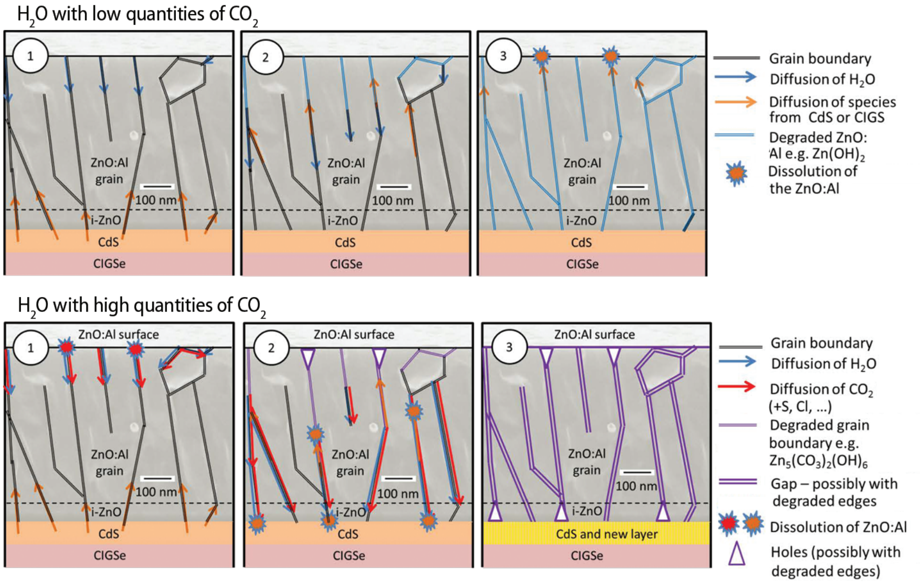
H_2O with low quantities of CO_2

H_2O with high quantities of CO_2

Figure 8.10:

Simplified schematic representation of the degradation of the zinc oxide layers in CIGS solar cells. (Top) and (bottom) show possible degradation routes for these solar cells in water with a low and a high concentration of CO_2 respectively.

for the CIGS solar cells. These effects mostly occurred in the $H_2O/CO_2/N_2$ and H_2O/air samples, so it is proposed that these gaps were formed in the presence of both H_2O and large quantities of CO_2. Proposed simplified representations of the dissolution of the zinc oxide layers in water in the presence and absence of large quantities of CO2 are shown in Figure 8.10.

It should be noted that gap formation in complete CIGS solar cells has been described before. Feist et al. [4] showed the formation of small circular holes (up to 20 nm) in the ZnO:Al layer close to the CIGSSe/ZnO:Al interface due to water exposure. In that case, these holes were observed in encapsulated minimodules exposed for 168 hours to 85°C H_2O purged with O_2. These samples also showed a very rapid decrease in current, leading to an efficiency decrease. Naturally, the high temperature contributes greatly to the reactivity of many species present, but alongside with the limited amounts of gaps observed in the H_2O/O_2 experiment in this study, this shows that also H_2O with O_2 can lead to degradation under certain conditions. However, the main driving force behind the dissolution of the zinc oxide appears to be H_2O combined with CO_2.

The most straightforward explanation of the dissolution of the zinc oxide can be found in the stability of zinc oxide as a function of pH. Zinc oxide is thermodynamically stable at a pH between 6 and 12, while it dissolves outside of this range [5]:

For acidic solutions, the following reaction can occur:

$$ZnO\ (s) + 2H^+(aq) \rightarrow Zn^{2+}\ (aq) + H_2O\ (l)\ [5] \tag{8.1}$$

In alkaline solutions, depending on among other things the OH^- content, this reaction occurs:

$$ZnO\ (s) + 2OH^-\ (aq) + H_2O\ (l) \rightarrow Zn(OH)_4^{2-}\ (aq)\ [5] \tag{8.2}$$

Although the global pH of all degradation vessels was always between 6 and 12, the local pH at the grain boundaries or in CIGS/CdS/i-ZnO region may have been different. This might have been caused by the presence of CO_2. It is possible that locally in the grain boundaries the following reaction occurred:

$$H_2O\ (l) + CO_2\ (g) \rightleftharpoons H_2CO_3\ (aq) \tag{8.3}$$

Carbonic acid (H_2CO_3) then can ionise in water forming low concentrations of hydronium and carbonate ions:

$$H_2O\ (l) + H_2CO_3\ (aq) \rightleftharpoons HCO_3^-\ (aq) + H_3O^+\ (aq) \tag{8.4}$$

High local concentrations of CO_2 could have been caused by a fast diffusion rate of CO_2 through the grain boundaries. It is also possible that an additional reaction between the atmospheric species and the CIGS solar cell components was involved, thereby lowering the pH.

The local pH in the grain boundaries could have become below 6, while the global pH of the complete aqueous solution was still safely above 6.5. Since zinc oxide dissolves at a pH below 6, this would led to local dissolution starting from the grain boundaries.

Since the H_2O/O_2 sample that did not contain CO_2 also showed traces of grain boundary dissolution, it is naturally proposed that the additional reactions with elements from the solar cells must have played a role. Unfortunately, more knowledge about the exact nature of the dissolution should be obtained by pH or elemental measurements at specified positions within the grain boundaries, which was not possible.

However, it is shown on the SEM pictures (Figure 8.5) that dissolution often starts near the CdS/i-ZnO region. Furthermore, a new layer seems to have formed in this region, so it is therefore likely that more elements, like copper, indium, gallium, selenium, cadmium or sulphur play a role in the dissolution of ZnO. It is proposed that one or more of these elements is involved in the change of the pH. One likely candidate is the sulphur present in CdS, since sulphur containing species like H_2SO_4 are known for their acidity.

8.4.2 Shunt resistance

The samples that degraded completely ($H_2O/CO_2/N_2$ and H_2O/air) showed a decrease in shunt resistance at the same time as the decrease of the J_{sc}, which might be explained by the formation of shunt paths. At a later point in time, the shunt resistance increased again - however, this was not necessarily a disappearance of the shunt paths, but more likely a complete change in the morphology, which then dominated over the shunt effects.

A more surprising result was the decrease in the shunt resistance for the sample degraded in H_2O/N_2. This repeatedly observed phenomenon might be explained by the formation of conductive materials along the edge of the samples. These materials (for example binary phases like $Cu_{2-x}Se$) will probably oxidise when oxygen is present in combination with water, leading to a non-conductive oxide. Therefore, no shunt resistance deterioration is observed for the H_2O and the H_2O/O_2 samples.

8.4.3 Impact on CIGS modules

This study has shown that CIGS solar cells degrade rapidly in the presence of both water and large quantities of CO_2. In order to protect the solar cells, the ingression of the polar water molecules can be prevented by water barriers, but one can also consider a barrier that hinders the ingression of the non-polar CO_2 molecules, even based on materials which are porous for water. This could greatly change the demands on the barrier material.

Additionally, knowledge about stability of ZnO:Al in low-pH environments can also help in the choice of the encapsulation material in a CIGS module. One of the standard encapsulation materials, Ethylene-Vinyl Acetate (EVA), is known to react with water. This can result in the formation of acetic acid, which can buffer aqueous solutions to a pH of 4.76 [6]. This would imply that a pH of below 6 can certainly be expected in CIGS modules. An effect of EVA has been presented by Lee et al. [7], who reported chemical reactions occurring in the presence of ZnO:Al, EVA and water, leading to an increase in the ZnO:Al resistivity. This confirms the conclusion of Kempe et al. [6] that careful consideration should be made when EVA is considered as encapsulant in CIGS modules. Similar questions should naturally be posed for other encapsulation materials.

8.5 Conclusions

In chapter 6, it has been shown that the combined impact of H_2O and CO_2 leads to the degradation of ZnO:Al layers in glass. In this chapter, similar observations have been made for complete CIGS solar cells. These solar cells degraded very fast when exposed to H_2O purged with CO_2 and N_2 as well as to H_2O purged with air, while they degraded only slowly in unpurged H_2O and H_2O purged with N_2 and O_2. The exposure of samples to H_2O with large concentrations of CO_2 led to the dissolution of part of the ZnO:Al layers. This was especially visible due to the formation of gaps in the zinc oxide near the CdS/i-ZnO region, alongside with disappearance of the zinc oxide in positions near the grain boundaries. Additionally, SEM pictures indicated the possible formation of a new intermediate layer in the CdS/i-ZnO region. These material changes led to an increased series resistance, likely related to an increase in resistivity of the ZnO:Al layer. Furthermore, the short-circuit current of these samples decreased very rapidly, leading to the complete loss of conversion efficiency. It is proposed that the dissolution of the ZnO:Al was caused by a local change in pH, since overall pH levels were outside the range at which zinc oxide normally dissolves in water.

Additionally, for all samples, a change in shunt resistance was observed. This effect was especially strong for samples exposed to H_2O purged with N_2, possible due to the formation of conductive phases in the presence of only these atmospheric species.

8.6 Acknowledgements

I would like to thank Frank Grob, Henk Steijvers, Linda van Gijzel, Emile van Veldhoven, Arjan Hovestad (TNO), Bertil Okkerse (Philips Innovation Services) and Denis Mangin (University de Lorraine) for their assistance by the measurements, analysis, the building of the setup or for fruitful discussions.

8.7 References

[1] M. Theelen, S. Dasgupta, Z. Vroon, B. Kniknie, N. Barreau, J. van Berkum, M. Zeman, Thin Solid Films 565 (2014) 149–154

[2] I. Hüpkes, J. Owen, M. Wimmer, F. Ruske, D. Greiner, R. Klenk, U. Zastrow, J. Hotovy, Thin Solid Films 555 (2014) 48-52

[3] M. Theelen, T. Boumans, F. Stegeman, F. Colberts, A. Illiberi, J. van Berkum, N. Barreau, Z. Vroon, M. Zeman, Thin Solid Films 550 (2014) 530-540

[4] R. Feist, S. Rozeveld, M. Mushrush, R. Haley, B. Lemon, J. Gerby, B. Nicols, R. Nilsson, T. Richardson, S. Sprague, R. Tesch, S. Torka, C. Wood, S. Wu, S. Yeung, M. Bernius, Proc. 33rd IEEE PVSC (2008) 1-5

[5] X. Zhang, Corrosion and electrochemistry of Zinc, Springer, 1996

[6] M. Kempe, G. Jorgensen, K. Terwilliger, T. McMahon, C. Kennedy, T. Borek, Solar Energy Materials & Solar Cells 91 (2007) 315–329

[7] D. Lee, W. Cho, J. Song, O. Kwon, W. Lee, C. Park, K. Park, H. Lee, Y. Kim, Progress in Photovoltaics: Research and Applications 23 (7) (2015) 829–837


I don't feel well

CHAPTER 9

Overview and recommendations

Overview and recommendations

Based on the results as obtained in the literature study and in the experiments as describes in this thesis, an overview of the most dominant degradation mechanisms in CIGS solar cells and modules is made. Additionally, the failure mechanisms are also linked to possible changes that can be observed in the electrical parameters. Finally, some very general suggestions, both inside and outside the scope of this thesis, are given for the study of CIGS stability.

CIGS degradation mechanisms

The modes and mechanisms leading to degradation of Cu(In,Ga)Se_2 (CIGS) solar cells and modules have been studied in order to better predict their long term behaviour. The changes in electrical and physical parameters associated with decreased performance, as well as the chemical reactions that are causing these changes are described.

The degradation of CIGS solar cells was mostly observed to lead to fill factor and open circuit voltage decreases, while short circuit current decreases are less prominent. The open circuit voltage was mostly impacted by changes in absorber and pn-junction properties, while the fill factor mostly changed due to the introduction of alternative shunt paths and due to increased series resistance. The latter was amongst others caused by a decrease of molybdenum, TCO, grid and interconnection scribe conductivity as well as increased contact resistance due to delamination.

For the molybdenum back contact, it was observed that a less reflective and badly conductive molybdenum oxide layer, potentially with incorporated Na^+, formed on top of the molybdenum due to damp heat exposure. It was also shown that ITO was more stable as front contact than ZnO:Al, which degraded slowly but steadily due to damp heat exposure. The degradation was probably caused by the diffusion of water and CO_2 via grain boundaries, and mainly led to reduced mobility and conductivity, while the transparency of the ZnO:Al was mostly relatively stable. When the stability of buffers was studied, it was observed that interdiffusion of CdS with for example zinc oxide occurred, leading to sulphate formation. Various types of other buffers seemed to show a similar damp heat stability as CdS.

When the CIGS absorber, and also complete CIGS solar cells were studied, it was often observed that sodium plays a role. Sodium migration, which can just occur when the absorber is exposed to damp heat, but also due to illumination or a bias, leads to fast decreases in CIGS cell efficiency. This sodium can either come from the soda lime glass substrate or from the molybdenum or CIGS layers themselves. Generally, illumination and bias exposure led to redistribution of the electrical charges in the CIGS/CdS, influence the diode behaviour.

The impact of two methods to make CIGS modules, showed that both methods have their vulnerabilities: In monolithically integrated modules, the molybdenum and the zinc oxide present in especially P2 and also in P3 in were shown to be unstable, leading to increased series resistance. When grid connected modules are considered, it seemed that nickel covered grids have a better environmental stability than silver or aluminium covered lines, but this also greatly depends on their chemical environment. The impact of encapsulation on CIGS (mini) modules was only scarcely studied in this thesis, but it was often observed that modules with the widely used encapsulant EVA often underperformed compared to alternatives. This might be caused by acetic acid formation.

CIGS degradation modes

Generally, the investigation of degradation processes in devices is complex and the definite identification of failure mechanisms can be complicated due to the stacking of multiple functional layers and thus the presence of multiple interfaces. However, changes in the IV parameters are simple to assess and serve as an indication how a solar cell degraded. Therefore, some factors are listed that influence the electrical parameters V_{oc}, J_{sc} and fill factor and, altogether, determine the cell efficiency. These factors should thus be kept in mind while trying to identify failures after accelerated lifetime tests focused on terrestrial applications:

Changes in open circuit voltage:

- Absorber properties
  - Doping
  - Impurities
  - Bulk defects (increased recombination)
  - Grain boundaries
- pn-junction properties
  - Interface defects (increased recombination)

Changes in short circuit current

- Changes in the transparency of TCO
- Changes in SCR width (related to bulk properties of the absorber)
- Collection of generated charge carriers
- Contact corrosion
  - Delamination

Changes in fill factor

- Series resistance (R_s)
  - Decrease of Mo conductivity (including scribe P3)
  - Decrease of TCO conductivity (including scribe P2)
  - Decrease of grid conductivity
  - Increase of contact resistances, e.g. due to delamination
- Shunt or parallel resistance (R_{shunt})
  - Introduction of alternative shunt paths (including scribe P1)
- Diode ideality factor
  - Changes in the quality of the pn-junction
  - Changes in inhomogeneity of the material

Recommendations

The most straightforward way to stop CIGS module degradation is the use of a good water barrier. This can limit the increase in resistivity of the ZnO:Al and possibly the molybdenum backcontact, thereby preventing the series resistance increase that is often observed. Additionally, many phenomena related to migration of species into the absorber layer, thereby affecting the pn-junction and thus the shunt resistance and the V_{oc} might be solved. However, alongside with the considerable costs of these barriers, this cannot solve all problems, as degradation was also observed for glass-encapsulated modules exposed to field testing.

In order to prevent degradation issues, identification of the degradation modes and mechanisms occurring during field testing are crucial. This information should be compared with accelerated lifetime test results, in order to be able to accelerate and study the correct phenomena during these tests. Additionally, lifetime studies should focus more on better understanding of the degradation, instead of simple go/no go judgments based on IEC tests. Possible laboratory routes to obtain better understanding include, but are certainly not limited to:

- In-situ analysis of cell characteristics, like electrical or optical parameters, during the degradation.
- The use of combined loads for CIGS solar cell degradation, for example combinations of external bias (positive or negative) or different levels of illumination combined with damp heat.
- The execution of single load experiments, like dry heat and room temperature illumination, in order to separate the impact of various loads.
- The use of spatially resolved microscopy techniques (EL, PL, LIT), combined with material analysis in order to identify the local degradation mechanism due to exposure.

- More extensive use of techniques to analyse the CIGS solar cells physical properties after degradation, like admittance spectroscopy, deep level transient spectroscopy (DLTS) and CV and IV(T) measurements
- More extensive use of techniques to analyse chemical changes in composition of the solar cell, like XPS, SIMS and XRD
- Round-robins between testing institutes to investigate whether differences in stability are caused by difference in samples or in testing methods.

H O H
O O
AtTack
I don'T Feel WeLl
TeamwORK
H O H
O C O
ZnO
CIGS
Mo
Na+
Come on..
ZnO:Al
ZnO:Al
BLUB
BLUB
BLUB

CHAPTER 10

Summaries

Summary in English

Samenvatting in het Nederlands

Résumé en Français

Summary

Large scale commercial introduction of CIGS photovoltaics (PV) requires modules with low costs, high efficiencies and long and predictable lifetimes. Unfortunately, knowledge about the lifetime of CIGS PV is limited, which is reflected in the results of field studies: degradation rates varying from 0% to about 4% per year have been observed. Since warrantees are given out that the modules will still yield 80% of their initial power after 20 years of field exposure, degradation rates are often too high as well as too unpredictable. In order to decreasing these degradation rates, knowledge about the degradation behaviour is very important.

Knowledge about this degradation would also enable lower production costs: Since both field and accelerated laboratory tests have already shown that elevated humidity and temperature have a negative impact on CIGS PV, modules are laminated with barrier materials to keep the moisture out. For rigid modules, glass is an excellent barrier choice, but for flexible modules, expensive organic-inorganic multilayer coatings are often used. An intrinsically more stable CIGS solar cell would therefore also limit the barrier costs and facilitate the large scale market introduction of flexible CIGS PV.

Therefore, I have focused in this work on the identification of de degradation mechanisms in thin film CIGS solar cells. Since these cells consist of at least five individual layers, that all influence each other and the degradation behaviour, various layers have also been studied individually. The knowledge obtained on these individual layers was then used to interpret the degradation behaviour of complete CIGS solar cells.

Within this thesis, I propose the degradation mechanisms for the molybdenum back contact and the zinc oxide front contact as well as for complete Cu(In,Ga)Se$_2$ solar cells. The study of these mechanisms has been executed by the exposure of samplesdeposited at different conditions to various accelerated lifetime testing. This was combined with extensive analysis of the samples before, during and after lifetime tests. These tests should give an indication about the long term field exposure of CIGS modules, but it should be mentioned that the validity of the comparison of laboratory testing on solar cells and field exposure on modules it still under discussion.

The following tests have been used in this study.

1. Standard 'damp heat' – exposure of samples to 85^{o}C and 85% relative humidity (RH). A thousand hours exposure to these standard conditions should be comparable to 20 years of field exposure in Miami (acceleration factor 175x). It should be noted that e.g. literature reported that the acceleration factors of these tests range from 10x to 700x, so this extrapolation should be treated with care.

2. ‘Hybrid degradation’ test (https://www.youtube.com/watch?v=Zmy5tb-2NK8) – a combination of damp heat exposure and AM 1.5 illumination. This allows simultaneous sample degradation with elevated temperature and humidity as well as illumination as loads, while the samples can also be in-situ monitored, in order to learn more about the degradation behaviour. This setup has been designed and built within this study and attracted interest from external parties. Therefore, a consortium of three Dutch SMEs (Eternal Sun, Hielkema Testequipment and ReRa Solutions) is currently working on the commercialisation of this setup.
3. ‘Atmospheric species’ exposure – the cells and layers have been exposed to individual species occurring in air, like oxygen, nitrogen, carbon dioxide and water, and combination of these species. This helps the identification of the species that are responsible for the degradation of CIGS solar cells. This can lead to the identification of the degradation mechanisms and can allow optimisation of cost-effective and effective barrier materials. This setup has been designed and built as part of this study.

Barrier materials are not used in any of these tests in order to even further accelerate the degradation rate.

These tests, combined with extensive analysis of samples with among others IV, EQE, IV(T), EL, PL, lock-in thermography, 4PP, Hall, UV-VIS-NIR, Raman, XRD, SEM-EDX, HIM and SIMS, have led to the following conclusion on the degradation of CIGS solar cells and its constituents:

Molybdenum back contact

The molybdenum back contact has been degraded under conditions 1 and 3. Molybdenum degraded very quickly in the combined presence of water and oxygen, while it is reasonably stable in the absence of either of these species.

It was observed that molybdenum degrades due to the formation of molybdenum oxides. This layer, which often forms at the surface of the molybdenum, is largely non-conductive and has a low reflectivity. The appearance of this top oxide layer, can therefore lead to a sudden disappearance of the conductivity, when measured on the surface. This layer consist of MoO_3 mixed with $MoO_{2.5}$,which forms due to the intercalation of Na^+ into a MoO_3 matrix. This is possible due to the layered structure of MoO_3 and leads to the partial reduction of Mo^{6+} to Mo^{5+}. This can lead to the formation of a more conductive degradation product.

Furthermore, it was observed that more porous molybdenum, deposited at higher deposition pressures, is more vulnerable to damp heat exposure than more dense material, while the formation of a top layer $MoSe_2$, which is also present in a CIGS solar cell, makes the molybdenum more stable under degrading conditions, like damp heat.

Zinc oxide front contact

The zinc oxide front contact has been degraded under conditions 1 and 3. Aluminium doped zinc oxide (ZnO:Al) degrades via a gradual process, which starts at the air/ZnO:Al interface and slowly proceeds in the direction of the substrate. This degradation is caused by the slow diffusion of water and CO_2 via the grain boundaries. In the absence of either of these species, the material is very stable.

Within degraded ZnO:Al, increased concentrations of water and CO_2 (as well as sulfur and chlorine) were observed, which might indicate the formation of materials like $Zn(OH)_2$ and $Zn_5(CO_3)_2(OH)_6$, or similar materials, based on chlorides or sulfides. The diffusion of and the reactions with water and CO_2 lead to an increase in the potential barrier at the grain boundaries in the polycrystalline ZnO:Al. This leads to a decrease of electron mobility and thus in conductivity, while the transmission remained majorly constant.

Complete CIGS solar cells

The complete CIGS solar cells, consisting of soda lime glass (SLG)/molybdenum (Mo)/ $Cu(In,Ga)Se_2$ (CIGS)/cadmium sulfide (CdS)/intrinsic zinc oxide (i-ZnO)/aluminium doped zinc oxide (ZnO:Al) were degraded under conditions 1, 2 and 3. The solar cells degraded due to diffusion of species from the atmosphere, like water and CO_2 as well as from the cell itself. The diffusion of water and CO_2mostly leads to an increased series resistance of the ZnO:Al, as well as to local dissolution of the CIGS solar cells, leading to the formation of voids and a rapid decrease of short circuit current.

It was also observed that the alkali elements and especially sodium, play an important role in the degradation of CIGS solar cells. When alkali-rich and alkali-poor CIGS solar cells were both exposed to damp heat and illumination, the alkali-rich samples gave higher initial conversion efficiencies, but degraded severely within 100 hours, while the alkali-poor samples were relatively stable. The degradation of the alkali-rich samples led to the formation of sodium rich spots in the depletion region. This is likely caused by to Na^+ migration from the grain boundaries in the CIGS layer to the depletion region. This migration can be due to the electric field resulting from exposure to illumination, caused by a PID-like mechanism. The migration likely resulted in the appearance of shunt paths, which were responsible for a very low shunt resistance and open-circuit voltage. Furthermore, ingression of water and other species into the ZnO:Al seems to be responsible for a slow but steady increase in series resistance for both types, while sodium migration led to a more severe increase for the series resistance for the alkali-rich samples.

Recommendations for future work

Since all CIGS solar cell companies and research institutes are using sodium and potassium to increase the PV efficiency, the research in the next steps should focus on the development of a stable solar cell with sodium and/or potassium, since the latter seems to diffuse slower. The current route to follow comprises the introduction of low quantities of sodium by post deposition treatment, or by the optimisation of solar cells with high quantities of potassium and low quantities of sodium. This can hopefully lead to both high initial efficiencies and reduced degradation.

Additionally, future tests should include CIGS solar cells deposited by alternative routes or containing different materials. This can for example include CIGS absorbers deposited by the two stage process, alternative buffers and TCOs and alternative interconnection methods.

On the long term, qualitative knowledge should also be translated into a quantitative model. This should be executed by the modelling of the change in the electrical, optical and compositional parameters that is caused by the degradation. This model can then help to actually predict the behaviour of CIGS panels that are in operation for many years.

Samenvatting

Om fotovoltaïsche (PV) CIGS panelen op grote schaal op de markt te brengen, zijn panelen met lage kosten, een hoge efficiëntie en een voorspelbare levensduur vereist. Helaas is de kennis over de levensduur van CIGS PV nog steeds beperkt, wat ook terug te zien is in de resultaten van veld studies: terwijl studies laten zien dat sommige panelen helemaal niet degraderen, degraderen andere panelen met een snelheid van wel vier procent per jaar. Aangezien er garanties worden gegeven dat de panelen na 20 jaar nog steeds 80% van hun initiële opbrengst leveren, zijn deze degradatiesnelheden zowel te hoog als te onvoorspelbaar. Om de degradatiesnelheden en hun spreiding te verlagen, is kennis over het degradatiegedrag van CIGS PV erg belangrijk.

Deze kennis over degradatie kan ook helpen met het verlagen van de productiekosten: Aangezien zowel veld- als versnelde laboratoriumtesten hebben laten zien dat luchtvochtigheid en verhoogde temperaturen een negatieve invloed op CIGS PV hebben, worden panelen gelamineerd met barrièrematerialen om het vocht buiten te houden. Voor rigide panelen is glas een goede keuze, maar voor flexibele modules zijn dure organisch-anorganische multistacks nodig. Daarom zouden intrinsiek stabiele CIGS panelen de barrièrekosten naar beneden brengen en ook de markt introductie van flexibele panelen kunnen versnellen.

Daarom heb ik in deze thesis gewerkt aan de identificatie van de degradatie mechanismen in dunne film CIGS zonnecellen. Aangezien deze cellen uit minimaal vijf individuele lagen en de bijbehorende interfaces bestaan, die allemaal individueel en samen invloed hebben op het degradatiegedrag, zijn ook een aantal individuele lagen bestudeerd. De kennis die hiermee is opgedaan is weer gebruikt om de degradatiemechanismen van complete CIGS zonnecellen te identificeren.

In dit proefschrift beschrijf ik de degradatiemechanismen voor het molybdeen achtercontact, het zink oxide frontcontact en ook complete CIGS zonnecellen. Deze mechanismen zijn bestudeerd door samples die onder verschillende condities zijn gedeponeerd, bloot te stellen aan verschillende versnelde levensduur testen. Deze testen zullen dan een indicatie moeten geven over het effect van langdurige operatie van de panelen in de werkelijkheid, maar er moet altijd rekening mee worden gehouden dat de effecten van laboratorium- en veldtesten niet hetzelfde hoeven te zijn. De volgende testen zijn gebruikt in dit proefschrift:

1. Standaard 'damp heat' testen – blootstelling van samples aan 85°C en 85% relatieve vochtigheid (RV). Duizend uur blootstelling aan deze test zou een vergelijkbaar effect moeten hebben als 20 jaar blootstelling in Miami ('versnellingsfactor' van 175). Overigens bleek uit de literatuur dat de versnellingsfactoren die door deze test worden geïnduceerd kunnen variëren van 10 tot

700 keer, dus er moet rekening worden gehouden met de beperkingen van deze extrapolatie.

2. 'Hybride' degradatie test (https://www.youtube.com/watch?v=Zmy5tb-2NK8) – blootstelling aan een combinatie van 'damp heat' en AM1.5 verlichting. Dit zorgt ervoor dat de samples gelijktijdig degraderen onder invloed van licht, verhoogde temperaturen en verhoogde luchtvochtigheid, en daarnaast continu gemeten kunnen worden. Deze opstelling is ontworpen en gebouwd binnen deze studie en heeft de aandacht van andere partijen getrokken. Daarom is er een consortium van drie Nederlandse MKB'ers (Eternal Sun, Hielkema Testequipment en ReRa Solutions) momenteel bezig met de commercialisering van deze opstelling
3. Blootstelling aan 'atmosferische moleculen' – de zonnecellen en lagen zijn blootgesteld aan de moleculen die aanwezig zijn in de lucht, zoals zuurstof, stikstof, koolstof dioxide en water en combinaties van deze materialen. Dit draagt bij aan de identificatie van de moleculen die verantwoordelijk zijn voor de degradatie van CIGS zonnecellen. Met behulp van deze kennis kunnen de degradatiemechanismen worden geïdentificeerd en kan er meer gericht worden gezocht naar een goedkope en effectieve barrièrematerialen. Deze opstelling is ook ontworpen en gebouwd als onderdeel van deze studie.

In geen van deze testen is gebruik gemaakt van een barrièremateriaal, zodat de degradatie waarschijnlijk sneller verloopt dan bij samples die beschermd getest zullen worden.

Deze test zijn gecombineerd met een uitgebreide analyse van de samples met o.a. IV, EQE, IV(T), EL, PL, lock-in-thermografie, 4PP, Hall, UV-VIS-NIR, Raman, XRD, SEM-EDX, HIM en SIMS. Dit heeft geleid tot de volgende conclusies op over de degradatie van CIGS cellen en zijn componenten:

Molybdeen achtercontact

Het molybdeen achtercontact is gedegradeerd onder condities 1 en 3. Molybdeen degradeerde erg snel in de gecombineerde aanwezigheid van water en zuurstof, terwijl het redelijk stabiel is in de afwezigheid van één van deze materialen.

Molybdeen degradeerde door de vorming van molybdeen oxides. Deze laag, die zich meestal vormt op het oppervalk van de molybdeen, geleidt en reflecteert slecht. Het verschijnen van deze oxide laag bovenop de molybdeen kan daarom leiden tot een sample dat binnen een paar uur van een goede naar een zeer slechte geleiding gaat, wanneer gemeten aan het oppervlak. Deze laag bestaat uit MoO_3 gemengd met $MoO_{2.5}$ die wordt gevormd door de inbouw ('intercalatie') van Na^+ in een MoO_3 matrix. De intercalatie is mogelijk door de gelaagde structuur van MoO_3 en leidt tot de reductie van Mo^{6+} naar Mo^{5+}. Dit kan leiden tot de vorming van een beter geleidend degradatieproduct.

Verder werd het duidelijk dat meer poreus molybdeen, die bij hogere druk gesputterd is, kwetsbaarder is voor blootstelling aan 'damp heat'. Aan de andere kant zorgt de vorming van een toplaag van $MoSe_2$, zoals die voorkomen in een CIGS zonnecel, voor samples die stabieler zijn onder 'damp heat' condities.

Zink oxide frontcontact

Het zink oxide frontcontact is gedegradeerd onder condities 1 en 3. Aluminium gedoteerd zink oxide (ZnO:Al) degradeert via een gradueel proces, die begint bij de lucht/ZnO:Al interface en langzaam doorgaat in de richting van het substraat. De degradatie wordt veroorzaakt door de langzame diffusie van water en CO_2door de korrelgrenzen. In de afwezigheid van water of CO_2 is ZnO:Al zeer stabiel.

In gedegradeerd ZnO:Al zijn verhoogde concentraties van water en CO_2 (en ook zwavel en chloor) aangetroffen. Dit wijst erop dat er $Zn(OH)_2$ en $Zn_5(CO_3)_2(OH)_6$ of vergelijkbare materialen, gebaseerd op chlorides en sulfaten gevormd zijn. De diffusie van en de reactie met water en CO_2 leidt tot een verhoogde potentiaal barrière in de korrelgrenzen in het polykristallijne ZnO:Al. Dit leidt dan weer tot een verlaging van de elektronmobiliteit en dus geleiding, terwijl de optische transmissie constant bleef.

Complete CIGS zonnecellen

De complete CIGS zonnecellen, die bestaan uit een stapel met natriumkalk glas substraat gevolgd door molybdeen (Mo)/$Cu(In,Ga)Se_2$ (CIGS)/Cadmium sulfide (CdS)/intrinsiek zink oxide (i-ZnO)/aluminium gedoteerd zink oxide (ZnO:Al), zijn gedegradeerd onder condities 1, 2 en 3. De zonnecellen degradeerden snel door de diffusie van moleculen vanuit de atmosfeer (zoals water en CO_2) en vanuit de cel zelf. De diffusie van water en CO_2 leidde vooral tot een verhoging van de serie weerstand van ZnO:Al en tot het oplossen van deze laag in de buurt van de korrelgrenzen wat leidde tot het verschijnen van gaten en een sterke afname in de kortsluitstroom.

Verder werd het duidelijk dat vooral natrium maar mogelijk ook het andere alkali-element kalium, een belangrijke rol spelen in de degradatie van CIGS zonnecellen. Wanneer alkali-rijke en alkali-arme CIGS zonnecellen werden blootgesteld aan 'damp heat' en verlichting, hebben de alkali-rijke samples een hogere initiële efficiëntie, maar degradeerden ook binnen honderd uur, terwijl de alkali-arme samples relatief stabiel waren. De degradatie van alkali-rijke samples leidde tot de vorming van natriumrijke gebieden in de depletieregio. Dit wordt waarschijnlijk veroorzaakt door de migratie van Na^+ vanuit de korrelgrenzen in de CIGS laag naar deze depletieregio. Deze migratie kan komen door het elektrisch veld dat gevormd wordt door het verlichten van de zonnecellen, in een proces dat vergelijkbaar is aan potentiaal geinduceerde degradatie (Potentiaal geInduceerde Degradatie, PID). Deze migratie resulteerde in de vorming van kortsluitpaden, die zorgde voor een erg lage kortsluitweerstand en open circuit voltage. Voor zowel de alkali-arme en rijke cellen treedt nog een andere faalmode op tijdens blootstelling aan damp heat en licht: Dit is het langzaam toenemen van de serieweerstand, dat waarschijnlijk deels veroorzaakt wordt door de migratie van water en andere atmosferische moleculen in de ZnO:Al. Aangezien de alkali-rijke cellen een snellere weerstandstoename laten zien, is het waarschijnlijk dat daarnaast ook de migratie van natrium een rol speelt.

Aanbevelingen voor de toekomst

Aangezien alle CIGS bedrijven en onderzoeksinstituten natrium en eventueel kalium gebruiken om de efficientie te verhogen, zou het onderzoek in de volgende stap zich moeten richten op de ontwikkeling van een stabiele zonnecel met natrium en/of kalium. Deze laatste lijkt langzamer te diffunderen en zou dus dezelfde efficiëntievoordelen, maar geen stabiliteitsnadelen kunnen hebben. De route die we kunnen gaan volgen is het maken van stabiele cellen door lage hoeveelheden natrium met een post depositie behandeling (Post Deposition Treatment, PDT) aan te brengen, of door een deel van het natrium te vervangen door kalium. Dit leidt hopelijk tot het verkrijgen van zonnecellen die zowel een hoge initiële efficiëntie en een lange, voorspelbare levensduur hebben.

Daarnaast zouden toekomstige testen zich ook moeten richten op CIGS zonnecellen en modules die zijn gemaakte met alternatieve depositietechnieken of met andere materialen. Kandidaten voor deze testen zijn onder andere CIGS absorber lagen gedeponeerd met een tweestaps proces en alternatieve buffers, transparante geleiders en alternatieve interconnectie methodes.

Op de langere termijn zou deze kwalitatieve kennis ook moeten worden vertaald in een kwantitatief model. Dit kan bijvoorbeeld worden aangepakt door het modelleren van de veranderingen van elektrische, optische en compositie parameters door de degradatie. Dit model kan dan worden gebruikt om het gedrag van werkende CIGS panelen te voorspellen.

Résumé

Une introduction commerciale à grande échelle de systèmes photovoltaïques (PV) au CIGS, nécessite des modules à bas prix, à haut rendement et une durée de vie longue et prédictive. Malheureusement, les connaissances sur la durée de vie des systèmes PV au CIGS sont limitées, ce qui se répercute dans les résultats des études sur le terrain : des vitesses de dégradation, variant de 0% jusqu'à 4% par an ont été observées. Considérant que les modules sont garantis de conserver 80% de leur rendement initial après 20 ans d'utilisation sur le terrain, les vitesses de dégradation sont souvent trop grandes mais aussi trop imprédictibles. Dans le but de réduire ces vitesses de dégradation, il est essentiel d'obtenir plus de connaissances sur le comportement de la dégradation.

Ces connaissances pourraient aussi permettre de réduire les coûts de production: comme les tests sur le terrains et les tests accélérés en laboratoire ont tous les deux montré qu'une humidité élevée et une haute température ont un impact néfaste sur les systèmes PV au CIGS, les modules sont laminés avec une barrière de matière qui empêchent la pénétration de l'humidité. Pour les modules rigides, le verre est un excellent choix de barrière, mais pour rendre les modules flexibles, un coûteux revêtement multicouches organique-inorganique est souvent utilisé. Des cellules solaires au CIGS intrinsèquement plus stables limiteraient aussi le coût de la barrière et faciliteraient une introduction à grande échelle sur le marché des systèmes PV au CIGS flexibles.

Par conséquent je me suis concentrée pendant cette étude sur l'identification des mécanismes de dégradation dans les cellules solaires à couches fines au CIGS. Comme ces cellules sont composées d'au moins cinq couches individuelles qui s'influencent les unes les autres mais qui influencent aussi le comportement de la dégradation, plusieurs couches ont aussi été étudiées individuellement. Les connaissances obtenues pendant l'étude de ces couches isolées, ont ensuite été utilisées pour interpréter le comportement de la dégradation des cellules solaire au CIGS complètes.

Dans cette thèse, je propose un mécanisme de dégradation pour le contact arrière en molybdène, le contact supérieur en oxyde de zinc et aussi pour les cellules solaires au $Cu(In,Ga)Se_2$ complètes. L'étude de ces mécanismes a été réalisée en exposant les échantillons déposés sous différentes conditions, à divers tests de durée de vie accélérée, combinée avec une analyse extensive des échantillons avant, pendant et après les tests de durée de vie. Ces tests devraient donner des indications sur l'exposition à long terme sur le terrain des modules au CIGS, il est cependant à noter que la validité de la comparaison des tests en laboratoires et des tests sur le terrain est toujours en discussion.

Les tests suivants ont été utilisés dans cette étude.

1. ‘Chaleur humide’ standard - exposition des échantillons à 85°C et 85% d’humidité relative (RH). Un millier d’heures d’exposition à ces conditions standard devrait être comparable à 20 ans d’exposition sur le terrain à Miami (facteur d’accélération 175x). Il est important de noter que la littérature a rapporté que les facteurs d’accélération de ces tests varient de 10x à 700x, donc l'extrapolation doit être manipulé avec précaution.
2. Test de ‘dégradation hybride’ (https://www.youtube.com/watch?v=Zmy5tb-2NK8) – une combinaison d’exposition à une ‘chaleur humide’ et d’une illumination à 1.5 AM. Cela permet simultanément de dégrader les échantillons avec une humidité et une température élevée tout en les exposant à la lumière. Les échantillons sont aussi en permanence surveillés in-situ, pour étudier le comportement de la dégradation. Cette installation a été imaginée et construite dans le cadre de cette étude et a attiré l’attention de partis extérieurs. Ainsi, un consortium de trois PME néerlandaises (Eternal Sun, Hielkema Testequipment et ReRa) travaillent actuellement sur la commercialisation de cette installation.
3. Exposition aux ‘substances atmospheriques’ – les cellules et les couches individuelles ont été exposées aux différentes substances présentes dans l’air, comme l’oxygène, l’azote, le dioxyde de carbone, l’eau et à des combinaisons de ces substances. Cela permet d’aider l’identification des substances responsables de la dégradation des cellules solaires au CIGS. Cela peut aussi mener à l’identification des mécanismes de dégradation et peut permettre l’optimisation de la rentabilité et de l’efficacité des matériaux utilisés pour l’encapsulation. Cette installation a aussi été imaginée et conçue dans le cadre de cette étude.

Ces tests, combinés avec une analyse extensive des échantillons, avec entre autres IV, EQE, IV(T), EL, PL, thermographie IR dynamique, 4PP, Hall, UVVIS, Raman, XRD, SEM-EDX, HIM et SIMS, ont conduits aux conclusions suivantes sur la dégradation des cellules solaires au CIGS et de ses constituants.

Contact arrière en molybdène

Le contact arrière en molybdène a été testé sous les conditions 1 et 3. Le molybdène se dégrade très rapidement en la présence combinée d’eau et d’oxygène, alors qu’il est raisonnablement stable lorsque l’une de ces deux espèces est absente.

Ces expériences nous ont appris que le molybdène se dégrade dû à la formation d’oxydes de molybdène. Cette couche, qui se forme souvent à la surface du molybdène est non-conductrice et a une faible réflectivité. L'apparition de cette couche d'oxyde peut donc mener à une brutale chute de la conductivité. Cette couche est composée de Mo(IV)O_3 mixée avec du Mo(V)$O_{2.5}$, qui se forme en la présence de sodium dû à l'intercalation de Na^+ dans MoO_3. Cela est rendu possible grâce à la structure stratifiée de MoO_3 et conduit à la réduction partielle de Mo^{6+} et Mo^{5+}. Cela peut aboutir à la formation d'un produit issu de la dégradation plus conducteur. Il a été observé qu'un molybdène plus poreux, déposé avec une pression plus importante, est plus vulnérable à l'exposition de chaleur humide qu'un molybdène plus dense, tandis que la formation d'une couche de $MoSe_2$ à sa surface rends le molybdène plus stable lorsque exposé à des conditions de dégradation, comme chaleur humide.

Contact supérieur en oxyde de zinc

Le contact supérieur en oxyde de zinc a été testé sous les conditions 1 et 3. L'oxyde de zinc dopé à l'aluminium (ZnO:Al) se dégrade via un processus graduel, qui commence à l'interface air/ZnO:Al et qui lentement progresse en direction du substrat. Cette dégradation est causée par la lente diffusion d'eau et de CO_2 via les joints de grains. En l'absence d'une de ces deux entités le matériau reste très stable.

A l'intérieur du ZnO:Al dégradé, une plus forte concentration d'eau et de CO_2 (mais aussi de souffre et de chlore) ont été observées, ce qui peut indiquer la formation de matériaux comme $Zn(OH)_2$ et $Zn_5(CO_3)_2(OH)_6$, ou d'autres composés similaires, à base de sulfate ou de chlorure. La diffusion et les réactions dues à l'eau et au CO_2 conduisent à une augmentation de la barrière de potentiel aux joints de grains dans la structure poly-cristalline de ZnO :Al. Cela entraîne une diminution de la mobilité des électrons et donc de la conductivité, la transmission de ZnO:Al reste globalement constante.

Cellule solaire au CIGS complète

Les cellules solaires complètes au CIGS, composées de verre sodocalcique (SC)/molybdène(Mo)/Cu(In,Ga)Se_2 (CIGS)/sulfure de cadmium (CdS)/oxyde de zinc intrinsèque (i-ZnO)/oxyde de zinc dopé à l'aluminium (ZnO:Al) ont été testées sous les conditions 1, 2 et 3. Il est important de noter qu'aucune barrière n'a été utilisée. Les cellules solaires se dégradent à cause de la diffusion d'entités issues de l'atmosphère, comme l'eau et le CO_2, mais aussi issues des cellules elles-mêmes. La diffusion de l'eau et du CO_2 conduit principalement à une augmentation de la résistance en série du ZnO :Al, ainsi qu'à une dissolution locale des cellules solaires au CIGS, conduisant à la formation de trous.

Il a aussi été observé que des éléments alcalins et notamment le sodium, jouent un rôle prépondérant dans la dégradation des cellules solaires au CIGS. Lorsque des cellules solaires au CIGS riches en alcalins et d'autres pauvres en alcalins ont été exposées à la lumière sous des conditions de chaleur humide, les échantillons riches en alcalins ont un meilleur rendement de conversion initial, mais se dégradent sévèrement dans les 100 premières heures, alors que les échantillons pauvres en alcalins restent relativement stables. La dégradation des échantillons riche en alcalins a conduit à la formation de points riches en sodium dans la zone de déplétion. Cela est vraisemblablement dû à la migration de Na^+ des joints de grains au sein de la couche de CIGS jusqu'à la zone de déplétion. Cette migration est peut-être liéà un champ électrique résultant de l'exposition à la lumière, causé par un mécanisme similaire à une dégradation à potentiel induit (PID). La migration mène probablement à la formation de voies de dérivation, responsables de la très faible valeur de la résistance en parallèle et de la tension en circuit ouvert. De plus, l'ingression de l'eau dans le ZnO:Al semble être responsable d'une lente mais constante augmentation de la résistance en série des deux types d'échantillons, tandis que la migration du sodium conduit à une augmentation plus sévère de la résistance en série pour les échantillons riches en alcalins .

Étude future

Comme la plupart des compagnies de cellules solaires au CIGS et des instituts de recherche utilisent du sodium et du potassium pour augmenter l'efficacité PV, la prochaine étape de la recherche devrait se concentrer sur la production de cellules solaires avec du sodium et/ou du potassium, car ce dernier semble se diffuser plus lentement. La route à suivre, consisterait en l'introduction de petites quantités de sodium par un traitement post déposition, ou en l'optimisation de cellules solaires avec une grande quantité de potassium et une faible quantité de sodium. On peut ainsi espérer obtenir un haut rendement initial et une dégradation réduite.

En outre, les essais futurs devraient se concentrer aussi sur les cellules solaires et des modules CIGS qui ont été obtenus avec d'autres techniques de dépôt ou d'autres matériaux. Les candidats à ces essais comprennent couches absorbantes CIGSdéposée en utilisant un procédé en deux étapes et d'autres couches d'interface, transparent conducteurs et les méthodes d'interconnexion alternatives.

À plus long terme, cette connaissance qualitative devrait également être traduit dans un modèle quantitatif. Cela peut par exemple être traitée par la modélisation des modifications de paramètres, de la composition, optiques ou électriques par le dégradation. Ce modèle peut alors être utilisé pour modifier le comportement de la CIGS de travail panneaux à prévoir.

APPENDICES

Appendix A: Analysis Techniques

Appendix B: Abbreviations Abbrevations

Publications and presentations

Dankwoord / Acknowledgements

Curriculum Vitae

Appendix A: Analysis techniques

All samples in this thesis have been extensively characterised before, after and in some case during degradation. The used analysis techniques have been summarised in Table A.1.

Table A.1 Analysis techniques and their abbreviations as used in this thesis.

Analysis technique	Abbreviation	Measured characteristics
Four-point probe		Resistivity and sheet resistance
Spectrophotometry	UV-VIS-NIR	Transmission, reflection and absorption
Light microscopy		Visual and optical characteristics
Scanning Electron Microscopy-Elemental Dispersive X-ray spectroscopy	SEM-EDX	Morphological, compositional and structural properties
X-Ray Diffraction	XRD	Structural and compositional parameters
Raman spectroscopy		Surface composition
(Time-of-Flight) Secondary Ion Mass Spectrometry	(ToF)-SIMS	Compositional depth profiling
X-ray photoelectron spectroscopy	XPS	Surface composition
Hall effect		Resistivity, electron mobility and carrier concentration
Dektak profilometer		Thickness and macroscopic roughness
Helium Ion Microscopy	HIM	Structural properties
Current-voltage measurements	IV	External parameters of the solar cell
External Quantum Efficiency / Spectral Response	EQE / SR	Wavelength dependent light absorption
Lock-In Thermography	LIT	Spatial defects
Inductively Coupled Plasma – Mass Spectrometry	ICP-MS	Metal content in water
Temperature dependent current-voltage measurements	IV(T)	External parameters of the solar cell at low temperature

More information about these techniques as used for thin film solar cells can be found in reference [1].

References

[1] D. Abou-Ras, T. Kirchartz U., Rau, Advanced Characterisation Techniques for Thin Film Solar Cells, Wiley-VCH Verlag GmbH & Co. KGa AWeinheim (2011)

Appendix B: Abbreviations A-O

a-Si:H	Hydrogenated amorphous silicon
AFM	Atomic Force Microscope
ALD	Atomic Layer Deposition
ALT	Accelerated lifetime testing
CBD	Chemical Bath Deposition
CIGS	$Cu(In,Ga)Se_2$
CIGSSe	$Cu(In,Ga)(Se,S)_2$
CIS	$CuInSe_2$
CISSe	$CuIn(Se,S)_2$
CTE	Coefficient of Thermal Expansion
CV	Capacitance Voltage
DC	Direct Current
DH	Damp heat
DLTS	Deep Level Transient Spectroscopy
EL	Electro Luminescence
EQE	External Quantum Efficiency
EVA	Ethylene-Vinyl Acetate
FF	Fill factor
FTO	Fluorine Doped Tin Oxide
GB	Grain Boundary
G_{sh}	Shunt conductivity
h	Hours
IEC	International Electrotechnical Commission
ILGAR	Ion Gas Layer Reaction
ITO	Indium Tin Oxide
IV(T)	Temperature dependent current-voltage measurement
IZO	Indium Zinc Oxide
J_{sc}	Short circuit current density
LIT	Lock-In Thermography
LPCVD	Low Pressure Chemical Vapour Deposition
µ	Mobility
m	Metre
µm	Micrometre
mm	Millimetre
n	Carrier concentration
nm	Nanometre
OVC	Ordered vacancy compound

Appendix B: Abbreviations P-X

PCB	Printed Circuit Board
PDT	Post Deposition Treatment
PECVD	Plasma Enhanced Chemical Vapour Deposition
PET	Polyethylene terephtalate
PID	Potential Induced Degradation
PL	PhotoLuminescence
PLD	Pulsed Laser Deposition
PV	Photovoltaics
PVB	Polyvinylbutyral
R	Sheet resistance
R_c	Contact resistance
RF	Radio Frequency
RH	Relative humidity
R_s	Series resistance
R_{sh}	Shunt resistance
RT	Room temperature
ρ	Resistivity
s-ALD	Spatial Atomic Layer Deposition
SKP	Scanning Kelvin Probe
SLG	Soda Lime Glass
TCO	Transparent Conductive Oxide
(TOF)-SIMS	(Time-Of-Flight) Secondary Ion Mass Spectrometry
TPAT	Tedlar/PET/Al foil/Tedlar
TPT	Tedlar/PET/Tedlar
TRPL	Time Resolved Photoluminescence
V_{oc}	Open circuit voltage
WVTR	Water Vapour Transmission Rate
XES	X-ray Emission Spectroscopy

Publications and presentations related to this PhD thesis

Articles and proceedings

1. **M. Theele**n, C. Foster, H. Steijvers, N. Barreau, C. Frijters, Z. Vroon, M. Zeman, *The impact of atmospheric species on the degradation of CIGS solar cells and molybdenum films*, submitted to Proc. SPIE (2015)
2. **M. Theelen**, A. Liakopoulou, F. Daume, V. Hans, H. Steijvers, N. Barreau, M. Tomassini, Z. Vroon, M. Zeman, *Temperature Dependency of CIGS solar cells on soda lime glass and polyimide: a comparison*, submitted to Progress in Photovoltaics: Research and Applications (2015)
3. **M. Theelen** and F. Daume, *Stability of Cu(In,Ga)Se$_2$ Solar Cells: A literature review,* submitted to Progress in Photovoltaics: Research and Applications (2015)
4. **M. Theelen**, S. Harel, M. Verschuren, M. Tomassini, A. Hovestad, N. Barreau, J. van Berkum, Z. Vroon, M. Zeman, *Degradation mechanisms of the molybdenum back contact for CIGS solar cells*, submitted to Surface and Coatings Technology (2015)
5. **M. Theelen**, N. Barreau, H. Steijvers, V. Hans, Z. Vroon, M. Zeman, *Degradation of CIGS solar cells due to the migration of alkali elements*, submitted to Proc. 42nd IEEE PVSC (2015)
6. **M. Theelen,** H. Steijvers, N. Barreau, M. Buffière, G. Brammertz, M.G. Flammini, R.J. van Vugt, Z. Vroon, M. Zeman, *In-situ monitoring of the accelerated performance degradation of thin film solar cells,* submitted to Proc. 42nd IEEE PVSC (2015)
7. **M. Theelen**, C. Foster, N. Barreau, H. Steijvers, Z. Vroon, M. Zeman, *Influence of atmospheric species water, oxygen, nitrogen and carbon dioxide on the degradation of CIGS solar cells,* Solar Energy Materials & Solar Cells 141 (2015) 49–56
8. **M. Theelen**, V. Hans, N. Barreau, H. Steijvers, Z. Vroon and M. Zeman, *The impact of sodium and potassium on the degradation of CIGS solar cells*, acceleration publication in Progress in Photovoltaics: Research and Applications 23 (2015) 537-545
9. **M. Theelen**, C. Foster, S. Dasgupta, Z. Vroon, N. Barreau, M. Zeman, *The influence of atmospheric species on the degradation of aluminum doped zinc oxide and Cu(In,Ga)Se$_2$ solar cells*, Proc. SPIE 9179, 91790K (2014)
10. **M. Theelen**, N. Barreau, F. Daume, H. Steijvers, V. Hans, A. Liakopoulou, Z. Vroon and M. Zeman, Accelerated performance degradation of CIGS solar cell determined by in-situ monitoring, Proc. SPIE 9179, 91790I (2014)
11. **M. Theelen**, S. Dasgupta, Z. Vroon, B. Kniknie, N. Barreau, J. van Berkum, M. Zeman, *Influence of atmospheric species water, oxygen, nitrogen and carbon dioxide on the degradation of aluminum doped zinc oxide layers*, Thin Solid Films 565 (2014) 149–154
12. **M. Theelen**, K. Polman, M. Tomassini, N. Barreau, H. Steijvers, J. van Berkum, Z. Vroon, M. Zeman*, Influence of deposition pressure and selenisation on damp heat*

degradation of the Cu(In,Ga)Se$_2$ back contact molybdenum, Surface & Coatings Technology 252 (2014) 157–167

13. **M. Theelen**, Z. Vroon, N. Barreau, M. Zeman, *Degradation studies of aluminum doped zinc oxide*, Photovoltaics International 23 (2014) 58-64
14. **M. Theelen**, T. Boumans, F. Stegeman, F. Colberts, A. Illiberi, J. van Berkum, N. Barreau, Z. Vroon, M. Zeman, *Physical and chemical degradation behavior of sputtered aluminum doped zinc oxide layers, for Cu(In,Ga)Se$_2$ solar cells*, Thin Solid Films 550 (2014) 530–540
15. A. Illiberi, R. Scherpenborg, **M. Theelen**, P. Poodt, F. Roozenboom, *On the environmental stability of ZnO thin films by spatial atomic layer deposition*, Journal of Vacuum Science and Technology A: Vacuum surfaces and films 31 6 (2013)
16. A. Kuypers, R. Knaapen, **M. Theelen**, M. Meuris, M. van der Vleuten, W. Zijlmans, *Cost-efficient equipment for CIGS production*, Photovoltaics International 20 (2013) 61-69
17. **M. Theelen**, M. Tomassini, H. Steijvers, Z. Vroon, N. Barreau, M. Zeman, *In-situ Analysis of the Degradation of Cu(In,Ga)Se$_2$ Solar Cells*, Proc. 39th IEEE PVSC (2013) 2047-2051
18. **M. Theelen**, H. Steijvers, Z. Vroon, M. Tomassini, N. Barreau and M. Zeman, *A unique hybrid degradation setup for CIGS solar cells*, Proc. 9th ICCG (2012) 161-164
19. **M. Theelen**, M. Tomassini, N. Barreau, H. Steijvers, Annalisa Branca, Sylvie Harel, Z. Vroon, M. Zeman, *The impact of selenisation on damp heat degradation of the CIGS back contact molybdenum*, Proc. 38th IEEE PVSC 2 (2012) 1-6

Oral presentations without proceedings

This work has been presented at the following workshops, companies and research institutes:

- SPIE Optics and Photonics (San Diego, USA)
- International Workshop on CIGS Solar Cell Technology (Berlin, Germany)
- Photovoltaic Technical Conference (Aix-en-Provence, France)
- M2i conference (Sint Michielsgestel, the Netherlands)
- Sunday (Den Bosch, the Netherlands)
- Stability and annealing effects of ZnO workshop (Jülich, Germany)
- Durasol workshop (Aix-en-Provence, France)
- Solarion (Leipzig, Germany)
- PVcomB (Berlin, Germany)
- Forschungszentrum Jülich (Jülich, Germany)
- University Luxembourg (Luxembourg)
- Université de Nantes (Nantes, France)
- Delft University of Technology (Delft, the Netherlands)

- TNO/Solliance (Eindhoven, the Netherlands)
- M2i meetings (the Netherlands)

This work has also been presented with posters at various occasions.

Awards and nominations

- **M. Theelen**, H. Steijvers, N. Barreau, Z. Vroon, M. Zeman, *A unique hybrid degradation setup of CIGS solar cells*, M2i conference (2013) in Noordwijkerhout
  – winner of the poster prize
- **M. Theelen**, H. Steijvers, Z. Vroon, N. Barreau and M. Zeman, *In-situ monitoring of the degradation of CIGS solar cells*, eMRS Spring meeting (2014)
  – winner of the poster prize
- **M. Theelen**, H. Steijvers, V. Hans, N. Barreau, Z. Vroon, M. Zeman, The impact of sodium on CIGS solar cell degradation, M2i conference (2014) in St Michielsgestels
  – winner of the poster prize
- **M. Theelen**, *Degraded molybdenum*
  – winner of TNO 'Show your art spirit' 2014
- **M. Theelen**, *Reliability of CIGS solar cells*
  – Nominated for Solar Thesis Award 2014
- **M. Theelen**, Unique lifetime testing for next generation solar cells
  – Nominated for the TNO Energieprijs 2013

Het dankwoord / the acknowledgements

Beste lezer,

Na ruim vier jaar werken aan dit proefschrift, heb ik ook nog een paar uur besteed aan het schrijven van het dankwoord. Mocht je de volledige wetenschappelijke inhoud hebben overgeslagen en meteen op weg zijn gegaan naar het dankwoord, allereerst een klein verzoekje: blader ook eens door de andere 287 pagina's, ik heb er best veel moeite in gestoken en er staan ook plaatjes in!

Dan nu het echte dankwoord: omdat ik bij drie groepen heb gewerkt, plus nog welkom ben geweest op vele andere plaatsen, wordt dit een lang verhaal (mogelijk draagt het feit dat ik soms een tikkeltje lang van stof ben hieraan bij). En dan heb ik natuurlijk niet iedereen genoemd die ik had moeten noemen!

In een dankwoord begin je meestal met de belangrijkste persoon voor het gedane werk en deze traditie zal ik zeker niet breken. Ik twijfel er wel een beetje aan of **Henk** zich werkelijk de belangrijkste persoon voelt, maar eerlijk is eerlijk, zonder Henk stond ik waarschijnlijk vertwijfeld in het lab naar een houtje-touwtje opstelling te staren. 'Mirjams promotie-opstelling' is eigenlijk wel Henks kindje, stiekem wilde hij helemaal niet dat ik er aan zou komen. Hopelijk komt onze opstelling over een paar jaar over de hele wereld voor.

Dan mijn adviseurs, of zoals **Zeger** het graag hoort: (co-)promotors. In **Miro** en Zeger had ik twee heel verschillende copromotors, die mij elk op hun eigen manier heel fijn gesteund heeft. Zeger, mijn excuses voor alle keren dat ik niet meteen naar je geluisterd heb, maar ik vond het erg prettig om met je te werken en bij tijd en wijlen een beetje te kibbelen. Bedankt voor al je tijd en moeite, en ik hoop dat we nog vaak zullen samenwerken, ik kan zeggen dat ik onze frequente overleggen nu al mis. Miro, jij bent een man die aan twee woorden genoeg heeft, in een half uur door de artikelen kon bladeren en exact de pijnpunten kon identificeren. En nog beter dan dat, ook kon vertellen hoe ik deze problemen in een paar uur kon oplossen. Beide heel erg bedankt voor jullie hulp!

Ook vanuit TNO had ik hulp om werkelijk aan mijn promotie te kunnen werken: **Peter** en **Ardi**. Ik ben me er altijd volledig van bewust geweest dat promoveren in een complexe en turbulente omgeving zoals TNO risico's met zich meebracht. Door jullie heb ik niet alleen de kans gekregen om hier aan te beginnen, maar, nog belangrijker, ook om het af te maken. De tijden leenden zich hier niet altijd even goed voor, dus dat hier een mooi boekje ligt heb ik ook aan jullie te danken.

Then I would like to move a little bit further away, to France. Because, let's face it: What is a CIGS PhD without a CIGS expert and samples? I can say I am really happy to have met my third advisor **Nicolas** during that PVSEC in beautiful Valencia. Nicolas, you don't care about politics, but you care about science and CIGS… and these were very important for me. I have to say that your knowledge about CIGS seems almost endless to me, and without your input the quality of this thesis would without doubt be a lot lower.

Of course the other people in Nantes were also very important for this thesis: **Matthieu**, your extensive study on molybdenum allowed me to study its degradation, a subject on which we have various articles together. **Sylvie, Ludo**, **Marie-Paule**, thank you for the XPS measurements and the many discussions we had, which really helped me forward. And Sylvie, thank you for the nice lunches and even dinner together! And of course thank you to all the other people in Nantes, including of course **Marie**, who I saw again in the Netherlands – my times in France helped me improve my French a lot, although I am ashamed to say that I still cannot follow your lunch table discussions.

Dan de studenten die aan dit werk hebben bijgedragen: omdat ik mijn promotie in de helft van de tijd heb moeten doen, was jullie werk erg belangrijk. Je kan dat ook wel zien aan de vele namen van stagiaires bij de artikelen in dit proefschrift. Mijn allereerst stagiair was **Fallon**: altijd erg bescheiden maar ik kan je verzekeren dat jouw werk een prachtige basis heeft gelegd voor veel van het werk dat er daarna nog is gekomen. Daarna de droom voor elke stage-begeleider: een soort van zelfsturend team bestaande uit **Twan** en **Felix,** die samen experimenten planden, uitvoerden en achterliggende theorieën hebben bedacht. Jullie metingen zijn integraal in een artikel en dit proefschrift opgenomen.

Then of course my foreign trio, that introduced me in the southern way of working: **Katerina**, with your cheerful conversations and southern temperament, I enjoyed meeting you. **Supratik,** I admired your eternal good mood, while **Vasileios** showed me the advantages of a laid-back life.

Krista: altijd bescheiden, een beetje stil, maar ondertussen zeer goed bezig: metingen, data-interpretatie en een fitprogramma dat ik zelf waarschijnlijk niet zo snel had kunnen schrijven. Krista's opvolger was **Melvin**: wederom erg goed werk, snel van begrip en nog goed in spelletjes ook: je bent, zover ik me kan herinneren, de eerste die mij in zijn eerste spel *Ballonvaarders* verslagen heeft. Jouw aanwezigheid maakte mijn trip naar Nantes een stuk leuker, en ook een stuk gezonder, aangezien onder jouw invloed de fiets de tramrit naar de universiteit boven op de heuvel vervangen had. Ook **Jos** moet ik nog even vermelden: je viel niet helemaal onder mijn promotie, maar je werk aan röntgendiffractie heeft zeker geholpen. Hierna kwam **Dyme**, met

vele theorieën en een groot enthousiasme.
Then another foreign student, this time the French **Vincent**. Since your background and your research topic was so different from mine, I was not really sure how to arrange everything. This uncertainty proved completely unnecessary, already from the beginning I noticed that you could arrange everything yourself. Your work has contributed greatly to the content of this thesis. At the same time I was so lucky to have **Chris** as a student: an intern with a high level of independence and knowledge, who could even correct my English writing.
En dan, als laatste **Robin**, die kwam terwijl onze groep net naar de High Tech Campus was verhuisd, terwijl zijn opstelling nog op de Rondom stond. Mijn dank is groot dat je zonder enige klachten vele malen op en neer bent gefietst tussen je degradatie en je meetopstelling. I also would like to thank **Marco** and **Kyo**: your work is no longer part of this thesis, but thanks to your efforts, we can still continue the work and get nice results.

Dan mijn vele TNO en Solliance collega's die mij op een of andere manier geholpen hebben, dan wel door hun input in dit werk, dan wel in de gezellige tijd die we samen hebben doorgebracht. Ik kan niet iedereen hier noemen, maar iedereen in ieder geval erg bedankt!

Allereerst mijn kamergenoten tijdens mijn promotie: de eerste jaren van mijn promotie heb ik mijn kamer gedeeld met 'de man die alles kan': **Frank**: een huis verbouwen, een machine opbouwen, mijn kast fixen (waarvoor dank), een fijn gesprek voeren en natuurlijk ook presentaties geven. Mijn volgende kamergenoot was **Ando**, met hem heb ik veel kunnen lachen, discussiëren over uiteenlopende onderwerpen en hij heeft mij ook veel geleerd, zoals het een goed schoolhoofd betaamt.
In het Solliancegebouw werd het wat drukker: gezelligheid kwam van vele collega's van Holst, TNO, VDL…. én mijn drie vaste kamergenoten **Harmen**, **Joop** en **Dorrit.** Harmen, bedankt voor je humor en scherpe blik! En voor al je hulp met en discussies over allerlei meettechnieken. Ik hoop dat je je bureau weer snel in gebruik gaat nemen. Joop, je bent de ideale sparringpartner voor van alles en nog wat (met de nadruk op 'nog wat'). Ik moet trouwens wel toegeven dat niet alleen 'onschuldige' toeschouwers, maar ook ikzelf, geregeld onze gesprekken niet kan volgen. En dan natuurlijk nog Dorrit: ze lijkt brave huismoeder, maar dat is slechts schijn… Meestal erg grappig en fijn om samen mee te werken, met lekker scherpe humor. Dorrit, bedankt voor de samenwerken aan het *betrouwbaarheid*sstuk van mijn onderzoek en voor het doorlezen en bekijken van talloze publicaties, presentaties en projectvoorstellen!
In dit proefschrift staan heel veel resultaten van vele typen metingen – en dan staat

er nog maar een klein deel van de resultaten werkelijk beschreven. Lang niet alle metingen zijn gedaan door mijzelf of mijn studenten: Een co-auteur van veel van mijn artikelen is **Jurgen** van Philips Innovation Services, die vele SIMS metingen heeft gedaan en de betekenis van de metingen heeft uitgelegd. I also want to thank **Denis** from the University Lorraine for his measurements. Deze metingen waren zeker essentieel voor dit proefschrift. Datzelfde geldt voor de SEM, HIM en XPS metingen van **Arthur, Monique, Hans, Emile** (TNO) en **Bertil** (Philips Innovation Services). Heel veel dank ben ik ook verschuldigd aan **Klaas** van ECN die mij en mijn stagiaires altijd vrolijk heeft geholpen met mijn talloze metingen in zijn lab. Ook is hij altijd een goedgehumeurde bemiddelaar geweest in mijn eeuwige vete met de EQE! I also want to thank **Yael** from Jülich for her help with EL and PL.

In dit proefschrift zijn ook veel samples getest die gedeponeerd of geëtst zijn bij Solliance. Mijn speciale dank gaat hierbij uit naar **Henk R**, **Leo, Corné, Bas** en **Robert** voor onder andere sample depositie en aan **Linda, Jeroen** en **Edwin** voor hulp in het lab. Bedankt voor alle deposities, want zonder goede samples is er weinig degradatie-onderzoek te doen.

Door de jaren heen heb ik ook vele malen aangeklopt bij vele collega's met zeer uiteenlopende vragen. Vaak konden zij mij in een half uurtje uitleggen waar ik zelf anders weken literatuuronderzoek voor nodig zou hebben gehad. In het bijzonder wil ik hier **Paul**, **Arjan**, **Andrea, Erik, Sander** en **Guy** (imec) bedanken voor discussies over onder andere diffusie, corrosie, Origin, TCO's, betrouwbaarheidsonderzoek en zonnecel fysica.

En dan zijn er natuurlijk nog heel veel (oud-)collega's, die ik dankbaar ben voor alle gezellige dingen die we samen hebben gedaan. Natuurlijk alle mensen van de Bozo en de Ozo, mijn mede KidS cursisten en ook heel veel anderen. In het bijzonder wil ik, naast de bovengenoemde mensen **Marcel**, **Marc, Marinda, Sibe, Annalisa, Jurjen, Jing** en **Fieke** en hun partners, maar ook nog vele anderen bedanken voor de gezellige reizen, barbecues, borrels, dinertjes en vele andere dingen.

Naast de bovengenoemde mensen, zou ik nog vele andere mensen van TNO, ECN, Holst Center en andere plaatsen moeten noemen, mijn dank aan jullie allen is groot.

My PhD naturally often brought me to Delft. Especially during the first years, I had the privilege to discuss with many nice people and learn many new things. I especially would like to thank my room mates: in my first office, my neighbour **Mark** and me could discuss the world in all its aspects. I also spend great times with postdocs **Michael** and **Karol**, now in Germany and Nijmegen, our tough Italian **Andrea** and fresh father **Martijn**. After that, I had the pleasure sharing the office with **Lihao** and **Klaus**. Thanks to Lihao, I now understand a lot more about China (and I hope you

understand more about that small flat country in Europe)… and with Klaus, who is both very smart and very kind, I had front row seats to the real life in Berlin.
Furthermore, I would really like to thank the other part of the 1 fte scientific women staff in Delft: **Joke**, as well as **Marinus** and **Jimmy**, for the trips to Quantsol and the PhD startup workshop. And of course **Rudi, Olindo, Rene** and **Arno** for their explanations of everything about photovoltaics. During my work in the laboratory in Delft, I also had a lot of help from the technicians: **Stefaan**, **Jan-Chris** and especially **Martijn**, thank you for all your help and especially for your eternal patience! Then I would like to thank all other people in Delft who I did not mention: I thank you for all the nice times and hope that many will follow!

Hulp kwam niet alleen van de vele voor de hand liggende kanalen, maar ook nog van een aantal andere plaatsen. Natuurlijk moet ik **Hans** van Scheuten niet vergeten, die mij alweer acht jaar geleden met CIGS in aanraking heeft gebracht, en al die jaren tijdens korte ontmoetingen mij de juiste informatie en aanwijzingen kon verstrekken om weer door te gaan. Ook zijn collega's, waaronder **Wouter** en **Volker** ben ik dankbaar voor hun input. Ook met Smit Ovens medewerkers kon ik fijn overleggen, gesprekken met **Maarten** en **Ross** en al hun collega's hebben mij veel geleerd over de meer industriële kant van de CIGS wereld, en hun klanten brachten mij vaak weer op nieuwe ideeën en de vragen vanuit de markt.
During a CIGS workshop in Berlin in 2011, I also met **Felix**, working on his PhD thesis at Solarion. When we found out we had similar research interests, we have been working together. Many parts in this thesis also contain his work. I would like to thank you for the pleasant collaboration.

Verder is de degradatie-opstelling natuurlijk een erg belangrijk resultaat van deze promotie. Omdat sleutelen, solderen, programmeren, hameren en vele andere zaken niet horen tot mijn (vele) talenten, heb ik daar gelukkig veel hulp bij gehad. Natuurlijk van Henk, maar ook van vele anderen. In het bijzonder wil ik hier **Peter** van Hielkema Testequipment, **Erik** van ReRa Solutions, **Danny** van DEMO en **Stefan** en **Robert-Jan** van Eternal Sun en al hun collega's voor bedanken. Stefan, ik wil even zeggen dat ik met bewondering van dichtbij heb mogen meemaken dat 'jouw stage enigszins uit de hand is gelopen'. Ik hoop dat wij de komende jaren met z'n allen kunnen werken aan de verdere verbetering en het vermarkten van de opstelling, en dat hij over een paar jaar over de hele wereld verspreid én op de cover van het PV magazine staat. **Ilse** en **Cecile** wil ik graag bedanken voor hun hulp met de opmaak en de plaatjes.

Gelukkig had ik naast het werk ook nog een leven… met vrienden, familie en buren.

Allereerst wil ik mijn (adoptie-)mentorbroertjes en -zusjes **Stefanie, Sanne, Marlinda, Michiel** en **Dick** en hun partners bedanken voor alle leuke tijden samen sinds 2001. Ook mijn *Honours*vriendinnen **Lidi, Sanne, Andia** en **Loes** en hun partners (hierbij op verzoek een specifieke vermelding voor J. met de drie H's en D.d.B.) wil ik graag bedanken. Onze vele dingen samen, met name de reisjes, door heel Europa, waren altijd een goede manier om te ontspannen. In Eindhoven natuurlijk een bijzondere dank voor velen Gewissers en hun partners. De wandelingen en vakanties met **Martine, Jan, Valerie, Remco, Susan** en **Niek** wil ik graag even specifiek noemen. Hoewel ik me nog steeds afvraag waarom iemand om zeven uur 's ochtends wil gaan wandelen.

Een speciale dank is er natuurlijk ook voor mijn familie en schoonfamilie. **Ellen** en **Peter Paul** en schoonbroers en schoonzusjes, dank je voor jullie interesse en gezelligheid. **Jeroen** en **Tara**, bedankt voor de gezelligheid, BBQ's, high-teas en al het andere. **Papa** en **mama** wil ik natuurlijk ook bedanken: voor jullie steun, voor jullie interesse, voor al onze gesprekken en omdat jullie mij altijd het gevoel hebben gegeven dat jullie onvoorwaardelijk in mij geloven. En papa, bedankt voor het doorlezen van dit complete proefschrift. Met jouw hulp heb ik nog heel veel kleine foutjes kunnen verwijderen!

Zoals het hoort, zal ik mijn dankwoord ook eindigen met de belangrijkste persoon in mijn leven: **Gijs**. Hoewel ik de eerste jaren van mijn promotie zonder al teveel problemen heb doorgemaakt, was het laatste stuk wat zwaarder. Mijn liefste Gijs, mijn eigen prins met de witte gadgets, je was er altijd voor mij, en ik hoop dat we nog heel erg lang samen zullen zijn.

Mirjam

PS: Voor alle mensen die niet geloven dat het plaatje op de cover een echte, onbewerkte microscoopfoto van gedegradeerd molybdeen is, op de volgende pagina staat dezelfde plek op het sample op een andere vergroting:

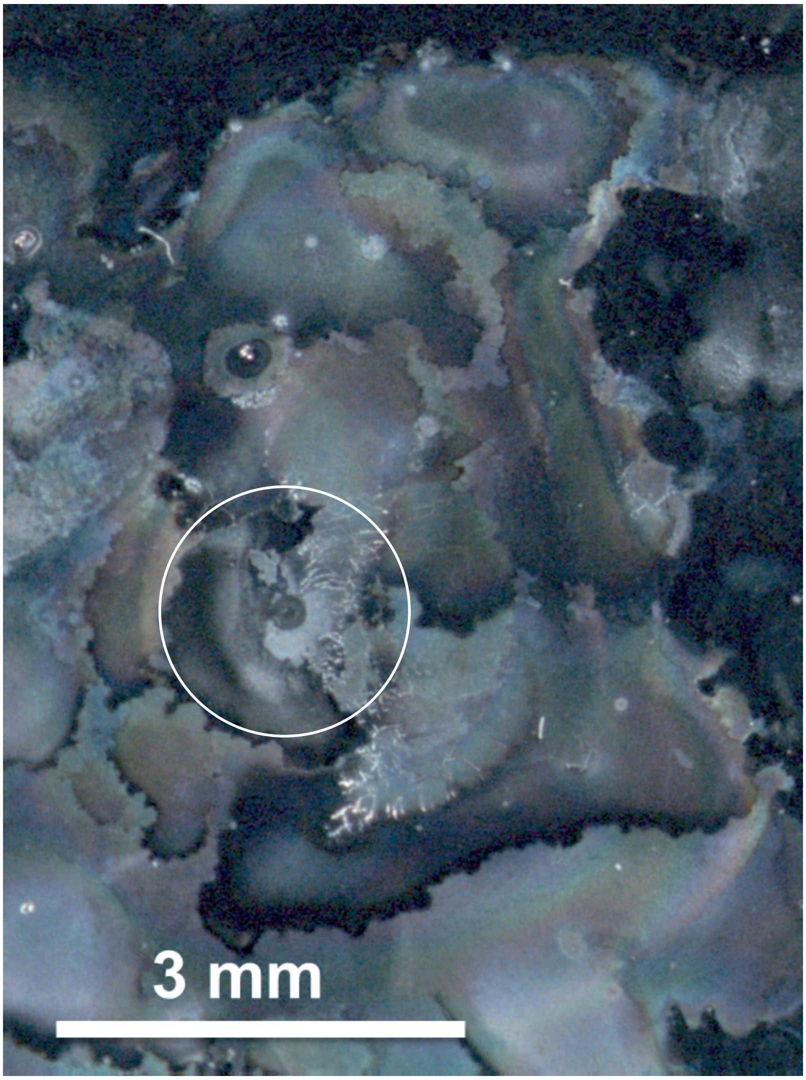
3 mm